ANALYSIS OF SOME MULTIPARTICLE FINAL STATES IN 10 AND 6 GeV/c K^-p INTERACTIONS

by

George Aristotle Grammatikakis

A Thesis presented for the degree of

Doctor of Philosophy

of the University of London

Department of Physics
Imperial College
London, S.W. 7

January 1972

ABSTRACT

The present thesis is mainly concerned with the study of some multiparticle final states occurring when 10 and 6 GeV/c negative kaons collide with stationary protons in a hydrogen bubble chamber.

After an introductory discussion on the 10 GeV/c K^-p experiment and its data collection, a detailed analysis of the reactions $K^-p \to p\bar{K}^o\pi^+\pi^-\pi^-$ and $K^-p \to p\bar{K}^o\pi^+\pi^-\pi^-\pi^o$ at this energy is presented; with data provided by an earlier experiment the same reactions and a third one, the $K^-p \to n\bar{K}^o\pi^+\pi^+\pi^-\pi^-$, are also investigated at 6 GeV/c incident momentum. The production of $K^{*-}(890)$, $\Delta^{++}(1236)$, ρ^o and ω resonances is copious at both energies and the partial cross-sections of the various channels contributing to each reaction are given; only in the third reaction there is appreciable non-resonant contribution. Though strongly produced in the first reaction, the ρ^o resonance is notably absent in the others.

Furthermore, a detailed study has been performed on the simultaneous resonance production $K^-p \to \Delta^{++} K^{*-}\pi^-$. Evidence is given for a double vector meson exchange dominance, and the process is well described by a Veneziano five-point amplitude based on this assumption.

The thesis concludes with a survey of other results of importance derived by the 10 GeV/c K^-p experiment.

To Eva

ἦ μεγάλα χάρις δώρῳ σύν ὀλίγῳ

And yet we should consider how we go forward.
To feel is not enough, nor to think, nor to move
nor to put your body in danger in front of an old loophole
when scalding oil and molten lead furrow the walls.

And yet we should consider towards what we go forward,
not as our pain would have it, and our hungry children
and the chasm between us and the companions calling from the opposite shore;
but it should be in some other way, I would say like
the long river that emerges from the great lakes enclosed deep in Africa
that was once a god and then became a road and a benefactor, a judge and
a delta;
that is never the same, as the ancient wise men taught,
and yet always remains the same body, the same bed, and the same sign
the same orientation.

G. SEFERIS

TABLE OF CONTENTS

INTRODUCTION

1. The Field of Elementary Particles, Ideas and Development . . . vi
2. The 10 GeV/c K^-p Experiment ix
3. The Present Thesis x

CHAPTER I. THE PRODUCTION AND THE DETECTION OF PARTICLES

1. THE ACCELERATOR 2
2. THE BEAM 2
3. THE BUBBLE CHAMBER 8
   3.1. Principle of Operation 8
   3.2. The CERN 2m Hydrogen Bubble Chamber 10
4. A NOTE ON THE HISTORY OF THE EXPERIMENT 11

CHAPTER II. EVENT PROCESSING

1. THE ANALYSIS OF PICTURES 20
   1.1. Scanning the Film 20
   1.2. Measuring the Events 21
2. GEOMETRICAL RECONSTRUCTION 24
   2.1. Transformation of Film Measurements 24
   2.2. Reconstruction of Points 25
   2.3. First Approximation of Track Parameters 26
   2.4. Final Determination of Track Parameters 27
3. EVENT IDENTIFICATION 29
   3.1. Kinematical Analysis 29
   3.2. Selection of Interpretation 33
   3.3. Automation of the Procedure 38
4. ORGANIZATION AND PROCESSING OF THE DATA 39
5. A NOTE ON THE COMPUTERS USED 40

CHAPTER III. THE SEARCH FOR SYSTEMATIC ERRORS

1. BEAM MOMENTUM AND PURITY 50
2. BIASES IN THE ANALYSIS OF PICTURES 50
   2.1. Scanning and Measuring Biases 50
   2.2. Bias in Observing Particle Decays 52
3. BIASES IN THE COURSE OF EVENT IDENTIFICATION 54
   3.1. Biases Due to Kinematic Fitting 54
   3.2. The Reliability of Event Interpretation 55
4. BIASES IN THE REACTIONS STUDIED 56
   4.1. General Remarks 56
   4.2. The Study of Ambiguities 57
   4.3. The Effect of the Selections Applied 58
5. THE CALCULATION OF CROSS-SECTIONS 59

CHAPTER IV. THE STUDY OF RESONANCE PRODUCTION IN TWO MULTIPARTICLE PROCESSES

1. MULTIPARTICLE REACTIONS AT HIGH ENERGY 68
2. THE REACTION CHANNEL ANALYSIS 71
   2.1. The Purpose of the Study 71
   2.2. The Method of Determining the Fractions 72
   2.3. The Form of the Matrix Element 74
   2.4. The T Dependence on a Chosen Variable 77
3. THE DATA 79
   3.1. Introductory Remarks 79
   3.2. Peripherality of the Processes 79
   3.3. Effective Mass Spectra 80
   3.4. Resonance Masses and Widths 81
   3.5. The Determination of the Channel Fractions 83

CHAPTER V. A SIMILAR STUDY AT 6 GEV/C, COMPARISON AND CONCLUSIONS

1. STUDY OF THREE MULTIBODY FINAL STATES AT 6 GEV/C 96
   1.1. The 6 GeV K^-p Experiment 96
   1.2. The Reactions Under Study 96
   1.3. Experimental Characteristics 97
   1.4. The Fractions of the Various Subprocesses 98
2. SOME COMMON FEATURES OF THE RESULTS AT THE TWO ENERGIES 99
   2.1. General Remarks 99
   2.2. The Prolific Resonance Production and Some Comments on the Fractions 100
   2.3. The ρ^o Meson Production 101
3. CROSS-SECTIONS VARIATION WITH ENERGY 103

CHAPTER VI. A STUDY OF THE REACTION $K^-p \to \Delta^{++}K^{*-}\pi^-$ AT 6 AND 10 GeV/c

1. THREE BODY SUBPROCESSES IN THE FINAL STATES STUDIED 121
2. THE REACTION $K^-p \to \Delta^{++}K^{*-}\pi^-$ AND ITS PRODUCTION MECHANISM 122
   2.1. Introductory Remarks on the Three-Body Problem 122
   2.2. The General Method of Studying the Exchanges 123
   2.3. The Data 127
3. TWO MODELS FOR HIGH ENERGY PROCESSES AND THEIR APPLICATION TO THE REACTION $K^-p \to \Delta^{++}K^{*-}\pi^-$ 134
   3.1. The Veneziano Model 134
   3.2. The CLA Multiperipheral Model 141

CHAPTER VII. THE PHYSICS OF 10 GeV/c K^-p EXPERIMENT. A SURVEY

1. TOTAL AND DIFFERENTIAL CROSS-SECTIONS IN TWO-BODY REACTIONS. . . 172
1.1. Total Cross-Sections 172
1.2. Elastic Differential Cross Section 173
1.3. Inelastic Differential Cross-Section 174
2. THE STUDY OF RESONANCES 176
2.1. The Q and L Mesons 176
2.2. The $K^*(890)$ Resonance 181
2.3. Baryon Resonant States With Strangeness S = -2 184
3. SOME ASPECTS OF STRANGE PARTICLES PRODUCTION 186
3.1. Λ-Production 186
3.2. Ξ^- Production 186
3.3. Ω^- Production 187
3.4. A Comparative Study 188
4. THE INVESTIGATION OF THEORETICAL MODELS 190
4.1. A Veneziano Model Study of the Reaction $K^-p \to p\bar{K}^0\pi^-$ . . . 190
4.2. The Veneziano Model with Pion and Pomeron Exchange: reaction $K^-p \to nK^-\pi^+$ 192
4.3. Testing the CLA Model on the Reaction $K^-p \to \Delta^{++}K^-\pi^-$ . . . 194

APPENDIX: List of 10 GeV/c K^-p Publications This Survey Was Based On 196

AS AN EPILOGUE: Some Hesitant Thoughts on the Future 224

ACKNOWLEDGEMENTS 227

INTRODUCTION

1. The Field of Elementary Particles, Ideas and Development

The search for elementary particles is as old as science itself. Rooted in philosophical ideas of ancient Greece, it has moved on from chemistry to atomic physics, and then into nuclear physics. But more than three decades ago the nucleus itself was split, and its components, the proton and neutron, together with the electron, the photon and the neutrino, were for some years the accredited "elementary" particles of our universe.

Soon though, as it is not unusual in physics, this picture became inadequate. With finer instruments and experimental work mostly on cosmic rays, the proton and neutron revealed a striking substructure of a host of other particles. Some were heavy, heavier than the neutrons and protons; others of intermediate mass were new types of mesons. By the mid-1950's physicists accounted for about 30 particles.

But it was mainly in the last fifteen years that, centered around the big accelerators, a real particle population explosion occurred. It was compounded by the discovery of many unstable states (resonances) and the confirmation (with the creation of antiproton in 1955) that there exists an "antiparticle" corresponding to each particle. Many physicists were thus led to the belief that none of these particles deserves to be singled out as elementary.

The particles discovered to date, except the photon and the four "leptons" (the electron, the muon and the two kinds of neutrino) participate in the strong interaction, the force which forms and maintains them. This force, of a short range of about 10^{-13} cm., is first in strength of the four forces that seem to underlie all the operations

of the physical universe (the others being the electromagnetic, the weak interaction and the gravity).

* * *

As the strongly interacting particles proliferated, attempts were made to find patterns that would show relations among them. To that aim, advantage was taken of the fact that nature conserves many quantities (in addition to energy and momentum) and shows various symmetries. These quantities were the baryonic number B (by definition, equal to 1 for baryons and -1 for their antiparticles, while 0 for mesons), the parity P (with values +1 and -1 and concerned with the left-right symmetry in nature), the isospin I (which relates a set of particles of different charges, i.e. the pion triplet consists of negative, neutral and positive charge states) and, finally, the strangeness, associated with the unusual behaviour of certain particles such as the K, Σ and Ξ.

A useful concept in this effort of particles classification was introduced by T. Regge who pointed out the existence, in many important cases, of a mathematical relation between the value of the angular momentum J and the particle mass; the smooth mathematical curve that gives the physical mass for different values of J is called a "Regge trajectory". The rule says that only states separated by two full integers can lie on the same trajectory. The particular points on the trajectory, which correspond to observable physical phenomena, are called "Regge poles": the particle N, for instance, has two poles associated, the N(939) and N(1688)--corresponding respectively to $J = \frac{1}{2}$ (the nucleon) and to $J = \frac{5}{2}$ (the 1688 resonance). For mesons,

it was shown that no trajectory can exist above the (unphysical) one which passes through $J = 1$ for zero mass, this being given the name of the Pomeranchuk trajectory; it appears that the $\eta(1250)$ does come on this line for $J = 2$.

The real breakthrough in classification schemes came, though, when Gell-Mann and V. Ne'eman, independently, discovered a system through which the particle multiplets could be formed logically into larger related groupings by means of algebraic systems developed in the 19th Century. When arranged according to this scheme, these supermultiplets fall into orderly geometrical patterns. The most common form is a hexagon, with two particles at the center and one at each of the six angles. Some groupings form triangles, and there exist particles that do not fall into these designs and remain singlets; mesons are found in supermultiplets of 8 and 1, baryons in supermultiplets of 10, 8 and 1, and so forth. Also, relations between masses and decay modes of members of these supermultiplets are derived, and many particles (the celebrated Ω^- for instance) predicted by the method and needed to fill in gaps in the patterns have since been discovered experimentally. Furthermore, it was suggested as an important consequence of the theory that all the known strongly interacting particles can be formed by combining just three primitive objects (named quarks) which would carry fractional electric charge. Every baryon is then an association of three quarks and every meson of a quark and an antiquark.

As an alternative approach to the search for fundamental quantities in nature, worth mentioning is perhaps the "bootstrap" hypothesis (formulated by G. Chew and S. Frautchi) according to which the strongly interacting particles are all dynamical structures that owe there existence to the same forces through which they normally interact.

* * *

On the pure theoretical side, the lack of a theory for strong interaction processes has focused the interest to their phenomenological aspects. Various models stressing the importance of some specific parameters are tested against the abundance of experimental results. Most of the present efforts are devoted to the prominant resonance importance, the high energy Regge behaviour of collision amplitude and a duality between these two somewhat extreme approaches. An equally important task, for both theorists and experimentalists, is the extracting of the quantum numbers of the many strongly interacting states existing and their subsequent testing against the various classification schemes. Although a solid theory is not still in sight, it can be said that the knowledge gained from the research in elementary particles opened up new perspectives for the understanding of the structure of matter.

2. The 10 GeV/c K^-p Experiment

This experiment commensed in February 1965 as a collaborative effort between five European groups (Aachen, Berlin, London, CERN, Vienna) and with rather broad objectives. Being at the time the highest energy K^-p bubble chamber experiment, it was mainly aiming at a search for new resonant states and the test of various models of reaction mechanism. Both the Regge pole model and the then proposed quark model have made interesting predictions, which in principle would be valid in the limit of very high energy.

The main results derived in the subsequent years of the analysis of the experimental data, will be discussed in detail later. Here, perhaps, worth mentioning is the discovery of a resonant state, the L-meson, of a controversial nature; the confirmation of a $S = -2$ resonant, the $\Xi(2500)$; the detailed study of the production of several

Ω^- and other rare particles; the study of the limitations and successes of various proposed models, such as the Veneziano and the CLA version of multiperipheral model; and, finally, the calculation of cross-sections and other important experimental quantities of interest to the phenomenological studies.

Lately, as more and more data in high energy physics accumulated, fruitful had proved the collaborative study of the 10 GeV/c K^-p results with those obtained from other experiments. For the study, for instance, of the $(p\pi\pi)$ isobar or of the t-channel helicity conservation data from the 16 GeV/c π^-p experiment have also been used; also, an analysis of the charge-exchange K^o producing reactions was based, apart from the 10 GeV K^-p, on data from the 5 and 8 GeV/c K^+p experiments.

3. The Present Thesis

The author joined the Imperial College High Energy Nuclear Physics Group in October, 1966. After attending the prescribed lecture courses, he joined the 10 GeV/c K^-p experiment, then in progress, and assisted in its data processing; he also participated in some stage of the beam tuning and the film exposure at CERN.

Apart from his share in the compilation of Imperial College data, the author was solely responsible for the study of some multiparticle final states at 10 GeV/c and, for comparative reasons, at 6 GeV/c K^-p interactions; the latter was an earlier experiment in which Imperial College had also taken part.

The present thesis necessarily reflects this research activity of the author. The first chapters are devoted to the instrumentation and

the various aspects of data collection; then follows the analysis of several multiparticle states and their more interesting subprocesses, and the thesis concludes with a survey of the physics so far investigated by the 10 GeV/c K^-p experiment.

CHAPTER I.

THE PRODUCTION AND THE DETECTION OF PARTICLES.

Experimentation in bubble chamber physics begins at a particle accelerator's injector and ends in the analysis of the data obtained at the chamber.[1] Figure 1 is a schematic diagram of the chain of operations. The present chapter covers the instrumentation necessary for the first part of this long process, i.e. it describes the beam used to transport the particles into the chamber, and examines the function and some characteristics of the latter.

Naturally, the discussion refers mainly to the 10 GeV/c K^-p experimental apparatus, with various information on the stages of the experiment concluding the chapter.

1. THE ACCELERATOR.

High energy particles occur naturally in cosmic rays, but in fact the particle beams for the vast majority of contemporary experiments are provided by particle accelerators constructed for this purpose. The CERN 28 GeV/c Proton Synchrotron, put into service in 1960, provided amongst many others the beam for the 10 GeV/c K^-p experiment.

2. THE BEAM.

The purpose of the high energy beam is to transport particles of the type and momentum required from the target to the experimental apparatus.[2] The selection of the particles, from the large number at first produced, is made by a suitable combination of electric and magnetic fields. In bubble chamber experiments the momentum spread of the beam should be small (at 10 GeV/c, for instance the "momentum bite" $\Delta p/_p$ is less than 1%) and the contamination by pions of a separated kaon or anti-proton beam must not exceed 5%.

The beam U5 at CERN[3] (known as O2, U3 and U4 in its earlier stages) is the one used for the present experiment. Figure 2 shows the layout of its basic elements, and also the horizontal and vertical paths taken by the beam. The function of the beam is commonly separated into three main stages, of which a brief description will be given in what follows

A. Stage of particle formation and first momentum selection.

This stage of the beam, of about 72m length, leads from the target to the cavity centre of the first radio frequency separator.

The negative particles, produced at the target (copper or tungsten is used) at a zero angle, have their angular acceptance first defined by the collimators C1 and C2, one horizontal and one vertical. The quadrupole lens system Q1-Q4 which[15] followed by two bending magnets BM1 and BM2 has a double function: vertically, it gives the beam a magnification sufficient as to enter the RF cavities under the best conditions, i.e. with an opening angle of ± 1 mrad; horizontally, it focuses the beam at the momentum slit C4, and a momentum bite of ± .25% may be obtained. The bending magnets BM3 and BM4 bend the beam in the same sense as BM1 and BM2, and together with the quadrupole Q5 produce a dispersion free and momentum selected beam behind BM4.

At this stage the beam has also been made parallel in the vertical plane. Its vertical divergence and the horizontal acceptance are defined by the collimators C3 and C5.

B. Stage of particle separation.

(a) The principle of radio frequency separation.

The 10 GeV/c K^- and K^+ mesons beam (then transporting particles to the 1.5m British National Bubble Chamber) was the first one to make use of the radio frequency separation technique; so this technique deserves perhaps a detailed examination.

The principle of the two-deflector system is illustrated in Fig. 3 for an axial pencil beam. Each cavity consists of cylindrical

wave guides with RF power supplied to them, and exerts a sinusoidally time varying deflecting force on the particles in the vertical plane.

Assume now that the momentum defined beam, containing two types of particles (π and K in this case) enters the first cavity RF1. Since their velocities are nearly equal, the particles will emerge from the cavity with the same deflection θ

$$\theta \propto \alpha \sin\phi$$

where α denotes the magnitude of the angular deflection and ϕ is the phase of the applied RF.

Since though they are not equal in mass, the particles will arrive in the second cavity RF2 at different times, and will enter this cavity with a phase difference

$$\Delta\phi = \omega \Delta t = {}^{\omega L}/_{c} \left({}^{1}/_{\beta_\pi} - {}^{1}/_{\beta_K} \right)$$

where ω is the angular frequency of the applied RF and L is the distance between RF1 and RF2.

In the relativistic limit, and if E_π and E_K are the rest energies of the particles, this relation gives

$$\Delta\phi = \frac{\omega L}{c} \left(\frac{E_\pi^2 - E_K^2}{2p^2 c^2} \right)$$

The quadrupole focusing system, QL, is designed to give unit magnification (M = -1) in the vertical plane. Therefore, if the phase of the RF voltage is adjusted so that the unwanted pions

enter both cavities at exactly the same phase, the deflection they experience at RF2 would cancel the one at RF1. The kaons, on the other hand, deflected now through a different angle, will emerge from the second cavity with a final non zero angle θ'

$$\theta' = -\alpha \sin\phi + \alpha \sin(\phi + \Delta\phi)$$

$$= 2\alpha \cos\left(\phi + \frac{\Delta\phi}{2}\right) \sin\frac{\Delta\phi}{2} .$$

While thus the pions will hit the beam stopper (centered on the beam axis) the wanted kaons will continue the beam line.

For the angle θ' to be maximum in this symmetric system we should have

$$\Delta\phi = \eta\,\pi \quad (\eta \text{ integer}).$$

Then

$$\theta' = 2\theta .$$

In the typical case of the CERN RF separator $L = 50$m, $\lambda = 10.5$ cm and the optimum momentum for the separation of pions and kaons is

$$(p_o c) = \{(E_\pi^2 - E_K^2)L/\lambda\}^{\frac{1}{2}}$$

$$\simeq 10.32 \text{ GeV/c} .$$

In fact, in most beams one wishes to remove two types of contaminants (e.g. π, p while K are wanted). Then the momentum and drift-space between the cavities has to be chosen such that

the phase difference between the unwanted particles is a multiple of 2π. For p and π the condition is satisfied at 10.12 GeV/c, very near to the optimum momentum for K/π seperation. Hence a momentum value of 10.12 GeV/c was chosen for the O2 beam in its initial running, and a satisfactory separation of K mesons was achieved.

(b) The separation stage in the U5 beam.

After discussing in principle the radio frequency separation technique, we now return to the description of the specific beam we are concerned with (Fig. 2). Effectively, the U5 separation stage begins at the vertical collimator C3 which is situated in front of the momentum slit and defines the vertical angular opening of the beam. The quadrupole doublet Q6-Q7 images the target in both planes at the center of the first cavity RF1. This produces both a horizontal and a vertical focus at RF1.

The center of RF1 is then imaged onto the center of RF2 by the quadrupoles Q8, Q9 and Q10. There is, in fact, no radio frequency cavity at RF2, but again the beam is brought to a horizontal and vertical focus at this position; the quadrupole Q10 is also not used for a two cavity beam.

Finally, the quadrupoles Q11, Q12, Q13 and Q14 image the center of RF2 onto the center of the radio frequency cavity RF3. Behind RF3 is situated the beam stopper BS, of a ~ 20mm typical thickness. The quadrupole Q5 and the intercavity optics image the collimator C3 onto the beam stopper.

C. Stage of final momentum analysis and shaping for the bubble chamber.

The beam stopper is followed by the collimator C6, which limits the number of secondary particles and reduces the muons contamination. Being leptons, the latter would not cause interactions in the bubble chamber but,if too many, will reduce the picture quality.

As the beam stopper only degrades the beam in energy by a few per cent, it is necessary to redefine the momentum to prevent these low momentum particles from entering the chamber. The quadrupoles Q15 and Q16 produce therefore horizontal and vertical foci in collimators C6, C7, which serve to redefine the target for the final stage. After C8 are the two bending magnets BM5 and BM6 to deflect the beam, and the vertical bending magnets VBM1 and VBM2 which are used to obtain the desired level and entry angle at the chamber. Between them, the quadrupoles Q17 and Q18 image C7 on C9 in the horizontal plane, and permit the production of a virtually parallel beam with a 90-110 mm vertical dispersion. The final momentum analysis of the beam is performed by the magnet system BM5-BM6 and the collimator C9.

The total length from the target to the 2m chamber is about 182 meters.

3. THE BUBBLE CHAMBER.

3.1. Principle of Operation.

The principle, on which the operation of the bubble chamber is based, is simple: If an ionizing particle passes through a superheated liquid, small bubbles are formed along its path; by photographing these tracks from two or more viewpoints one is able to record their three dimensional arrangement and later elucidate the nature of the event.

According to classical thermodynamics, for the critical bubble (that is, of the minimum size from which the bubble can grow to macroscopic dimensions) to be formed, work is required. A theory, which attributes bubble nucleation to production of local thermal spikes, is perhaps the most satisfactory: According to it, in its passage through a medium a charged particle transfers energy to electrons by collision, thereby ionizing the atoms along its path. The Knock-on electrons (δ-rays) lose energy by creating more ions which, for a low energy electron, are concentrated in a volume at least as small as that of the critical bubble (10-20 mm radius); all the heat of ion recombination is thus released within this volume. However, the experimental evidence that δ-rays appear to have much lower efficiency for nucleating bubbles than low energy nuclei (also capable of depositing the necessary energy in the required volume) remains a discrepancy not understood by the heat spike theory.

Needless to say, since the time that track bubbles from cosmic ray muons were first observed in a small glass chamber filled with ether,[4] the bubble chamber has grown into a large and necessarily sophisticated device.[5] The superheated state of the

liquid hydrogen is achieved by a rapid pressure deduction, which should coincide with the entry of the burst of particles. After the bubbles have reached a suitable size (~ 150μ) the chamber is illuminated and photographed. Then the pressure is reapplied to prevent boiling and a clearing field removes the bubbles, thus preparing the next cycle of the operation. In the large chambers, pressure is varied by means of a piston. A typical cycle of the operation takes no more than 50-100 m sec.

Due to a magnetic field applied, the particle trajectory is approximately a helix with curvature related to its momentum.

3.2. The CERN 2m Hydrogen Bubble Chamber.

In the early stages of the present experiment, the British 1.5m National Bubble Chamber was used; later it was replaced by the CERN 2m chamber, of which a simplified vertical sketch is shown in Fig. 4.

The chamber has two parallel glass windows, one to take the pictures and one for the illumination. The cameras, four altogether, are mounted on a plate at the end of the vacuum tank with their objectives on a circle of 60 cms diameter. The optic axes are parallel and are perpendicular to the chamber windows. Wide angle lenses permit each camera to view most of the chamber; because the intensity of the light scattered by a bubble falls off rapidly as the scattering angle increases, a compromise value of 7^{o}, which allows a sufficient stereoscopic view, is chosen.

The illumination system of the chamber, of obvious importance for the quality of pictures, is of a straight-through dark field type;[6] it consists of three independent flash tubes as light sources, focused by the ellipsoidal mirror precondensers into the field lenses.

Two direct viewing windows and polaroid cameras help to monitor the chamber during the run. Since the density of bubbles along a path is a function of particle velocity (of the empirical form $b = c/\beta^2$), it is a rather important parameter. In the relativistic limit, all tracks will approach a "minimum ionization" limit. A suitable bubble density of 10.15 bubbles per cm is kept by choosing the value of the pressure change during the expansion stage. Throughout a run, the bubble density is checked on test-strips taken from the end of each roll.

In Table 1, some important parameters of the CERN 2 m chamber are given.

4. A NOTE ON THE HISTORY OF THE EXPERIMENT

In Table 2, the various stages in the history of 10 GeV/c K^-p experiment are summarized. Information is given on the number of events obtained at each stage and the present status in their processing.

REFERENCES AND FOOTNOTES

1. For an excellent collection of articles on High Energy Physics Instrumentation see R. P. Shutt, "Bubble and Spark Chambers", Vol. 1 and 2.

2. B. de Raad, A. Minten, E. Keil, "Lectures on Beam Optics," CERN 66-21.

   Also S. Baker, "Lectures on High Energy Instrumentation", Imperial College.

3. P. Lazeyras, "Faisceau U5" (in French) CERN/D.Ph.II/Beam/68-2.

   F. R. Heathcote, "Notes on Tuning the U5 Beam" CERN 1970.

4. By Glaser, the inventor of the bubble chamber.

   See D. A. Glaser Phys. Rev. 87 (1952) 665 and 91 (1953) 762; also Sci. Am. 192 (1955) 46.

5. See, for instance

   N. C. Barford "Bubble Chamber Technology, Progr. Cryog. 2 (1960) 89

   F. W. Bullock "Bubble Chambers" Sci. Progr. Oxf. 58 (1970) 301.

   Proceedings of International Colloquium on bubble chambers (1967) CERN Report 67-26.

6. See W. T. Welford, "Bubble Chamber Optics", App. Opt. Oct. 1963.

   Also, by the same author, the article in Vol. 1, p. 233 of Ref. 1.

TABLE I-1

PARAMETERS OF THE CERN 2M HYDROGEN BUBBLE CHAMBER

MAGNETIC FIELD	Central value	17.34 KG
CAMERAS	Number	4
	Central plane demagnification	1:13
ILLUMINATED REGION	Dimensions (in cm)	177 length
		56 height
		50 width
ILLUMINATION	Number of sources	3
	Method	straight through
	Scattering angle	7^{o}
WINDOWS	Number	2
	Dimensions (in cm)	218 length
		77 height
	Thickness (in cm)	17
TEMPERATURE		$26\ ^{o}K$
TIME DELAY		1.0 m sec.

TABLE I-2

THE STAGES OF THE 10 GeV/c K^-p EXPERIMENT

Experiment	Chamber	Frames	Date	K-/frame	Fits	No-fits	Status
75	1.5 B N HBC	200 K	Mar.'65	~ 5	12 K	18 K	Finished
10	2 m CERN HBC	70 K	Aug.'66	~10	10 K	14 K	Finished
12	"	240 K	Feb.'68	~10	35 K	49 K	Finished*
13	"	213 K	Apr.'69	~ 8	~30 K	~45 K	Processing
Total		723 K			87 K	126 K	

*This thesis is mainly based on the events from Exps. 12 (not including the I.C. events) + 10 + 75.

Fig. I-1

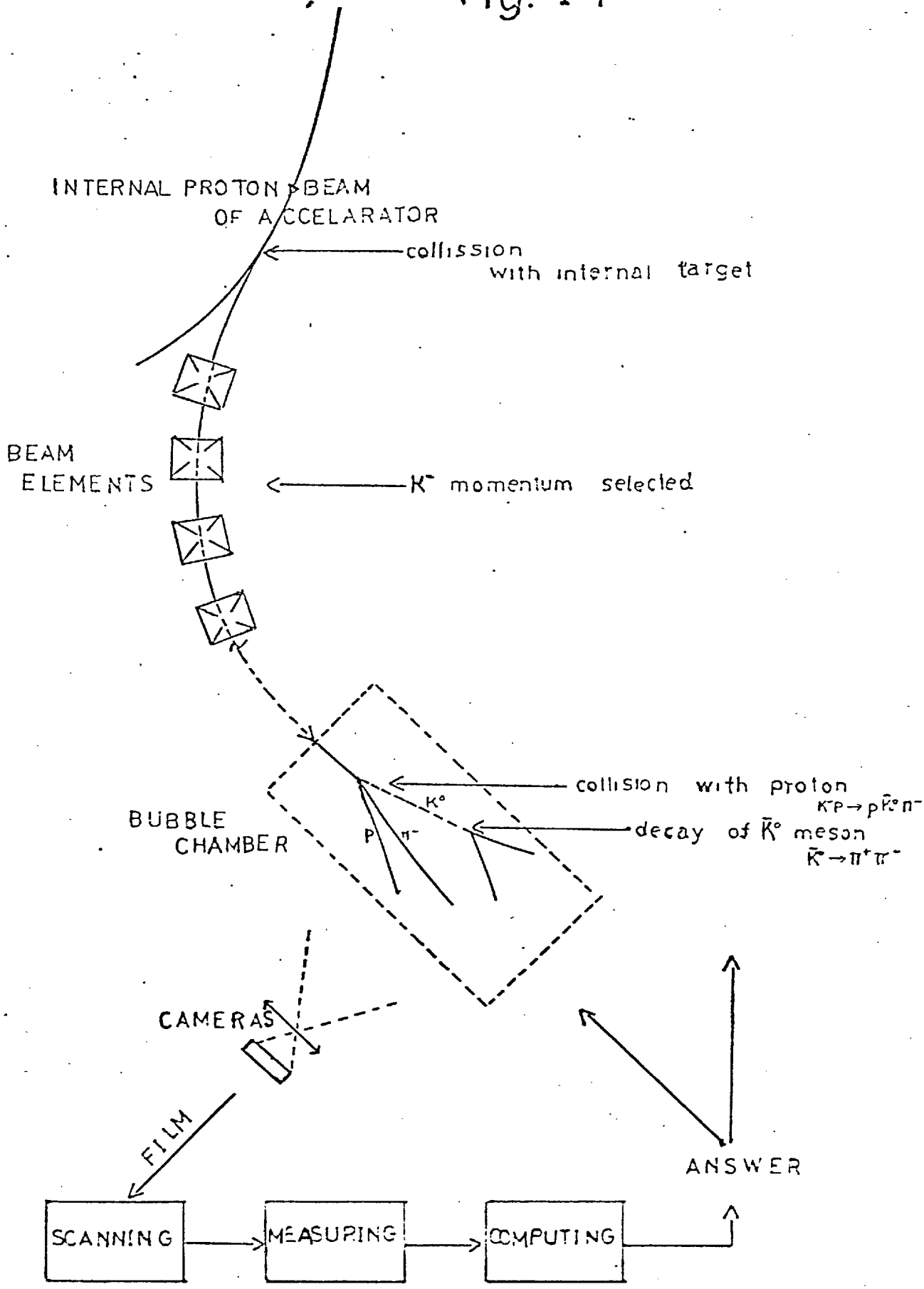
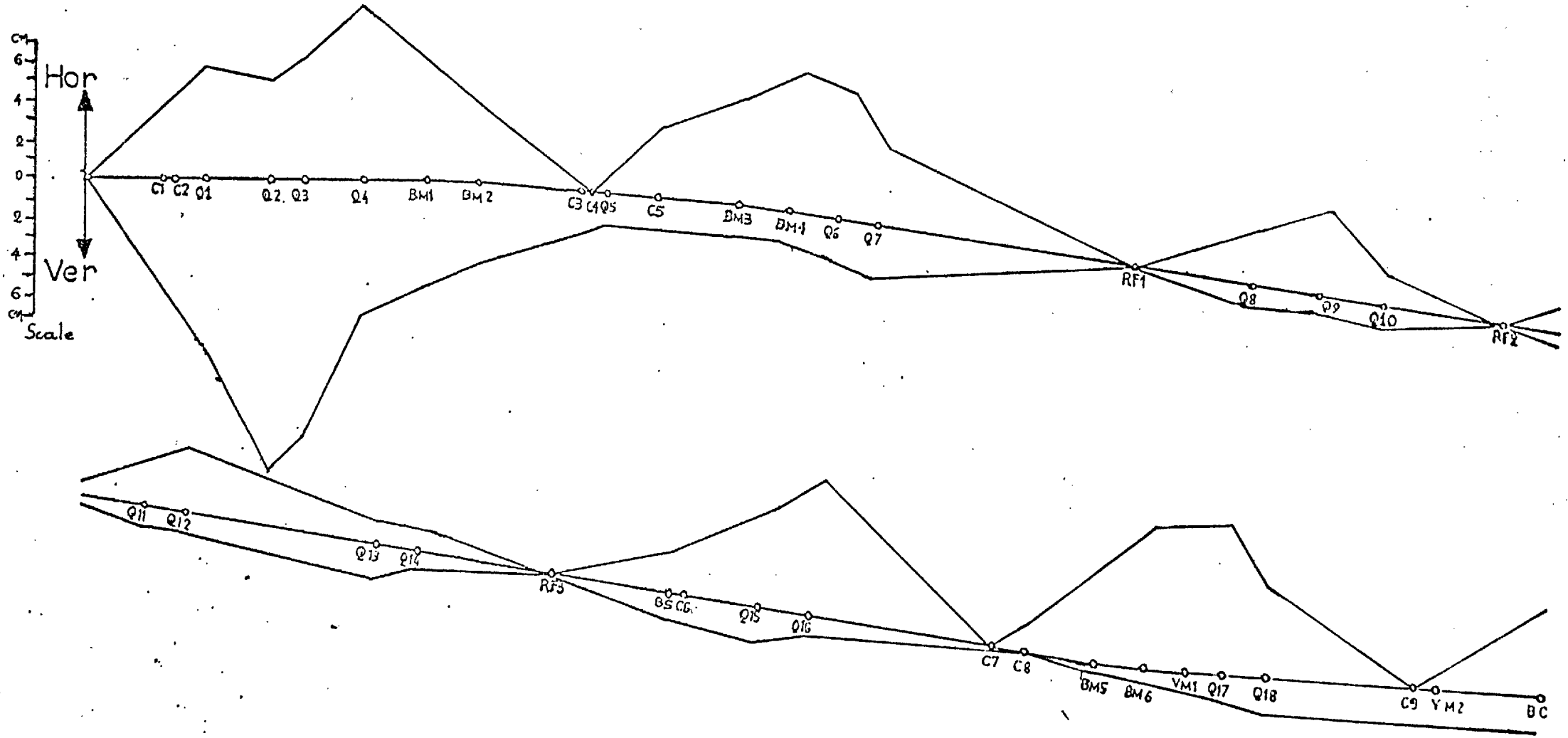
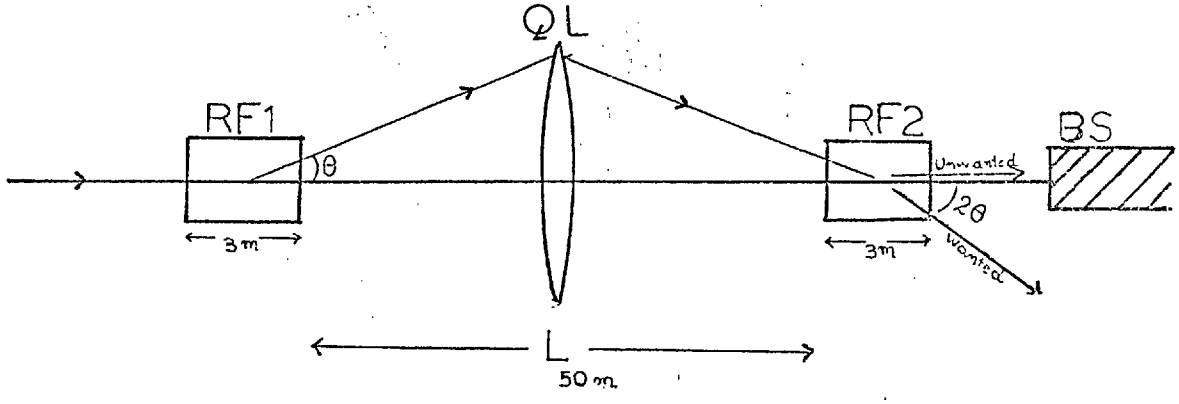

INTERNAL PROTON BEAM
OF ACCELARATOR
collission
with internal target
BEAM
ELEMENTS
K⁻ momentum selected
BUBBLE
CHAMBER
collision with proton
K⁻P → pK°n⁻
decay of K° meson
K° → π⁺π⁻
K°
P
π⁻
CAMERAS
FILM
ANSWER
SCANNING
MEASURING
COMPUTING

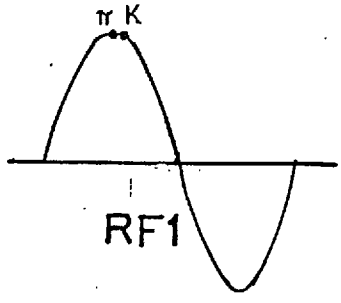
Fig. I-2

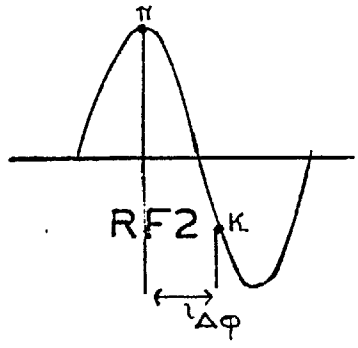


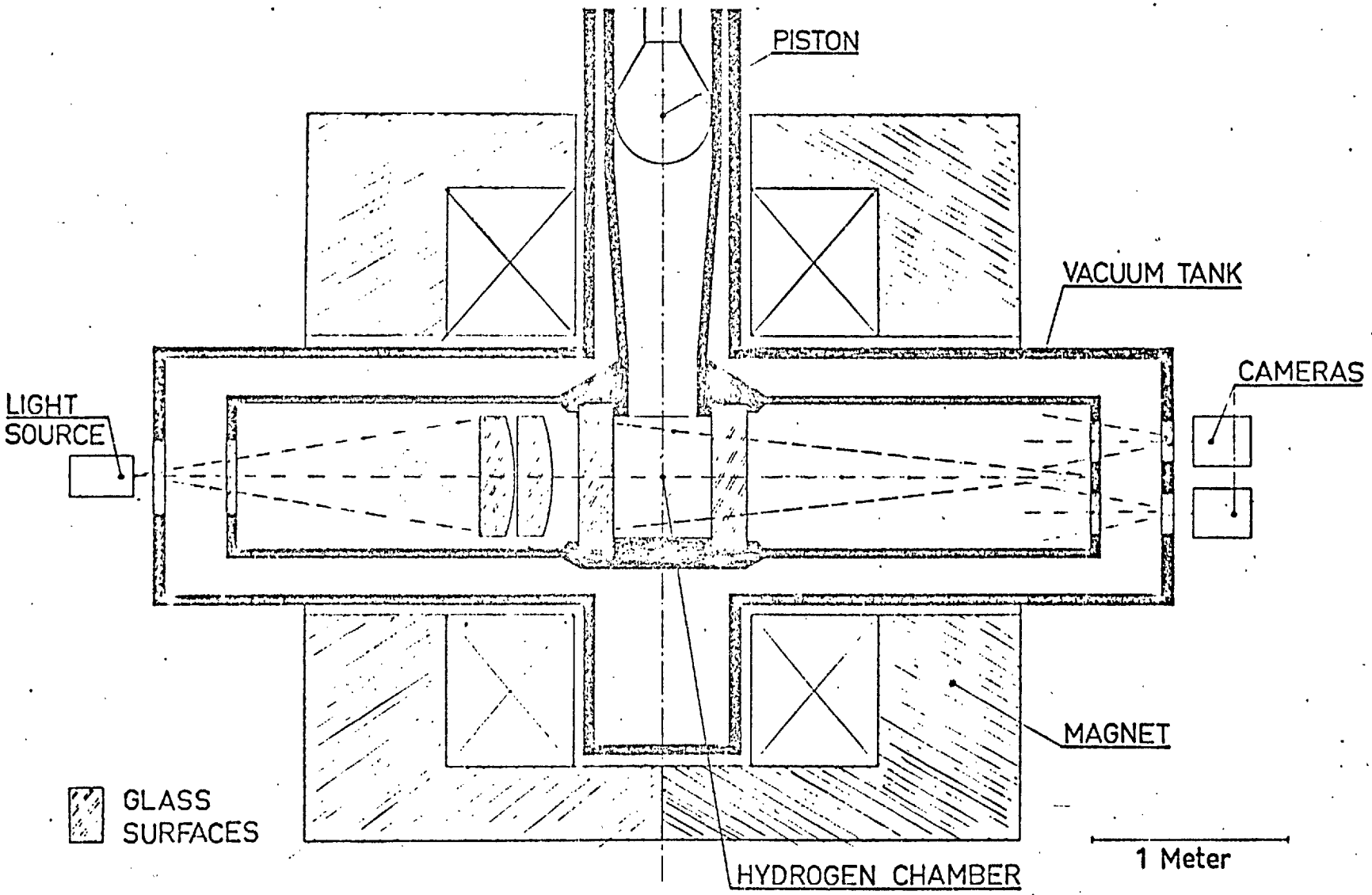
U5 Beam Profile

Fig. I-3








PISTON
VACUUM TANK
CAMERAS
LIGHT SOURCE
MAGNET
GLASS SURFACES
HYDROGEN CHAMBER
1 Meter

CHAPTER II

EVENT PROCESSING.

This chapter describes the systems and techniques used in analyzing the film and processing the data of the experiment.[1] The whole operation aims at offering kinematical interpretations, as complete as possible, of interactions which occurred in the bubble chamber; to that purpose digital computers are used extensively.

The event processing may naturally be separated in four main stages, as follows

1. Analysis of the pictures obtained in the bubble chamber.
2. Spatial reconstruction of each track.
3. Kinematic analysis at each vertex, interpretation of the event and calculation of its basic physical quantities.
4. Organization of the data into records.

Figure 1 illustrates the general flow of the event processing.

1. THE ANALYSIS OF PICTURES.

1.1 Scanning the Film.

Scanning aims at finding and recording interesting events on the film, for subsequent measurement and analysis. The whole film is divided into rolls (one for each view) of about 1250 frames, and two independent scans are performed by technical assistants. To each event a code number klm is assigned, where K is the number of charged tracks emanating from the production vertex, l stands for the number of charged decays seen and m for the number of neutral decays seen. A third scan, done by physicists, finally compares the results of the two previous scans. At this "check" stage any discrepancies are resolved; a special card, containing not only the above described topology but also the roll-frame-event number and a rough sketch of the event to assist the measurer, is filled for each event.

Sometimes additional information, if existing, is also worthy of recording: Stopping protons, since, by an empirical relation, the initial momentum may then be determined from the range; this is useful, because a stopping proton track is often too short to get an accurate momentum measurement from its curvature. K^- decays into a single charged particle and one or more neutrals (~95% of all K^- decays), to assist in the estimate of the total K^- flux. K^- decays into three pions (~5% of all) for an independent determination of the beam momentum. Electron pairs, mostly coming from the decay $\pi^o \to 2\gamma \to e^+e^-$. In this case, measurement is justified only if the electron pair is ambiguous with a genuine neutral particle decay happening to have a small opening angle. (The opening angle of an electron pair is always practically zero, with both tracks showing minimum ionization.)

The following general criteria[2] were applied in scanning and measuring the events:

(i) All three views must have existed[3] for an event to be recorded. To this, exception was made for the "rare" events, where a measurement was tried even if only two views were available. As "rare"are classified the events with two or more strange particle decays.

(ii) The interacting beam track was accepted at the scanning table if it diverged less than 1^{o} from the other beam tracks, and on view 1 had a minimum length of about ~15 cm (fixed by the fiducial region definition).

(iii) A fiducial region was chosen (Fig. 2), which was a compromise between the wish to have as many events as possible recorded, and the need for the tracks to be long enough as to allow their accurate curvature measurement. This region was further divided into two smaller regions and:

On the first of them (~88 cm long), all events were scanned--except 000's, later corrected for--so as to estimate the absolute cross-sections. Topologies 410, 610, 810..., however, were not measured.

On the second (~39 cm long), only rare events were scanned and measured.

1.2. Measuring the Events.

The measurement of an event consists of recording the coordinates of several points on each track (in all views), and of the fiducial marks on the photograph. Two modes of the operation were used in this experiment.

(a) Manual Measuring

Measurement may be made on manually operated digitized projectors; the photographs are projected on to a screen, and the operator brings the point to be measured into coincidence with a reference mark. Then

by pressing a button he causes the (x,y) coordinates of the point to be either punched on paper tape (earlier stages) or transmitted to a PDP-6 computer. In the latter case, constituting a semi-automatic "on line" system, the computer carries out a number of checks on the measurements as they are made and leads the operator through the measuring sequence. Thus a considerable speed up of the measurement procedure is achieved.

Normally, 5-10 points are measured on each view for each track of the event; in addition we have the measurement of four fiducial marks, of the production apex, and of points of special interest (e.g. stopping protons end-points or tracks of secondary interactions.) Using a keyboard the operator can also introduce labelling information which is used by various programs to identify the measurements and the topology of the event.

(b) Measuring by the Flying-Spot Digitizer

A faster and more accurate system known as HPD and based on the Hough-Powell Device,[3] has now taken up most of the measurements of the experiment. The system consists of optical, mechanical and electronic parts,[4] which allow the bubble chamber photograph to be scanned by a small spot of light; the coordinates of the tracks scanned by the spot are then transmitted to a PDP-8 computer and handled by a suitable series of programs.

In practice, to facilitate the identification of tracks of interest, additional information needs to be given to the computer. Thus, rough measurements are taken by suitable machines at each extremity and in the middle of each track and a zone is defined (known as a "road"), 800 μm wide approximately. This information is processed by program MIST (Fig. 1) and checked for completeness

and operator errors; the output tape then becomes a guiding reference for the accurate digitizer. Only those of the HPD coordinates, which lie within the roads or represent fiducial marks, are retained and processed consequently.

Further data reduction, including the recognition of the tracks making up the event, is made by the on- line program FILTER. Points arising from crossing tracks and background are rejected, so the remaining should in principle belong to a track of interest.

Program SMOG then merges the measured data for the separate views, and produces the output tape to be used as input to the geometrical reconstruction program. The measurements are presented in the form of a set of evenly spaced points (known as "master points") on each track.

To improve further the efficiency of the system, a facility has been introduced[5] which enables the operator to remeasure, with a "light pen" and the CRT, tracks inadequately filtered. A program called RESCUE inspects the FILTER results for any sign of failure. If a track fails, the road contents and master points are displayed on the CRT and the operator may accept, remeasure the track or request a display of all digitizings near the road.

If a display is requested, any of the three road points may be moved continuously in the $\pm$ y direction with the light pen; when the operator is satisfied with the positions of the road points, the track is refiltered. To measure a track, the operator runs the light pen along it, and the program recalculates and displays the master points on the road contents display.

If further remeasurement is required, the program proceeds by dividing the track into equal length slices and calculating a master point for each slice. This information is then transformed into the HPD coordinate system.

With the HPD measuring, a speed of about 30 events/hr. has been achieved for the 10 GeV/c K^-p experiment.

2. GEOMETRICAL RECONSTRUCTION.

The second step in the event processing is to compute the particle trajectories in the bubble chamber from the precision measurements of fiducials and track points on the film. The curvature of a track, its azimuthal and dip angles and also the errors in these quantities are to be determined.

The spatial reconstruction of each track is achieved by program THRESH,[7] which proceeds in the main steps outlined below.

2.1. Transformation of Film Measurements.

Instead of working with the direct film coordinates (x,y) from the measuring instrument, it is convenient to transform them into the $Z = 0$ plane of the chamber coordinate system. This system is defined with the inside of the front glass as XY plane, and the Z-axis pointing towards the cameras (Fig. 3). The transformation is assumed to be linear, i.e.

$$X_i = \alpha_1 + \alpha_3 x_i + \alpha_5 y_i$$

$$Y_i = \alpha_2 + \alpha_4 x_i + \alpha_6 y_i$$

where i runs over the three views.

A least square fit can determine the coefficients α's, by using the film measurements of the fiducial marks engraved on the inside glass surfaces and their standard reference positions for each view. Four fiducial marks should be

measured, to have redundant information; if only three are available, by imposing orthogonality ($\alpha_5 = -\alpha_4, \alpha_6 = \alpha_3$) the number of coefficients is reduced to four; with fewer than three fiducials, the whole view is rejected.

This transformation is immediately applied to all measurements in the view (fiducials, points, tracks). The coordinates thus obtained are corrected for lens distortion and any other non-linear effect.

2.2. Reconstruction of points.

The space coordinates of a point in the chamber (such as an interaction apex or the end point of a stopping track) are calculated by first associating with each measurement a "reconstruction line", given by the relations

$$X_R = Z_R F_x + G_x$$

$$Y_R = Z_R F_y + G_y .$$

This is in fact the segment of the light ray, inside the liquid of the bubble chamber, which joins the point of interest to a given camera. F and G are functions of the apparent position of the point in the $Z = 0$ plane and are easily computed.

If a point is measured on at least two views, its position in space may then be found by the closest approach of its reconstruction lines (not expected, in general, to intersect each other in one point because of the errors.) So a least square fit is performed to the above relations and the coordinates (X,Y,Z) of the point, with their standard errors, are obtained.

To calculate F and G, the thickness and refractive indices of the media are needed, and also the camera coordinates in the chamber system. All these constants, together with the fiducial positions, allowed tolerances for measured points, etc. are given independently to the program and are known as "titles".

2.3 First Approximation of Track Parameters.

The method we just described assumes that the measurements in the different views belong to the same space point, and thus it is used for interaction vertices. Measurements along a track, however, give non-corresponding measured points and this method does not apply.

Consequently, it is necessary to generate an artificial corresponding point in one of the views by interpolation between two measured points. When, say, it is known that a reconstruction line in view A comes from a measurement point which lies between two measured points in view B, then a space point may be found by letting the line from A cut a surface which contains the two reconstruction lines in B.

In applying this method, the reconstruction lines are first calculated for every measured point in all views. The space points to be reconstructed are then defined by the measurements on the view on which the track is most nearly seen as an orthogonal projection. A second view is chosen so as to ensure good stereoscopic conditions, and the coefficients of the reconstruction lines which correspond to the required space points are determined by interpolation (sometimes extrapolation) from the known reconstruction lines on this view.

Although this method of "near corresponding points" should, in principle, permit the reconstruction of any space trajectory, it is actually used to provide approximate values of the track parameters for the more refined procedure to be described in the next section. For that purpose, to the set of points

reconstructed by the method, a helix (which is a good approximation of the trajectory) is fitted, described by the relations

$$X' = \rho(\cos\theta - 1)$$

$$Y' = \rho \sin\theta$$

$$Z' = \rho\, \theta \tan\lambda \quad .$$

The coordinate system (X'Y'Z') is chosen to simplify the least squares equations. It is defined (Fig. 3) as the chamber system (XYZ) translated to the starting point (A,B,C) of the track, and rotated through an angle β so that the Y' axis lies parallel to the XY projection of the tangent to the track at (A,B,C). The helix axis is in the Z-direction, i.e. parallel to the main component of the magnetic field. ρ is the radius of the cylinder on which the helix lies, λ is the dip angle (measured from the X'Y' plane) and θ is the angular distance (measured in the X' Y' plane) from the starting point to a point on the helix.

In this first approximation ρ,β are determined by a least square fit to the circle given by the first two equations above; λ is obtained by fitting to the straight line given by the third equation; the coordinates (A,B,C) are taken from the point reconstruction or, if that was not successful, they are found by the method of corresponding points.

2.4. Final Determination of Track Parameters.

To obtain the final values of track parameters, a least square fit is made to a trajectory which takes into account the energy loss due to ionization and small variations in the magnetic field. For a

given momentum of the particle, the energy loss depends on its mass; therefore the procedure to be described does not only give the geometrical description of the trajectory but also information about the particle's mass.

The two parameters ρ and λ, as defined in the helix fit, are replaced now by $1/p_o$, the inverse momentum at the starting point (A,B,C), and λ_o, the dip at the starting point. Also, out of the three parameters A,B and C only two should be fitted, otherwise the point (A,B,C) can move freely along the fitted curve. In practive, either A or B is fixed but never C which is not as well determined. Hence, the five parameters to be fitted are $1/p_o$, λ_o, β, A (or B) and C.

The first step in the fitting procedure consists of calculating the perpendicular distance d_i from a measured point to the projected particle trajectory in the film plane. The expressions for d_i's are then expanded in terms of small corrections to the approximate track parameters derived by the helix fit. Finally, the sum of d_i^2, where i runs from 1 to the total number of measured points in all views, is minimized by the program, and the iteration procedure repeated until the corrections are sufficiently small.

In the procedure, it is necessary to be able to find the coordinates of a point at a given distance along the track from the vertex, as well as to compute their derivatives with respect to the track parameters. The trajectory no longer has the simple analytic form of an helix, and to do this a method of numerical integration along the track is applied. Tables are used to provide the momentum losses for each particle mass (usually pion, kaon and proton) and the values of the magnetic field[8] at the required points.

The least square fit is repeated for each track and the geometrical reconstruction is completed. Throughout the reconstruction program various tests are made on the convergence of iterations, spread of fitted values, etc. The output from the program consists of the space coordinates of all vertices, and the parameters β , $\tan \lambda$ and $1/p$ for each track reconstructed under a certain mass assumption. The errors on these quantities and information summarizing any difficulties in reconstructing tracks are also given.

3. EVENT IDENTIFICATION

From the geometrical reconstruction, values of momentum and direction of all visible tracks at each vertex are obtained; the problem is now to acquire a physical interpretation of the event as a whole.

A particular mass assignment to each track, has, in fact, to fulfill a set of conservation laws at the vertex. This requirement can therefore be used to obtain all possible interpretations of an event, and also to reduce the uncertainties in the kinematic variables assigned to each particle. Several selection criteria are then applied--the main one being the consistency with the expected ionization--and the most probable interpretation is chosen.

3.1. Kinematical Analysis

This is performed by program GRIND[9] on the basis of a least squares fitting procedure.

At first, the set of possible mass assignments for a given topology is defined by the conservation rules of quantum numbers (charge, strangeness, baryonic number) between the initial and the

final state. These different assignments are given to the program as input data, and its main task is to test them against the conservation of energy and momentum at the vertex. In Cartesian coordinates, there are four constraint equations

$$\Sigma(\pm p_x) = \Sigma(\pm p_y) = \Sigma(\pm p_z) = \Sigma(\pm E) = 0$$

where the sum is taken over the total number of particles at the vertex, the negative signs refer to the incident or target particles and the positive signs to the secondary particles produced in the interaction.

The numerical values of the left-hand sides of the constraint equations form the vector of constraints, (f_λ), and this is to be reduced to zero by the fit.

The obvious choice of variables p_x, p_z, p_z and of mass m as parameters has to be excluded, because the distribution of errors on these quantities is very far from being Gaussian. Thus $1/p$, λ(dip), ϕ (azimuth) and m are taken,[10] which reasonably fulfill this condition and allow a meaningfull error analysis to be carried out. These parameters are related to the Cartesian components of the momentum with

$$\begin{Bmatrix} p_x \\ p_y \\ p_z \\ E \end{Bmatrix} = \begin{Bmatrix} p\cos\lambda\cos\phi \\ p\cos\lambda\sin\phi \\ p\sin\lambda \\ \sqrt{m^2+p^2} \end{Bmatrix}$$

To decide between the possible mass assignments one could simply see how well (in terms of errors) the conservation law is fulfilled. For the correct mass assignment, however, a fit to the conservation law can yield fitted values of the momenta having smaller errors, as additional information is used. Furthermore, the existence of the four relations allows up to four missing track parameters to be determined by the fit.

Let then

(m_i) be the vector of well measured variables

(g^{-1}_{ij}) the error matrix for m

(d_i) the vector of corrections to m_i to be found by the fit

As poorly measured (short tracks) and unmeasured (neutral tracks or unknown masses) variables also occur, let

(M_k) be the vector of badly measured variables (for unmeasured variables first guesses are assumed)

(G_{kl}) the inverse of the error matrix for M (elements referring to unmeasured variables are zero)

(D_k) The vector of corrections to M, to be found by the fit.

The indices run from 1 to the number say, n of the well measured variables for the first set of definitions, or to the number N of badly measured variables for the second. The distinction between good and poor variables is made to avoid numerical difficulties in matrix manipulations; poorly measured variables have very large errors assigned to them and they receive much larger adjustments than well measured variables, for which the errors transmitted from the geometry program are used.

With the above formalism, the task of the fit consists now in finding the vectors d,D which minimize the scalar

$$\chi^2 = d^T\, gd + D^T\, GD \quad (11)$$

(T indicates the transpose matrix)

and fulfill

$$f(m + d,\ M + D) = \text{zero vector}$$

for the vector f_λ of constraints (λ runs from 1 to the number n_c of constraints).

The constraint equations have to be linearized and so are expanded in terms of first order approximations to d,D and the derivatives with respect to these variables. By the method of Lagrangian multipliers, they are then combined with the χ^2-equations into

$$\chi^2 = d^T\, gd + D^T\, GD + 2\,\alpha f = \min$$

(α is the vector of multipliers) .

The zeroing of the χ^2 derivatives with respect to d, D, and α will yield a system of $n + N + n_c$ linear equations with an equal number of unknowns. The solution procedure is an iterative one, and, if converging, the adjusted values of the track parameters are obtained, along with an χ^2 probability corresponding to the number of degrees of freedom, which can be used for deciding the goodness of the fit.

If a variable entering the equations is unknown, it may be determined by the fit — of which the number of degrees of freedom is then reduced. A frequent case of missing measurements is when one neutral particle participates in the interaction; its three track parameters are then determined from the fit. When more than one neutral is present there are more unknowns than constraint equations and no fit is possible. In that case all neutrals are lumped together as one particle with unknown mass and track parameters; these four missing quantities may then be found as explained.

The kinematic fit is repeated for each interaction vertex in an event, and a final fit is then attempted over all vertices simultaneously. The output from the program consists of a set of adjusted values for the track parameters, their error matrix and a χ^2 value for each interpretation assumed.

3.2. Selection of Interpretation.

Amongst the set of kinematically possible mass assignments (each one constituting a "hypothesis"), the most probable ones have now to be selected.

Let us first make some introductory remarks. As already stated, only hypothesis which conserve the quantum numbers are attempted in the kinematical fit. For the K^-p interactions, this implies that additional strange particles or baryons in the final state can only be produced in pairs (and with opposite values of strangeness or baryonic number). The cross-sections for such reactions are known to be much smaller, by factors of 30 and 400 respectively, than for reactions with just one strange particle and one baryon in the final state. Therefore, the production of strange particle pairs is

considered only if two or more strange particles decays are seen, while the possibility of baryon-antibaryon pairs is ignored in the general course of hypothesis testing. At a later stage, a few events belonging to these categories have been individually identified.

In general, events are broadly classified by the number of missing particles as "fits" and "no-fits". In the "fit" type of events, there is at most one missing particle; then a further distinction may be made on the basis of the number of constraints, e.g. if three variables are unmeasured the fit is of one constraint (1 -C). In the "no-fit" category, on the other hand, a χ^2-analysis is not possible, as more than one neutral particles are missing; as mentioned earlier, a fictitious particle (denoted by Z^o) then represents all the missing ones, and the momentum and energy needed to balance the constraint equations are assigned to it.

For completeness, we also refer here to a very small set of "zero constraint" events (four parameters unknown) e.g. a charged Σ or Ξ production with one neutral, where the hyperon track is too short for the measurement of its momentum; attempts are made to solve these events with additional information from secondary fits.

We now proceed in describing the criteria applied to select the most probable interpretations, and reduce ambiguities to a minimum.

(i) Consistency with ionization.

The ionization produced by a charged particle in the chamber liquid is, roughly speaking, the number of bubbles generated per unit length of track. Assuming $\beta(= V/c)$ for the beam tracks to be $\simeq 1$, GRIND calculates the expected ionization for all charged tracks with

$$I = I_o \left(1 + \frac{m^2}{p^2}\right) \sec \lambda ,$$

where I_o is the density of beam track.

If at least one track of a particular hypothesis has ionization inconsistent with the observed bubble density, the hypothesis is discarded.

By eye, one can safely decide between 1.0 and 1.4 times minimum ionization (represented by the beam track). For π/K identification, this implies an upper limit of .8 GeV/c for the laboratory momentum, while for a π/p identification the limit goes up to 1.5 GeV/c.

(ii) 4-C fit favoured over the 1-C fit.

A four-constraint fit is more reliable and thus preferred in case of ambiguity to the corresponding one-constraint fit (which has the same assignment of seen particles and an additional π^o).

(iii) Probability limits

For a pure sample of events, the χ^2-probability distribution should be flat. But as in reality events are misfitted, χ^2 values will tend to be higher and an accumulation of events is observed for small probabilities. By suitable cuts, a large number of these wrongly identified events can be removed.

The probability limits chosen, on the basis of experience from other experiments, are 1% for 4-C and 3-C fits, and 5% for 1-C, 2-C fits. Figure 4a shows the χ^2-probability distribution for a sample of 4-C events ($K^- p \to p K^o \pi^+ \pi^- \pi^-$), reasonably constant after the applied cut. On the other hand, a slight upward gradient is seen in the 1-C ($K^- p \to p \bar{K}^o \pi^+ \pi^- \pi^- \pi^o$) probability distribution of Fig. 3b, indicating an overestimation of the errors involved; this is not serious, as no fits are lost.

(iv) Missing mass limits (for 1-C fits)

The missing mass in an event is defined by the relation

$$MM^2 = \sum_{i=1}^{n} (E_i)^2 - \left(\sum_{i=1}^{n} \vec{p}_i \right)^2$$

n is the number of seen particles

and may be interpreted as the invariant mass of the neutral particle system required to satisfy energy-momentum conservation. Based on a preliminary sample of events, the following missing mass squared limits were used for π^o, $\overline{K}^o$ and neutron to distinguish between the fitted and no-fit channels:

$$-0.12 < MM^2 < .10 \quad \text{for } \pi^o$$

$$.10 < MM^2 < .35 \quad \text{for } \overline{K}^o$$

$$.40 < MM^2 < 1.20 \quad \text{for n} .$$

Figure 5 shows the $(MM)^2$ distributions for the two prong fitted (1-C) and no-fit channels. The upper limit lies at a value where the number of 1-C events is approximately equal to the number of events with an additional π^o missing. The lower limit is just accommodating measurement errors.

(v) Unseen Λ^o or Σ^o neglected

One-constraint fits with Λ^o or Σ^o missing were rejected in the analysis, as in a preliminary investigation it was realized that the number of fitted Λ^o was twenty times larger than the number predicted by the known branching ratio of the Λ^o.

(vi) Limits on particle momenta

Due to the peripherality in high energy interactions, while the pion laboratory momentum usually has a long tail over the high momentum region, there are relatively few high momentum protons. As no distinction by ionization is possible above ~1.5 GeV/c, the following conditions were imposed on the proton momentum for 1-C fits and non-fits.

$$P_{LAB}(\text{proton}) < 1.5 \text{ GeV/c for two, two + } V^o\text{-prongs events}$$
$$P_{LAB}(\text{proton}) < 3.0 \text{ GeV/c for four, four + } V^o\text{-prongs events.}$$

No cuts are applied for higher multiplicity events(because they are less peripheral) or for 4-C fits (usually not ambiguous).

Figure 6 shows the lab.momentum distribution of proton for some of the 1-C channels. The distribution "tails-off" well before 2 GeV/c for the three body final state $p\,K^-\pi^o$, whereas it extends up to 3 GeV/c for the five body one $pK^-\pi^+\pi^-\pi^o$. This justifies the limits chosen.

Furthermore, it was found that in low multiplicity channels with the $\overline{K}^o$ kinematically fitted, the $\overline{K}^o$ lab. momentum distribution showed an accumulation of events below 2 GeV/c, not to be observed in the same channels with the $\overline{K}^o$ seen to decay; thus to remove any spurious fits a lab momentum cut-off at 2 GeV/c was applied for the fitted $\overline{K}^o$ in two and four prongs events (Fig. 5c shows an example).

(vii) A probability ratio criterion

In case of ambiguity between fits with the same number of constraints, any fit with a probability less than one third of that of the best fit was rejected.

(viii) Restriction to three hypotheses per event

In the very few cases where more than three fits remain after applying all previous criteria, the three with the highest probabilities were selected.

For no-fit events, however, there is no way of choosing between more than three interpretations, as probability criteria are not applicable; hence all charged tracks not clearly identified as protons or K^- are treated as pions.

3.3. Automation of the Procedure.

The procedure concerning the kinematical fitting has been substantially automated by using the program AUTOGRIND.[13] This program, which accepts the GRIND library tape as input, applies the selection criteria outlined in the previous section; it also prints out relevant information for checking the ionization predictions on the scanning table.

To eliminate this manual scanning, and also to improve the accuracy of the ionization estimates, is a task of obvious importance. To that purpose, bubble density measurements are currently performed by the automatic measuring machine.[14] When the HPD spot crosses a track, it may either touch a bubble, or just cross the gap between bubbles (in this case we have a "miss"). A relation is derived between the ionization K and the measured number M of misses in a length α of the track,

$$e^{-K\alpha} = \frac{M}{T}$$

where T is the number of scan lines sampling the track.

The remaining treatment is now standard. A χ^2 is defined by the measured and expected ionizations of tracks on all three views, and

subsequently minimized by AUTOGRIND. The corresponding cut-off probability is used as a selection criterion for discarding as before wrong mass assignments. Checking on the scan table is reduced to about 10%, just in the cases the ionization fit had failed.

4. ORGANIZATION AND PROCESSING OF THE DATA

The result of the event identification consists of a file with uniquely identified or still ambiguous events, described by the masses and momentum vectors of the participating particles and their covariance matrices.

In order to facilitate the statistical analysis, the information from all the events in a required category is gathered together by SLICE, the first program in the post-kinematic chain.[15] SLICE uses the GRIND library tape as input, together with cards to communicate the selected interpretations. In the mode used in the present experiment, up to three fits could be accepted per event. To each ambiguous fit a weight $1/n$ is assigned, where n is the number of the ambiguities.

In addition, from the particle masses and momenta SLICE calculates some quantities of particular interest to the analysis, such as the energy of particle subsystems, the center of mass momenta, etc. With this information added to the basic event description, binary records of the events are finally written on magnetic tapes, and are known as the Data Summary Tapes (DST) of the experiment.

The DST data files constitute the basis for all following physics analysis, which can be considered as having two main aspects: statistical analysis and functional analysis.

The statistical analysis is performed by SUMX,[16] which essentially scans the data summary tapes and accumulates information

to form histograms, correllation plots, etc., or make tests against specified criteria. Provision is also made for the user to perform auxiliary computations, which may be necessary if the relevant information does not exist on the DST.

The functional analysis, on the other hand, is a complex problem concerned with the fitting of experimental data to theoretical models of particle interactions. Here the operations involve mainly the minimization of multivariable functions, and Monte Carlo methods of integration[17] are used to produce distributions that may be compared with the experimental results.

5. A NOTE ON THE COMPUTERS USED

Looking back through the different stages of the event analysis, we can describe the whole process as a huge data reduction and a stepwise extraction of more and more global information. To this purpose, the very extensive use of digital computers is seen as indispensable.[18]

The Imperial College part of the 10 GeV/c K^-p data was analysed in an IBM 7094 (earlier stages), to be succeeded later by the CDC-6600 of the University of London. The ON-LINE measurements and the HPD programs chain are controlled by a PDP-6 belonging to the High Energy group. Part of the final computations, i.e. the compilation of DST's was performed at the CERN CDC-6600.

REFERENCES AND FOOTNOTES

1. For a general discussion, see, for instance P. Villemoe, "Data Processing in Bubble Chamber Experiment" in the "Proceedings of the 1970 CERN computing and Data Processing School" CERN Report 71-6.

2. As the criteria were slightly modified in the subsequent runs of the experiment, we are mostly referring to Exp. 12.

3. The fourth one, resulting from the camera towards the beam entry, is not used in the analysis.

4. P.V.C. Hough and B.W. Powell, N.C. 18 (1960) 1184.

5. "The HPD MARK 2 flying-spot digitizer at CERN, CERN Report 68-4.

6. See the article by B.K. Penney in the proceedings of the "International Conference on Data Handling Systems in High Energy Physics" CERN Report 70-21.

7. For the original formulation see:

   G. R. McLeod, CERN Report 60-11, and

   W. G. Moorhead, CERN Report 60-33.

   THRESH Programming details can be found in CERN T.C. Program Library, updated from time to time with the various modifications made.

8. X and Y components of the magnetic field are neglected in the present version of the program.

9. R. Bock, Program GRIND, CERN T.C. Program Library.

10. The two angles λ,ϕ are related to those used in the geometrical reconstruction (THRESH) by the relations

$$\lambda = \pm \lambda_T$$

$$\phi = \beta \pm \pi/2 \ .$$

11. If we neglect correlations, in indexed notation this takes the familiar form

$$\chi^2 = \sum_i \left(\frac{d_i}{\delta(m_i)}\right)^2 + \sum_K \left(\frac{D_K}{\delta(D_K)}\right)^2 = \text{minimum}$$

where $\delta(m_i)$, $\delta(M_K)$ stand for the standard deviation of m_i, M_K. Thus one has a quantitative formulation of the requirement that the d_i's, D_K's should be as small as possible.

12. See, for instance J. Bartsch, et al., N.P. B 14 (69) 255.

13. G. Kellner, CERN, and M. Mermikides, Imperial College, private communication.

14. H. Atherton, et. al., on the Proc. Int. Conf. on Advanced Data Processing, Argonne, 1968, Argonne Report ANL-7515 (1969), p. 344.

P. Duinkee, CERN Internal Report, DD/DH/69/20 (1969).

15. E. Pagiola, CERN T.C. Program Library.

16. A program originally written in Berkeley and introduced to CERN in 1963. See J. Zoll, CERN T.C. Program Library.

17. See F. James, "Monte Carlo for Particle Physicists", Herceg Novi School Notes (1968).

18. For a general survey see G. R. Macleod, "Computers and Computation in High Energy Physics", CERN/DD/DH/69/8.

Fig. II-1

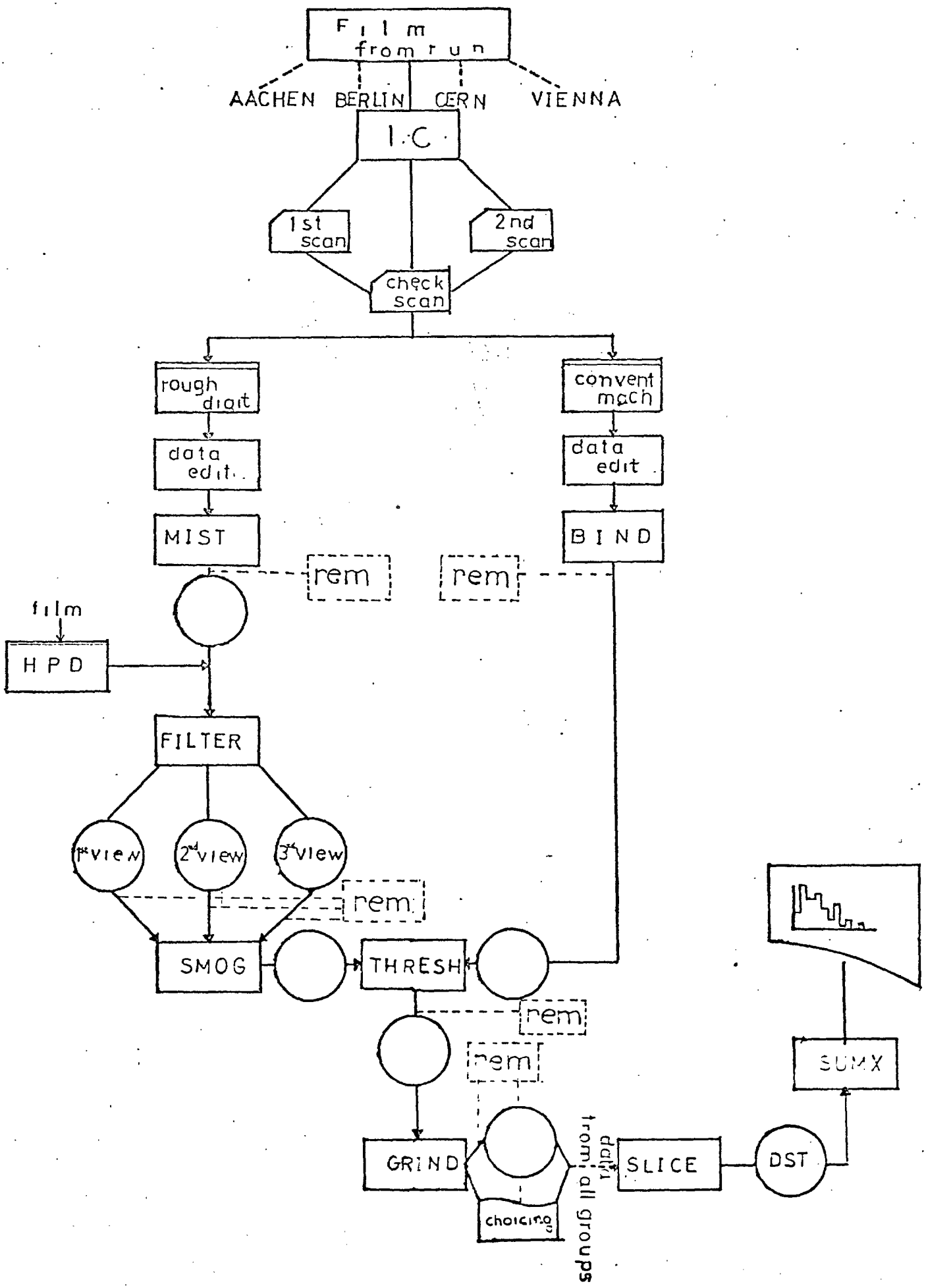

Film from run
AACHEN
BERLIN
CERN
VIENNA
I.C.
1st scan
2nd scan
check scan
rough digit
convent mach
data edit
data edit
MIST
BIND
rem
rem
film
H P D
FILTER
1st view
2nd view
3rd view
rem
SMOG
THRESH
rem
rem
SUMX
GRIND
data from all groups
SLICE
DST
choicing

Fig. II-2

200 HBC - TOP, CAMERA 1

10 GeV/c K^- JAN.1968

Exp. 12

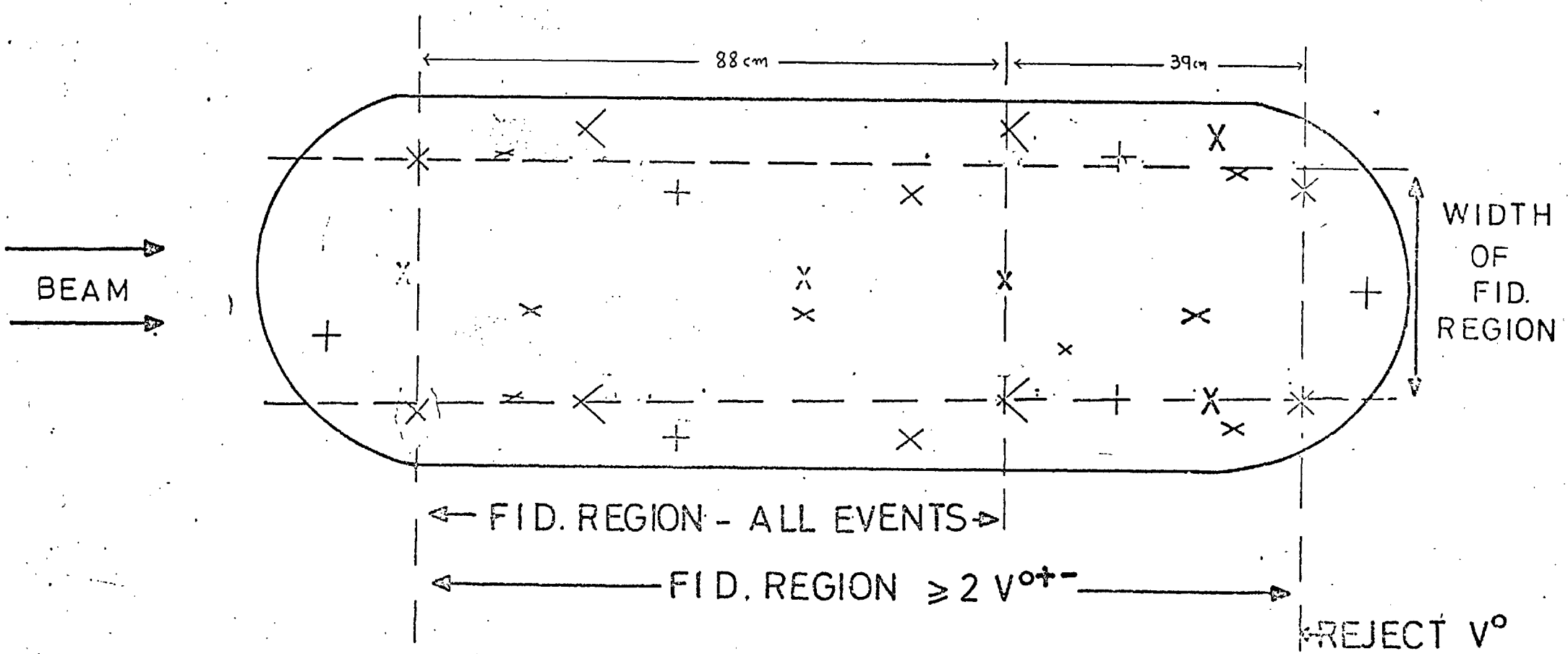


Fig. II-3

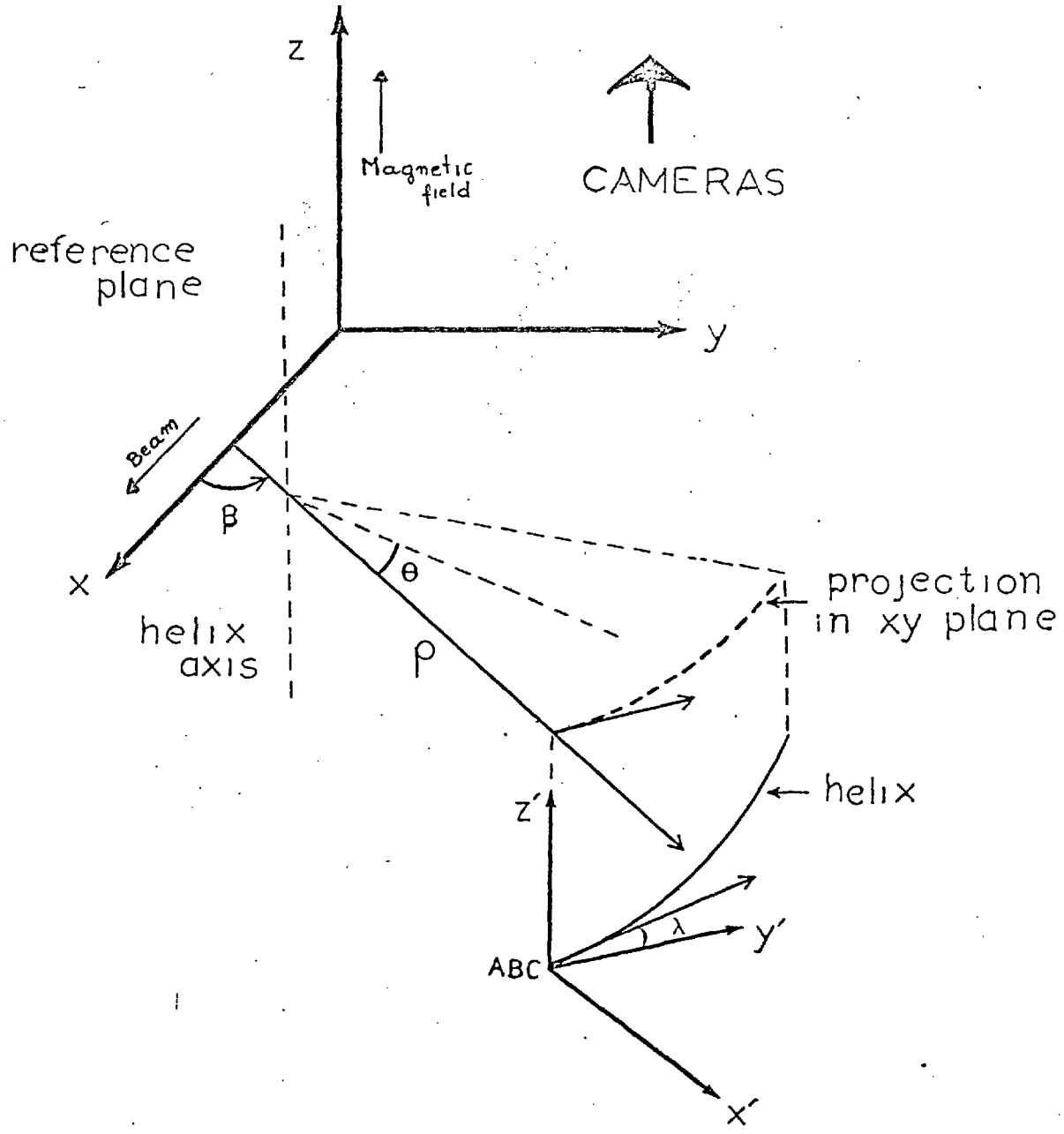

z
Magnetic field
CAMERAS
reference plane
y
Beam
β
x
θ
projection in xy plane
helix axis
ρ
helix
z'
λ
y'
ABC
x'

Fig. II-4

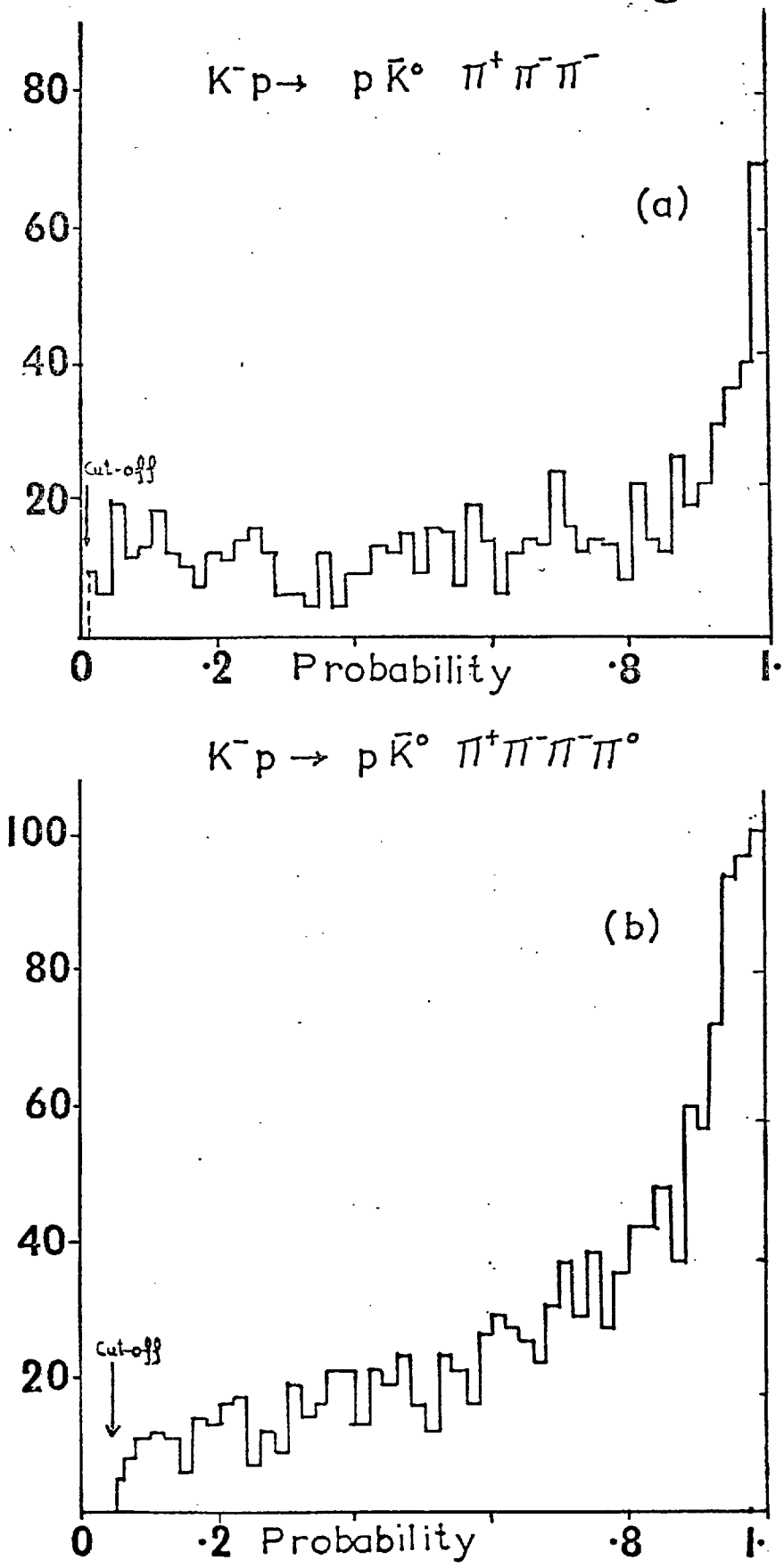

$K^- p \rightarrow p \bar{K}^0 \pi^+ \pi^- \pi^-$
(a)
80
60
40
20
Cut-off
0
·2
Probability
·8
1·
$K^- p \rightarrow p \bar{K}^0 \pi^+ \pi^- \pi^- \pi^0$
(b)
100
80
60
40
20
Cut-off
0
·2
Probability
·8
1·

Fig. II-5

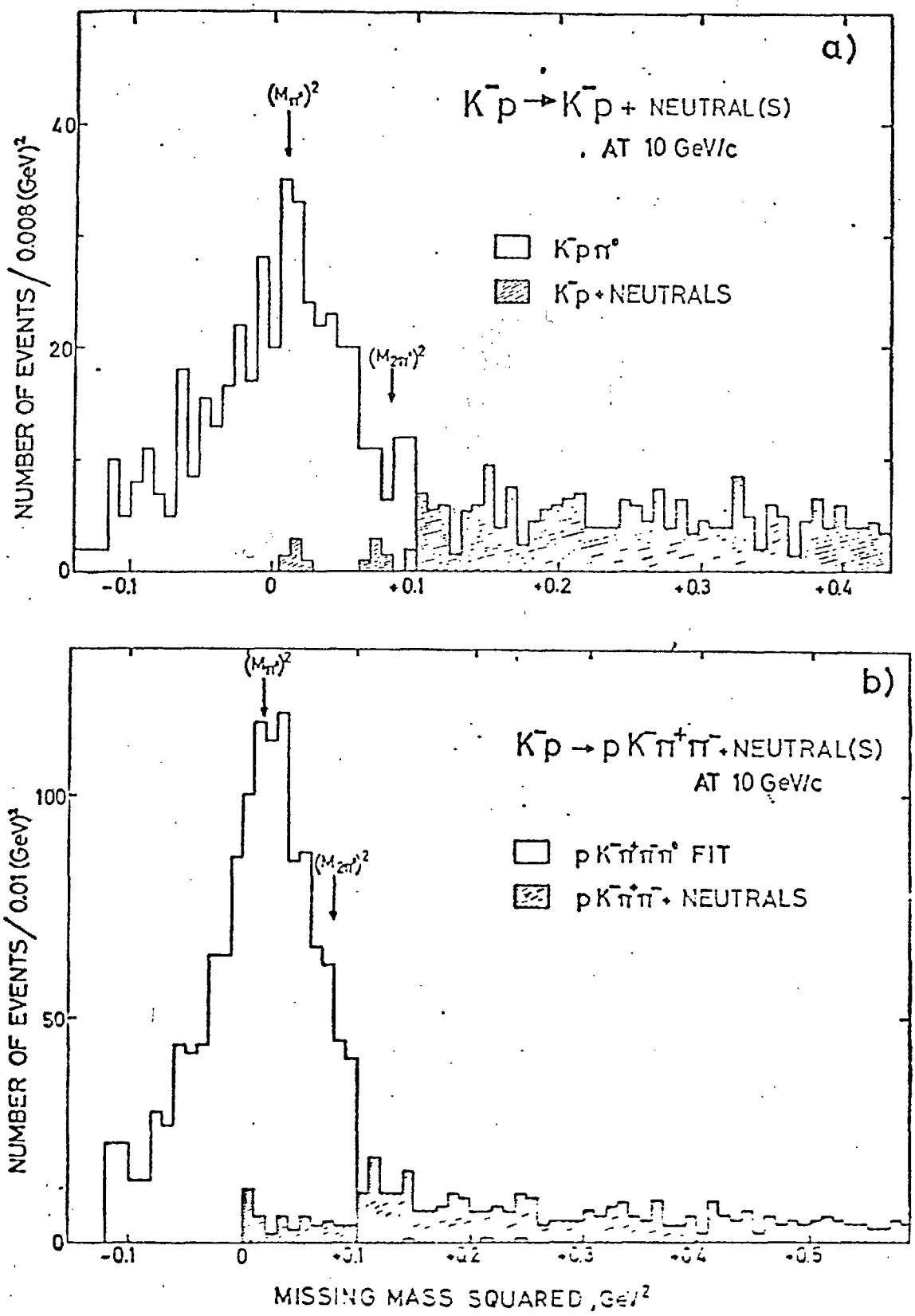
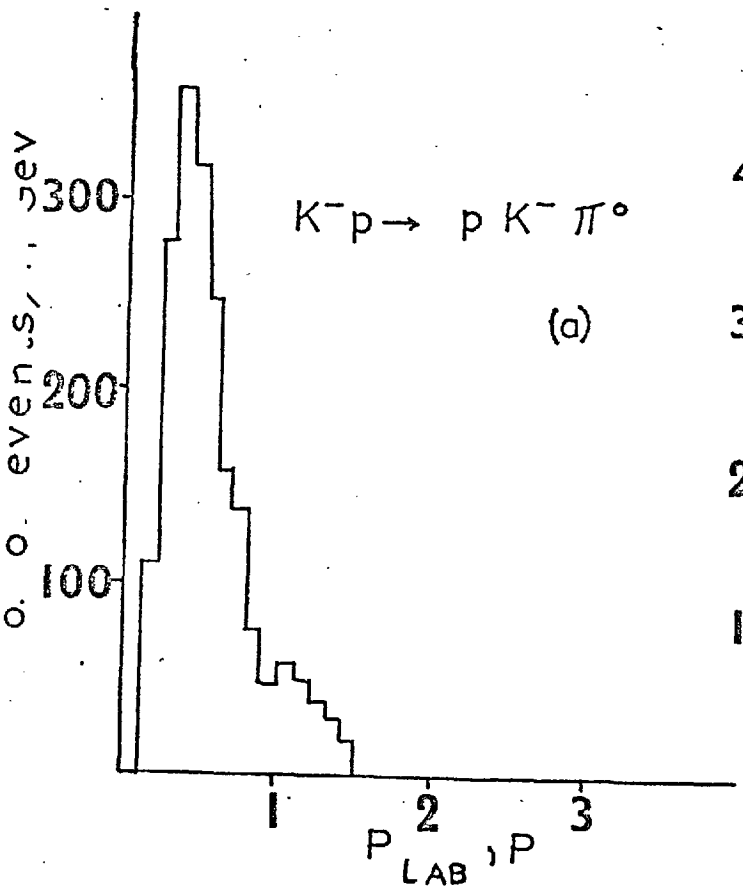
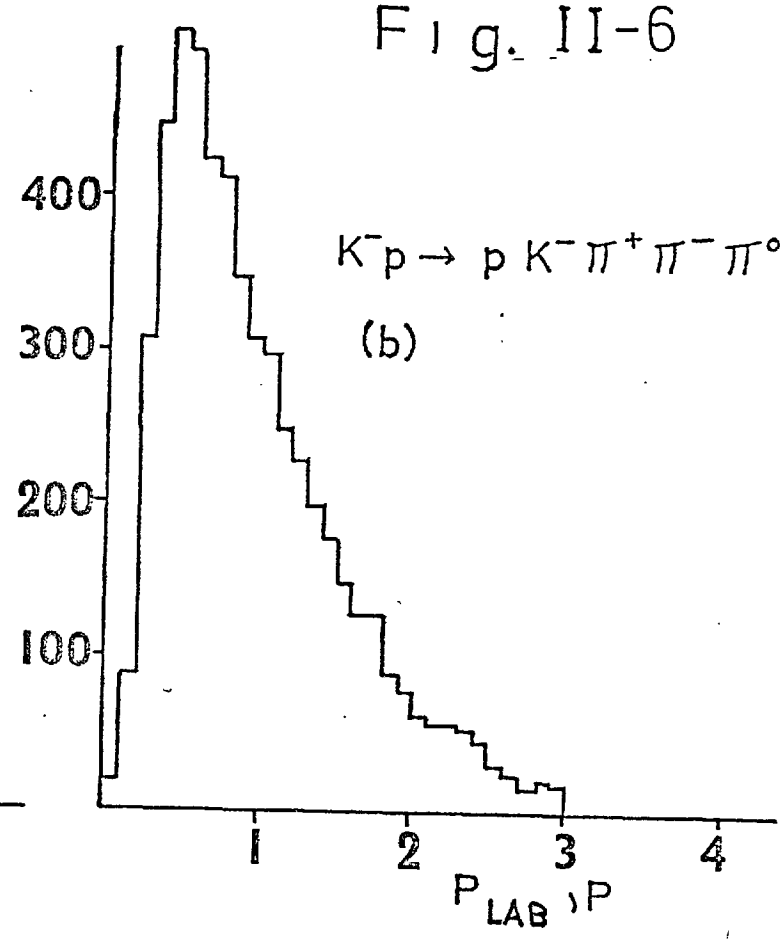
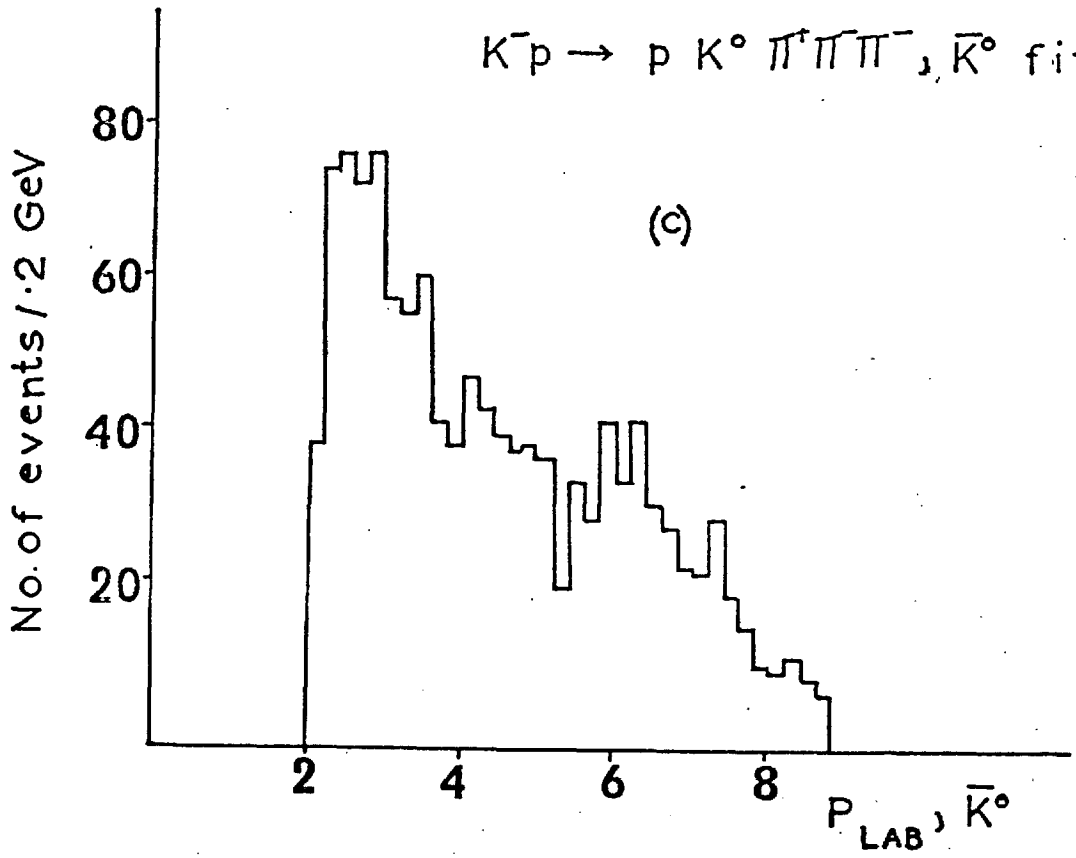

a)
$K^-p \to K^-p$ + NEUTRAL(S)
AT 10 GeV/c
$K^-p\pi^0$
K^-p + NEUTRALS
$(M_{\pi^0})^2$
$(M_{2\pi^0})^2$
NUMBER OF EVENTS / 0.008 (GeV)²
40
20
0
-0.1
0
+0.1
+0.2
+0.3
+0.4
b)
$K^-p \to p K^-\pi^+\pi^-$ + NEUTRAL(S)
AT 10 GeV/c
$p K^-\pi^+\pi^-\pi^0$ FIT
$p K^-\pi^+\pi^-$ + NEUTRALS
$(M_{\pi^0})^2$
$(M_{2\pi^0})^2$
NUMBER OF EVENTS / 0.01 (GeV)²
100
50
0
-0.1
0
+0.1
+0.2
+0.3
+0.4
+0.5
MISSING MASS SQUARED, GeV²

Fig. II-6


300
200
100
1
2
3
P_{LAB}, P
$K^- p \rightarrow p K^- \pi^\circ$
(a)


400
300
200
100
1
2
3
4
P_{LAB}, P
$K^- p \rightarrow p K^- \pi^+ \pi^- \pi^\circ$
(b)


80
60
40
20
No. of events / ·2 GeV
2
4
6
8
P_{LAB}, $\bar{K}^\circ$
$K^- p \rightarrow p K^\circ \pi^+ \pi^- \pi^-$, $\bar{K}^\circ$ fitted
(c)

CHAPTER III.

THE SEARCH FOR SYSTEMATIC ERRORS

In the present chapter we discuss some sources of biases and errors as they arise in the instrumentation and the analysis system. The channels of particular interest to this thesis are examined in some detail, and the chapter concludes with methods and data on the cross-sections calculations.

1. BEAM MOMENTUM AND PURITY

We have to ensure that the observed interactions are really due to incident negative kaons having the desired momentum.

The measurement of high energy beam tracks is rather inaccurate, so the beam parameters (i.e. its momentum, dip and azimuth angle) were in addition determined from a separate experiment.[1] For the momentum, in particular, a value of 10.12 ± .08 GeV/c was obtained; the error includes the ionization losses in the chamber and the momentum spread of the beam. These beam parameters are given as input data to GRIND, and, if they are within three standard deviations of the measured values for the event, a weighted average is used for each parameter; otherwise the event is rejected as off-beam.

The possibility of interactions due to non-kaon tracks was also investigated. From the known K^-p total cross-section at 10 GeV/c,[2] and the counting of interactions with the RF separators switched off, the pion contamination is found to be below 5%; this agrees with an independent estimate based on the number of associated V^o's in a sample of film. The muon contamination reaches 20%, but this is not serious since muons do not interact strongly. Finally, any anti-proton contamination is virtually eliminated at the tuning stage of the beam.

2. BIASES IN THE ANALYSIS OF PICTURES

2.1. Scanning and Measuring Biases.

Both random and systematic errors are connected with the missing of events at the scanning stage.

To estimate the random losses, let us assume that the probability of finding each type of event is the same, and represent with

N the total number of events in a sample

n_1, n_2 the number of events seen in the first and second scan respectively

n_{12} the number of events seen in both scans

P_1, P_2 the probability of finding an event in first and second scan respectively.

We then have

$$N = \frac{n_1}{P_1} = \frac{n_2}{P_2} = \frac{n_{12}}{P_1 P_2} .$$

The total number of distinct events seen in both scans is $n_1 + n_2 - n_{12}$, and so the following relation holds for the overall scanning efficiency

$$\text{eff} = \frac{n_1+n_2-n_{12}}{N} = \frac{(n_1+n_2-n_{12})n_{12}}{n_1 n_2} .$$

In Table 1, the scanning efficiencies for various topologies of an 1-C sample of events (from Exp. 12) are given. The numbers of recorded events are corrected accordingly when calculating the cross-sections.

In fact, certain types of events present a greater chance to be missed in both scans, and therefore a systematic error is introduced. They mainly are:

(i) Elastic reactions, with a very short recoil proton. These can be corrected by introducing a t-dependent correction factor.[3]

(ii) Events of 000 topology. In this case a $\overline{K}^o$ or a Λ^o (not seen) has to be involved in the final state. Using the charged/neutrals branching ratio of these particles,[4] we can estimate the correct number of 000 events from the number of $\overline{K}^o$'s and Λ^o's which are seen in the corresponding topology 001.

The ambiguity between V^o's and electron pairs might also be a source of systematic bias at the scanning stage. In fact, only high momentum Λ^o's, with the proton going forward in the Λ^o center of mass, can simulate electron pairs, and any such bias will introduce an anisotropy in the decay angle distribution. This has not been observed in the present experiment.

At the measuring stage of the analysis, situations also arise where events are lost or misidentified. Some events are unmeasurable, for instance, because of poor quality of film or other tracks overlapping; also, events having a secondary interaction on one of the tracks close to the vertex, will usually give a zero constraint fit, because the momentum of this track is unmeasurable. Of course, these sets of events, being counted at scanning, would introduce no bias if distributed randomly to all topologies. But in fact failures of this sort are again biased towards a certain type of events, e.g. slow tracks have larger cross sections for secondary interactions.

2.2. Bias in Observing Particle Decays.

Due to the finite size of the bubble chamber strange particle decays are lost if occurring outside the fiducial volume. Also, decays too close to the production vertex are often misidentified at the scanning stage, or present difficulties in measuring. To correct for these losses, the probability of a V^o decay taking place and being seen is calculated. Let us represent with

ℓ_{min} the minimum detectable decay length in chamber space, set at 3mm for this experiment.

ℓ_{max} the distance (along the line of flight) between the production vertex of the strange particle and the end of the fiducial region; this is the potential length over which the decay could have been seen.

ℓ_o the theoretical mean decay length of the particle ; for a particle of mean lifetime τ, the corresponding ℓ_o is given by $\ell_o = \tau\beta\, p/m$, where β is its velocity, p the momentum and m the mass.

With these definitions, the probability of a V^o not decaying in the distance ℓ_{max} is now $e^{-\ell_{max}/\ell_o}$, while the probability of it surviving past the minimum detectable length is $e^{-\ell_{min}/\ell_o \cos\lambda}$ (Note that $\ell_{min}/\cos\lambda$, with λ the dip, is the minimum length projected on to the line of flight.). Therefore, the probability that the particle will decay after traveling a distance between ℓ_{min} (projected) and ℓ_{max} is

$$P = e^{-\ell_{min}/\ell_o \cos\lambda} - e^{-\ell_{max}/\ell_o} .$$

The inverse of this probability is the weight applied to each observed event to correct for the decay losses.

This simple method leads in fact to the dependence of the weight on the position and orientation of the event inside the chamber. A very large weight might then arise if ℓ_{max} is very small compared to the ℓ_o of the particle, and for that reason an upper limit is imposed on the decay weights.

In addition, in order to obtain the physical cross-sections in the $\overline{K}^o$ or Λ^o channels, the unseen decay modes of these particles have to be taken into account. The following values[4] for the branching ratios are used

$$\frac{\overline{K}^o \to \pi^+\pi^-}{\overline{K}^o \to \text{total}} = .342 \pm .005$$

$$\frac{\Lambda^o \to p\pi^-}{\Lambda^o \to \text{total}} = .653 \pm .012$$

where we have assumed that all $\overline{K}^o$ seen decays are $\overline{K}^o_s$,[5] and have neglected rare decay modes of the Λ^o and $\overline{K}^o$.

3. BIASES IN THE COURSE OF EVENT IDENTIFICATION

3.1. Biases Due to Kinematic Fitting.

The reasonableness of the χ^2-probability distributions (some were shown in Fig. II-4) is a first suggestion that no serious systematic bias is introduced by the kinematic fitting procedure.

A further test is provided by the so called "stretch" function, defined for a variable x as

$$S(x) = \frac{(x_f - x_m)}{(\Delta x_f^2 - \Delta x_m^2)^{\frac{1}{2}}}$$

where x_f is the fitted and x_m the measured (unfitted) value of x .

If the random errors are properly estimated and there are no systematic errors in the measurement, $S(x)$ has mean value zero. Also, the expected width of the distribution of $S(x)$ has to be unity, because of the denominator in the above relation. Furthermore, since in the case of kinematical fit the variables are chosen in such a way that they are approximately distributed as Gaussians (i.e. $1/p$, λ,ϕ), so it has to be and for the relevant stretch function.

Figure lab shows the stretches in $1/p$, λ and ϕ, first for some beam tracks (4C and 1C fits), and then for the fitted tracks in a sample of 4C fits only; the dotted lines are the normal distributions normalized to the data. The behavior of the stretches is consistent with what was expected; a slightly excessive broadness, noted only for the beam tracks, might be due to a not very precise error estimation (because of the smaller number of constraints) in this case.

3.2. The Reliability of Event Interpretation.

The criteria discussed in the previous chapter are efficient enough to allocate in most cases a single hypothesis to each event. But it is not, of course, always certain that the selected hypothesis is the correct one. Therefore, in a sample of events which have been classified as belonging to a certain reaction, some inevitably would have been misidentified; furthermore, as only one interpretation can be true for each event, only a part of the ambiguous events attached to the reaction would really belong to it. On the other hand, one has also to think of the good events (that is, belonging to the reaction) which for some reason have been excluded from the sample.

The events in these subcategories are not known individually, but in some cases the relevant corrections to the cross-sections may be estimated--as shown, for instance, for the $\overline{K}^o$'s decaying outside the chamber.

In addition to bias introduced by the analysis system of the film, some situations in the interpretation procedure might also contribute in loosing or misidentifying events.[6] In several cases, at first, the correct hypothesis might not have been attempted at all. This occurs, for example, when the cross section for one process is known to be very small: more than one strange particle or baryon in the final state, missing Λ^o or Σ^o--or pions in the beam which, since π and K have a rather small mass square difference, are likely to give a fit to the kaon hypothesis. A similar situation arises when one or two prongs are incorrectly added to the event at the scanning stage, either because one or both electrons from a Dalitz pair are indistinguishable from pions (momentum above 200 MeV/c), or because of a V^o decaying very close to the production apex. Also, the fit to

the genuine hypothesis for an event may fail, due to a small error in the geometry constant; this is more likely for 4-C fits, as they are the most highly constrained.

Finally, of importance is the severe loss of events occurring when the selection criteria in deciding between various interpretations are applied. This problem is dealt with in the following section, on the examplary basis of two reactions of particular interest to this thesis.

4. BIASES IN THE REACTIONS STUDIED

4.1. General Remarks.

The following reactions are the main ones to be discussed in the ensuing chapters

$$K^- p \to p\bar{K}^o \pi^+\pi^-\pi^- \quad (1)$$

$$K^- p \to p\bar{K}^o \pi^+\pi^-\pi^-\pi^o \quad (2) \ .$$

For reaction (1), the total of two subcategories has in fact been considered, namely

$$K^- p \to p\bar{K}^o \pi^+\pi^-\pi^- \ , \ \bar{K}^o \text{ seen} \quad (1a)$$

$$K^- p \to p\bar{K}^o \pi^+\pi^-\pi^- \ , \ \bar{K}^o \text{ fitted} \quad (1b) \ .$$

It is first to be noticed that (1a) and (2) belong to the 4 prongs $+V^o$ topology of events, requiring a 4-C and 1-C fit respectively. Reaction (1b), also of one constraint, is seen as a four prong final state in the scanning table, with the $\bar{K}^o$ assigned to it by the kinematic fit.

Table 2 gives the number of unique and ambiguous (with the corresponding weight) fits allocated to these reactions. The number of resulting events, and, where applicable, the final number of events after correcting for the decay losses, are also given.

4.2. The Study of Ambiguities.

As can be seen from this table, the number of ambiguous fits to the reaction (1a) is very small. Since 4-C fits are always preferred to 1-C fits, no ambiguity of this reaction with the corresponding 1-C is possible. The ambiguities are then of "internal" type, i.e. they are due to the existence of two positive tracks, in which the assignment of particles (p/π^+) might be allowed kinematically to interchange; in these cases, of course, the tracks should be above the limit for identification by ionization (1.5 GeV/c for p/π^+) and, since the proton momentum is preferentially low, the number of ambiguities is kept small. The cross section is obviously not affected by the internal type of ambiguity.

Reaction 1b, where the $\overline{K}^o$ is fitted, presents us with a greater number of ambiguities, mainly related to the four-prong reaction $p\,\pi^o\pi^+\pi^-K^-$ (that is, to difference in the assignment of the negative track); a small number of internal (p/π^+) ambiguities is also expected in both hypothesis. To investigate the matter further, some experimental quantities are plotted in Fig. 2 separately for $\overline{K}^o_{\text{seen}}$ and $\overline{K}^o_{\text{fitted}}$ events contributing to reaction (1); the differences observed are not substantial within statistics, an indication that a reasonable number of the ambiguous events in 1b belong in fact to the reaction. Other consistency tests, related to physical quantities of interest to this thesis, are discussed in the next chapter.

Internal ambiguities, at most, count for the ambiguous fits of reaction (2); a very small number is perhaps ambiguous with the $n\bar{K}^o\pi^+\pi^+\pi^-\pi^-$ hypothesis.

In principle, ambiguities of the K^o/Λ^o type might also be involved in both (1a) and (2) channels; but as they should be accompanied by a simultaneous p/π^+ internal ambiguity, their overall contribution may be considered as negligible.

4.3. The Effect of the Selections Applied.

In general, reactions (1a), (1b) and (2) are of course subject to biases rooted in scanning losses, $\bar{K}^o$ decays outside the chamber, misfits, etc., as discussed earlier; whenever possible, these losses are taken into account when calculating the cross sections. It is perhaps of interest to discuss now, as an illustrative case, the effect the relevant selection criteria might have on these reactions.

(i) The criterion, which prefers a 4-C fit over the corresponding 1-C fit, may affect the pair of reactions (1a) and (2). However, the additional π^o must necessarily have a small laboratory momentum, since for the seen particles alone momentum is approximately conserved. In fact, no peak above zero, which would have been caused by any genuine 4-C events fitted as 1-C, is observed (Fig. 3a) in the π^o laboratory momentum distribution for reaction (2).

(ii) Fig. 3bc shows the missing mass squared distributions for reactions (1b) and (2). As expected, they peak close to the mass squared of the missing particle ($\bar{K}^o$ and π^o), and follow a reasonably Gaussian shape.

The amount of misidentified events included in these reactions can be roughly approximated in the following way: the lower half of the peak (where the contamination is expected to be small) is reflected

onto the upper half, and the difference between the folded and original distributions is estimated. This gives a percentage of 2% and 3% bad events included in reactions (1b) and (2), respectively.

On the other hand, the amount of the good events, not included in these reactions as a result of the missing mass cut, is approximated by what the region above the cut contributes to the integral of the Gaussian. On the basis of a sample of events from Exp. 75, this was found to be 5% and 2% for reactions (1b) and (2), respectively.

(iii) Genuine events are also left out by the proton laboratory momentum cut applied in the 1-C reactions (1b) and (2). For (1b), the number of fits lost can be calculated by the number of events in (1a) which have protons of momentum greater than 3 GeV/c; this amounts to about 3%.

Reaction (1b) is furthermore subject to a $\overline{K}^{o}_{\text{fitted}}$ laboratory momentum cut, which can be estimated in a similar manner; a percentage of 16% events is now found to be wrongly excluded.

(iv) Finally, the probability cuts cause the loss of about 1% events in reaction (1a), and of about 5% in reactions (1b) and (2). Hard to estimate, though, is the bias due to inclusion of bad events, but this might be considered neglibible since none of the relevant distributions (see Fig. II-4 for example) showed any peaking above the cut-off.

5. THE CALCULATION OF CROSS-SECTIONS

The calculation of cross-sections is of primary concern for the bubble chamber analysis; it is often a difficult task, due to the large number of reactions present and the various corrections which have to be made.

The cross-section equivalent to just one event can in principle be calculated by counting the $K^- \to \pi^+\pi^-\pi^-$ decays (τ-decays) in the experiment; this leads to an estimate of the total path length L of the K^-, the cross-section then being 1/nL (n is the number of protons per cm^3). But as the number of seen τ-decays is small, the method is subject to rather large statistical errors and is simply used as a consistency check.(7)

Instead, the microbarn equivalent is found by normalizing the total number of observed interactions to the total cross-section, known from an accurate counter experiment(2) to be 22.5 ± .2 mb. In experiment 75, the total number of interactions in region 1 (corrected for scanning efficiency, loss of elastic events for small four-momentum transferred squared and other biases) was 31837 ± 178. Thus a μb equivalent (for region 1) equal to .707 ± 010 is obtained.

To reach the cross-sections for particular channels, we have however to take into account that separate fiducial regions were used for various topologies, and that the relative sizes of the regions were different in the two chambers. So another approach is sometimes followed, i.e. the "topology" cross-section is calculated, and the cross-section for a particular channel is then derived from the ratio of the number of events in this channel to the total number of events in the topology considered. For some channels, in fact, further corrections may be necessary if this method is applied; but in an experiment continuing over several years, it is important that new data may be added with the least possible readjustments.

Table 1 presents the up to six-prongs topology cross sections, and also the cross-sections for some common channels of the experiment.

REFERENCES AND FOOTNOTES

1. G. Kellner, CERN, private communication.

2. W. Galbraith, et. al., P.R. 138B (1965) 913.

3. See the paper on the elastic scattering of the experiment J. Bartsch, et. al., N.P. B29 (1971) 398.

4. Particle Data Group, Reviews of Modern Physics 43 (1971).

5. With about 34.3 meters per GeV/c decay length, the $\overline{K}^o_L$ decay into $\pi^+\pi^-\pi^o$ is almost never seen, and will seldom fit anyway to $\overline{K}^o \to \pi^+\pi^-$ without the missing neutral pion.

6. For a detailed study see D. Dallman, Ph.D. thesis, Imperial College (unpublished).

7. N. Mukhopadmyay, Ph.D. thesis, Imperial College (unpublished).

TABLE III-1

EFFICIENCIES, TOPOLOGICAL CROSS-SECTIONS AND CROSS-SECTIONS FOR SOME SELECTED CHANNELS

Topology	Scanning Efficiency	Cross-section mb	Selected final states	Cross-section mb
0-prongs	54.0	.474 ± .017	See Sec. 2.2	
0-prongs+V^o	97.3	.277 ± .010	$\Lambda\pi^o$	.013 ± .005
2-prongs	88.0	8.206 ± .110	K^-p	3.150 ± .080
			$pK^-\pi^o$	.280 ± .010
2-prongs+V^o	99.7	1.768 ± .021	$p\bar{K}^o\pi^-$	.220 ± .020
			$p\bar{K}^o\pi^-\pi^o$	.550 ± .030
			$n\bar{K}^o\pi^+\pi^-$	.310 ± .020
			$\Lambda\pi^+\pi^-$	.046 ± .008
			$\Lambda\pi^+\pi^-\pi^o$	.123 ± .014
2-prongs+$V^\pm$	99.3	.287 ± .012	$\Sigma^+\pi^-$	Not yet available
4-prongs	99.95	6.160 ± .086	$pK^-\pi^+\pi^-$	.883 ± .022
			$pK^-\pi^+\pi^-\pi^o$	.820 ± .020
			$nK^-\pi^+\pi^+\pi^-$	.430 ± .020
4-prongs+V^o	99.6	1.477 ± .018	$p\bar{K}^o\pi^+\pi^-\pi^-$	.290 ± .020
			$p\bar{K}^o\pi^+\pi^-\pi^-\pi^o$	.470 ± .030
			$n\bar{K}^o\pi^+\pi^+\pi^-\pi^-$	.210 ± .020
			$\Lambda\pi^+\pi^+\pi^-\pi^-$	.049 ± .008
			$\Lambda\pi^+\pi^+\pi^-\pi^-\pi^o$	.157 ± .016
4-prongs+$V^\pm$	99.6	.619 ± .016	$\Sigma^+\pi^+\pi^-\pi^-$	Not yet available
6-prongs	96.8	1.962 ± .038	$pK^-\pi^+\pi^+\pi^-\pi^-$	.200 ± .020

TABLE III-2

EVENTS CONTRIBUTING TO THE REACTIONS STUDIED

Reaction Number	Reaction	Number of Constraints	Unique Fits	Ambiguous Fits (with the Corresponding weight)	Total Nbr. of Fits	Total Nbr. of events	With Decay Weight
1a	$K^- p \to p\overline{K}^o_{seen}\pi^+\pi^-\pi^-$	4	728	21(1/2)	749	739	789
1b	$K^- p \to p\overline{K}^o_{fit}\pi^+\pi^-\pi^-$	1	1055	646(1/2) 128(1/3)	1829	1421	-
2	$K^- p \to p\overline{K}^o_{seen}\pi^+\pi^-\pi^-\pi^o$	1	1250	102(1/2) 3(1/3)	1355	1302	1377

Fig. III-1

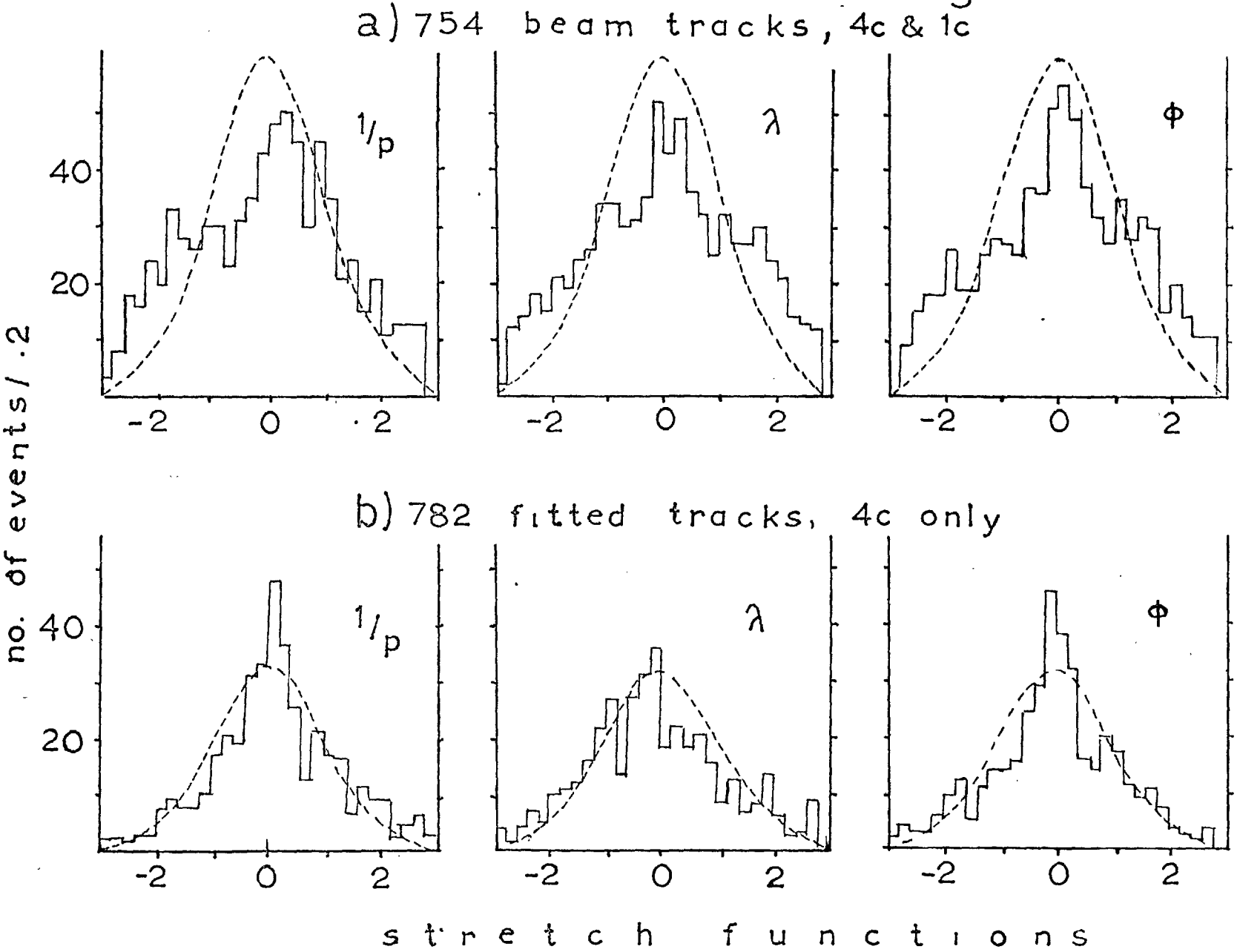

a) 754 beam tracks, 4c & 1c
1/p
λ
φ
40
20
-2
0
2
b) 782 fitted tracks, 4c only
no. of events/.2
stretch functions

Fig. III-2

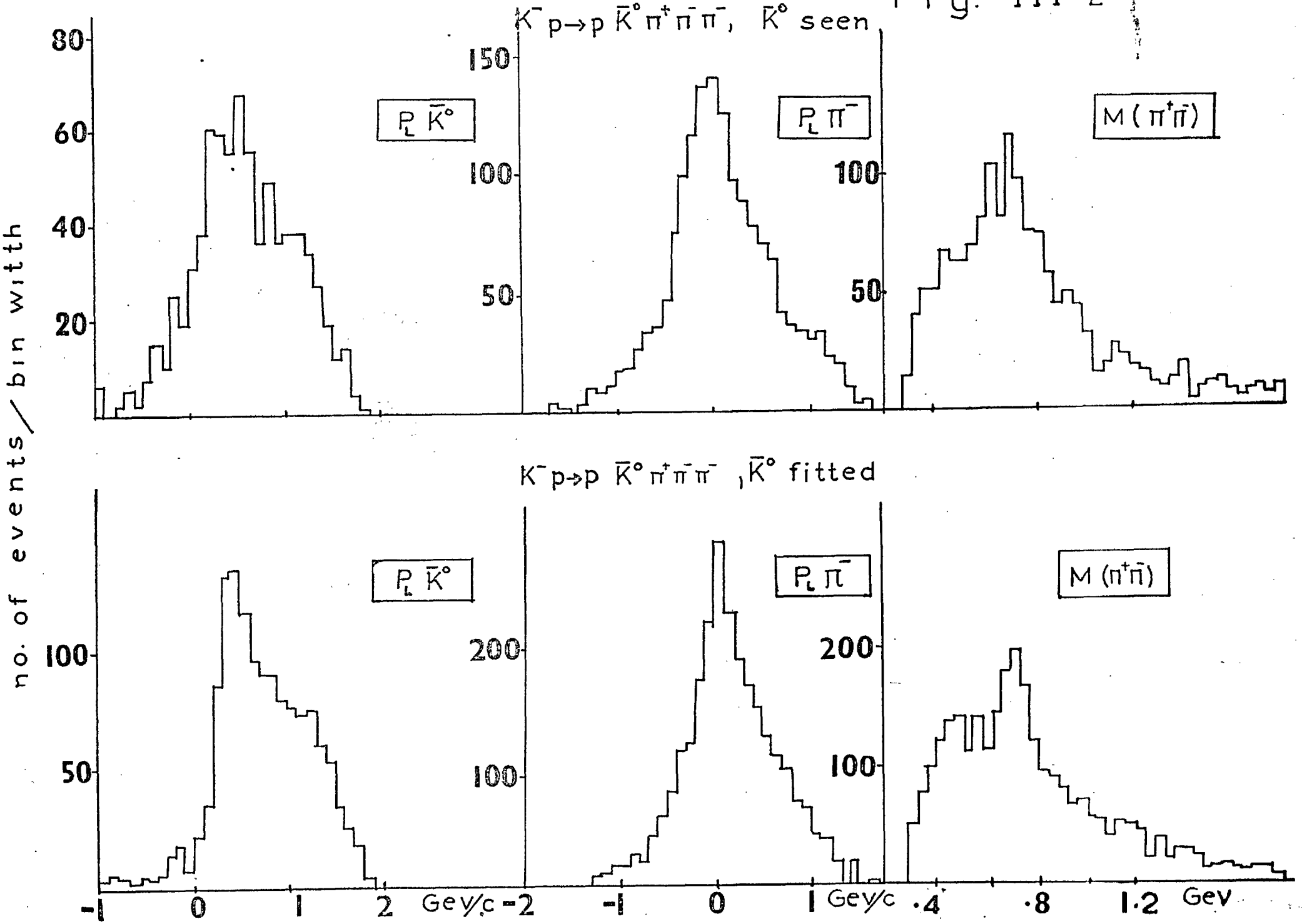
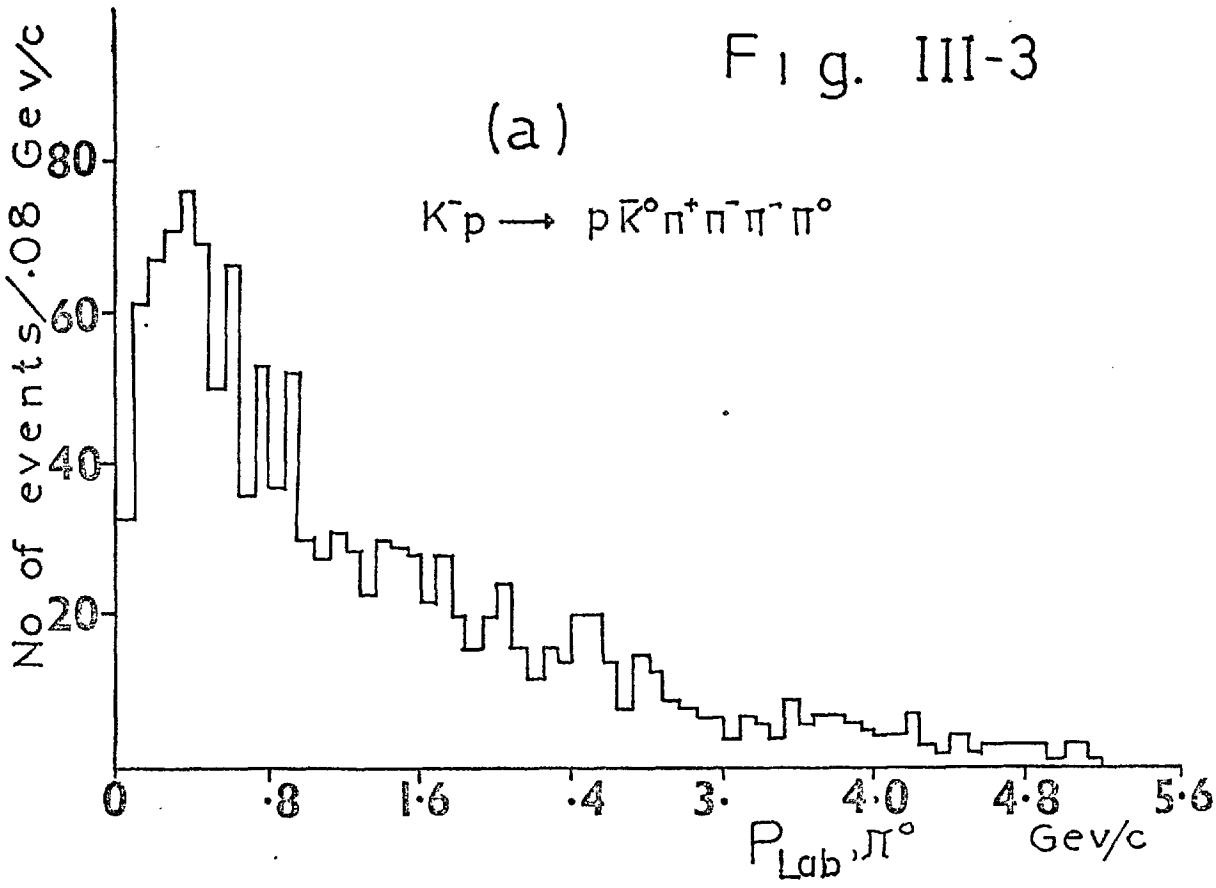
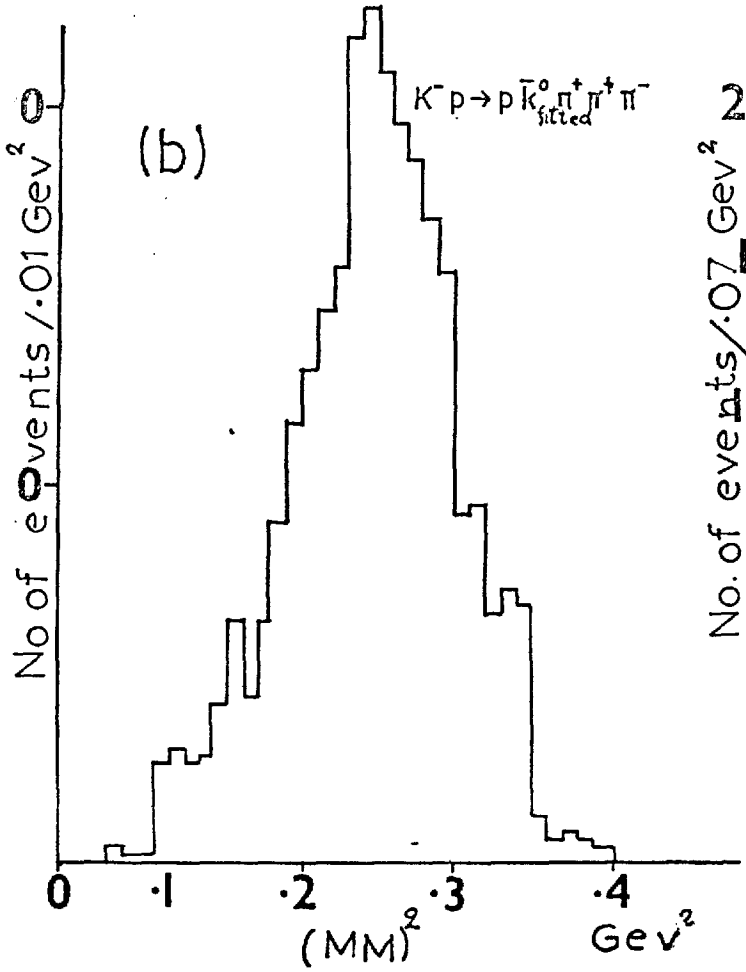
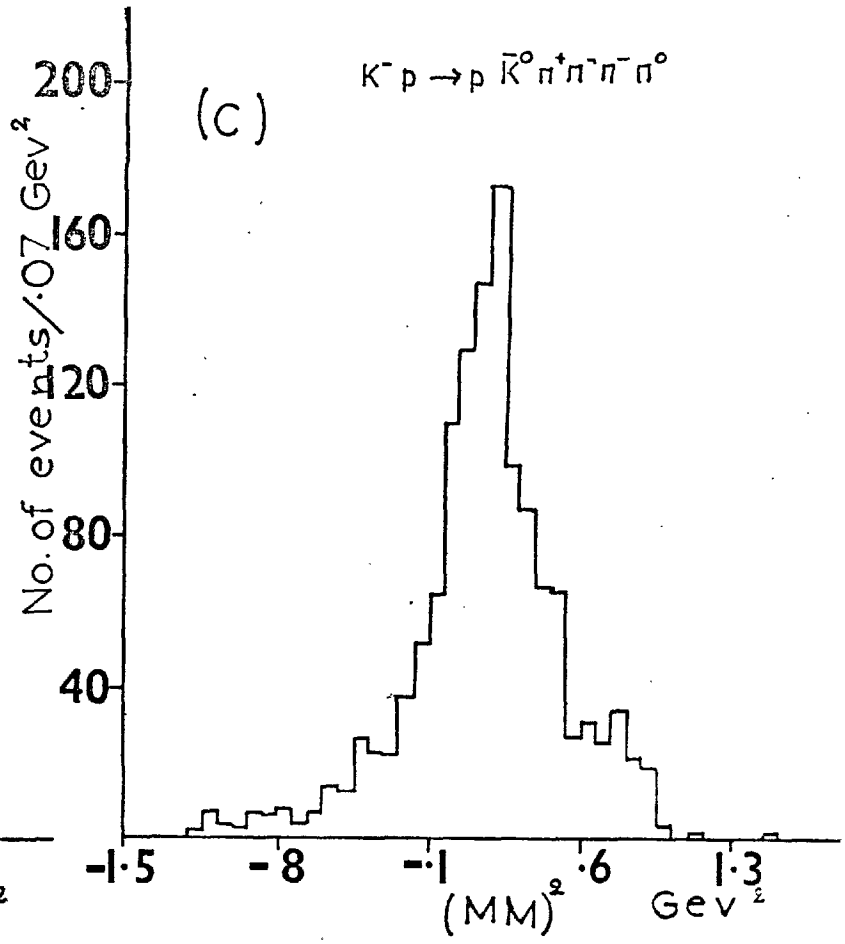

$K^- p \to p \bar{K}^0 \pi^+ \pi^- \pi^-$, $\bar{K}^0$ seen
$P_L \bar{K}^0$
$P_L \pi^-$
$M(\pi^+\pi^-)$
$K^- p \to p \bar{K}^0 \pi^+ \pi^- \pi^-$, $\bar{K}^0$ fitted
$P_L \bar{K}^0$
$P_L \pi^-$
$M(\pi^+\pi^-)$
no. of events / bin width
80
60
40
20
150
100
50
100
50
100
50
200
100
200
100
-1
0
1
2
Gev/c
-2
-1
0
1
Gev/c
.4
.8
1.2
Gev

Fig. III-3


(a)
$K^- p \longrightarrow p \bar{K}^0 \pi^+ \pi^- \pi^- \pi^0$
No of events/·08 Gev/c
80
60
40
20
0
·8
1·6
·4
3·
4·0
4·8
5·6
P_{Lab}, Λ^0
Gev/c


(b)
$K^- p \to p \bar{K}^0_{fitted} \pi^+ \pi^+ \pi^-$
No of events/·01 Gev²
0
0
0
·1
·2
·3
·4
$(MM)^2$
Gev²


(c)
$K^- p \to p \bar{K}^0 \pi^+ \pi^- \pi^- \pi^0$
No. of events/·07 Gev²
200
160
120
80
40
-1·5
-·8
-·1
·6
1·3
$(MM)^2$
Gev²

CHAPTER IV.

THE STUDY OF RESONANCE PRODUCTION IN TWO MULTIPARTICLE PROCESSES

Problems and results, mainly associated with resonance production in the processes

$$K^- p \to p \bar{K}^o \pi^+ \pi^- \pi^-$$

$$K^- p \to p \bar{K}^o \pi^+ \pi^- \pi^- \pi^o$$

at 10 GeV/c

are presented and discussed in this chapter. A maximum likelihood method is used for most of the analysis. A short survey of many body dynamics serves as an introduction to the work.

1. MULTIPARTICLE REACTIONS AT HIGH ENERGY

Much interest has arisen in recent years over the study of multiparticle (number of particles greater or equal to three) final states in high energy collisions. Progress in this direction is of great importance, since multiparticle processes account for the largest part (~70% at 10 GeV/c K^-p) of the total cross-section, and even simple two-body collisions would be influenced by the many-particle channels.

The intrinsic complexity of these processes present the experimentalist and the theorist with difficult problems. One has to deal with a large number of independent variables ($3n-4$ when n particles are present in the final state) and even the problem of organizing the data is therefore serious. Obvious in the situation is the need for a true theory, suggesting the direction we have to move in order to reveal the underlying physics.

Although a comprehensive theory is still lacking, some definite features of multiparticle processes have so far been established. At first, the precise bubble chamber analysis has confirmed a fundamental law already suggested by cosmic ray experiments: that the transverse momenta of the secondaries (i.e. the momenta orthogonal to the incident beam axis) have always a value of 300-500 MeV, rather independent of the incident energy and the type of reaction. Thus, a bound on transverse momenta is found to exist in processes as different as inelastic πN interactions and $p\bar{p}$ annihilation into pions. Also, it was noticed that the energy of the secondaries was not distributed statistically; instead, "leading" particles occurred, i.e. the incident particles in a collision tended to continue in the same direction with a large fraction of the total energy.

Recent results deserving, perhaps, to be mentioned refer to the cross-sections. The data from the Serpukhov machine,[1] for instance, seem to indicate that the total cross-sections of π^-, K^- and $\bar{p}$ on protons and deuterium remain practically constant in the energy domain corresponding to an incident lab. momentum between 20 and 60 GeV/c. In another direction, some successful steps have been taken[2] in separating the dynamical content 6^* of the inelastic cross-sections from the kinematic part; 6^* is then related to p_{LAB} by a simple power low

$$6^* \propto p_{LAB}^{-\eta}$$

similar to that for two-body reactions.

Various other attempts have been made to extract generally valid conclusions by looking at the topological cross-sections,[3] or at the correlations existing in the distribution of the angle between two pions.[4] The number of times a given number of secondaries is produced in high energy collisions, the so called "multiplicity distribution", is also examined.[5] The relations proposed in these cases, of mostly empirical form, have however to be taken with caution. In another work of, perhaps, interest[6] it is shown that the angular distribution with respect to the momentum of one of the outgoing particles is factorizable as a function of the longidudinal p_L and transverse p_T components of the c.m. momentum, i.e.

$$d^2 6/d\Omega dp = F(p_L)\, G(p_T)$$

where p, p_L and p_T refer to any of the outgoing particles.

Such "exclusive" analysis is becoming very difficult as the multiplicity increases. So of great interest is a recent, "inclusive"

way approach, where the experimental distributions of specific particles are analysed, summing over everything else; these inclusive distributions may obey simple scaling and factorization properties associated for instance with the name of pionization[7] or limiting fragmentation.[8]

The remarks made above are simply hints on a very intense experimental activity, reviewed in detail by several authors.[9]

But much of the effort in the domain of high multiplicity reactions is in fact directed towards the construction of theoretical models. To that, two possible approaches appear.[10] A description, first, can be formulated, suitable for large particle numbers and essentially modifying statistical and thermodynamical considerations to include the observed deviations from a momentum space equidistribution, e.g. resonances are empirically bumps, exceeding the invariant mass distribution given by "phase space". In Hagedorn's thermodynamical model,[11] for instance, one has a "fireball" formation with p_T restriction in each localized region of the interaction area. To account for the peripherality observed, a relative velocity between different such localized regions is then introduced in the form of a velocity distribution function. Such a model, in not considering a fixed particle number predicts only very inclusive quantities ("spectra") and is therefore of limited applicability.

An alternative approach, as opposed to statistical considerations, is to construct a specific dynamical model (Reggeized one particle exchange model, Veneziano model) for a two or three body final state, and aim at describing correctly as many as possible of the observed features of an experiment. Attempts are then made to generalize the model for an arbitrary number N of particles (multiperipheral models, multi-Regge models, generalized Veneziano amplitude). Here the difficulties encountered are of a different nature. The calculations,

relatively easy for four or even five body final states, do become cumbersome very quickly. As $N \to \infty$, one would prefer a limiting form giving for large particle numbers essentially the same results as the exact N-point function; but this limit has not been found for most dynamical models of interest.

Some of the problems mentioned in this introduction and others of specific nature, are to be dealt with in the present and the following chapters.

2. THE REACTION CHANNEL ANALYSIS.

2.1. The Purpose of the Study.

One of the basic questions that concern us here is how the particles are grouped into different reaction channels. For instance, the expression

$$K^- p \to p \bar{K}^o \pi^+ \pi^- \pi^-$$

represents only the initial and the final state, but the reaction in fact proceeds through intermediary states that are of particular interest, e.g.

$$K^- p \to \Delta^{++} K^* \pi^- \quad , \quad K^* \to p \bar{K}^o \pi^+ \pi^- \quad .$$

As a first step towards the analysis of the reaction, the quantitative contributions of these channels (to which proportional are the partial cross sections) are important to be determined.

2.2. The Method of Determining the Fractions.

A collision with n particles in the final state

$$A + B \rightarrow 1 + 2 + \ldots + n$$

is characterized by $3n$ variables associated with the momenta of the final state particles; the energy momentum conservation reduces to $3n - 4$ the number of independent variables. As in general there is a dynamical mechanism at work, the transition probability (per unit time per unit volume) for the reaction deviates from phase space and is expressed[12] by the relation

$$dP = |M|^2 \, dR \tag{2.1}$$

where the matrix element modulus $|M|^2$ contains all the dynamics of the reaction, and dR is the volume element of the relativistically invariant phase space for the n-outgoing particles. With p denoting the four momenta of the particles and E their energies, dR is usually written in the form

$$dR = \prod_{i=1}^{n} \frac{d^3 p_i}{2 E_i} \; \delta^4 \left(\sum_{i=1}^{n} p_i - p_A - p_B \right) . \tag{2.2}$$

The total transition probability is then given by n three-dimensional integrals over the momenta of the final state particles

$$S = \underbrace{\int \ldots \int}_{3n\text{-fold}} |M|^2 \, dR . \tag{2.3}$$

Divided by the incoming flux and properly normalized, this would yield the cross section for the reaction.

For a particular channel i, the probability distribution of the events which really occur this way is therefore given by the ratio dP_i/S_i. Assume now that the same final state can be reached through a

number of non interfering channels, each contributing with a fraction β_i ; a set of events is then obtained, which may be given a likelihood (the logarith is taken for convenience)

$$\mathcal{L} = \sum_{\text{events}} \log \sum_{i=1}^{\text{channels}} \beta_i \frac{dP_i}{S_i} \quad . \tag{2.4}$$

The fractions are subject to the obvious constraints

$$\beta_i \geq 0 \quad \text{and} \quad \Sigma\beta_i = 1 \tag{2.5}$$

which are safeguarded by the substitution

$$\beta_i = \frac{\alpha_i^2 S_i}{\sum_{j=1}^{\text{channels}} \alpha_j^2 S_j} \quad . \tag{2.6}$$

Taking into account the relations (2.1), (2.3) and (2.6) we finally obtain for the likelihood function

$$\mathcal{L} = \sum_{\text{events}} \log \frac{\sum_{i=1}^{\text{channels}} \alpha_i^2 |M_i|^2}{\sum_{i=1}^{\text{channels}} \alpha_i^2 \int |M_i|^2 \, dR} \quad . \tag{2.7}$$

M_i's are the matrix elements of the contributing channels, and, as seen from the formula, are added incoherently. Since we are summing over many overall angular momentum states, interference effects should be negligible.

Assuming that any internal parameters (e.g. the mass or width of a resonance) are kept fixed, only the parameters α_i in (2.7) are to be varied so as to maximize $\mathcal{L}$; some method has, of course, to provide the integrals $\int |M_i|^2 \, dR$.

With the maximum likelihood fit determining the best values of α_i's, the channel fractions are then easily obtained with relation (2.6).

2.3. The Form of the Matrix Element.

As already stated, the matrix element square for a raction contains all significant physics, as opposed to effects arising from pure phase space considerations. The exact form of M is not known, but in the course of making some suggestions about it two phenomenological cases are distinguished.

(i) No resonance production in reaction $A + B \rightarrow 1 + 2 + \ldots + n$.

This process, which assumes that all particles produced in the final state are stable, is shown schematically in Fig. 1a. M is in that case the transition matrix element for the process

$$M = T(AB \rightarrow 1 \ldots n), \tag{2.8}$$

an unknown function of $3n-5$ variables (for fixed energy), which gives the transition rate from the incoming two particle state to the final multiparticle quantum system. An approximation which is occasionally of some use is to consider the transition matrix element to be constant, i.e. assume a pure phase space distribution. But preferably, a dependence of T on a chosen variable is inserted, mainly to account for the observed experimental characteristics. To that we will return later.

(ii) The reaction goes via some resonance production.

The formation of resonances between pairs or larger groups of the final state particles is a prominent feature of high energy reactions. To describe the process, a propagator and a decay vertex amplitude V for the resonance have to be included in the matrix element.

Consider, for instance, that a two body resonance R is formed by particles (1,2) in the above reaction (as illustrated in Fig. 1b). The matrix element for the process may then be written

$$M = T(AB \to R\ 3\ldots n).\ \text{Propagator}.V\ (R \to 12)\ . \tag{2.9}$$

T describes now the transition to the (n - 1) final state "particles", while for the propagator we assume a form

$$\text{Prop} \propto \frac{1}{(\mu^2 - m_o^2)^2 + (m_o\,\Gamma(\mu))^2} \tag{2.10}$$

m_o, Γ are the mass and width of the resonance and μ is the invariant mass of particles 1 and 2, i.e. $\mu^2 = -(p_1 + p_2)^2$.

Furthermore, if we assume R to be spinless, the decay amplitude V is not dependent on angles and is given by[13]

$$|V|^2 = \text{const}\ \frac{\mu}{q}\ \Gamma(\mu) \tag{2.11}$$

where q is the 3-momentum of the resonant particles in their rest frame.

Relation (2.9) takes then finally the form

$$|M|^2 = \text{const}\ |\ T(AB \to R3\ldots n)|^2\ \frac{\Gamma}{(\mu^2 - m_o^2) + (m_o\Gamma)^2}\ \frac{\mu}{q} \tag{2.12}$$

and is seen to contain an ordinary Breit-Wigner term and a factor (μ/q) for the phase space decay of the resonance into two particles. It is valid only if the resonance is produced "cleanly", as implied

in Fig. 1b; interference effects in the final state are ignored.

For a two-body decay, the width varies with energy in the general form

$$\Gamma(\mu) = \Gamma_o (q/q_o)^{2\ell+1} \frac{\rho(\mu)}{\rho(\mu_o)} \qquad (2.13)$$

where ℓ is the orbital angular momentum, Γ_o and q_o are the width and the internal momentum of the system at $\mu = m_o$, and $\rho(\mu)$ is a relatively slowly varying factor found from lowest-order perturbation theory (its form for the resonances present in our data will be given later).

Similar to the two-body case is the treatment of a three-body resonance formation in the reaction (illustrated in Fig. 1-C). The matrix element is written

$$M = T(AB \rightarrow R4...n). \text{ Propagator } V(R \rightarrow 123) \qquad (2.14)$$

but we now assume for simplicity $|V|^2 = 1$ and usually consider no variation of width with energy. Practically this implies $\Gamma = \Gamma_o$ and an omission of the phase space factor in an expression similar to (2.12), with negligible overall effect.

The reaction may also involve the production of two (or more) resonances, as shown in Fig. 1d. The matrix element is then written in terms of T and the relevant factors of these resonances

$$M = T(AB \rightarrow R3\ Q...n). \text{ Propag}(R).V(R \rightarrow 12).\text{Propag}(Q).V(Q \rightarrow 45) \qquad (2.15)$$

which leads as before to the expression

$$|M|^2 = \text{const. } T(AB\to R3Q\ldots n)\ \frac{\Gamma_R}{(\mu_{12}^2-m_R^2)^2+(m_R\Gamma_R)^2}\ \frac{\mu_{12}}{q_{12}}\ \frac{\Gamma_Q}{(\mu_{45}^2-m_Q^2)+(m_Q\Gamma_Q)^2}\ \frac{\mu_{45}}{Q_{45}} \tag{2.16}$$

2.4. The T Dependence on a Chosen Variable.

In all forms of the matrix element so far discussed, the factor $|T|^2$ describes the transition to the final state and, as already stated, would be constant in the absence of dynamics. In general, T is a function of the momenta of the n, say, secondary particles

$$T = T(p_1, p_2, \ldots p_n) \tag{2.17}$$

but its exact form not being known, one tries some times to derive its dependence on a chosen variable by averaging over all the others.

Let this variable be, for instance, the four momentum transfer to the secondary nucleon

$$t = (p_1 - p_o)^2 \tag{2.18}$$

where the indices 1 and 0 stand for the secondary nucleon and the target proton, respectively.

If by $N_e(t)$ we denote the experimentally observed t-distribution, the search for any t-dependence of $|T|^2$ implies to find a function F(t) which would yield this distribution correctly, i.e.

$$N_e(t) = F(t)\ N_{ps}(t) \tag{2.19}$$

where $N_{ps}(t)$ is the t-distribution predicted by the Lorentz invariant phase space.

The evaluation of $F(t)$ in some $\pi^+ p \to p + n\pi$ channels[14] showed a general behaviour similar to the t-distribution in two body reaction --that is, a peak for small $|t|$ values which diminishes approximately exponentially with t . Thus,

$$F(t) \propto e^{-A|t|} \tag{2.20}$$

with the slope A chosen so that the experimental t-distribution of the reaction is correctly described.

In the presence of resonances, it would have been more appropriate to insert in the relevant matrix elements a dependence on the four momentum transfer to the resonance produced. But, in fact, any choice for the $F(t)$ was seen to have very little influence on our results; so the simple form (2.20) was considered adequate in describing all transition matrix elements square irrespective of any resonances being formed between the particles.

Of course, other forms of $|T|^2$ dependence might equally be tried. Starting, for instance, from the (approximately similar) transverse momentum behaviour of all secondary particles one could suggest

$$F(p_T) \propto e^{-\text{const.} \sum_{i=1}^{n} (p_T)_i^2} \tag{2.21}$$

and see how well the experimental distributions are described. Although such an investigation was carried out on a part of our data, no further persistence was justified. We did not really aim at constructing a model for high energy collisions and any optimization in the choice of matrix element would not, as before stated, significantly affect the calculation of partial cross sections which was our main concern.

3. THE DATA

3.1. Introductory Remarks.

The two reactions, to be examined in detail in this section, are

$$K^- p \rightarrow p\bar{K}^o \pi^+\pi^-\pi^- \qquad (1)$$

$$K^- p \rightarrow p\bar{K}^o \pi^+\pi^-\pi^-\pi^o \qquad (2)$$

Reaction (1) consists of 2210 events (789 with the $\bar{K}^o$ seen to decay and 1421 with the $\bar{K}^o$ kinematically fitted), and reaction (2) of 1376 events. Corrections have been made for $\bar{K}^o$'s decaying outside the chamber or very near the production vertex, and ambiguous events have been assigned a weight $1/n$ (n is the number of acceptable kinematic fits).

The identification of the reactions was discussed in detail in Section 4 of the previous chapter.

3.2. Peripherality of the Processes.

Even at these high multiplicities, the peripherality manifested in both processes is substantial. This is illustrated in Fig. 2, where the four momentum transfer distributions from the target to the outgoing proton are presented. The events are seen to accumulate preferably at low values of $|t|$, as opposed to phase space predictions (dashed lines on Fig. 2).

The solid lines superimposed on the experimental distributions are proportional to the phase space t-predictions multiplied by the exponential form $e^{-A\,|t|}$ (see section 2.4). The slope A is chosen so as to achieve a good description of the experimental distributions, and has the values 1.5 and 2.5 GeV^{-2} for reactions (1) and (2), respectively.

3.3. Effective Mass Spectra.

Because of its short lifetime a resonance does not travel a measurable distance in a bubble chamber, so only the final state of the reaction is observed experimentally. In order to find out if the reaction proceeds via a certain resonance production, one plots the effective mass (M_{eff}) distribution of the relevant system of particles; M_{eff} is a relativistically invariant quantity, defined for a system of n particles by the relation

$$M_{eff}^2 = \left(\sum_{i=1}^{n} E_i\right)^2 - \left(\sum_{i=1}^{n} \vec{p}_i\right)^2 .$$

If a substantial proportion of the events are produced through intermediate short lived states, in plotting the effective mass one gets a peak corresponding to the mass of the short lived particle. This will stand on a continuous background arising from events which did not proceed this way.

In this respect, the effective mass distributions of all groups of final state particles in our reactions were examined carefully, and the following conclusions were drawn.

(a) Reaction $K^- p \to p\bar{K}^o \pi^+\pi^-\pi^-$

The process is clearly dominated by the production of $K^{*-}(890)$, $\Delta^{++}(1236)$ and ρ^o resonances. Fig. 3 presents the relevant effective masses distributions, and the peaks corresponding to these resonances are seen to be very strong. A shoulder at around ~1400 MeV in the $(K^o\pi^-)$ mass spectrum might be attributed to the very weak presence of the $K^{*-}(1420)$ resonance; its $K\pi\pi$ decay mode might also cause the small similar peak observed in the $(\bar{K}^o\pi^+\pi^-)$ eff. mass distribution (Fig. 4). No convincing signal for the production of any other two

or three body resonance was found when inspecting the particle mass plots; statistical fluctuations or kinematic reflections might of course cause deceptive peaks to appear.

None of the effective mass distributions, on the other hand, shows complete agreement with the predictions of uniform phase space, even when no resonant states are evident. (See, for instance, the three body mass spectra of Fig. 4; the dashed lines are the phase space predictions.) It is believed that these deviations are mainly due to peripheralism in the data and possibly to kinematic reflections of resonances.

(b) Reaction $K^- p \rightarrow p\bar{K}^o \pi^+\pi^-\pi^-\pi^o$

The effective mass spectra inspection leads to the conclusion that this reaction is dominated by $K^{*-}(890)$, $\Delta^{++}(1236)$ and ω production (Fig. 5); the $\Delta^+(1236)$ resonance is also weakly present (Fig. 6b). A most striking feature of the data, which will be discussed later, is the absence of a ρ^o resonance signal in the $(\pi^+\pi^-)$ effective mass distribution (Fig. 6a).

The phase space predictions (dashed lines in Fig. 6) are also given for some two body effective masses, and again are seen to be inconsistent with the experimental data.

3.4. Resonance Masses and Widths.

The mass and width values of a resonant state, as determined in an experiment, depend in a complex way on the experimental resolution, the number of events, and the theoretical shape assumed for the resonance function and the background.[15]

A common method for the evaluation of resonance masses and widths, which has been followed here, is to fit by a maximum likelihood method

the effective mass distributions of interest to a Breit-Wigner form plus a background term. The general form of the function used to describe the distribution is then

$$\frac{dN}{dM} = \text{Background} + \beta(\text{PPS}) \frac{1/4\ \Gamma_T^2}{(M - M_o)^2 + 1/4\ \Gamma_T^2} .$$

The quantities M_o, Γ_T and β are, respectively, the central mass value, the width at half height and the fraction of the resonance. These are the parameters to be varied in the fit. The Breit-Wigner term, written in a simplified form as M is close to M_o, is multiplied by peripheral phase space (PPS)--that is, the phase space distribution weighted as explained before by an appropriate exponential factor. Finally, and in the absence of any better suggestion, the background is estimated by extrapolation of the observed distribution outside the resonance in a smooth way. This is usually referred to as a smooth hand-drawn background.

On the basis of these one-dimensional fits, the masses and widths of the strongly produced resonances in our reactions were determined; the results are presented in Table 1. A separate fit was made for $\overline{K}^o_{\text{seen}}$ and $\overline{K}^o_{\text{fitted}}$ events of reaction (1), and although the expected difference in the experimental resolution is noted, it is not considered as substantial.

The results of the fit are, at most, consistent with the commonly accepted values derived by averaging over many experiments.[16] Only the ρ^o resonance fit is poor, owing to some statistical fluctuations near its peak, together with the fact that the resonance sits near the peak of the background.

3.5. The Determination of the Channel Fractions.

We proceed now to an important part of our study, concerning the quantitative evaluation of the various channels contributing to the final states (1) and (2). The discussion follows the formulation developed in Section 2 of this chapter. The maximum likelihood method, to be used, fits the density of events in the multidimensional phase space, which contains considerably more information about particle correlations than the individual mass plots. The following steps may be distinguished in the procedure.

(a) The formation of the likelihood function.

In connection with the remarks made earlier about the resonances produced, the subprocesses listed below are considered to contribute in the reactions

Reaction (1): $K^- p \to p\bar{K}^o \pi^+ \pi^- \pi^-$

$\to \Delta^{++} \bar{K}^o \pi^- \pi^-$

$\to p K^{*-} \pi^- \pi^+$

$\to \Delta^{++} K^{*-} \pi^-$

$\to p\bar{K}^o \rho^o \pi^-$

$\to p K^{*-} \rho^o$

Reaction (2): $K^- p \to p\bar{K}^o \pi^+ \pi^- \pi^- \pi^o$

$\to \Delta^{++} \bar{K}^o \pi^- \pi^- \pi^o$

$\to \Delta^{++} K^{*-} \pi^- \pi^o$

$\to p K^{*-} \pi^+ \pi^- \pi^o$

$\to p\bar{K}^o \pi^- \omega$

$\to p K^{*-} \omega$

Possible minor contributions from resonances not clearly visible in the effective mass plots have been neglected. This leads to the reduction

of fit parameters in the interest of its reliability. It is to be noted, though , that early attempts to include in the fit the $K^{*-}(1420)$ for reaction (1) and the ρ^{o}, ρ^{+} and Δ^{+} (1236) resonances for reaction (2), gave either no significant contribution, or produced results decidedly inconsistent with the experimental observations.

To each reaction subprocess a matrix element is assigned, seen to consist (sections 2.3 - 2.4) of two factors: A factor (including the Breit-Wigner amplitude) which describes the decay of the resonance, and a factor of the form $e^{-A|tpp|}$ to allow for the peripheral nature of the interaction.

To clarify this with some examples, the following matrix element is suggested - on the basis of formula (2.12) - for the production of Δ^{++} in reaction (1)

$$|M_{\Delta^{++}}|^2 = \frac{\Gamma_\Delta}{(M^2_{p\pi^+} - M^2_\Delta)^2 + (M_\Delta \Gamma_\Delta)^2} \cdot \frac{M_{p\pi^+}}{p_\pi} e^{-2.5|tpp|}$$

For some channels, the matrix elements need symmetrization due to the presence of two identical π^- in the reactions. For instance, we write

$$|M_{K^{*-}}|^2 = \frac{\Gamma_{K^*} \cdot M_{K^o\pi^-_1/p\pi^-_1}}{(M^2_{K^o\pi^-_1} - M^2_{K^*})^2 + (M_{K^*}\Gamma_{K^*})^2} + \frac{\Gamma_{K^*} \cdot M_{K_o\pi^-_2/p\pi^-_2}}{(M^2_{K^o\pi^-_2} - M^2_{K^*})^2 + (M_{K^*}\Gamma_{K^*})^2} e^{-2.5|tpp|}$$

For the simultaneous resonance production $K^- p \to \Delta^{++} K^{*-} \pi^-$, on the other hand, relation (2.16) yields

$$|M_{\Delta^{++}K^{*-}}|^2 = \frac{\Gamma_\Delta}{(M^2_{p\pi^+} - M^2_\Delta)^2 + (M_\Delta \Gamma_\Delta)^2} \cdot \frac{M_{p\pi^+}}{p_-} \cdot |M_{K^{*-}}|^2$$

The resonance widths, entering all similar expressions for the matrix elements, follow for two body decays a variation with energy as

given in (2.13). For the resonances of present interest, the slowing factor $\rho(\mu)$ has the following forms

(i) for $K^* \to K\pi$ and $\rho \to \pi\pi$, i.e. $(1^-) \to (0^-)(0^-)$

$$\rho(\mu) = \mu^{-1}$$

(ii) for $\Delta \to p\pi$, i.e. $(3/2^+) \to (\frac{1}{2}^+)(0^-)$

$$\rho(\mu) = \frac{(\mu + m_p)^2 - m_\pi^2}{\mu^2}$$

When fitting for the fractions, the resonance masses and the corresponding widths (denoted by Γ_o in relation 2.13) are kept fixed in the values given in Table 1. In most cases, the commonly accepted values[16] are used--which is justified since the Breit Wigner fits to our data gave results reasonably close. Exceptional is only the case of ω (reaction (2)) where, due to the limited experimental resolution, we thought it appropriate to use the values of mass and width as derived from the fit. A similar treatment for the ρ^o is not advisable, as the fit there is seen to be poor and leads to an anomalously high width. Further more, it was verified on a test basis that sensible changes in the values of resonance masses and widths used have not much effect on the resonance fractions.

Having expressed in the terms described all matrix elements for the contributing channels, we are now able to construct the likelihood function corresponding to each of our reaction. We note that six subprocesses lead to the final state (1), and, by coincidence, the same is true for reaction (2); so the formalism below is applicable to both cases.

If we write

$$\int |M_i|^2 \, dR = S_i \qquad i = 1, \ldots 6$$

for the normalization integrals, the general form (2.7) of the likelihood

function reads now

$$\mathcal{L} = \sum_{\text{events}} WT \log \frac{\alpha_1^2|M_1|^2 + \alpha_2^2|M_2|^2 + \ldots + \alpha_6^2|M_6|^2}{\alpha_1^2 S_1 + \alpha_2^2 S_2 + \ldots + \alpha_6^2 S_6}$$

where WT is the experimental weight associated with each of the events. The maximization procedure leads to the determination of the parameters $\alpha_1, \ldots, \alpha_6$ (which, in fact, may be reduced to five by taking $\alpha_2' = \frac{\alpha_2}{\alpha_1}, \ldots, \alpha_6' = \frac{\alpha_6}{\alpha_1}$); the percentage of each contribution is then calculated by

$$\beta_i = \frac{\alpha_i^2 S_i}{S_1 + \alpha_2^2 S_2 + \ldots + \alpha_6^2 S_6} \qquad i = 1, \ldots, 6$$

(b) The computational procedure[17]

From what has been said earlier, it is concluded that two main operations have to be performed in order to determine the resonance fractions.

(i) Obtain the integrals $\int |M_i|^2 \, dR$ of the squared matrix element over the available phase space.

(ii) Calculate the likelihood function from the experimental data, and adopt an optimization procedure to find the best fit parameters.

There exist analytic methods to calculate the phase space integrals[18]. However, their range of applicability is limited, and the much more powerful Monte-Carlo simulation methods are instead applied. Thus, with program FOWL[19] -- extensively used in the present analysis -- random "events" are generated over the allowed phase space; to each event a weight proportional to the matrix element square is associated. The integral $S_i = \int |M_i|^2 \, dR$ is then given by the overall weight of the generated events.

In fact, the peripherality of high energy interactions, i.e. the smallness of transverse momenta of particles or of the four-momentum

transfers between groups of particles, makes inefficient the generation of events uniformly throughout the available phase space. A large fraction of events, multiplied by a very small matrix element, is then practically lost. A better way is to apply the so-called "importance sampling" method; then events are generated mainly in the region of phase space where a large matrix element is expected. A version of FOWL based on this approach[20] uses as integration variables the momenta of the outgoing particles, distinguishing between their longitudinal components (which grow with energy) and their transverse ones (which remain essentially constant at all energies). This version provided for most of our calculations. In a similar approach[21], also used occasionally in the present analysis, invariant momentum transfers were included among the variables.

After the normalization integrals have been evaluated, the rest of the procedure is now trivial. Program MINUIT[22] provides the necessary facilities of forming the likelihood function from the experimental data and then maximize it (in practice, minimize its negative) by an iterative process. The best values of the parameters are thus obtained.

Although a first estimate of the resonance fractions is possible on the basis of the effective mass distributions, this is not really necessary, since a Monte Carlo search optional in the program may produce reasonable starting values of the parameters.

(c) The results.

Some results of the multidimensional fit, which may be considered as preliminary, are presented in Table 2. The purest sample of events -- those from reaction $K^- p \to p \bar{K}^o \pi^+ \pi^- \pi^-$ with the $\bar{K}^o$ seen-- was used, and both a phase space ($|T|^2 = 1$) and a peripheral ($|T|^2 = e^{-2.5|tpp|}$) form of production were assumed in turn. No significant difference is noted.

The final results of the fit are displayed in Table 3 (reaction (1)) and Table 4 (reaction (2)); the peripheral factor is now included in the matrix element. The Tables give also the corresponding cross sections for all channels. It is noted that the inclusion of $\overline{K}^o$ fitted events in reaction (1) has little effect on the fractions, a fact supporting the reliability of these events identification and allowing much higher statistics.

The maximum likelihood method does not provide us with a direct test on the goodness of the fits. However, the matrix elements used and the fractions obtained for each channel formulate in effect an incoherent resonance model, which predicts the distributions superimposed on the experimental mass plots of Figs. 3 - 6. The data is very well described in general. Even when the predictions are less satisfactory (e.g. in the cases of $\overline{K}^o \pi^+\pi^-$ or the $p\pi^o$ effective masses) they still constitute a notable improvement if compared with the phase space distributions. Where resonance peaks are present on the effective mass plots, the predicted background distributions below them are also shown.[23]

The results obtained are to be fully discussed after a similar work on the 6 GeV/c K^-p data is presented. Based on these results, a paper was submitted to the Amsterdam Conference on Elementary Particles (1971).[24]

REFERENCES AND FOOTNOTES

1. Serpukhov - CERN collaboration, PL 30B (1969) 500.

   Also presented as a paper at the Kiev Conference (1970).

2. T. Hofmoki and A. Wroblenski PL 31B (1970) 391.

   J. D. Hansen, W. Kittel, D.R.O. Morrison, N.P. B25 (1971) 605.

3. A. Wroblenski PL 32B (1970) 145.

4. G. Goldhaber, et. al., PRL 3 (1959) 181.

5. J. Brandt, paper presented at the Vienna Conference (1968).

6. J. L. Day, et. al. PRL 23 (1969) 1055.

7. R. P. Feynman PRL 23 (1969) 1415.

8. J. Benecke, et. al., PR 188 (1970) 2159.

9. See, for instance S. J. Goldsack, Review Talk at the Lancaster Conference (April 1971).

   O. Cryzewski, Herceg-novi School (1969).

   A. Giovannini and E. Predazzi, Survey of manybody hadrodynamics, Part I.

   Review papers by A. Wroblewski, A. Krzywicki, K. Zalewski in the "Colloquium on high multiplicity hadronic interactions" Paris, 1970.

10. Discussed in detail by M. Jacob "Strong interactions" TH 1328-CERN.

11. R. Hagedorn, Supp. NC 3 (1965) 147.

12. For a detailed discussion see G. Kallen, "Elementary Particle Physics" Chapter 1.

13. Much of the following formulation is inspired by the well-known paper on the phenomenological analysis of resonances by J. D. Jackson (NC 34 (1964) 1644). In it the original literature on the subject can also be found.

14. G. Biatkowski and R. Sosnowski, PL 25B (1967) 519.

15. For an illustration of it see, for instance, the work refering on the ω width by D.G. Coyne et. al., Laurence Laboratory Preprint 20088. Also Ref. 13.

16. Review of Particle Properties, Particle Data Group, Reviews of Modern Physics 43 (1971).

17. The overall procedure is similar to that applied in program MAVE, written at CERN by J.M. Perreau. This program was modified and introduced for general use at I.C. by the author of the present thesis. See G.A. Grammatikakis "MAVE, a fitting program for reaction channel analysis" Imperial College Physics Notes. The computational method used here is based on a better optimization technique and allows for more flexibility. It has been worked out by G. Otter and the author. Several tests in a part of our data have checked the consistency of both methods.

18. F. Lurcat and P. Mazur, NC 31 (1964) 140.
A. Krzywicki, J. Math. Phys. 6 (1965) 485.

19. F. James, FOWL, CERN Program Library (1970) W 50£.

20. W. Kittel, L. Van Hove and W. Wojcik CERN/D.Ph. II/PHYS 70-8.

21. E. Byckling and K.Kajantie NP B9 (1969) 568.
E. Byckling et. al., Journal of Computational Physics 4 (1969) 521.

22. F. James and M. Ross, program MINUIT, CERN Program Library (1971) D 506.

23. Where each event has two combinations, the contribution in the fit from resonance production includes the resonance events in the "wrong" combination. The background shows all non-resonant events in both combinations.

24. "Resonance production in the reactions $K^- p \to p\bar{K}^o \pi^+\pi^-\pi^-$ and $K^- p \to p\,\bar{K}^o\pi^+\pi^-\pi^-\pi^o$ at 10 GeV/c" ABCLV Collaboration. Also presented at the Helsinki Colloquium on Multiparticle Dynamics (1971).

TABLE IV - 1

EFFECTIVE MASS FITS.

REACTION	RESONANCE	VALUES OBTAINED FROM ONE DIMENSIONAL FITS				VALUES USED IN MULTIDIMENSIONAL FITS	
		Mass (MeV)		Width (MeV)		Mass (MeV)	Width (MeV)
		$\bar{K}^o$ seen	$\bar{K}^o$ fitted	$\bar{K}^o$ seen	$\bar{K}^o$ fitted		
$K^- p \to p\bar{K}^o \pi^+ \pi^- \pi^-$	$K^*(890)$	892 ± 2	892 ± 3	56 ± 5	137 ± 13	892	50
	$\Delta^{++}(1236)$	1225 ± 5	1213 ± 5	87 ± 13	115 ± 16	1236	120
	ρ^o	708 ± 12	-	304 ± 35	-	765	125
$K^- p \to p\bar{K}^o \pi^+ \pi^- \pi^- \pi^o$	$K^*(890)$	893 ± 3		99 ± 7		892	50
	$\Delta^{++}(1236)$	1233 ± 14		85 ± 12		1236	120
	ω	808 ± 2		47 ± 6		808	47

TABLE IV - 2

$K^- p \to p\bar{K}^o \pi^+ \pi^- \pi^-$, $\bar{K}^o$ SEEN (789 EVENTS)

Channel	Fraction %	
	$\|T\|^2 = 1$	$\|T\|^2 = e^{-2.5\|tpp\|}$
$K^- p \to p\bar{K}^o \pi^+ \pi^- \pi^-$	~ 0* ± 2	~ 0* ± 2
$\to \Delta^{++} \bar{K}^o \pi^- \pi^-$	10 ± 3	11 ± 3
$\to p\ K^{*-} \pi^- \pi^+$	19 ± 5	22 ± 5
$\to \Delta^{++} K^{*-} \pi^-$	18 ± 4	17 ± 4
$\to p\bar{K}^o \rho^o \pi^-$	29 ± 5	30 ± 5
$\to pK^{*-} \rho^o$	24 ± 5	20 ± 6

* of the order of .001

TABLE IV - 3

$K^- p \to p \bar{K}^o \pi^+ \pi^- \pi^-$ (2220 EVENTS)

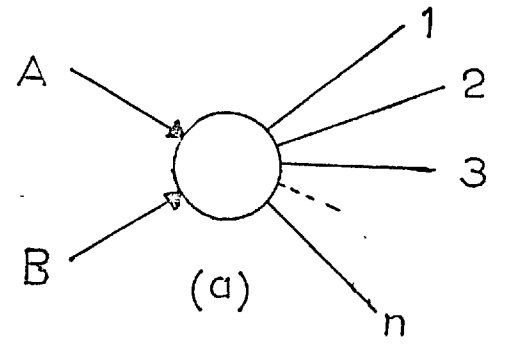
Channel	Fraction %	Cross section μb
$K^- p \to p\bar{K}^o \pi^+ \pi^- \pi^-$	0 ± 2	0 ± 5
$\to \Delta^{++} \bar{K}^o \pi^- \pi^-$	14 ± 2	41 ± 6
$\to pK^{*-} \pi^+ \pi^-$	21 ± 4	61 ± 11
$\to \Delta^{++} K^{*-} \pi^-$	15 ± 5	43 ± 14
$\to p\bar{K}^o \rho^o \pi^-$	31 ± 3	89 ± 9
$\to pK^{*-} \rho^o$	19 ± 4	55 ± 12

TABLE IV - 4

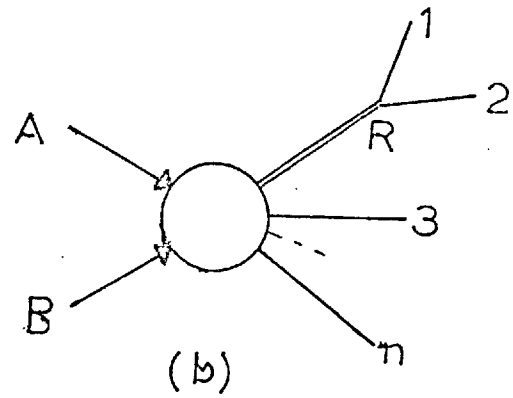
$K^- p \rightarrow p \bar{K}^o \pi^+ \pi^- \pi^- \pi^o$ (1377 EVENTS)

Channel	Fraction%	Cross section μb
$K^- p \rightarrow p\bar{K}^o \pi^+\pi^-\pi^-\pi^o$	0 ± 2	0 ± 5
$\rightarrow \Delta^{++} \bar{K}^o \pi^-\pi^-\pi^o$	23 ± 4	108 ± 18
$\rightarrow p K^{*-} \pi^+\pi^-\pi^o$	46 ± 5	216 ± 36
$\rightarrow \Delta^{++} K^{*-} \pi^-\pi^o$	3 ± 2	14 ± 10
$\rightarrow p\bar{K}^o \pi^- \omega$	15 ± 3	70 ± 14
$\rightarrow pK^{*-} \omega$	13 ± 3	61 ± 14

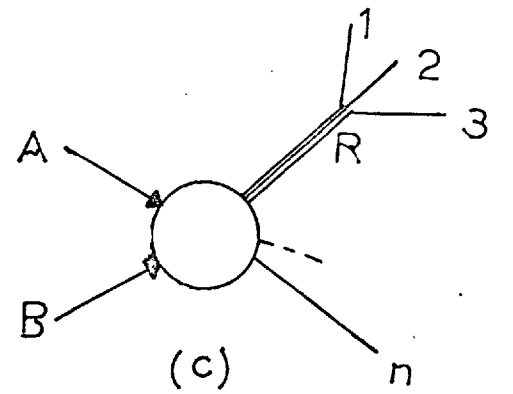
Fig. IV-1



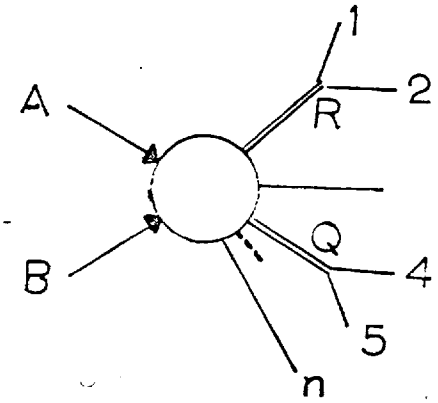
(a)



(b)

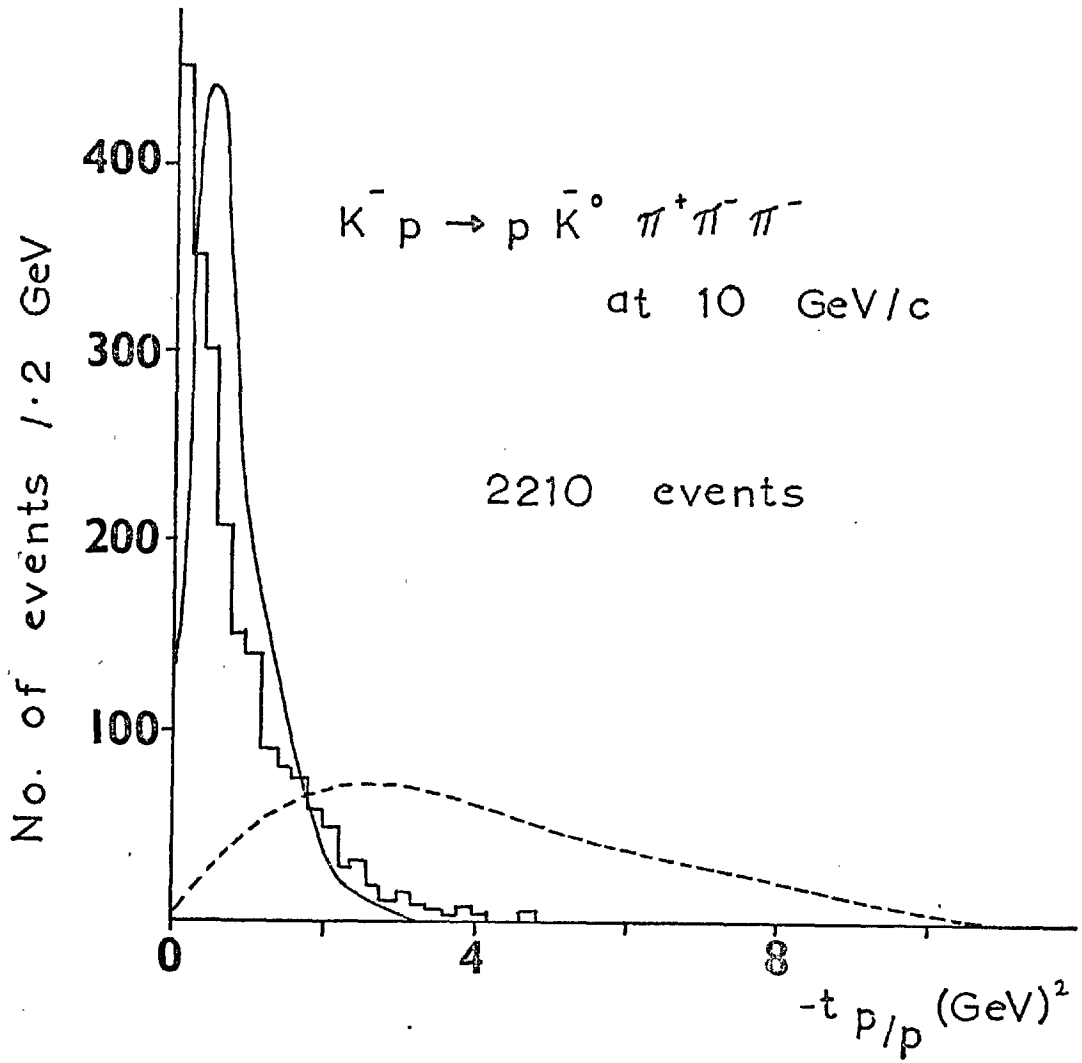


(c)



(d)

Fig. IV-2


$K^- p \to p \bar{K}^0 \pi^+ \pi^- \pi^-$
at 10 GeV/c
2210 events
No. of events / 2 GeV
400
300
200
100
0
4
8
$-t\ p/p\ (GeV)^2$

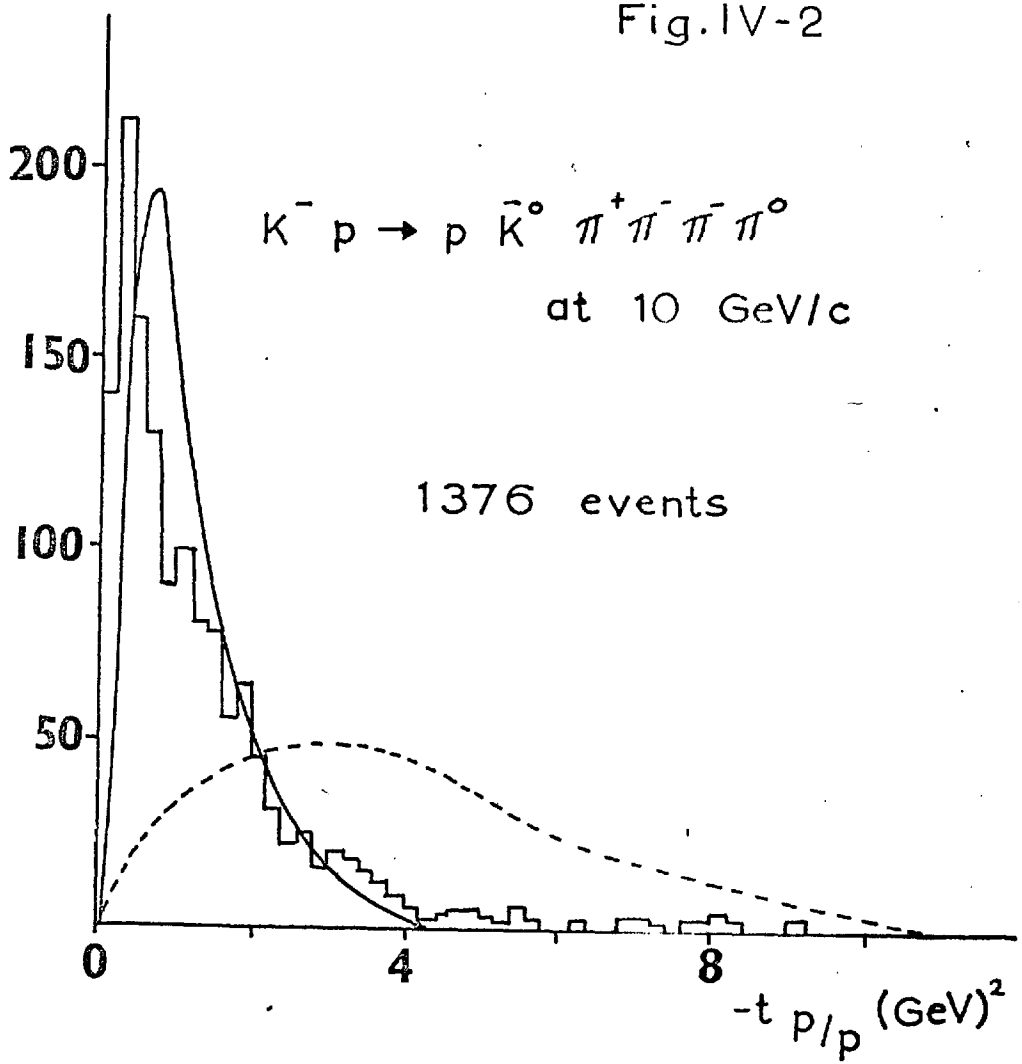

$K^- p \to p \bar{K}^0 \pi^+ \pi^- \pi^- \pi^0$
at 10 GeV/c
1376 events
200
150
100
50
0
4
8
$-t\ p/p\ (GeV)^2$

Fig. IV-3

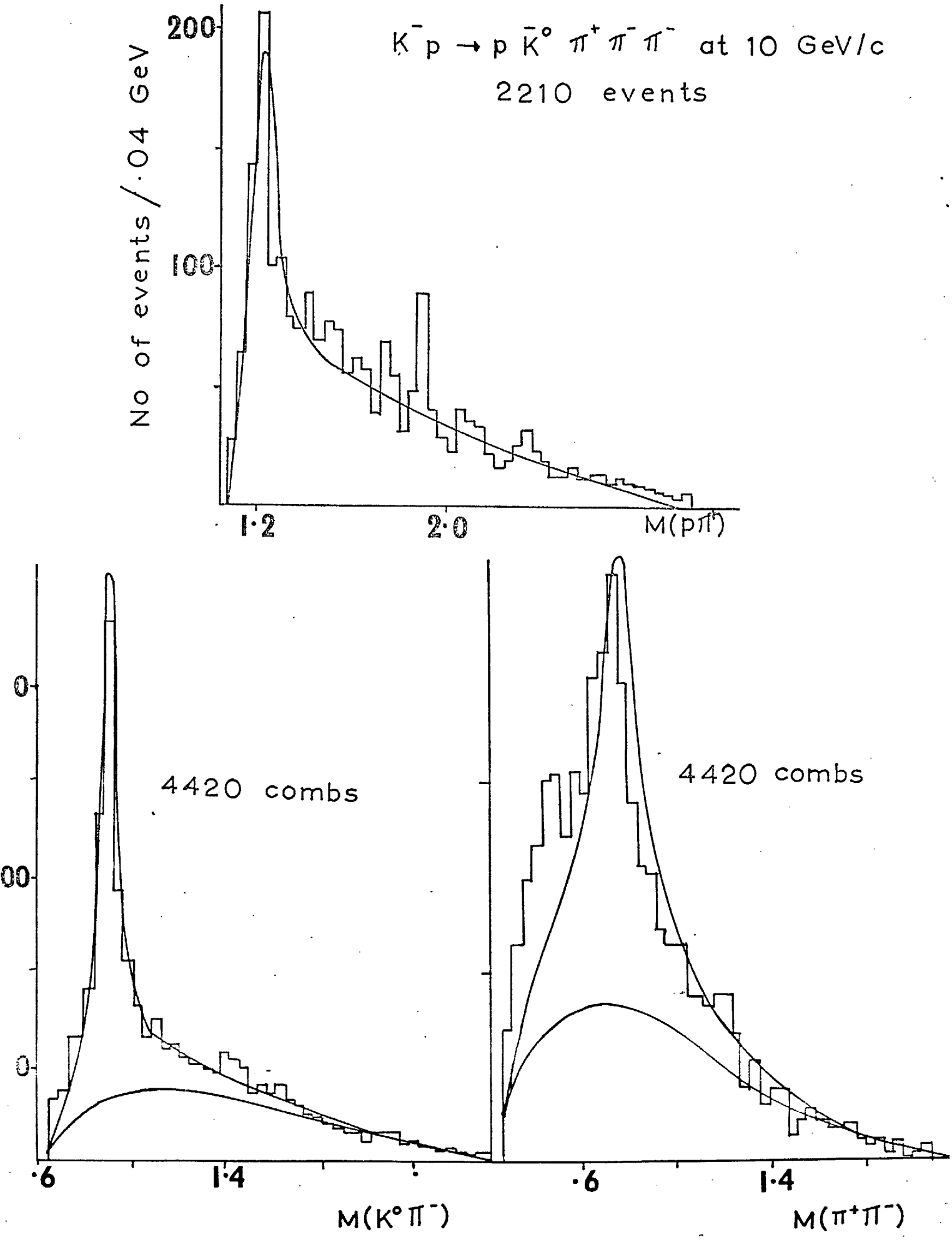

$K^- p \rightarrow p \bar{K}^0 \pi^+ \pi^- \pi^-$ at 10 GeV/c
2210 events
No of events / .04 GeV
200
100
1·2
2·0
M(pπ⁻)
4420 combs
4420 combs
·6
1·4
M(K°π⁻)
·6
1·4
M(π⁺π⁻)

Fig. IV-4

$K^- p \rightarrow p \bar{K}^0 \pi^+ \pi^- \pi^-$ at 10 GeV/c

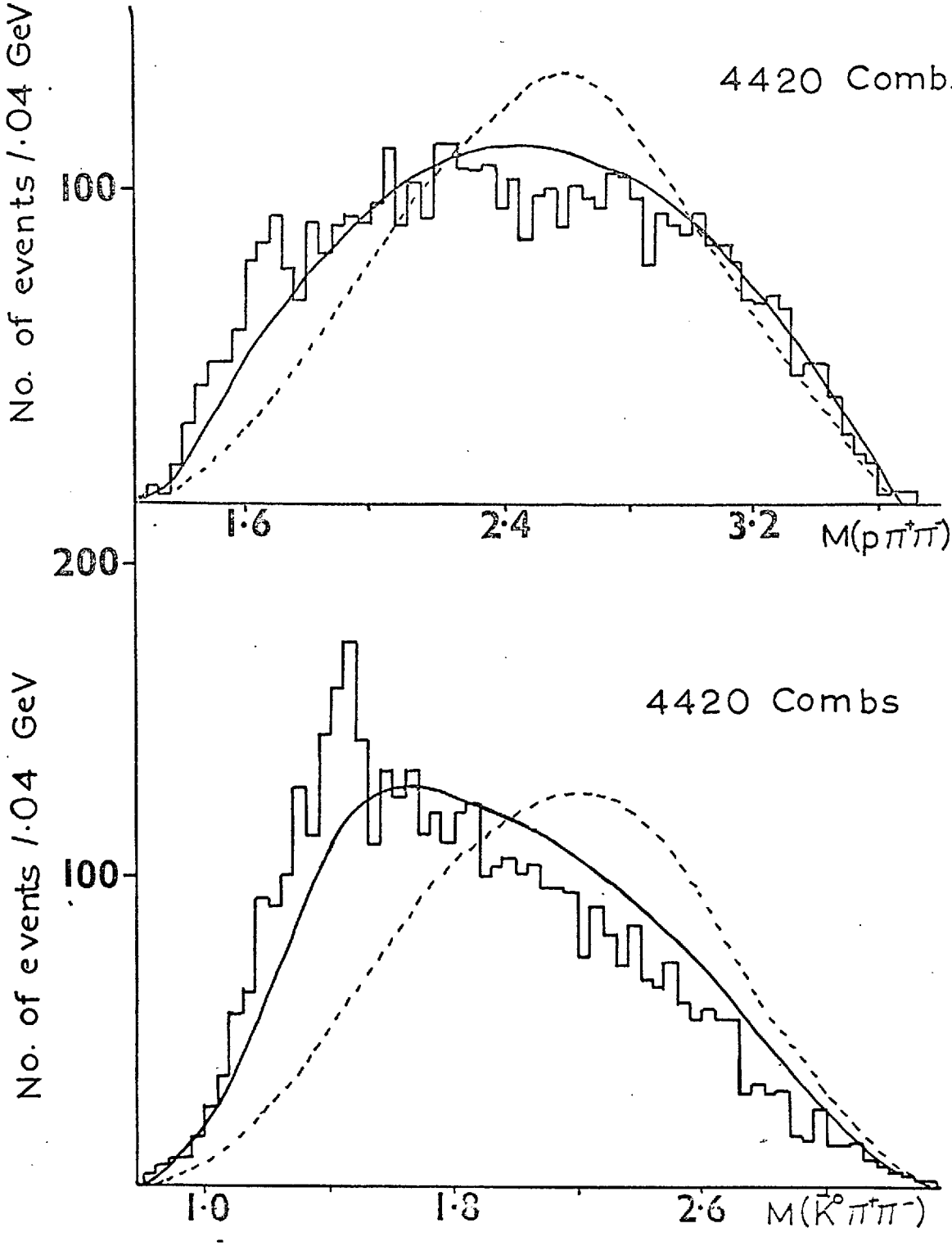
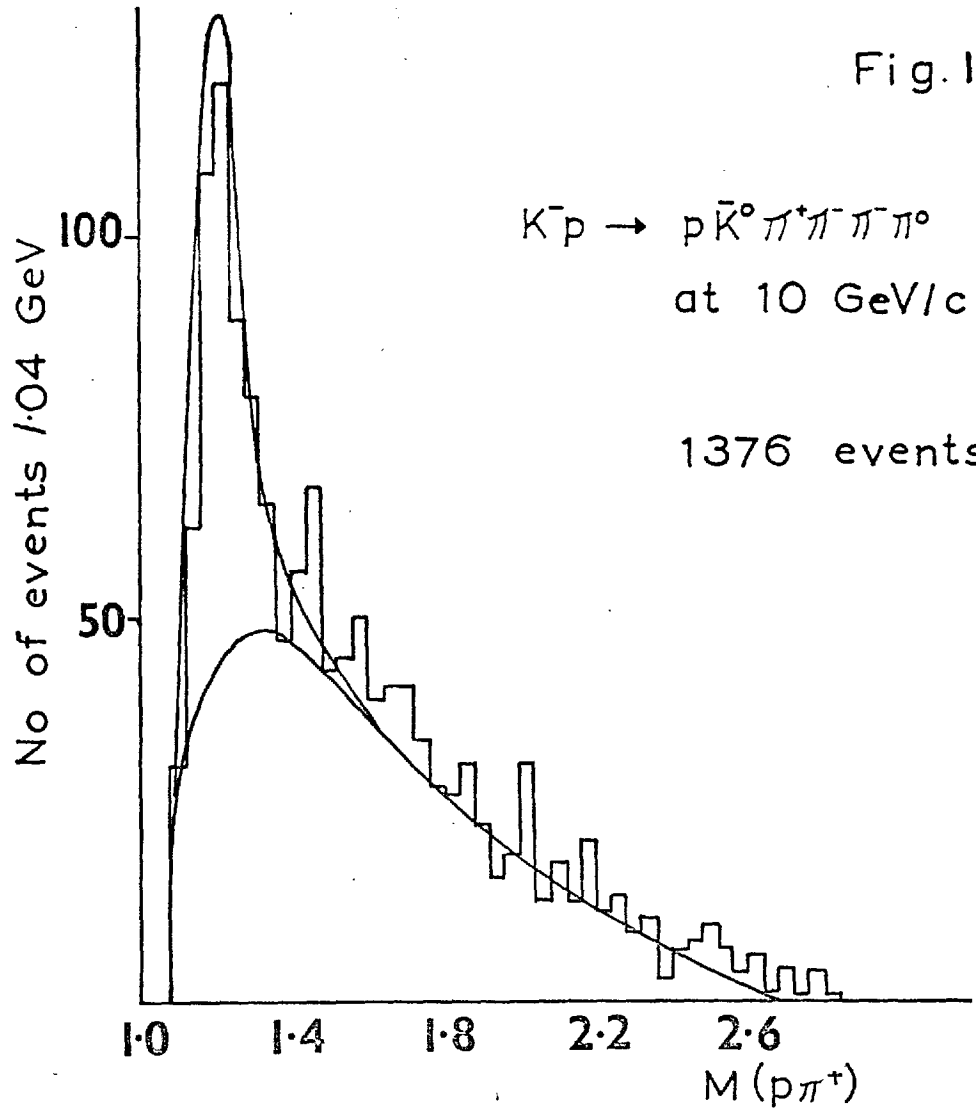


Fig. IV-5


$K^-p \rightarrow p\bar{K}^0\pi^+\pi^-\pi^-\pi^0$
at 10 GeV/c
1376 events
No of events /·04 GeV
100
50
1·0
1·4
1·8
2·2
2·6
M(pπ⁺)

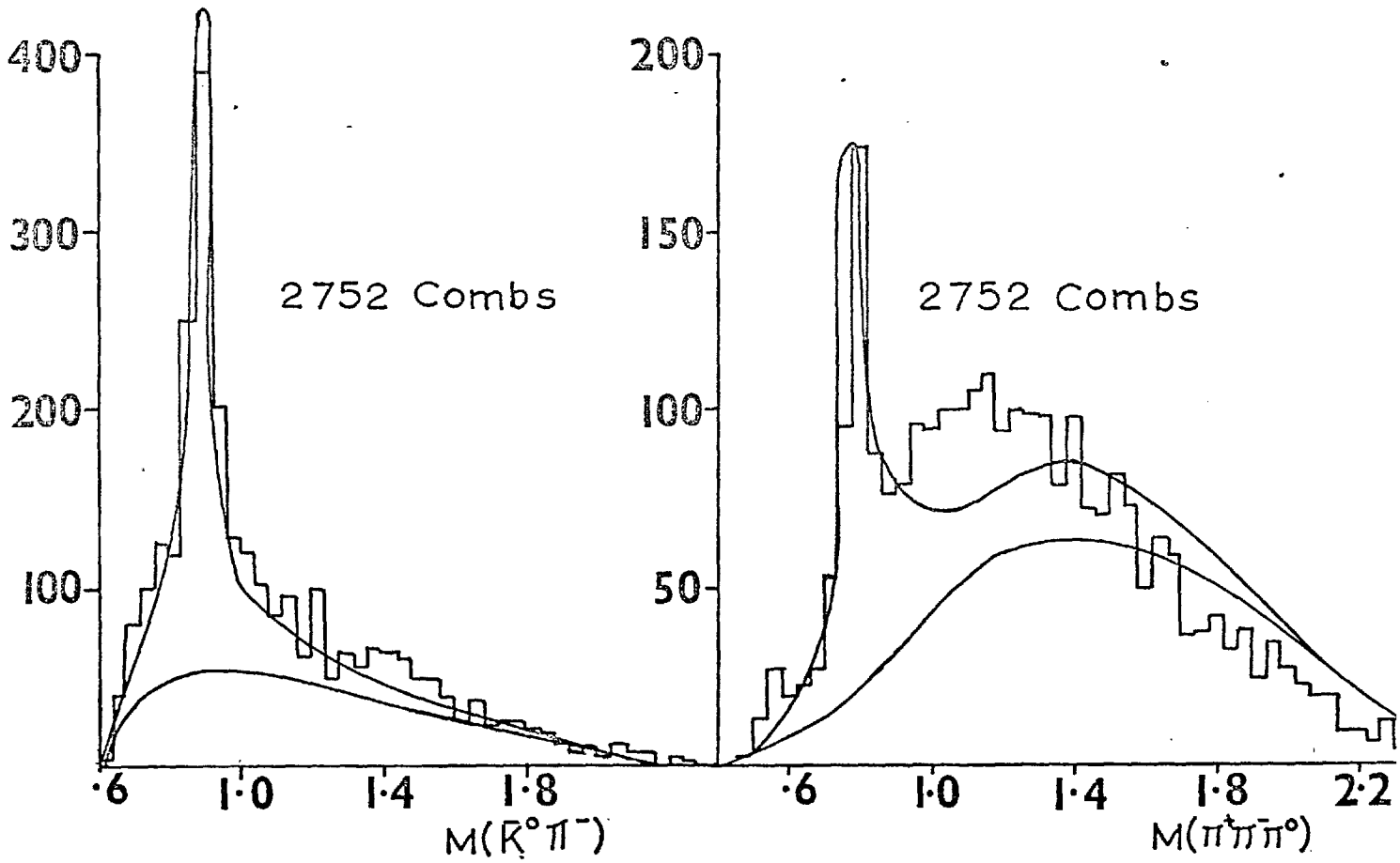
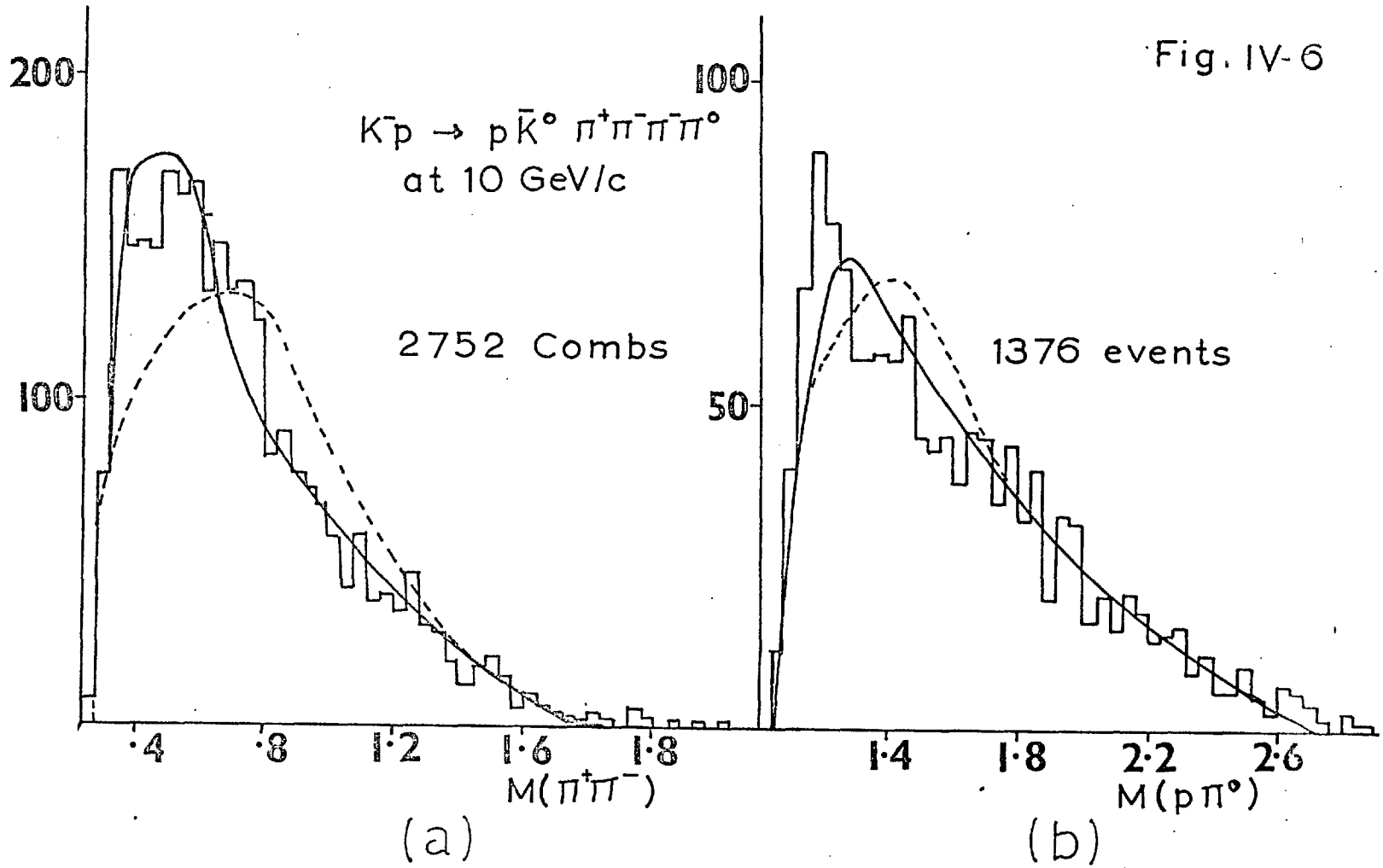

400
300
200
100
2752 Combs
·6
1·0
1·4
1·8
M(K̄°π⁻)
200
150
100
50
2752 Combs
·6
1·0
1·4
1·8
2·2
M(π⁺π⁻π°)

Fig. IV-6


200
100
$K^-p \rightarrow p\bar{K}^0 \pi^+\pi^-\pi^-\pi^0$
at 10 GeV/c
2752 Combs
·4
·8
1·2
1·6
1·8
$M(\pi^+\pi^-)$
(a)
100
50
1376 events
1·4
1·8
2·2
2·6
$M(p\pi^0)$
(b)

CHAPTER V.

A SIMILAR STUDY AT 6 GEV/C, COMPARISON AND CONCLUSIONS

As the interest in multibody final states has arisen in recent years, a study of the reactions already discussed at 10 GeV/c, i.e.

$$K^- p \to p\bar{K}^o \pi^+ \pi^- \pi^-$$
$$K^- p \to p\bar{K}^o \pi^+ \pi^- \pi^- \pi^o$$

and of a third one, the

$$K^- p \to n\bar{K}^o \pi^+ \pi^+ \pi^- \pi^-$$

was also undertaken at 6 GeV/c K^- incident momentum; the procedure followed is essentially identical.

In this chapter we first present the 6 GeV/c results, and then we discuss the emerging conclusions from both energies.

1. STUDY OF THREE MULTIBODY FINAL STATES AT 6 GEV/C.

1.1 The 6 GeV K^-p experiment

The reactions to be discussed here were produced by a separated beam of 6 GeV/c K^- mesons in the 1.5 m British National Bubble Chamber at the CERN Proton Synchrotron. The pion contamination of the beam relative to the number of K^- particles was $(6 \pm 3)\%$. A total of about 300 000 good pictures were taken, with the analysis carried out by a collaboration of six European groups[1].

For the geometrical and kinematical reconstruction of tracks, a series of Rutherford Laboratory programs was used[2]. The following χ^2-probability limits were agreed upon in fitting for the various reactions:

Production vertex fits

3C or 4C $p \geq 1\%$

1C $p \geq 5\%$

V^0 fits

2C or 3C $p \geq 1\%$

The results of the 6 GeV/c K^-p experiment have been reported in several publications[3]. Separate mention may be made of a later paper[4], where most of the results this chapter refers to were presented.

1.2 The reactions under study

Events, leading to four charged particles and a neutral K meson (seen to decay in the chamber) have been fitted to the following reactions

$$K^-p \to p\bar{K}^0\pi^+\pi^-\pi^- \quad (1)$$

$$K^-p \to p\bar{K}^0\pi^+\pi^-\pi^-\pi^0 \quad (2)$$

$$K^-p \to n\bar{K}^0\pi^+\pi^+\pi^-\pi^- \quad (3)$$

The number of events for each and the corresponding cross sections are presented in Table 1.

1.3 Experimental characteristics

Figs. 1 - 3 show the scatter plots of longitudinal versus transverse momentum (Peyrou plots), for each type of particle produced in the three reactions. A strong peripherality is apparent.

This is further illustrated in Fig. 4 by the four-momentum transfer distributions from proton to proton (or proton to neutron in reaction (3)). The distributions deviate considerably from the phase space predictions (dashed lines); a peripheral factor of the form $e^{-A|tpp|}$ (or $e^{-A|tpn|}$ for reaction (3)) is therefore needed to describe them correctly, with the slope A found to have the values 1.5, 1 and 1 GeV^{-2} for reactions (1), (2) and (3) respectively. These values are smaller than the corresponding at 10 GeV/c, as less energy is now available .

In Figs. 5-7 some effective mass distributions for the reactions are shown. The processes are clearly dominated by the production of resonances K*(890), $\Delta^{++}(1236)$, $\Delta^{-}(1236)$, ρ^{o} (in channel (1) only) and ω. Possible very small contributions from $K^{*-}(1420)$ in reaction (1), η^{o} in reaction (2) and ρ^{o} in reaction (3) were neglected in the analysis, in view of the limited statistics.

To these effective mass plots, one-dimensional fits were made, using a Breit-Wigner amplitude over a hand drawn background. The results are given in Table 2. Due mainly to the smaller statistics, a poorer experimental resolution as compared with the 10 GeV/c fits is obtained, but still the fitted values of resonance masses and widths are consistent with their best accepted values. Similar remarks, as at 10 GeV/c, may be

made for the ρ^o fit, while no reasonable value for the width proved possible for $\Delta^-(1236)$ in channel (3) as the peak corresponding to the resonance is not distinct; the $\Delta^-(1236)$ mass was thus fitted by fixing the width at the conventional value.

1.4 The Fractions of the Various Subprocesses

The same subprocesses as listed in section (3.5) of the previous chapter are considered here as possibly leading to final states (1) and (2); this is in consequence of the effective mass distributions manifesting essentially similar festures at the two energies. In addition, we have for reaction (3) the following channels:

$$\begin{aligned} K^- p &\to n\, \bar{K}^o \pi^+ \pi^+ \pi^- \pi^- \\ &\to \Delta^- \bar{K}^o \pi^+ \pi^+ \pi^- \\ &\to n\, K^{*-} \pi^+ \pi^+ \pi^- \\ &\to \Delta^- K^{*-} \pi^+ \pi^+ \end{aligned}$$

The details of the maximum likelihood fit to determine the fractions have been given earlier and need not to be repeated. Apart from ω, the $K^{*-}(890)$ resonance in reaction (3) has now (due to the limited experimental resolution) to have its mass and width fixed in the fitted values.

In a further effort to investigate the sensitivity of the channel fractions in respect of the production mechanism assumed, several forms of $|T|^2$ --see section 2.4 chapter IV-- were tried for reaction (1):

(i) A constant form, corresponding to simple phase space assumption.

(ii) A form $\simeq e^{-A|t_{pp}|}$, with $A = 1.5\ \text{GeV}^{-2}$ chosen so that the four momentum transfer distribution t_{pp} is correctly described.

(iii) The same form as (ii), but with the constant A considerably increased ($A = 7\ GeV^{-2}$, equal to the slope of the differential cross section in the elastic scattering).

(iv) A form $\propto e^{-b\Sigma p_T^2}$, where b is a constant ($b = .3\ GeV^{-2}$) and p_T are the transverse momenta of the particles in the final state. Such a factor gives the observed p_T distributions of the particles, but fails to describe the distributions of other exerimental variables.

(v) A product $\propto e^{-1.5|t_{pp}|}\ e^{-0.3\Sigma p_T^2}$, with its terms originated as explained above.[5]

The fractions obtained (Table 3) are not seen to differ significantly. So the forms $|T|^2 \propto e^{-1.5|t_{pp}|}$ ($e^{-1|t_{pp}|}$ and $e^{-1|t_{pn}|}$ for reactions (2) and (3), respectively), which have a sound physical meaning, were kept thereafter.

Tables 3 - 5 give the final channel fractions for the reactions, together with the corresponding cross-sections. The predictions of the likelihood fit for the resonance and background distributions are superimposed on the experimental results of Figs. 5 - 7. As at 10 GeV/c, a very good description of the data is achieved.

The reliability of our method is further supported by the work of Ref. (6), where least square fits to the individual mass distributions of the reactions had produced results compatible with ours.

2. SOME COMMON FEATURES OF THE RESULTS AT THE TWO ENERGIES.

2.1 General Remarks

In the last two chapters we have presented a detailed analysis of the production of the five and six body final states (1) and (2), at both 6 and 10 GeV/c incident momentum. Another six-body final state,

the $K^- p \to n \bar{K}^o \pi^+ \pi^+ \pi^- \pi^-$, has also been studied at 6 GeV/c, with the analysis at 10 GeV/c on its way at the moment of writing.

In the course of this study, several remarks concerning common experimental features of the reactions have been made. It was noted, for instance, that even at those high multiplicities, the reactions exhibit strong peripheral characteristics and in this respect the exponential behaviour of the four-momentum transfers has been discussed. Also, the study of effective mass distributions has shown that at both energies, reaction (1) is dominated by the K^{*-}, Δ^{++} and ρ^o resonances, while (2) is mainly associated with K^{*-}, Δ^{++} and ω. Although deviations exist due to the limited experimental resolution, the masses and widths of these resonances are at most consistent with the world average values.

2.2 The Prolific Resonance Production and Some Comments on the Fractions

We now refer to some prominent features of the analysis, which mainly concern the fractions of the various reaction channels, as estimated by the maximum likelihood fits (Tables IV - 3,4 and V - 3,4,5).

A first very interesting feature of the data is the abundant resonance production: in reactions (1) and (2) at either energy, there is more than one resonance per event on the average. Non-resonant contribution is negligible in both reactions. In constrast, much of the reaction (3) at 6 GeV/c is non-resonant, but the existence there of two pairs of identical pions might have obscured the presence of some resonances in the effective mass plots and thus excluded them from the fits.

An important part of the total cross-sections is seen to consist of simultaneous resonance production. These subprocesses will be

discussed in detail in the next chapter, but some remarks are of relevance here. Take, for instance, the $K^- p \to \Delta^{++} K^{*-} \pi^-$ quasi-three body final state in reaction (1). From the results already presented, some relations between the fractions may be derived (Table 6). It is of interest to note that, the fraction of K^{*-} in the events where Δ^{++} is produced, is about the same as the fraction of K^{*-} in the whole sample. The same is true of the fraction of Δ^{++} when K^{*-} is produced. Thus, although simultaneous K^{*-} and Δ^{++} production is an important part of the total cross-section, it does not seem that it represents any co-operative behaviour between the resonances. The fraction of K^{*-} events with ρ^o is less than in the whole sample, but this is to be expected, since each resonance uses one of the negative pions.

In contrast with reaction (1), simultaneous K^{*-} and Δ^{++} production in reaction (2) is weak. Now the fraction of Δ^{++} events with K^{*-} is decidedly less than in the whole sample, so in this case it seems that we have incompatibility between these resonances.

Finally, it is interesting to note that the channel fractions for the two energies change very little. To this we will return later.

2.3 The ρ^o meson production

One of the most striking results obtained in the analysis is the prolific production of ρ^o mesons in channel (1) and their almost complete absence in channel (2).

A similar result has been reported[7] for the annihilation $\bar{p}p \to 2\pi^+ 2\pi^-$ and $\bar{p}p \to 2\pi^+ 2\pi^- \pi^o$ (Fig. 8a) and it is interesting to note that the processes could be regarded as having some similarities.

Figure 8b indicates how the pion system for reaction (1) is formed in a multi-peripheral manner with K-meson and proton as leading particles; certain interdependent conclusions are possible about the exchanged particles e_1 and e_2.

(i) e_1 must have I-spin 1 and cannot have $J^P = 0^-$. A ρ-meson is clearly preferred.

(ii) e_2 is neutral, and must have the opposite g-parity to e_1. Clearly a pion is preferred, and a pomeron disfavoured.

In this case the dynamics of the five point graph for the pion system are extremely similar to 4-pion annihilation, where the $\bar{p}p$ must be in a state of even g-parity.

There are now very few permutations which are allowed in any dual model without exotics. In fact, the only diagrams likely to contribute appreciably are that of Fig. 8b and the one with the negative pions interchanged. It has been emphasized[8] that in this case the importance of the resonances will be very great.

If any additional pion is added these statements are all weakened. There are now a large number of possible non-exotic dual graphs, and pomeron exchange could be important at the lower vertex.

We have not been able to give these ideas any quantitative basis at present, but wish to emphasize that, even in these high-multiplicity events, simple-minded ideas of a purely statistical nature are not adequate. The quantum numbers of particles, and in particular the pseudo-scalar nature of the pion and its g-parity, excercise important constraints on the dynamics.

3. CROSS-SECTIONS VARIATION WITH ENERGY.

The cross-sections at various energies[9] for the reactions we have studied are given in Table 7. If plotted (Fig. 9) against the laboratory momentum on a log-log plot, the following observations, holding in general for the multiparticle final states, may be made

(i) The cross-sections rise steeply from threshold and then decrease at high momentum.

(ii) The position of the resultant maximum is found to depend mainly on the multiplicity and slightly on the type of the reaction.

(iii) At high momentum, the decrease in the cross-section is seen to be linear on the log-log plot, indicating that the momentum dependence of the cross-section behaves similarly to the two-body reactions.[10]

Cross-sections for many-body reactions have been studied[11] in an attempt to separate the effect of the reaction mechanism, i.e. the "physics", from phase-space effects. The cross-section, σ, is written as

$$\sigma = \sigma_A \times \text{(phase space term)} .$$

The phase space term is chosen such that at asymptotic high energies it tends to the value of one, and has the form

$$\text{(phase space volume)}/P_L^{K-2}$$

where P_L is the incident laboratory momentum and K is the particles multiplicity in the final state. The "physics" is then represented by σ_A which is found experimentally to have the form

$$\sigma_A = \text{(constant)} \times P_L^{-n_A} .$$

As in two body reactions, n_A is a constant independent of multiplicity, but depending on the reaction mechanism.

For the reactions $K^- p \rightarrow p\bar{K}^o \pi^+ \pi^- \pi^-$ and $K^- p \rightarrow p\bar{K}^o \pi^+ \pi^- \pi^- \pi^o$, the fitting of this formula gives values of $n_A \approx 1.95 \pm 0.08$ and 1.92 ± 0.12 respectively. According to the phenomenological approach outlined above, a value of $nA \approx 2$ indicates, if the sum of all possible ladder graphs is considered,[12] that a non-strange meson exchange dominates, with some contribution from pomeron and baryon-exchange.

In fact, it was shown that an important feature at many body processes is the resonance nature of interactions between the final state particles. When, say, a 5-body channel is dominated by resonances, it is reasonable to ask whether there is any sense in treating it as a 5-body rather than as a quasi 4-body process. One of the nice implications of the asymptotic behaviour described is that it actually does not matter, since the energy dependence will be the same. This further implies that the resonance fractions should remain constant with energy, since we should have the same energy dependence for, say, the process $K^- p \rightarrow pK^{*-} \pi^+ \pi^-$ as for the process $K^- p \rightarrow p\bar{K}^o \pi^+ \pi^- \pi^-$ of which the first forms a subset.

As already stated there seems little change in the resonance fractions at 10 and 6 GeV/c; so our results are, within the errors, clearly consistent with the above condition. Similar indications are given in a compilation of the fractions of ρ mesons and of Δ in π - p interactions over a wide range of incident momentum.[13]

REFERENCES AND FOOTNOTES

1. The Birmingham, Glasgow and Oxford Universities, the Imperial College (London), the Rutherford Laboratory and the Max-Planck Institut fur Physik and Astrophysik, Munchen.

2. See, for instance K. Paler, Ph.D. thesis, Imperial College, unpublished.

3. (i) W.W.M. Allison, et.al.
P.L. 25B (67) 619.

(ii) D.C. Colley, et. al.
N.C. 59A (69) 519.

(iii) D.C. Colley, et. al.
N.C. 53A (68) 522.

(iv) D. Scotter, et al.
P.L. 26B (68) 474.

(v) L. K. Sisterson, et al.
N.P. B6 (68) 205.

4. S. J. Goldsack, G. A. Grammatikakis, G. Otter (I.C.) A. Cruz Flor, L. Lyons (Oxford) N.P. B29 (1971) 529.

5. Simply on a test basis. If the experimental distribution in one variable can be fitted by $N_1(x_1)$ and a second is consistent with $N_2(x_2)$, there is no justification for assuming that the factor $N_1(x_1)\ N_2(x_2)$ should be used to fit any other distribution $N_3(x_3)$. See L. Lyons "On the analysis of multibody final states" Oxford University preprint.

6. A. Gruz Flor, Ph.D. thesis, Oxford University (unpublished).

7. C. Baltay, et. al., P.R. 145B (1966) 1103.

8. H.R. Rubinstein, P. L. 32B (1970) 370.

9. High-Energy Reactions Analysis Group CERN/HERA 70-6.

10. D.R.O. Morrison, Proc. of Stony Brook Conference (1966) and P.L. 22 (1966) 528.

11. J.D. Hansen, et. al.,
N.P. B25 (1971) 605.

12. D. Amati, et. al.,
N.C. 26 (1962) 896.

13. A. Wroblenski, Proceedings of the XVth International Conference on High Energy Physics, Kiev (1970).

TABLE V-1

NUMBER OF EVENTS AND CROSS SECTIONS

Reaction	No. of Events	Cross-Section μb
$K^- p \to p\bar{K}^o \pi^+ \pi^- \pi^-$	514	272 ± 44
$K^- p \to p\bar{K}^o \pi^+ \pi^+ \pi^- \pi^o$	822	386 ± 62
$K^- p \to \bar{K}^o \pi^+ \pi^+ \pi^- \pi^-$	526	260 ± 55

TABLE V-2

RESONANCE MASSES AND WIDTHS

Channel	Resonance	Breit-Wigner Fits	
		mass (MeV)	width (MeV)
$K^- p \to p\bar{K}^o \pi^+ \pi^- \pi^-$	$K^*(890)$	896 ± 3	58 ± 8
	$\Delta^{++}(1236)$	1212 ± 6	84 ± 16
	ρ^o	736 ± 10	386 ± 77
$\to p\bar{K}^o \pi^+ \pi^- \pi^- \pi^o$	$K^*(890)$	893 ± 2	54 ± 7
	$\Delta^{++}(1236)$	1182 ± 13	161 ± 40
	ω	784 ± 4	56 ± 11
$\to n\bar{K}^o \pi^+ \pi^+ \pi^- \pi^-$	$K^*(890)$	865 ± 5	97 ± 22
	$\Delta^-(1236)$	1265 ± 18	-

TABLE V-3

$K^- p \to p\bar{K}^o \pi^+ \pi^- \pi^-$ AT 6 GeV/c, 514 EVENTS ($\bar{K}^o$ seen)

Channel	Fractions					Cross-Sections (μb)
	Phase space	$e^{-1.5\|t_{pp}\|}$	$e^{-7\|t_{pp}\|}$	$e^{-\cdot 3\Sigma p_T^2}$	$e^{\cdot 3\Sigma p_T^2}\ e^{-1.5\|t_{pp}\|}$	$e^{-1.5\|t_{pp}\|}$
$p\bar{K}^o\pi^+\pi^-\pi^-$	~0 ± 2	~0 ± 2	~0 ± 2	~0 ± 2	~0 ± 2	~0 ± 5
$\Delta^{++}K^o\pi^-\pi^-$	13 ± 4	13 ± 4	16 ± 4	13 ± 4	14 ± 4	35 ± 12
$pK^{*-}\pi^-\pi^+$	26 ± 6	25 ± 6	33 ± 6	24 ± 6	25 ± 6	67 ± 18
$\Delta^{++}K^{*-}\pi^-$	18 ± 4	20 ± 4	14 ± 3	20 ± 5	20 ± 4	54 ± 13
$p\bar{K}^o\rho^o\pi^-$	26 ± 5	25 ± 5	32 ± 5	26 ± 5	25 ± 5	68 ± 16
$pK^{*-}\rho^o$	17 ± 5	17 ± 6	5 ± 5	17 ± 6	17 ± 4	47 ± 17

TABLE V-4

$K^- p \to p\bar{K}^o \pi^+ \pi^- \pi^- \pi^o$ AT 6 GeV/c, 822 EVENTS

Channel	Fraction	Cross-Section (μb)
$K^- p \to p\bar{K}^o \pi^+ \pi^- \pi^- \pi^o$	0 ± 1	0 ± 4
$\to \Delta^{++} \bar{K}^o \pi^- \pi^- \pi^o$	20 ± 5	77 ± 19
$\to \Delta^{++} K^{*-} \pi^- \pi^o$	1.5 ± 5	6 ± 19
$\to p K^{*-} \pi^+ \pi^- \pi^o$	50 ± 5	193 ± 19
$\to p\bar{K}^o \pi^- \omega$	17 ± 4	66 ± 15
$\to p K^{*-} \omega$	13 ± 3	50 ± 12

TABLE V-5

$K^- p \to n\bar{K}^o \pi^+ \pi^+ \pi^- \pi^-$ AT 6 GeV/c, 526 EVENTS

Channel	Fraction	Cross-Section (μb)
$K^- p \to n\bar{K}^o \pi^+ \pi^+ \pi^- \pi^-$	41 ± 12	106 ± 28
$\to \Delta^- \bar{K}^o \pi^+ \pi^+ \pi^o$	14 ± 10	36 ± 25
$\to n K^{*-} \pi^+ \pi^+ \pi^-$	38 ± 11	99 ± 26
$\to \Delta^- K^{*-} \pi^+ \pi^+$	07 ± 8	18 ± 20

TABLE V-6

RESONANCE FRACTIONS IN $\bar{K}p \to p\bar{K}^o\pi^+\pi^-\pi^-$

	6 GeV/c	10 GeV/c
Total K^*	62 ± 8	55 ± 4
Total Δ^{++}	33 ± 7	34 ± 4
Total ρ^o	42 ± 8	50 ± 4
K^* fraction of Δ^{++}	60 ± 9	56 ± 6
Δ^{++} fraction of K^*	30 ± 7	27 ± 5
K^* fraction of ρ^o	40 ± 9	38 ± 3

TABLE V-7

CROSS-SECTIONS AT VARIOUS ENERGIES

P_{LAB}	CROSS SECTIONS		
	$K^-p \to p\bar{K}^o\pi^+\pi^-\pi^-$	$K^-p \to p\bar{K}^o\pi^+\pi^-\pi^-\pi^o$	$K^-p \to n\bar{K}^o\pi^+\pi^+\pi^-\pi^-$
3.00			5 ± 3
3.50	220 ± 20	90 ± 10	60 ± 10
4.25	390 ± 35		
6.00	272 ± 44	386 ± 62	260 ± 55
10.10	290 ± 20	470 ± 30	210 ± 20

Fig.V-1

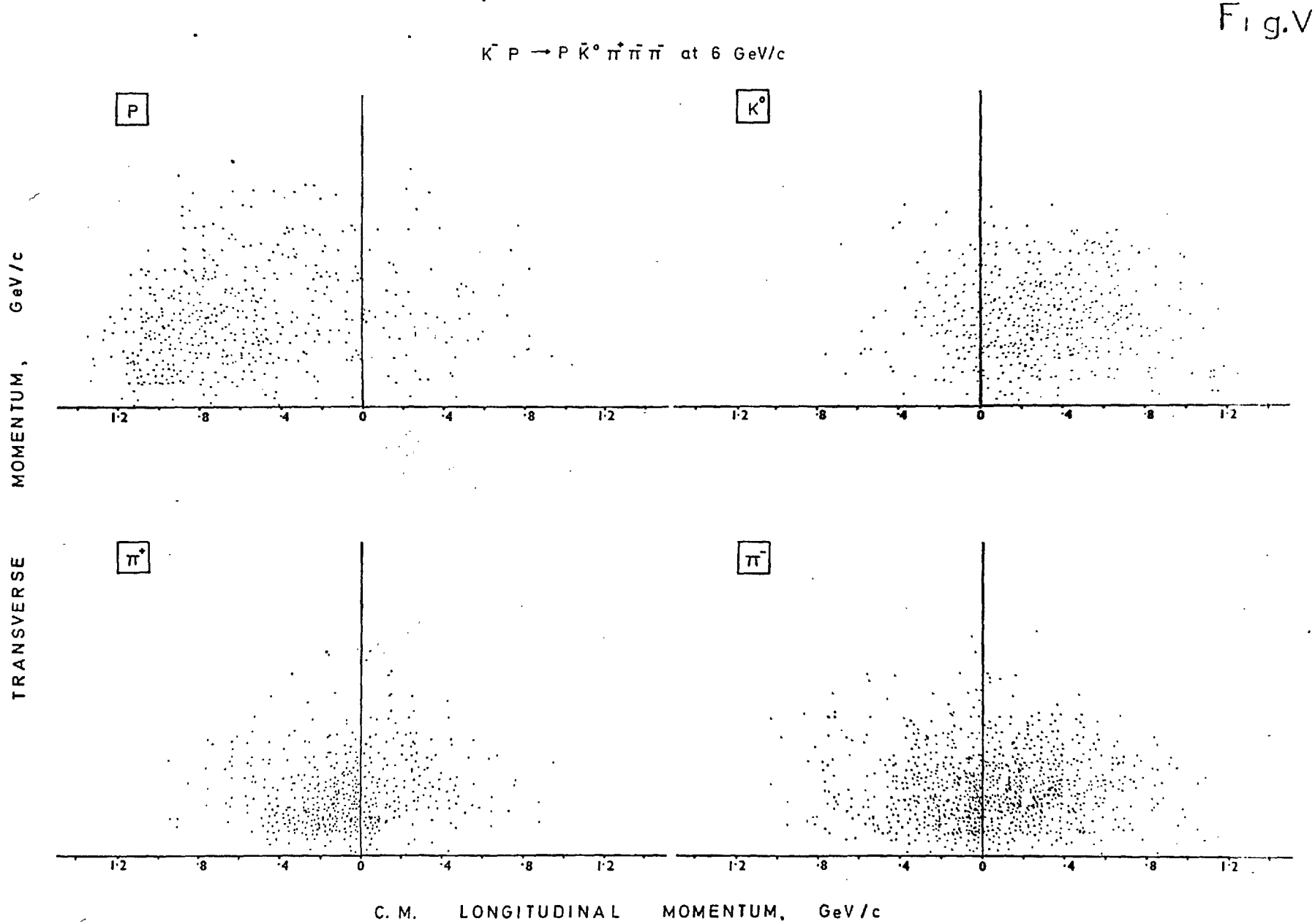

$K^- P \rightarrow P \bar{K}^0 \pi^+ \pi^- \pi^-$ at 6 GeV/c
P
K^0
π^+
π^-
TRANSVERSE MOMENTUM, GeV/c
C. M. LONGITUDINAL MOMENTUM, GeV/c
1·2
·8
·4
0
·4
·8
1·2

Fig. V-2

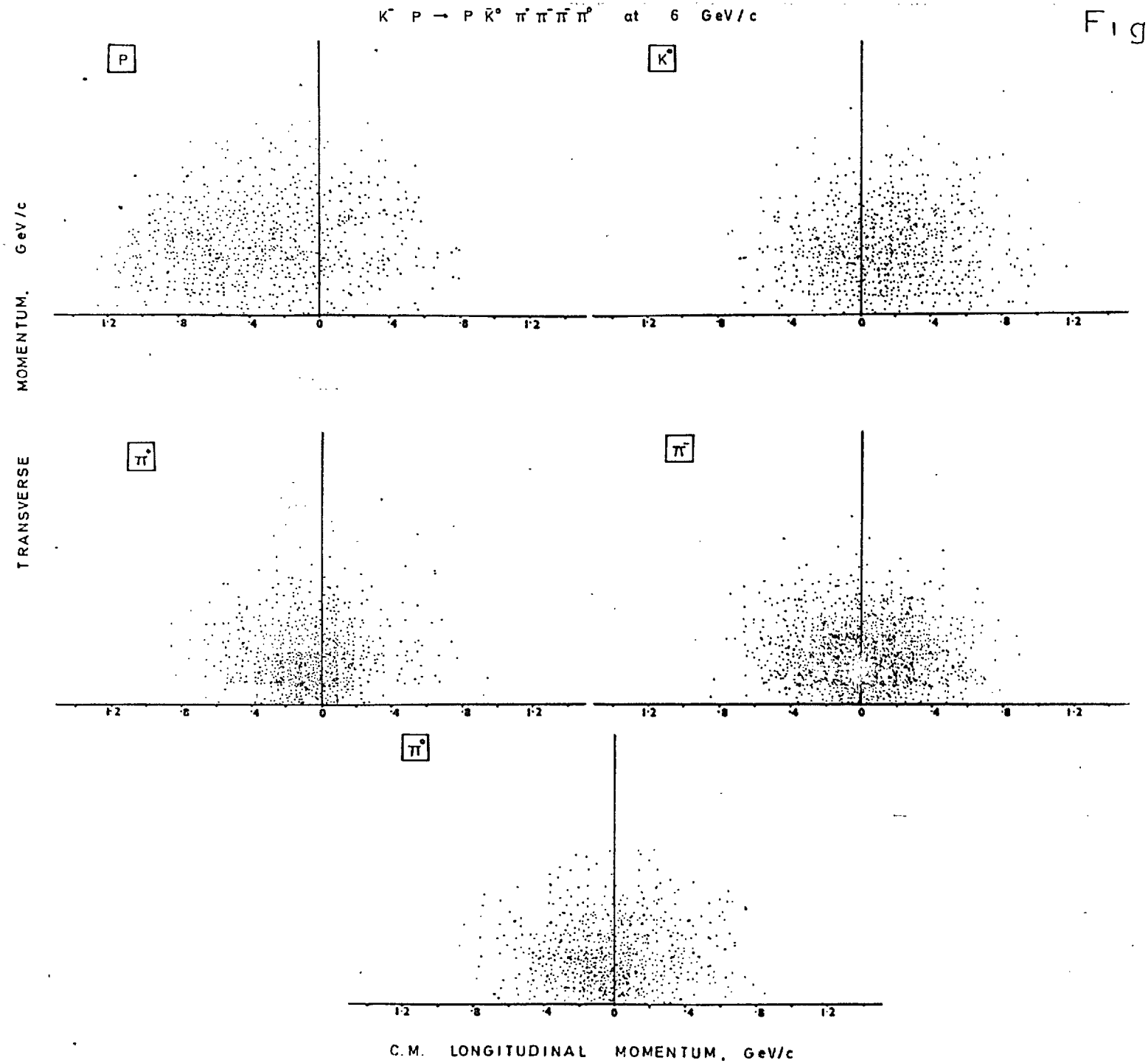

K⁻ P → P K⁰ π⁺π⁻π⁺π⁻ at 6 GeV/c
P
K⁰
π⁺
π⁻
π⁰
TRANSVERSE MOMENTUM, GeV/c
C.M. LONGITUDINAL MOMENTUM, GeV/c
1·2
·8
·4
0
·4
·8
1·2

Fig V-3

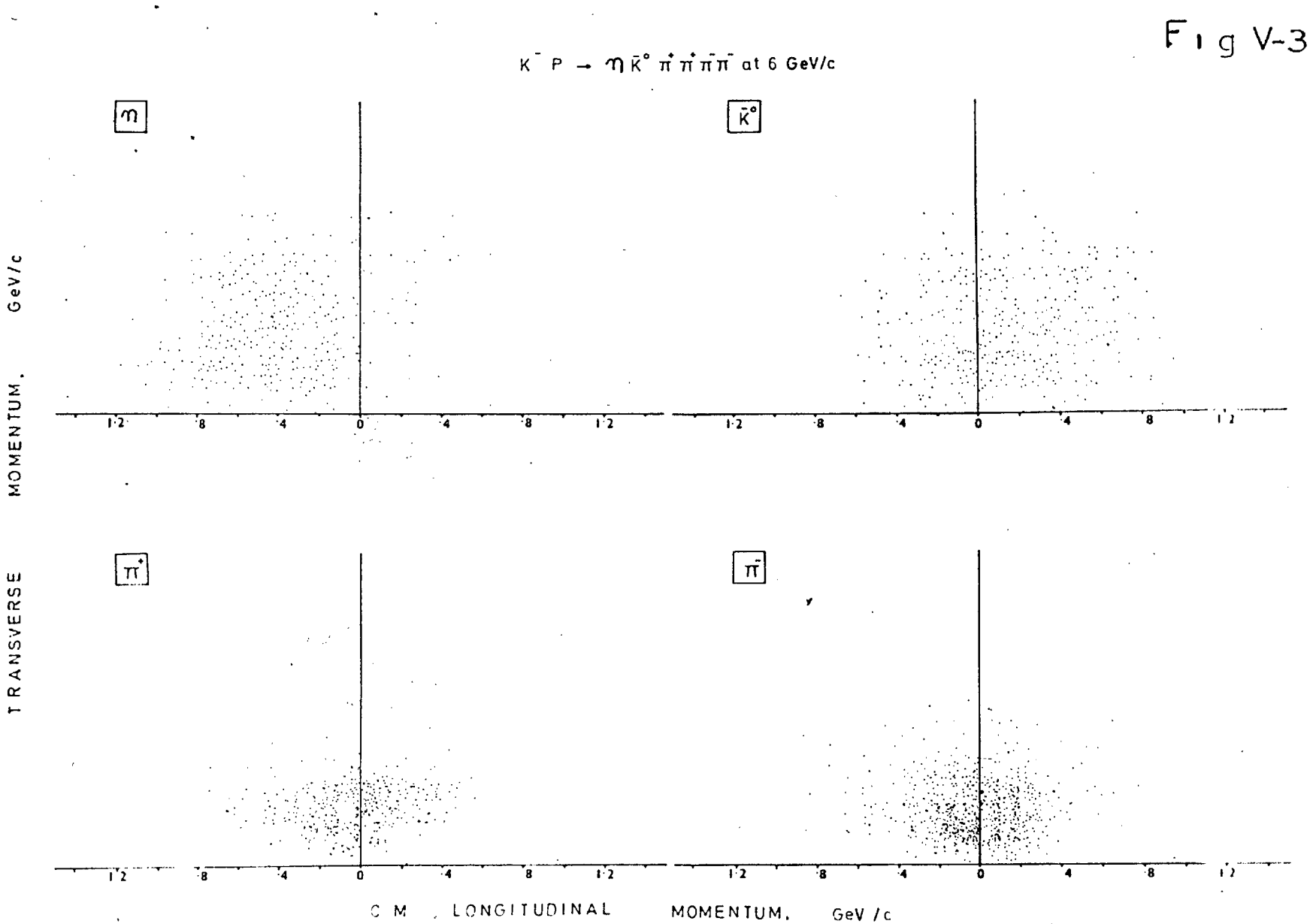

K⁻ P → η K̄° π⁺ π⁺ π⁻ π⁻ at 6 GeV/c
η
K̄°
π⁺
π⁻
TRANSVERSE MOMENTUM, GeV/c
C M LONGITUDINAL MOMENTUM, GeV/c
1·2
·8
·4
0
·4
·8
1·2

Fig. V-4

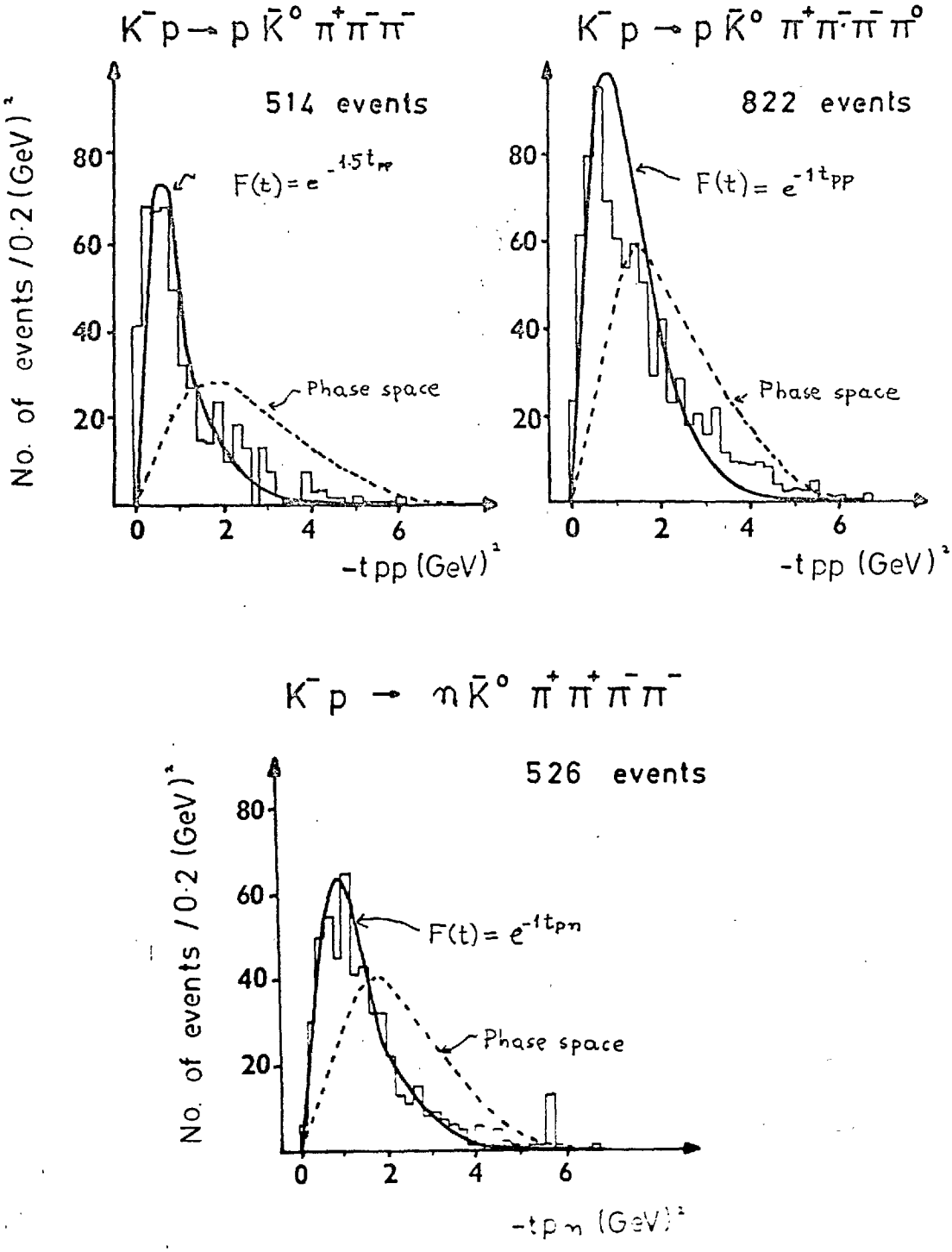

$K^- p \to p \bar{K}^0 \pi^+ \pi^- \pi^-$
514 events
$F(t) = e^{-1.5 t_{pp}}$
Phase space
No. of events /0·2 (GeV)²
80
60
40
20
0
2
4
6
$-t\,pp\ (GeV)^2$
$K^- p \to p \bar{K}^0 \pi^+ \pi^- \pi^- \pi^0$
822 events
$F(t) = e^{-1 t_{pp}}$
Phase space
$-t\,pp\ (GeV)^2$
$K^- p \to n \bar{K}^0 \pi^+ \pi^+ \pi^- \pi^-$
526 events
$F(t) = e^{-1 t_{pn}}$
Phase space
$-t\,pn\ (GeV)^2$

Fig V-5

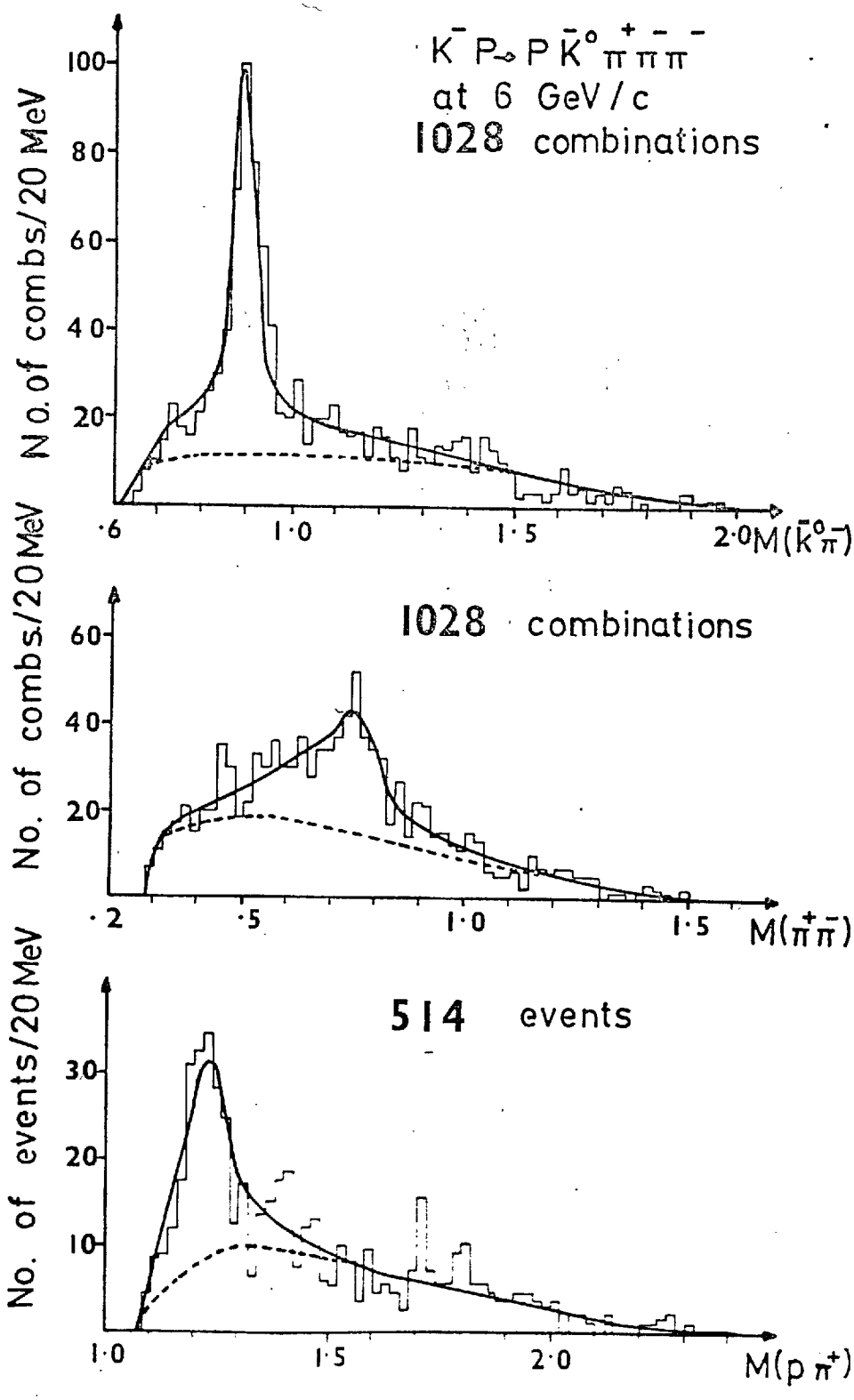

$K^- P \to P \bar{K}^0 \pi^+ \pi^- \pi^-$
at 6 GeV/c
1028 combinations
No. of combs/20 MeV
100
80
60
40
20
·6
1·0
1·5
2·0
$M(\bar{K}^0\pi^-)$
1028 combinations
No. of combs/20 MeV
60
40
20
·2
·5
1·0
1·5
$M(\pi^+\pi^-)$
514 events
No. of events/20 MeV
30
20
10
1·0
1·5
2·0
$M(p\pi^+)$

Fig V-6

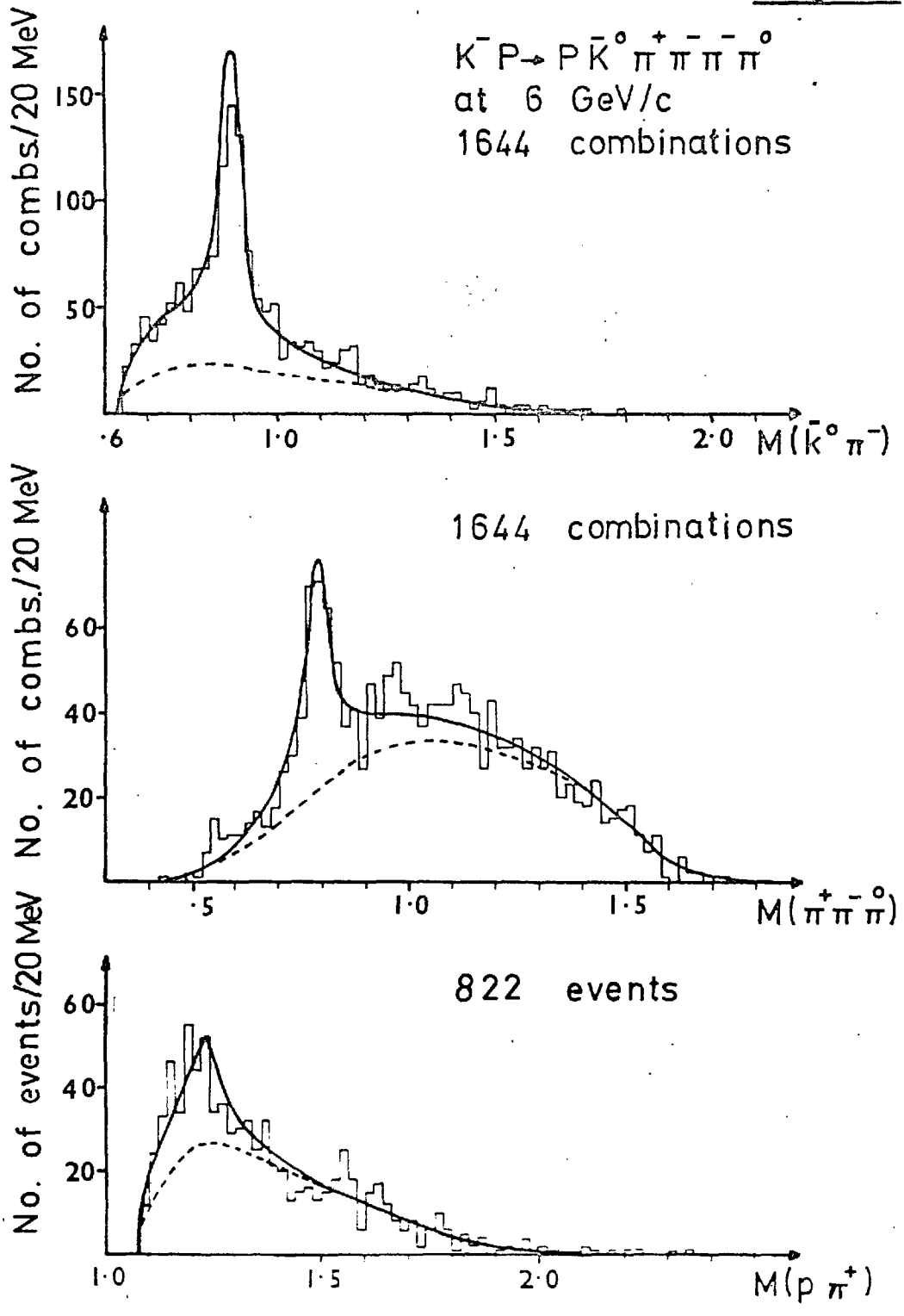

$K^- P \to P \bar{K}^0 \pi^+ \pi^- \pi^- \pi^0$
at 6 GeV/c
1644 combinations
No. of combs./20 MeV
150
100
50
·6
1·0
1·5
2·0
$M(\bar{k}^0 \pi^-)$
1644 combinations
No. of combs./20 MeV
60
40
20
·5
1·0
1·5
$M(\pi^+ \pi^- \pi^0)$
822 events
No. of events/20 MeV
60
40
20
1·0
1·5
2·0
$M(p \pi^+)$

Fig. V-7

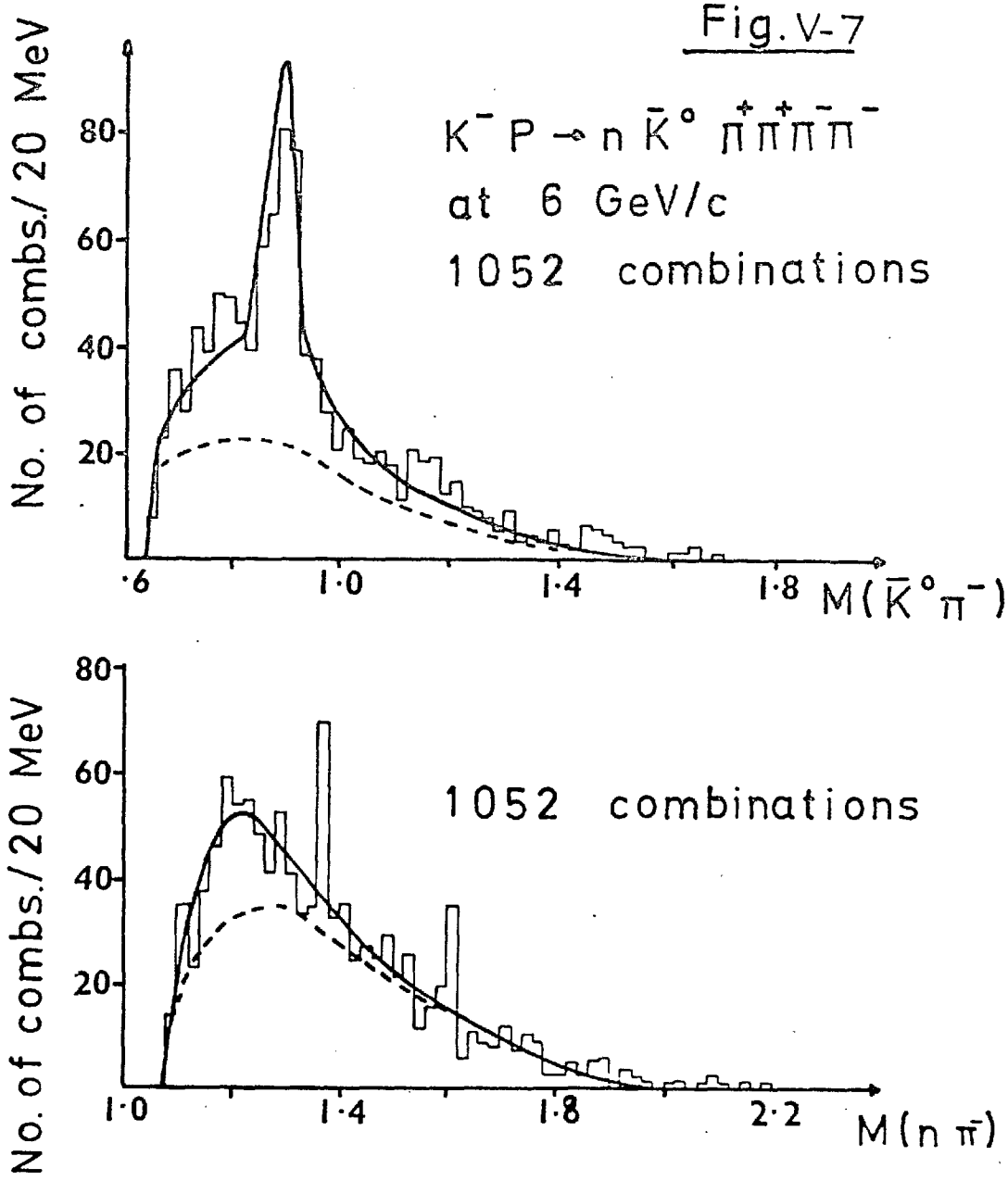
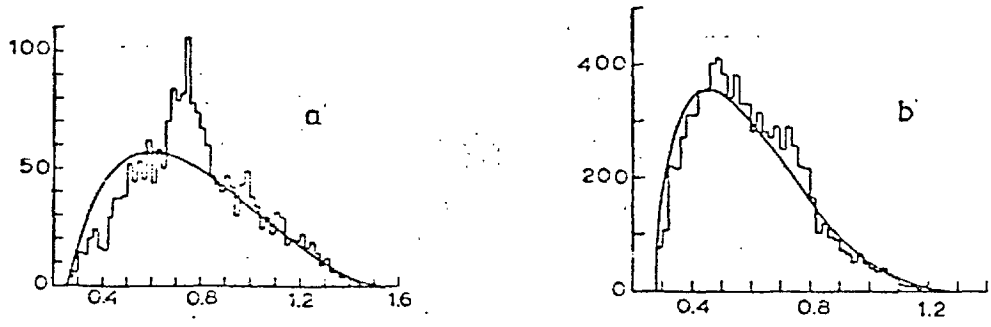

$K^- P \to n \bar{K}^0 \pi^+\pi^+\pi^-\pi^-$
at 6 GeV/c
1052 combinations
No. of combs./20 MeV
80
60
40
20
·6
1·0
1·4
1·8
$M(\bar{K}^0\pi^-)$
1052 combinations
No. of combs./20 MeV
80
60
40
20
1·0
1·4
1·8
2·2
$M(n\pi^-)$

Fig. V-8

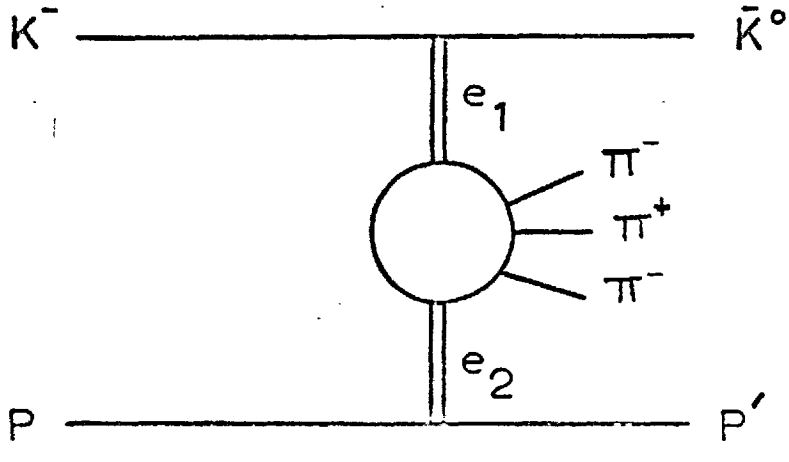
$\bar{P}P$ anihillation at rest

a) $\pi^+\pi^-$ in $2\pi^+ 2\pi^-$

b) $\pi^+\pi^-$ in $2\pi^+ 2\pi^- \pi^0$.

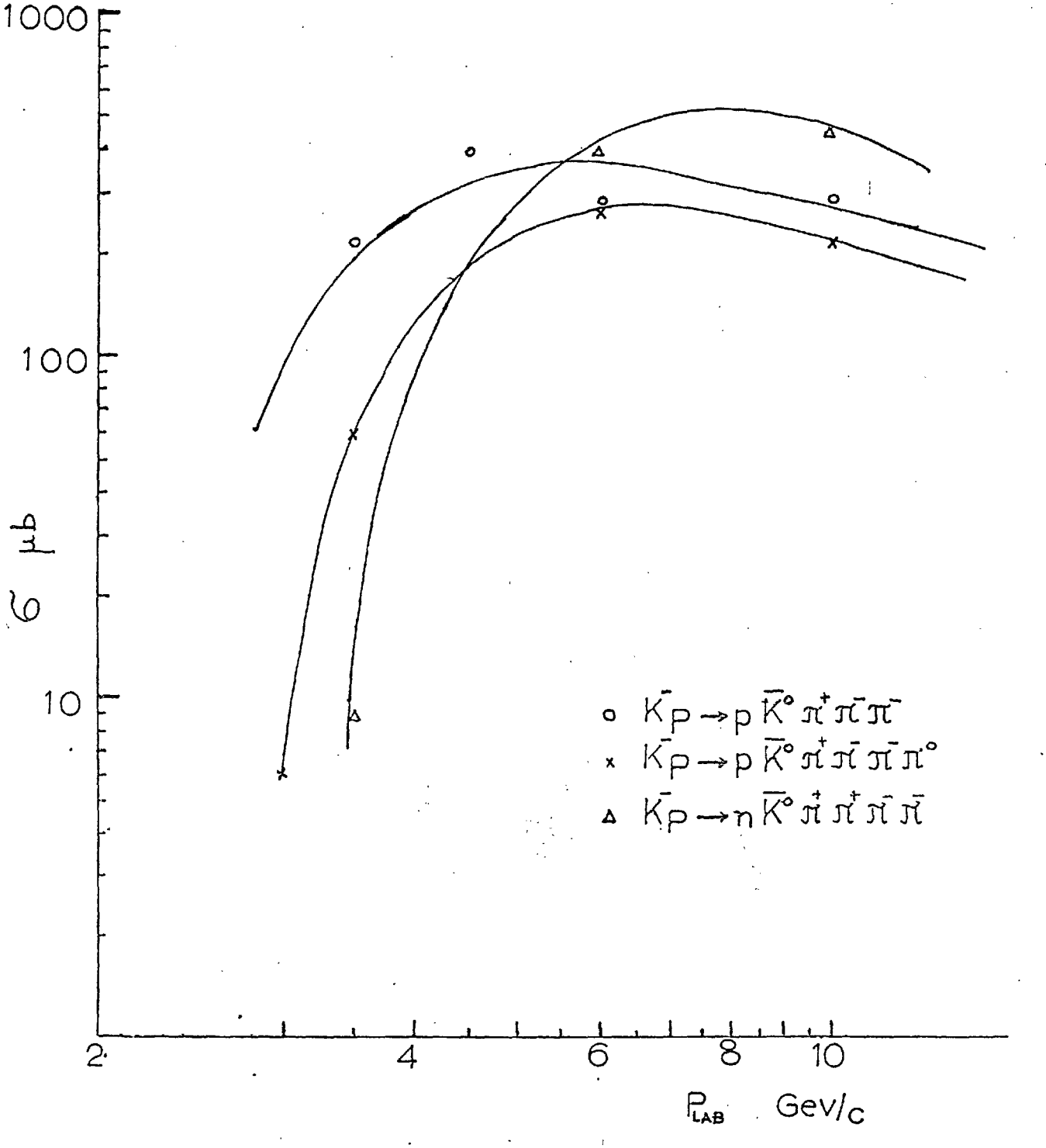


(a)



(b)

Fig. V-9


1000
100
10
σ μb
2
4
6
8
10
P_LAB Gev/c
o K⁻p → p K̄° π⁺ π⁻ π⁻
x K⁻p → p K̄° π⁺ π⁻ π⁻ π°
Δ K⁻p → n K̄° π⁺ π⁺ π⁻ π⁻

CHAPTER VI

A STUDY OF THE REACTION $K^- p \to \Delta^{++} K^{*-} \pi^-$ AT 6 AND 10 GeV/c

The quasi three-body reaction $K^- p \to \Delta^{++} K^{*-} \pi^-$, which shows a sufficient separation from background, is analyzed in detail in this chapter. Its general features at 6 and 10 GeV/c incoming energies are discussed, and an attempt is made to determine the dominating production mechanism. A description of this reaction on the basis of two theoretical models (the Veneziano and the CLA) concludes the chapter.

1. THREE BODY SUBPROCESSES IN THE FINAL STATES STUDIED

Among the subprocesses which contribute to the final states studied, worthy of further investigation are the quasi three-body reactions

$$K^- p \rightarrow \Delta^{++} K^{*-} \pi^-$$

$$K^- p \rightarrow p K^{*-} \rho^0$$

$$K^- p \rightarrow p K^{*-} \omega$$

seen to occur in substantial percentages at both 6 and 10 GeV/c incoming momenta.

To select the events of these reactions the following limits (in GeV) are imposed on the effective masses involved:

$K^{*-}(890)$	:	.84	$\leqq$	$M(\bar{K}^0\pi^-)$	$\leqq$	.94
Δ^{++}	:	1.14	$\leqq$	$M(p\pi^+)$	$\leqq$	1.32
ρ^0	:	.64	$\leqq$	$M(\pi^+\pi^-)$	$\leqq$	.84
ω	:	.72	$\leqq$	$M(\pi^+\pi^-\pi^0)$	$\leqq$	.84

In the mass scatter plots of Figs. 1 and 2 the presence of simultaneously produced resonances is indicated by the accumulation of events along the resonance bands; since there are two combinations per event, each cluster represents a larger fraction of events than the plot density alone would indicate.

When the mass cuts refered above are applied to the data, the samples of events obtained for each reaction will presumably contain a considerable amount of background events. Table 1 presents the percentages of contributing channels in the overlapping regions of

$K^{*-} - \Delta^{++}$, $K^{*} - \rho$ and $K^{*} - \omega$ resonances, as estimated from the maximum likelihood fit described earlier. Only reaction $K^{-}p \to \Delta^{++} K^{*-} \pi^{-}$ is found to be reasonably separated from background (the background contamination being ~47% and ~40% at 6 and 10 GeV/c, respectively). It is therefore the only one which we will attempt to study in greater detail.

2. THE REACTION $K^{-}p \to \Delta^{++} K^{*-} \pi^{-}$ AND ITS PRODUCTION MECHANISM

2.1 Introductory Remarks on the Three-Body Problem

The extensive study of production mechanism in two body reactions has naturally led--from both theoretical and experimental points of view--in similar attempts to investigate the three body problem.[1] Early models for a reaction of the type

$$A + B \to C + D + E$$

were assuming the mechanism shown in Fig. 3a, where information on the virtual reaction of the exchanged particle (usually a pion) could be obtained from the experimental data on the two-body reaction

$$e + B \to D + E \ .$$

In a more symmetric approach (based on the peripheral characteristics of high energy collisions) the double peripheral mechanism of Fig. 3b is considered; e_1 and e_2 represent the two (often different) trajectories being exchanged. This is obviously a special case of the general "multiperipheral" diagram of Fig. 3c, where the

"particles" 1 2...n may be single particles or groups of particles produced at low effective mass.

When one or more of the outgoing "particles" in a three-body reaction is a resonance, important information concerning the spin of the exchanges can possibly be obtained from the decay of the resonance. Since several diagrams like the one of Fig. 3b can be drawn for the same final state; the dominance of one has to be assumed by examining the relevant experimental distributions of the particles.

2.2 The General Method of Studying the Exchanges

(a) Decay Angular Distributions of the Produced Resonances

To determine the quantum numbers of both exchanged particles e_1 and e_2 in Fig. 3b, we consider the upper and lower part of the diagram separately;[2] our discussion has, therefore, to be concentrated on the two body problem.

Let us assume that in the reaction

$$A + B \rightarrow C + D$$

the particle D is a resonance with spin J which decays (Fig. 4a) according to

$$D \rightarrow \alpha + \beta \ .$$

After its production, D is in general in a quantum mechanical mixture of pure spin states. The mixture depends on the spin and parity of the exchanged particle, and is described by the (2J+1) dimensional density matrix of D with the elements $\rho_{mm'}$, (m,m' are the magnetic quantum numbers of D running from -J to +J). A discussion on the

properties of the density matrix elements can be found elsewhere;[3] what is important though for our purpose is that the decay angular distribution of D depends on the mixture of spin states and, therefore, on some of the density matrix elements.[4] By working backward, from the angular distribution we can determine the density matrix elements and investigate via a comparison with theory which particle is likely to be exchanged in the mechanism producing D .

In following this procedure, we have first to define a coordinate system in terms of which we can analyze the substates of D . It is a natural choice to work in the rest frame of D (Fig. 4b), and thus the coordinate system shown in Fig. 4c seems the most suitable: The Z-axis is taken along the direction of B, whose momentum vector lies on the same (the production) plane with A and C. The Y-axis is then usually defined as the normal to the production plane; alternative choices are also possible and will be discussed later. In this coordinate system the decay angles θ and ϕ are the polar and azimuth angles, respectively, of one of the decay particles (α or β).

We may now express[3] in terms of the matrix elements the decay angular distributions for two cases of D which are of interest to our study

(I) $\underline{J = 1, J_\alpha = J_\beta = 0}$ (a situation realized in the decay $K^* \to K\pi$).

The decay distribution is given by

$$W(\cos\theta,\phi) = \frac{3}{4\pi}\{\frac{1}{2}(1 - \rho_{00}) + \frac{1}{2}(3\rho_{00} - 1)\cos^2\theta - \rho_{1,-1}\sin^2\theta\cos2\phi - 2\ \mathrm{Re}\ \rho_{10}\ \sin2\theta\cos\phi\} \tag{2.1}$$

with the normalization constant chosen such that

$$\int_0^{2\pi} d\phi \int_{-1}^{+1} d\cos\theta \; W(\cos\theta,\phi) = 1 \qquad (2.2)$$

By measuring the decay distribution $W(\cos\theta,\phi)$ we can determine from formula (2.1) the density matrix elements ρ_{00}, ρ_{1-1} and $\mathrm{Re}\,\rho_{10}$ of the resonance. Integration over $\cos\theta$ or ϕ yields the distribution in $\cos\theta$ or ϕ

$$W(\cos\theta) = \frac{3}{4}\{(1-\rho_{00}) + (3\rho_{00}-1)\cos^2\theta\} \qquad (2.3)$$

$$W(\phi) = \frac{1}{2\pi}\{(1+2\rho_{1,-1}) - 4\rho_{1,-1}\cos^2\phi\} \qquad (2.4)$$

(II) $\underline{J=\frac{3}{2}}$, $\underline{J_\alpha=\frac{1}{2}}$, $\underline{J_\beta=0}$ (which is the case of the decay $\Delta^{++}\to p\pi^+$)

The normalized decay distribution reads now

$$W(\cos\theta,\phi) = \frac{3}{4\pi}\{\frac{1}{6}(1+4\rho_{33}) + \frac{1}{2}(1-4\rho_{33})\cos^2\theta - \frac{2}{\sqrt{3}}\,\mathrm{Re}\rho_{3,-1}\sin^2\theta\cos2\phi \qquad (2.5)$$

$$- \frac{2}{\sqrt{3}}\,\mathrm{Re}\rho_{31}\sin2\theta\cos\phi\}$$

while the distributions in $\cos\theta$ and ϕ alone are given by

$$W(\cos\theta) = \frac{1}{4}\{(1+4\rho_{33}) + (3-12\rho_{33})\cos^2\theta\} \qquad (2.6)$$

$$W(\phi) = \frac{1}{2\pi}\{(1+\frac{4}{\sqrt{3}}\,\mathrm{Re}\rho_{3,-1}) - \frac{8}{\sqrt{3}}\,\mathrm{Re}\rho_{3,-1}\cos^2\phi\} \qquad (2.7)$$

(b) Predictions of the One Meson Exchange Model on the Density Matrix Elements

For reactions of the type

$$A + B \to C + D$$

where C or/and D are strongly decaying resonances, a one meson exchange model (OME) has been developed to describe the production and the decay of resonances.[3] The incident particles A and B are assumed to be a pseudo scalar meson (0^-) and a nucleon ($\frac{1}{2}^+$), respectively, a situation realized in almost all experiments. From angular momentum and parity conservation at the vertices, predictions about the density matrix elements are made by the model depending on the spin J_e and parity P_e of the exchanged meson.

The following cases are again of interest to the present study

(I) Production of a vector meson (1^-) resonance (e.g. K^*)

We first note that by conservation of spin and parity in the meson vertex AeC (Fig. 4a), the exchange of a 0^+ particle is forbidden. For the allowed exchanges, the OME model makes the following predictions about the density matrix elements (and, consequently, the decay angular distributions) of the resonance

(i) $J_e^{P_e} = 0^-$ (pseudoscalar exchange)

Then

$$\rho_{\pm 1,m} = \rho_{m,\pm 1} = 0 \ , \ \rho_{00} = 1 \qquad (2.8)$$

and

$$W(\cos\theta) = \frac{3}{2}\cos^2\theta \ , \ W(\phi) = \frac{1}{2\pi} = \text{const} \qquad (2.9)$$

(ii) $P_e = (-1)^{J_e}$, $J_e \geq 1$ (natural parity)

In this case

$$\rho_{0m} = \rho_{m0} = \rho_{00} = 0 \qquad (2.10)$$

while all other elements are different from zero.

Also

$$W(\cos\theta) = \frac{3}{4}\sin^2\theta \ , \ W(\phi) = \frac{1}{4\pi}\{(1 \mp 2\rho_{1,-1}) - 4\rho_{1,-1}\cos^2\phi\} \qquad (2.11)$$

(iii) $P_e = (-1)^{J_e}$, $J_e \geq 1$ (Unnatural parity)

All density matrix elements are allowed to be different from zero; this is the only situation in which we can have $\rho_{10} \neq 0$.

(II) Production of a $\frac{3^+}{2}$ Baryon Resonance (e.g. Δ^{++})

Since the incident nucleon B has spin, the baryon vertex BeD (Fig. 4a) cannot be treated as easily as the meson vertex AeC; only for $J_e = 0$ predictions about the density matrix elements of the resonance D can be made. However, for the N^* production by ρ (1^-) exchange, a specific model has been developed[5] in which the vertex $N \rho N^*$ is treated in analogy with the vertex $N \gamma N^*$ occuring in photoproduction.

Thus

(i) When a spin zero particle (π) is exchanged

$$\rho_{\pm 3,m} = \rho_{m\pm 3} = 0 \qquad (2.12)$$

and

$$W(\cos\theta) = \frac{1}{4}(1 + 3\cos^2\theta),\ W(\phi) = \frac{1}{2\pi} = \text{const} \qquad (2.13)$$

(ii) When a vector particle (ρ) is exchanged

$$\rho_{33} = .375 \quad \mathrm{Re}\rho_{3,-1} = .216 \quad \mathrm{Re}\rho_{3,1} = 0 \qquad (2.14)$$

with the angular distributions readily given by formulas (2.6) and (2.7).

2.3 The Data

(a) General Features and LPS Analysis of the Reaction

Some experimental quantities of importance for the reaction $K^- p \to \Delta^{++} K^{*-} \pi^-$ are displayed in Figs. 5-6 (6 GeV/c) and Figs. 7-8 (10 GeV/c). The well known "low-mass" enhancement is observed in the

($\Delta^{++}\pi^-$) mass spectrum;[6] it is stronger in the 10 GeV/c data. The longitudinal momenta of the three final state "particles" show that the Δ^{++} and K^{*-} are strongly collimated backward and forward with respect to the beam momentum, while the π^- is produced symmetrically. The same is suggested by the four momentum trasfer distributions from K^- to K^{*-} and proton to Δ^{++}, which are simultaneously small. It is thus evident that a double peripheral mechanism prevails in the reaction.

A recent method of examining the dynamic properties of a reaction--the so called longitudinal phase (LPS) analysis[7]--is based on the fact that in high-energy collisions the transverse momentum of all secondary particles is limited to small values; only the longitudinal momenta are therefore considered in the analysis. For a three body final state, each event is described by its distance from three axis which are oriented at 120° with respect to each other (Fig. 9). These distances are the longitudinal momenta of the three secondary particles, $P_{L,i}$, in the reaction c.m system. The points lie all on a plane because of longitudinal momentum conservation

$$\sum_{i=1}^{3} P_{L,i} = 0 .$$

Besides, the available space is further restricted to the inside of a regular hexagon by energy conservation

$$\sum_{i=1}^{3} |P_{L,i}| \leq W$$

where W is the total c.m energy. For non zero masses, the contour (K_1) differs from the hexagon (H_1) by a rounding of the corners.

In fact, and because the transverse momenta of all three particles are small, the experimental points would all lie near the boundary of the plot. This allows us to convert the two dimensional LPS plot into a simpler one dimensional distribution. The polar angle ω (Fig. 9) is therefore introduced (counted anticlockwise from the axis $P_{L,1} = 0$) and essentially determines the complete longitudinal configuration of an event. From the angle ω the relative order of the longitudinal momenta (e.g. $P_{L,1} < P_{L,2} < P_{L,3}$) can then be deduced.

The definition of ω for the specific case of the reaction $K^- p \to \Delta^{++} K^{*-} \pi^-$ is indicated in Fig. 10; the experimental distributions of this angle at both 6 and 10 GeV/c are also presented in the same figure. It may be seen that these distributions are characterized by a pronounced peak near $\omega = 60^\circ$, which corresponds to the double peripheral diagram shown in Fig. 11. The conclusion is in agreement with the remarks made when looking at the single distributions of the particles.

In another way of data presentation,[8] refered here for completeness, we calculate for each emitted particle the four momentum transfer with respect to the same initial particle (say A). The three variables t_{A1}, t_{A2}, t_{A3} thus defined are taken as the variables to be plotted with their axis inclined at 120° to one another. Since we have

$$t_{A1} + t_{A2} + t_{A3} = \text{const}$$

the boundary in the high energy limit is a triangle.

The triangular plot for the reaction $K^- p \to \Delta^{++} K^{*-} \pi^-$ (only the 6 GeV/c data are used) is displayed in Fig. 12. The experimental points are seen to be limited to certain regions of the boundary corresponding as before to the dominance of the production mechanism of Fig. 11.

(b) The Nature of the Exchanges

We attempt now to determine the nature of the exchanged particles considering only the Feynman graph of Fig. 11; as already noted, the upper and lower vertex of the graph are treated separately.

Some first information on the spin of the exchanges can possibly be obtained by looking at the distribution of Treiman-Yang angle[8a] at each vertex. If a pseudoscalar exchange is occuring at the vertex, the corresponding distribution must be flat. For the present reaction these angles are defined as follows

$\underline{K^- - K^*}$ vertex

$$\cos\theta_1 = \frac{(\Delta^{++} \times \pi^-)(K^-_{inc} \times K^{*-})}{|\Delta^{++} \times \pi^-|\ |K^-_{inc} \times K^{*-}|}$$

where Δ^{++}, π^-, etc. represent the three momenta of the particles evaluated in the proton rest frame

$\underline{p - \Delta^{++}}$ vertex

$$\cos\theta_2 = \frac{(K^{*-} \times \pi^-)(p_{inc} \times \Delta^{++})}{|K^{*-} \times \pi^-|\ |p_{inc} \times \Delta^{++}|}$$

where the three momenta K^{*-}, π^-, etc. are now evaluated in the K^- incident rest frame.

In the 10 GeV/c data (Fig. 13), at least θ_1 does not have a flat distribution; this suggests that a vector exchange mechanism is involved at the upper vertex of Fig. 11. No definite conclusions, on the other hand, can be drawn from the corresponding distributions at 6 GeV/c (not shown here).

Furthermore, the decay angular correlations of K^* and Δ^{++} are investigated, following the formalism developed in section 2.2. Two orthogonal coordinate systems x,y,z and x', y', z', suitable for peripheral collisions, are used for each resonance. In both systems the direction of the incident particle is naturally chosen as z (or z') axis. The y-axis is conventionally defined as the normal to the production plane, while an alternative choice y' is also considered in the hope of exhibiting a stronger resonance alignment. Explicitly:

<u>For the K^{*-} decay</u>

$$z = K^-_{inc} \qquad y = K^-_{inc} \times p_{inc}$$

$$z' = K^-_{inc} \qquad y' = (p_{inc} - \Delta^{++}) \times \pi^-$$

All momenta K^{*-}, Δ^{++}, etc. are evaluated in the K^{*-} rest frame

<u>For the Δ^{++} decay</u>

$$z = p_{inc} \qquad y = p_{inc} \times K^-_{inc}$$

$$z' = p_{inc} \qquad y' = (K^-_{inc} - K^{*-}) \times \pi^-$$

where the momenta are now evaluated in the Δ^{++} rest frame.

Figures 14-15 show now the polar θ (by definition, the same in both frames) and azimuthal ϕ (xyz frame) or ϕ' (x'y'z' frame) angular distributions of the decaying particles ($\overline{K}^{o}$ and p for K^{*} and Δ^{++}, respectively). The azimuthal dependence characteristic of reactions dominated by vector exchange is clear in both the 6 and 10 GeV/c data; the $\cos\theta$ distribution, however, deviates from the behaviour expected by this type of exchange.(See relations 2.6 and 2.7 in connection with 2.14 for the Δ^{++}, and 2.11 for K^{*}.)

In a more sensitive investigation, a maximum likelihood fit is performed to calculate the density matrix elements of the decaying resonances. If, say, we have n events in which the decay angles θ_ν and ϕ_ν are measured, and denote with x_1, x_2 and x_3 the matrix elements occuring, the likelihood function is defined in the usual way as

$$\mathcal{L}(x_1, x_2, x_3) = \prod_{\nu=1}^{n} W(\cos\theta_\nu, \phi_\nu ; x_1, x_2, x_3)$$

where W is the distribution function given by formulas 2.1 (for K^{*-}) and 2.5 (for Δ^{++}). The set (x_1, x_2, x_3) of the parameters, which gives the maximum value of $\mathcal{L}$, is the best estimate for the matrix elements. To carry out the necessary computations, program MINUIT is again used.

Table 2 presents the fitted values of the density matrix elements for each resonance; it may be seen that the choice of coordinate system (x, y, z) or (x', y', z'), in which the decay angles are measured, makes no significant difference to the results. The decay distributions, corresponding to the values of the matrix elements obtained in the fit, are the curves superimposed on the experimental data of Figs. 14-15.

When compared with the density matrix elements predicted for various exchanges by the one meson exchange theory (section 2.2), our results allow several conclusions to be drawn; we refer here to both the 6 and 10 GeV/c data, as the differences observed in the fitted values do not justify (within statistics) a separate treatment at the two energies.

At the $K^- - K^*$ vertex, dominance by π exchange predicts $\rho_{11} = 0$, and therefore seems to be ruled out. It also appears that we cannot account for the data completely by assuming the exchange of a single particle of natural spin parity (then $\rho_{00} = 0$ and $\mathrm{Re}\ \rho_{10} = 0$). So we require either the exchange of a single trajectory of unnatural spin-parity with $J \neq 0$, or the exchange of a mixture of trajectories.

At the $p - \Delta^{++}$ vertex, by I-spin considerations we require the exchange of an $I \geq 1$ trajectory, so the principal candidates are the ρ and the π. The data are perhaps consistent qualitatively with ρ exchange, but a significant contribution of π exchange cannot be ruled out.

Since G parity has to be conserved at the middle vertex, ρ exchange at the lower vertex requires $G = -1$ exchange to the K^{*-}. A π dominance (which has G- parity -1) at this vertex has been ruled out; this leaves us with ω, ϕ, A_1 or A_2 trajectories possibly exchanged at the $K - K^*$ vertex.

It is worth noticing that a similar study of the reaction $K^- p \to \Delta^{++} K^{*} \pi^-$ at 4.25 GeV/c[9] has also concluded a ω, ρ^+ exchange dominance to the K^{*-} and Δ^{++} vertices, respectively.

3. TWO MODELS FOR HIGH ENERGY PROCESSES AND THEIR APPLICATION TO THE REACTION $K^- p \to \Delta^{++} K^{*-} \pi^-$

3.1 The Veneziano Model

(a) Formulation of the Model

The creation of Veneziano model was perhaps one of the most fruitful developments in high energy theory in recent years.[10] Originated from the relatively simple closed form (Euler's beta function, in fact!) Veneziano wrote down[11] for the invariant amplitude of the process $\pi\pi \to \pi\omega$, the model has quickly been generalized to the cases of five[12] or more[13] external particles. With the interest due to the remarkable properties the Veneziano amplitude possesses, applications and modifications appeared in every conceivable direction.

We limit ourselves to the problem of five external particles (Fig. 16a) and the generalized beta function (often called B_5) corresponding to the case. The amplitude for a five particle process is in general a function of five independent kinematic variables; within the framework of the Veneziano model these are chosen as the squared subenergies $s_{i,i+1}$ between the adjacent particles, i.e.

$$s_{12} = (p_1 + p_2)^2 = (p_3 + p_4 + p_5)^2$$

$$s_{23} = (p_2 + p_3)^2 = (p_4 + p_5 + p_1)^2 \text{ , etc.}$$

One writes then the reaction amplitude as a five-point function B_5 multiplied by a kinematical factor K (which depends on the external momenta) and a normalization constant β ; the whole expression is summed over all 12 non-cyclic permutations of the external particles

$$T = \sum_{\text{perm}}^{12} \beta K B_5 .$$

The five point function, expressed in a way which displays its cyclic symmetry, is

$$B_5(-\alpha_{12},-\alpha_{23},-\alpha_{34},-\alpha_{45},-\alpha_{51}) = \int_0^1\int_0^1 \frac{du_i du_j}{1-u_i u_j} \; u_1^{-\alpha_{12}} \; u_2^{-\alpha_{23}} \; u_3^{-\alpha_{34}} \; u_4^{-\alpha_{45}} \; u_5^{-\alpha_{51}}$$

where $\alpha_{k\ell}$ are linear Regge trajectories

$$\alpha_{k\ell} = \alpha_o + \alpha' s_{k\ell}$$

the u_i are auxiliary variables not all independent but restricted by the algebraic conditions

$$u_i = 1-u_{i-1} \; u_{i+1}, \; i = 1,\ldots,5 \; ; \quad u_6 = u_1$$

and i and j are two non-successive integers between one and five, which label the particles.

The generalized beta function is thus a multiple integral with as many variables as there are allowed simultaneous poles (two for the five-particle amplitude); the integrand consists of a product of factors, each of which varies from zero to one over the range of integration and is raised to the power $-\alpha_{i,i+1}$ (there being as many factors as there are independent subenergies).

These functions are shown[14] to possess several properties, which due to theoretical or experimental arguments, are believed to be present in strong interations:

(i) Analyticity.

(ii) Cyclic and reflective symmetry; by adding 12 non-cyclic permutations, one obtains a fully crossing symmetric amplitude.

(iii) Simple poles (resonances) for positive integer values of α_{ij}, and double poles in channels without a common index (e.g. α_{12} and α_{45}, which would correspond to the Feynman diagram of Fig. 16b).

(iv) Regge asymptotic behaviour when one or two subenergies become large; from this it follows that duality between direct channel resonances and Regge poles also holds.

Though these properties underline the theoretical beauty of Veneziano model, there are some serious drawbacks which need perhaps to be mentioned. The B_5 function is at first inconsistent with unitarity, i.e. it has poles only on the real axis. For phenomenological purposes, one may simulate the effects of unitarity by artificially introducing an imaginary part to the trajectory function; this also serves in giving a finite width to the resonance poles.

A further weakness of the model is that it can be applied only with linear rising trajectories. This means that it is incapable of describing processes where vacuum exchanges occur, i.e. the pomeron contributes. Several attempts have been made[15] to overcome this serious limitation.

Finally, the fact that the model does not take into account the spin of the external particles further restricts its range of applications. With bosons it is often possible to allow for spin by introducing a suitable kinematic factor, but there is no way at present of allowing for the spin of fermions. It is thus usual to treat the particles as spinless, assuming that this would represent sufficiently well the sum over the spins.

(b) Application to the Reaction $K^- p \to \Delta^{++} K^{*-} \pi^-$

The Veneziano model, as generalized to the case of a five particle amplitude, has been applied with considerable success to several three body final states.[16] It is in view of this success that we proceed to study with it the reaction $K^- p \to \Delta^{++} K^{*-} \pi^-$; this particular process does not show resonance structure in the effective mass distribution for any pair of final particles, therefore our calculation is more a test of the double Regge exchange behaviour of the model rather than of resonance production.

It is an impressive experimental fact that states the quantum numbers of which cannot be associated with a three-quark system when a baryon or a quark-antiquark system when a meson do not occur in high energy collisions; these are the so called "exotic" states (resonances with isospin or strangeness 2, for example). From the 12 non-cyclic permutations of the particles possible in the reaction $K^- p \to \Delta^{++} K^{*-} \pi^-$, only two are free from exotic channels and are therefore considered. They are shown in Fig. 17, along with the double or single Regge pole exchange graphs to which the Veneziano five point functions go over in the high energy limit; the figure also indicates the contributions of the two five-point functions to the Regge-pole limits.

Let us now consider the trajectories which are possibly exchanged in graphs I and II of Fig. 17. The reaction is seen to be dominated to a large extent by double vector meson exchange (ω exchange at the $K^- - K^*$ vertex and ρ exchange at the $p - \Delta^{++}$ vertex); this fact, along with the conservation of quantum numbers, implies a unique choice of the trajectory between most of the two-particle channels. Uncertainties arise only between (K^-_{in}, p_{in}) and (Δ^{++}, π^-); in its present form the model allows only one trajectory to be exchanged in

each channel, so for the first pair the Y_o^* trajectory is chosen, which is shown to couple much stronger to the $\bar{K}N$ system than the also allowed Y_1^* ;[17] for the second pair, the exchange of N-trajectory (Δ is also possible) was found a posteriori to give a slightly better description of the data.

Thus, the dominant trajectories indicated in Fig. 17 have finally been considered. These trajectories have in general the form

$$\alpha = \alpha(0) + \alpha' s + i \ \text{Ima}$$

where $\alpha(0)$ and α' are the intercept and the slope, respectively.

The imaginary part is introduced to give a finite width to the resonances which appear in the physical region; its parametrization is arbitrary. We have used

$$\text{Ima} = A\,(s - s_0)$$

with A a constant and $s_0 = (m_1 + m_2)^2$, m_1, m_2 being the masses of the resonant particles.

The trajectories considered in this work are then

$$\alpha_{Y_o^*} = -0.62 + 0.9s + i\ 0.13\,(s - s_0)$$

$$\alpha_{Y_1^*} = -0.22 + 0.9s + i\ 0.13\,(s - s_0)$$

$$\alpha_\omega = \alpha_\rho = 0.48 + 0.95\,s$$

$$\alpha_{K^*} = 0.35 + 0.82\,s + i\ 0.095\,(s - s_0)$$

$$\alpha_N = -0.37 + s + i\,0.14\,(s - s_0)$$

$$\alpha_\Delta = 0.13 + 0.9\,s + i\,0.3\,(s - s_0)\ .$$

As determined by the exchanged trajectories, the explicit representation of the B_5 functions corresponding to graphs I and II (Fig. 17) is

$$B_5(I) = B_5\left(\frac{1}{2} - \alpha_{Y_0^*},\ 1 - \alpha_\omega,\ \frac{3}{2} - \alpha_{Y_1^*},\ \frac{1}{2} - \alpha_N,\ \frac{3}{2} - \alpha_\Delta\right)$$

$$B_5(II) = B_5\left(1 - \alpha_{K^*},\ 1 - \alpha_\omega,\ \frac{3}{2} - \alpha_{Y_1^*},\ 1 - \alpha_\rho,\ \frac{3}{2} - \alpha_\Delta\right).$$

The amplitude for the reaction is written as a linear combination of these functions, namely

$$T = \beta\, K\, (B_5(I) + B_5(II))$$

where β is an overall normalization constant and K a kinematic factor.

In analogy with Ref. (12), K is assumed to have the form

$$K = \varepsilon_{\alpha\beta\gamma\delta}\ P_\alpha^{\,1}\ P_\beta^{\,2}\ P_\gamma^{\,3}\ P_\delta^{\,4}$$

where $P_\alpha^{\,1}\ P_\beta^{\,2}\ldots$ are four independent four momenta of the five "particles" considered.

The amplitude thus formulated has been used to calculate (at 6 and 10 GeV/c incoming momentum) the model predictions for the reaction $K^- p \to \Delta^{++} K^{*-} \pi^-$; note that after choosing the trajectories

we are left with only one free parameter (namely the overall normalization) for all incoming energies. The actual calculations are performed with FOWL, and one is faced with the difficult computational task of integrating (over different regions of phase space) the five point function, a complex function of five complex arguments ; a program to achieve this has been written by Hopkinson[18] on the basis of a series expansion of the B_5.[19]

The model predictions are the solid lines superimposed on the experimental results already presented for the reaction in Figs. 5-8 (mass spectra, P_L^*, P_T and $|t|$ distributions) and Fig. 10 (Van Hove angle). The agreement with the data is in most cases remarkably good, considering the small amount of freedom in the model and the various assumptions made when applying it. Only the effective mass distributions at 10 GeV/c are rather poorly described, due perhaps to the $(\Delta^{++}\pi^-)$ low mass enhancement present in the data and the serious contamination by background events; less satisfactory is also the description of the four momentum transfer distribution of Δ^{++} at this energy.

Furthermore, the model predictions for the variation of the total $K^-p \to \Delta^{++} K^{*-}\pi^-$ cross-section with the momentum of the incident kaon (in the laboratory system) were calculated. If these predictions are normalized to the experimental value of the cross-section at 6 GeV/c, the curve shown in Fig. 18 is obtained. The curve has the shape expected for a three body reaction; however, the experimental point at 10 GeV/c lies higher than the value predicted by the model. Unfortunately no reliable information exists at present for the cross-sections of the reaction at other energies.

It is appropriate to mention here that a Veneziano model study of the reaction $K^- p \to \Delta^{++} K^{*-} \pi^-$ has also been performed at 4.25 GeV/c incoming momentum.[20] The same amplitude was essentially used, but now the description of the data is less satisfactory (full lines in Fig. 19). Some additional remarks may be of interest:

(i) The omition of the kinematic factor (broken lines in Fig. 19bcd) disturbs the right behaviour of the amplitude at low effective masses.

(ii) The choice of the Ima Y_1^* (which was identical to ours) for the Y_1^* trajectory gives rather large Y_1^* widths, so an alternative choice which would give much smaller widths was considered. Only the $(K^{*-} \Delta^{++})$ mass distribution is then practically effected, and an unwanted structure has now been produced (Fig. 19c, dash-dot line).

(iii) The choice of the Δ- trajectory in the $(\Delta^{++}\pi^-)$ channel results in a much worse description of the $(\Delta^{++}\pi^-)$ mass distribution (Fig. 19d, dash-dot line) than the N-trajectory originally used.

3.2 The CLA Multiperipheral Model

(a) The formulation of the Model

Though the Veneziano model possesses many desirable properties, there are the difficulties mentioned in adopting it to realistic cases. There do exist however earlier models, which may be regarded as approximating the picture so far emerging in hadron physics. Amongst them the so called CLA model,[21] simple though it was, gave good results in an extensive range of applications.[22]

The model attempts to describe a given high-energy reaction by folding together all the contributing multiperipheral channels. It

retains the Regge behaviour whenever any energy or effective mass is large, but instead of being dominated by resonances at the low effective mass region, is smoothed over by an effective constant. However, when arranged over many degrees of freedom, as in plotting single particle distributions, this phase space approximation may not be too bad.

The full form of the CLA amplitude for each permutation of the diagram shown in Fig. 3c reads

$$|T| \sim \prod_{i=1}^{n-1} \left(\frac{g_i s_i + a}{s_i + a}\right) \left(\frac{s_i + a}{a}\right)^{\alpha_i} \left(\frac{s_i + b_i}{b_i}\right)^{t_i}$$

s_i is the subenergy of the i^{th} exchanged defined with

$$s_i = (p_i + p_{i+1})^2 - (m_1 + m_{i+1})^2 .$$

t_i is the squared four momentum transferred across the i^{th} exchange, i.e.

$$t_i = (p_A - \sum_{i=1}^{i} p)^2 .$$

a is the approximate subenergy cut-off for the Regge behaviour of the amplitude.

g_i is the strength of the Regge coupling at vertices.

α_i is the intercept at the exchanged Regge trajectory on the angular momentum axis.

b_i is a parameter describing the dependence of the amplitude on the four-momentum transfer t_i .

c finally, is the phase-space constant for the small subenergy region.

In the region of phase space where all s_i are $>> \alpha$ and b_i, the amplitude becomes

$$\prod_i g_i \left(\frac{s_i}{a}\right)^{\alpha_i} \exp\left[B_i + \log s_i\right] t_i$$

$$\text{with } B_i = -\log b_i$$

which is of the multi-Regge form. For $s_i \to 0$, instead, the i^{th} term in the product becomes a constant c. The high and low mass regions are then interpolated in a simple-minded manner.

Further simplifications--such as the neglect of the particles charge--reduce the n particle amplitude to only three or four parameters, which have been used to correlate a wide range of experimental data. An interesting modification of the model[23] permits the inclusion of resonances in the sub-systems in a dual manner.

(b) The Description of the $K^- p \to \Delta^{++} K^{*-} \pi^-$ Reaction

The absence of any resonant combination in this final state allows in principle the application of the CLA model, while the treatment of the Δ^{++} and K^{*-} resonances as particles is justified by their relatively small width.

From the six peripheral diagrams obtained by considering all permutations of the outgoing particles, only the three shown in Fig. 20 remain when the requirements of quantum numbers conservation at each vertex are taken into account; the allowed exchange trajectories are also indicated in the figure. Apart from the meson (M) trajectory (of positive or negative G-parity) and the trajectory corresponding to $K^*(890)$, which were considered in the original work of Chan, et al.,

the Δ-trajectory needs also to be included in this case. The values of α (intercept) and g (coupling constant) used for thewe trajectories are summarized in Table 3.

Some of the parameters entering the CLA amplitude are fixed at the values suggested in Ref. 21, i.e. $a = 1\ GeV^2$, $c = 1.4$ and $b_{internal} = 1.2\ GeV^{-2}$. For the remaining two parameters the values $b_{upper\ vertex} = 3\ GeV^{-2}$ and $b_{lower\ vertex} = 2\ GeV^{-2}$ are used, which achieve a more satisfactory description of the peripheral characteristics of our reaction than the originally suggested. In view of the crudity of the model the parameter values are not, however, to be taken too seriously.

To each of the diagrams of Fig. 20 corresponds now an amplitude (of the form given above) properly parametrized. By adding them incoherently we obtain the overall amplitude for the reaction

$$|W|^2 = |W_1|^2 + |W_2|^2 + |W_3|^2 \quad .$$

The CLA amplitude predicts the distributions superimposed (dashed lines) on the experimental results of the reaction $K^- p \to \Delta^{++} K^{*-} \pi^-$ at 10 GeV/c (Figs. 7, 8 and 10). With the exception of the $(\Delta^{++}\pi^-)$ effective mass distribution, the gross features of the data are satisfactorily reproduced. In almost all cases, however, notably better is the description of the data achieved by the Veneziano model.

If the relative contribution to the amplitude of the individual exchange diagrams is calculated, it is of interest that the contribution of the diagram which involves Δ^{++} exchange is found to be negligible and could have been omitted.

REFERENCES AND FOOTNOTES

1. Chan Hong-Mo, 14th International Conference on High Energy Physics, Vienna, 1968, p. 341.

   O. Gzyzewski, ibid, p. 367.

2. For a justification of it see, G. Yost, Ph.D. Thesis, University of Maryland, p. 154.

3. N. Schmitz, CERN 65-24, Vol. I.

4. K. Gottfried and J. D. Jackson, N.C. 33 (1964) 309.

5. L. Stodolsky and J. J. Sakurai, PRL 11 (1963) 90

6. See, for instance, K. Boesebeck, et. al., N.P. B33 (1971) 445.

7. L. Van Hove, P.L. 28B (1969) 429
   and N.P. B9 (1969) 331.

8. Known as triangular t-plot and suggested by H. Muirhead. A similar plot has been used by W. Beusch, et. al., P.L. 28B (1968) 211.

8a. S.B. Treiman and C.N. Yang P.R.L. 8 (1962) 140.

9. Yost, et. al., paper submitted to the Vienna Conference (1968).

10. An excellent review on the models for high energy processes is given by J. D. Jackson in Reviews of Modern Physics, Jan. 1970.

11. G. Veneziano, N.C. 57A (1968) 190.

12. K. Bardakci and H. Ruegg, P.L. 28B (1967) 242.

13. For example:
   Chan Hong-Mo, P.L. 28B (1969) 425
   J. L. Hopkinson and E. Phante, P.L. 28B (1969) 489.
   Z. Koba and H. B. Nielsen, N. P. B10 (1969) 633.

14. For an extensive discussion see:
   M. Jacob, "Duality in strong interaction physics" TH-1010 CERN.
   Chan Hong-Mo, "Multiparticle phenomenology" TH-1089 CERN.

15. S. Pokorski and H. Satz, N.P. B19 (1970) 351.
   J. Bartsch, et al., N. P. B24 (1970) 221.

16. See, for instance the pioneering work on the $\bar{K}p \to \bar{\tau}\pi^{+}\Lambda$,
   B. Peterson and N. A. Tornquist, N.P. B13 (1969) 629
   Also,
   Chan Hong-Mo, et al., N. P. B19 (1970) 173.
   J. Bartsch, et al., N. P. B20 (1970) 63.

17. C. Schmid, Nuovo Cimento Letters 1 (1969).

18. J. F. L. Hopkinson, Daresbury Preprint, DNPL/P21 (1969).

19. J. F. L. Hopkinson and E. Plahte, P.L. 28B (1969) 489.

20. R. Baier, et al., N. P. B27 (1971) 372.

21. Chan Hong-Mo, J. Loskiewicz and W. W. M. Allison, N.C. 57A (1968) 93.

22. Aachen-Berlin-Bonn-CERN-Cracow-Heidelberg-Warsaw collaboration N.P. B13 (1969) 571

C. Caso, et al. N. C. 66A (1970) 11

J. Bartsh, et al. N. P. B11 (1969) 373

G. Ranft and R. Turnbull N. C. 61B (1969) 317

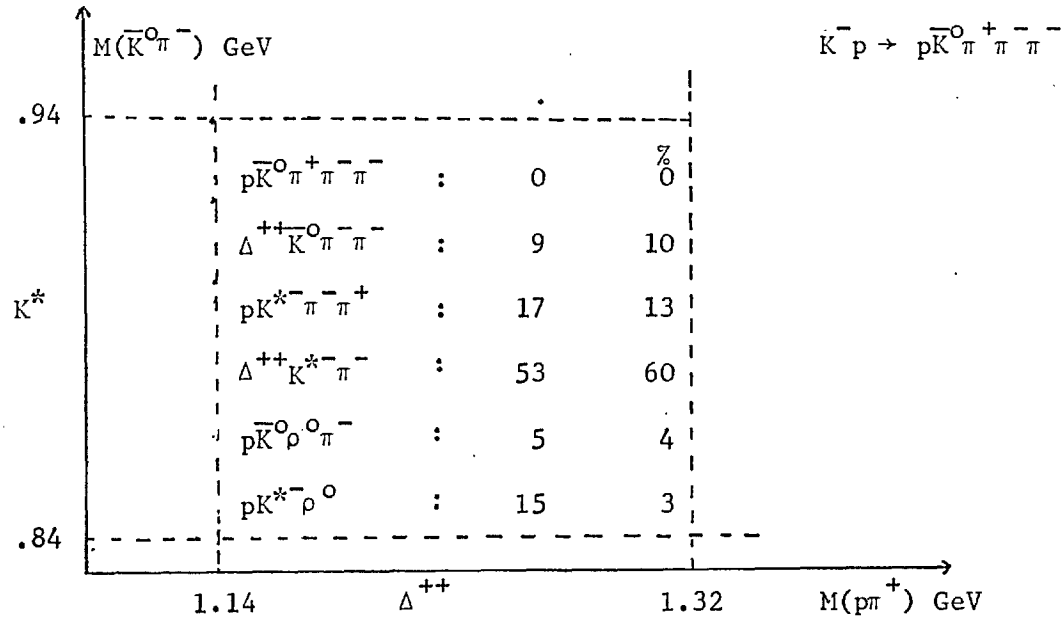
G. W. Brandenburg, et al. N.P. B22 (1970) 157.

23. E. Phante and R. G. Roberts, Lett. al N.C. 1 (1969) 187.

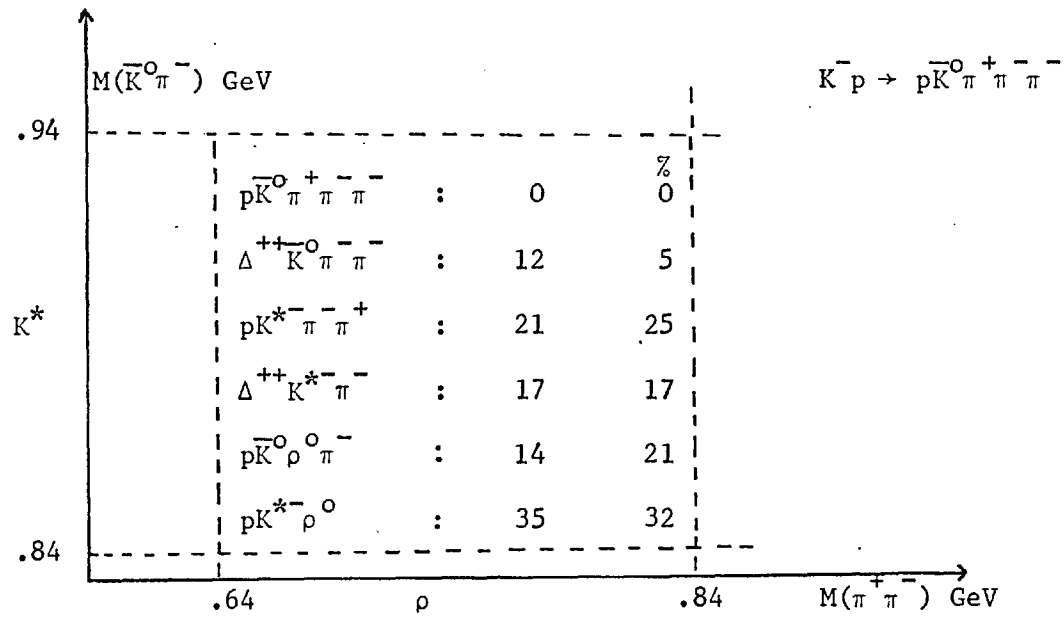
TABLE VI - 1

PERCENTAGE CONTRIBUTION OF EVENTS TO THE QUASI-THREE BODY CHANNELS

(The first column refers to the 6 and the second to the 10 GeV/c data)



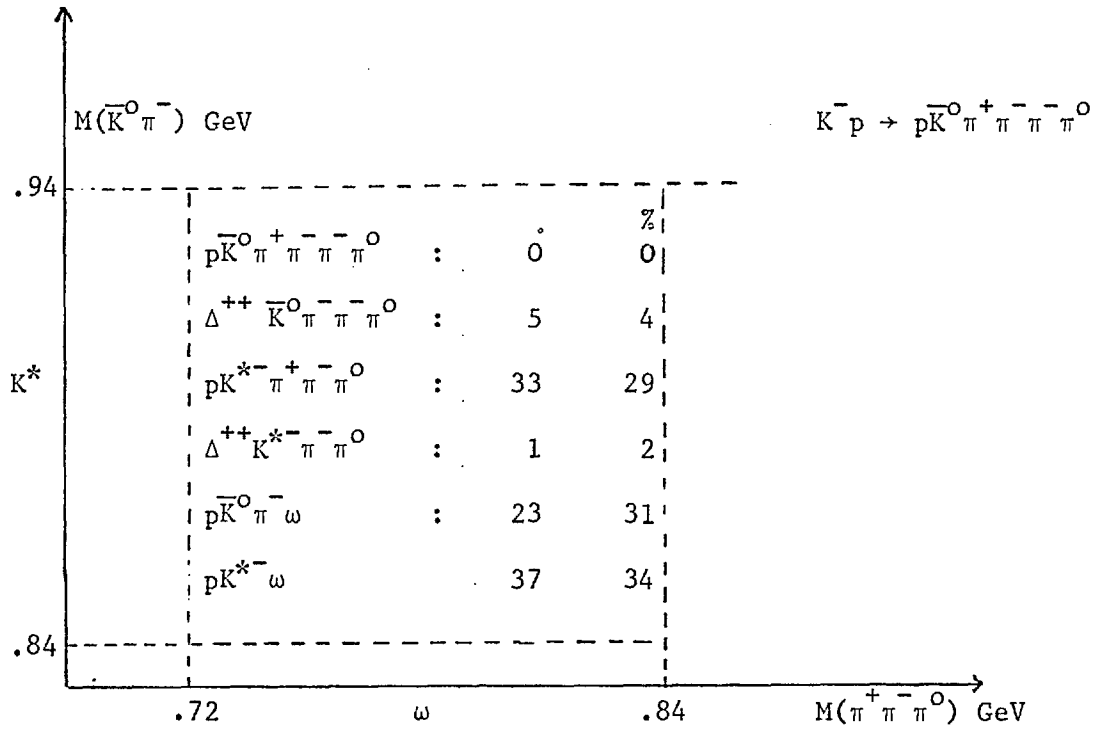
		%
$p\bar{K}^0\pi^+\pi^-\pi^-$	0	0
$\Delta^{++}\bar{K}^0\pi^-\pi^-$	9	10
$pK^{*-}\pi^-\pi^+$	17	13
$\Delta^{++}K^{*-}\pi^-$	53	60
$p\bar{K}^0\rho^0\pi^-$	5	4
$pK^{*-}\rho^0$	15	3



		%
$p\bar{K}^0\pi^+\pi^-\pi^-$	0	0
$\Delta^{++}\bar{K}^0\pi^-\pi^-$	12	5
$pK^{*-}\pi^-\pi^+$	21	25
$\Delta^{++}K^{*-}\pi^-$	17	17
$p\bar{K}^0\rho^0\pi^-$	14	21
$pK^{*-}\rho^0$	35	32

(continued)

TABLE VI - 1 (continued)



		%
$p\bar{K}^0\pi^+\pi^-\pi^-\pi^0$	0	0
$\Delta^{++}\bar{K}^0\pi^-\pi^-\pi^0$	5	4
$pK^{*-}\pi^+\pi^-\pi^0$	33	29
$\Delta^{++}K^{*-}\pi^-\pi^0$	1	2
$p\bar{K}^0\pi^-\omega$	23	31
$pK^{*-}\omega$	37	34

TABLE VI - 2

DENSITY MATRIX ELEMENTS OF THE RESONANCES

IN THE $K^- p \to \Delta^{++} K^{*-} \pi^-$ CHANNEL

		6 GeV/c		10 GeV/c	
		x, y, z	x', y', z'	x, y, z	x', y', z'
K^{*-}	ρ_{00}	0.33±0.07	0.34±0.07	0.33±0.10	0.33±0.10
	ρ_{1-1}	0.17±0.07	0.13±0.06	0.11±0.03	0.16±0.05
	$Re\rho_{10}$	0.01±0.02	-0.01±0.02	0.01±0.02	-0.01±0.03
Δ^{++}	ρ_{33}	0.31±0.05	0.33±0.05	0.19±0.10	0.17±0.10
	$Re\rho_{3-1}$	0.13±0.05	0.21±0.05	0.19±0.04	0.10±0.04
	$Re\rho_{31}$	0.05±0.05	-0.01±0.05	0.03±0.04	-0.05±0.04

TABLE VI - 3

EXCHANGE TRAJECTORIES USED IN THE CLA APPLICATION

Trajectory	Strangeness	Baryon number	Charge	G-parity	α-intercept of trajectory	g-relative coupling constant
meson	0	0	1, -1	+1	1.0	1.0
	0	0	0, -1, 1	-1	0.5	1.0
K^*	1,-1	0	0, -1, 1	-1	0.3	1.0
Δ	0	1	+2,+1,0,-1		.15	.1

Fig. VI-1

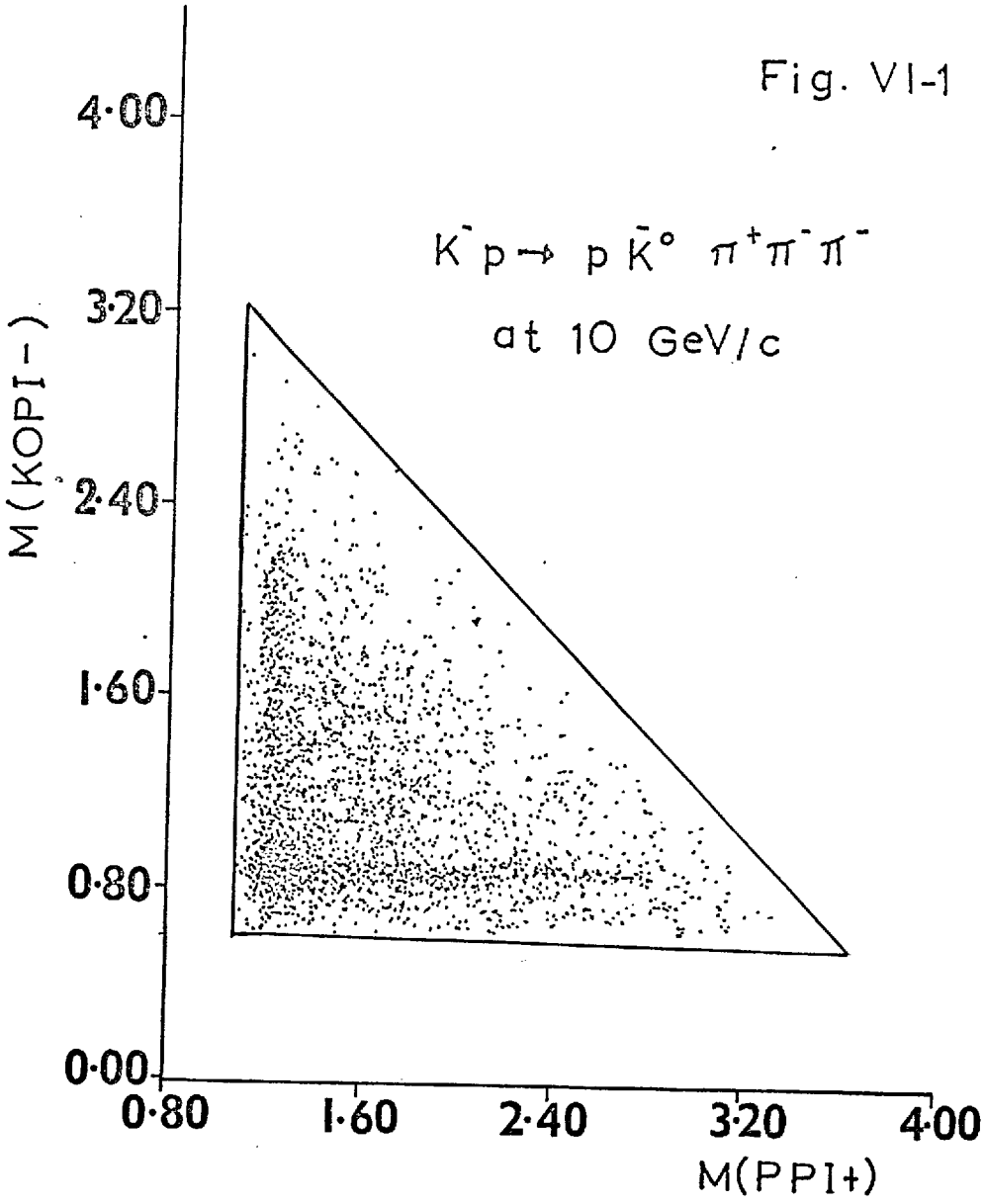
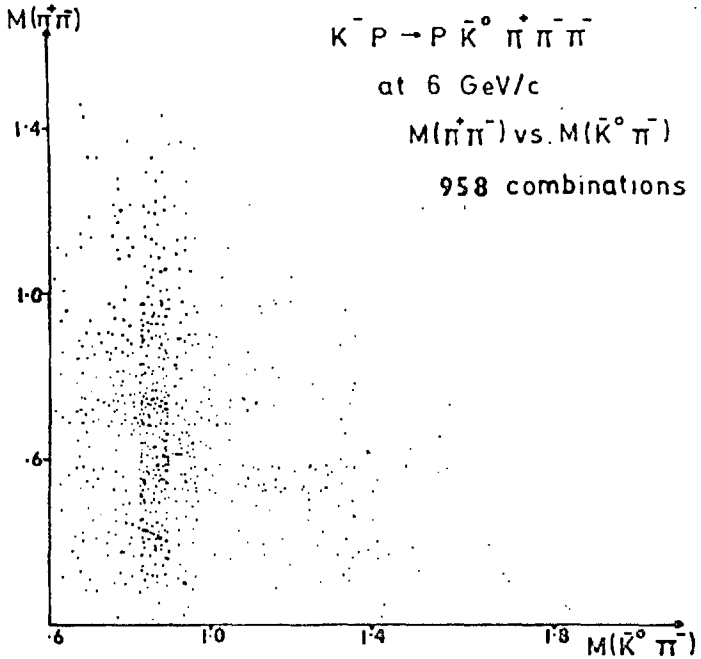

$K^- p \to p \bar{K}^0 \pi^+ \pi^- \pi^-$
at 10 GeV/c
M(KOPI-)
4·00
3·20
2·40
1·60
0·80
0·00
0·80
1·60
2·40
3·20
4·00
M(PPI+)

Fig. VI-2

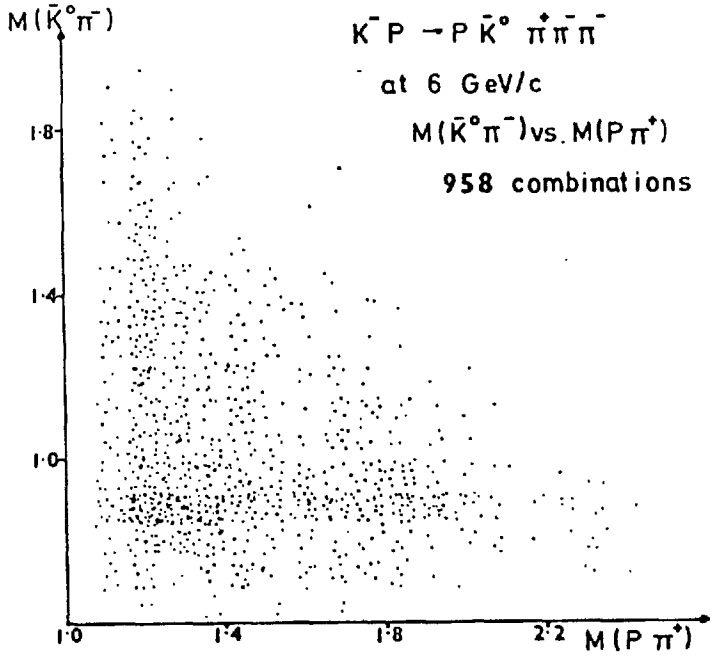


$K^- P \to P \bar{K}^0 \pi^+ \pi^- \pi^-$

at 6 GeV/c

$M(\pi^+\pi^-)$ vs. $M(\bar{K}^0\pi^-)$

958 combinations

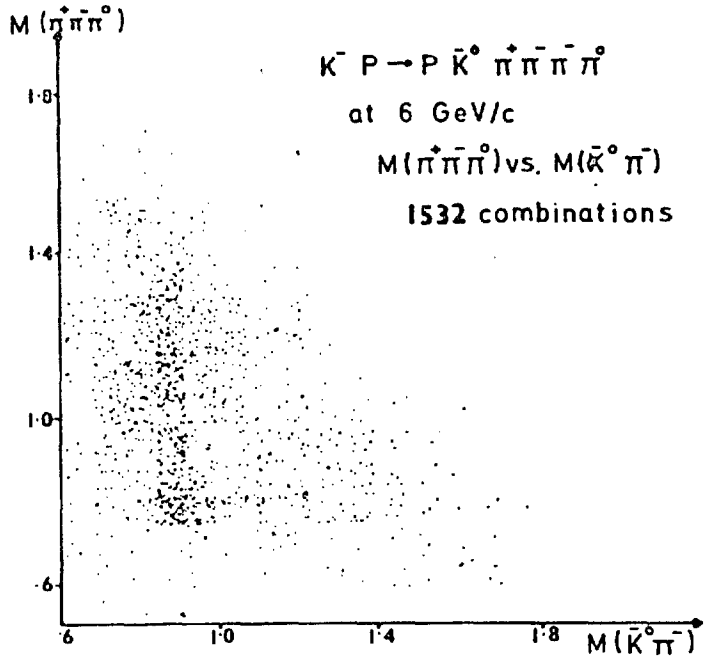


$K^- P \to P \bar{K}^0 \pi^+ \pi^- \pi^-$

at 6 GeV/c

$M(\bar{K}^0\pi^-)$ vs. $M(P\pi^+)$

958 combinations



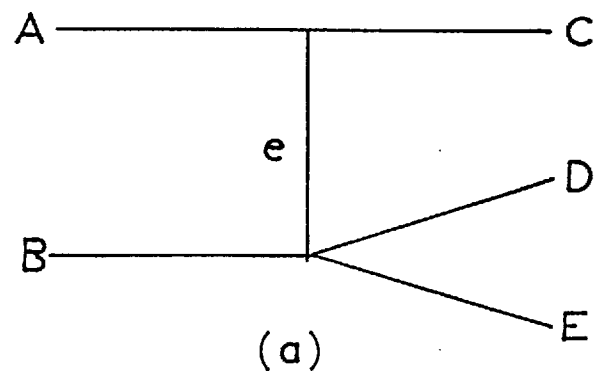
$K^- P \to P \bar{K}^0 \pi^+ \pi^- \pi^- \pi^0$

at 6 GeV/c

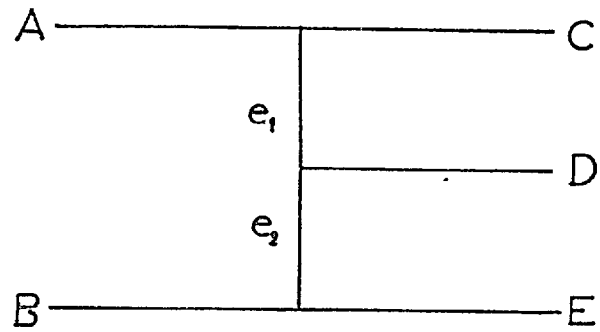
$M(\pi^+\pi^-\pi^0)$ vs. $M(\bar{K}^0\pi^-)$

1532 combinations

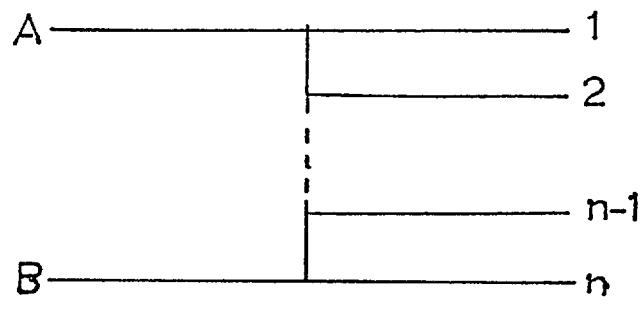
Fig. VI-3



(a)

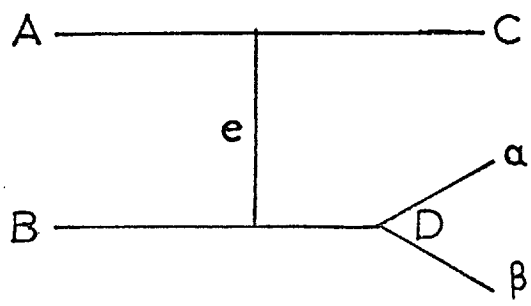


(b)

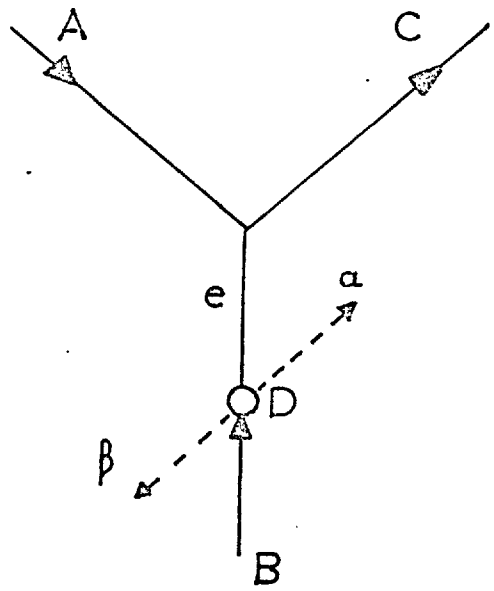


(c)

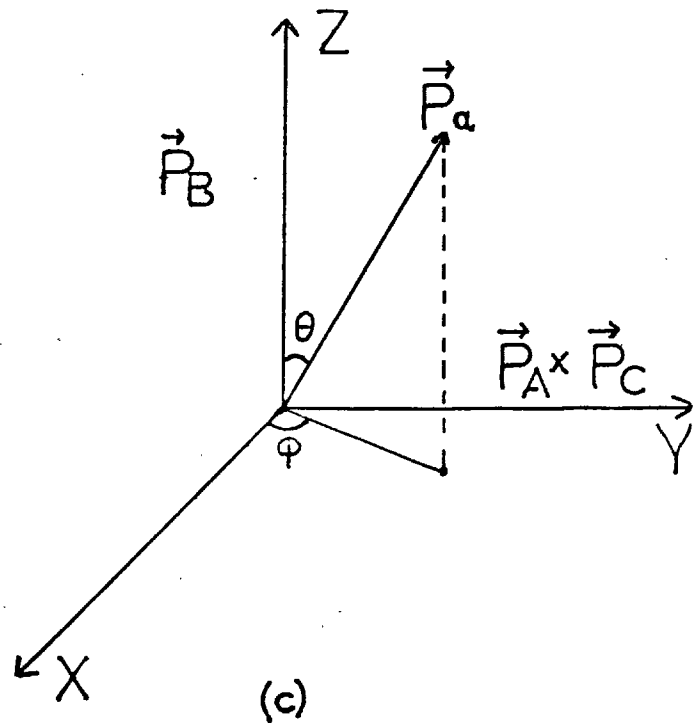
Fig. VI-4



(a)



(b)



(c)

Fig. VI-5

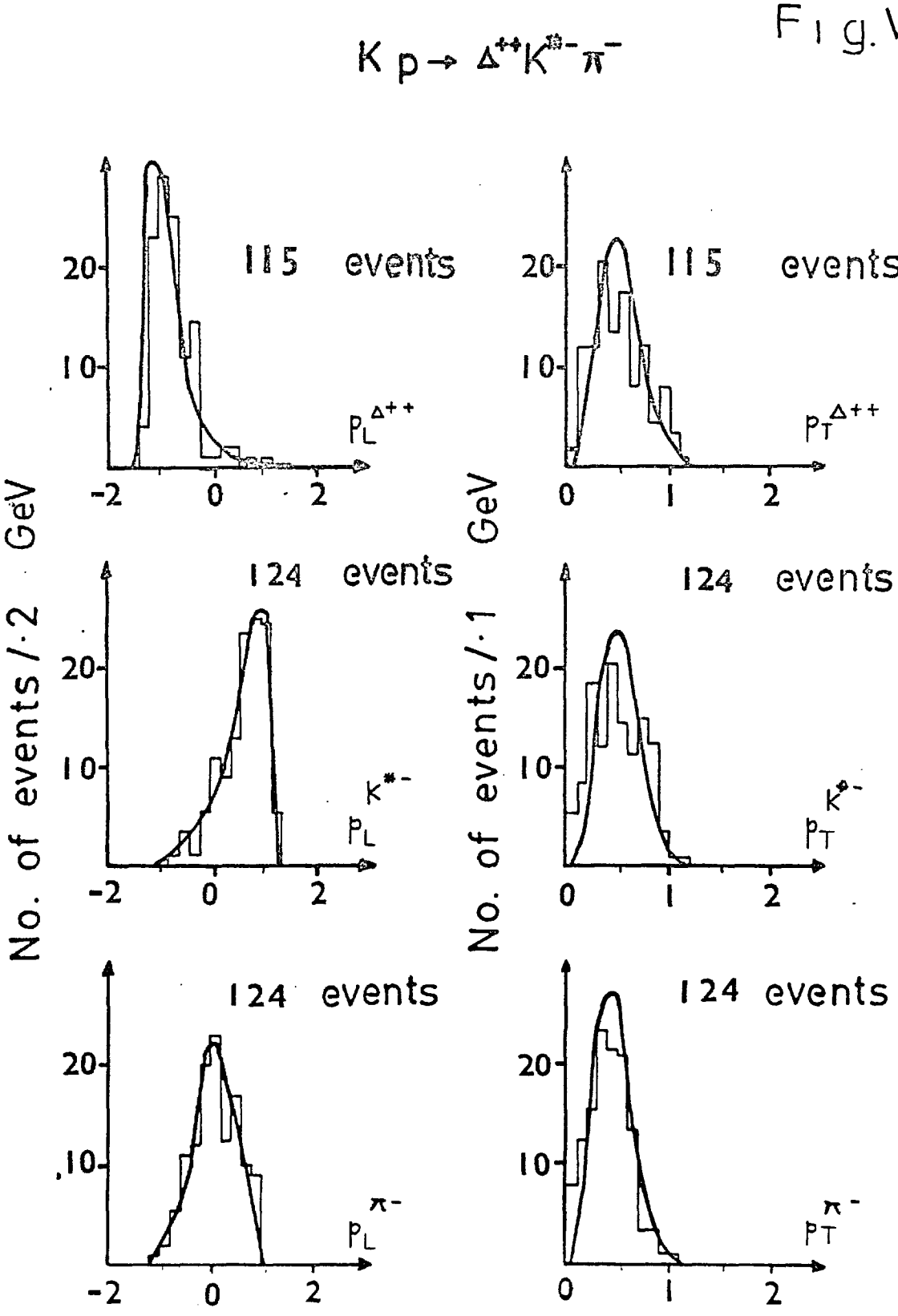
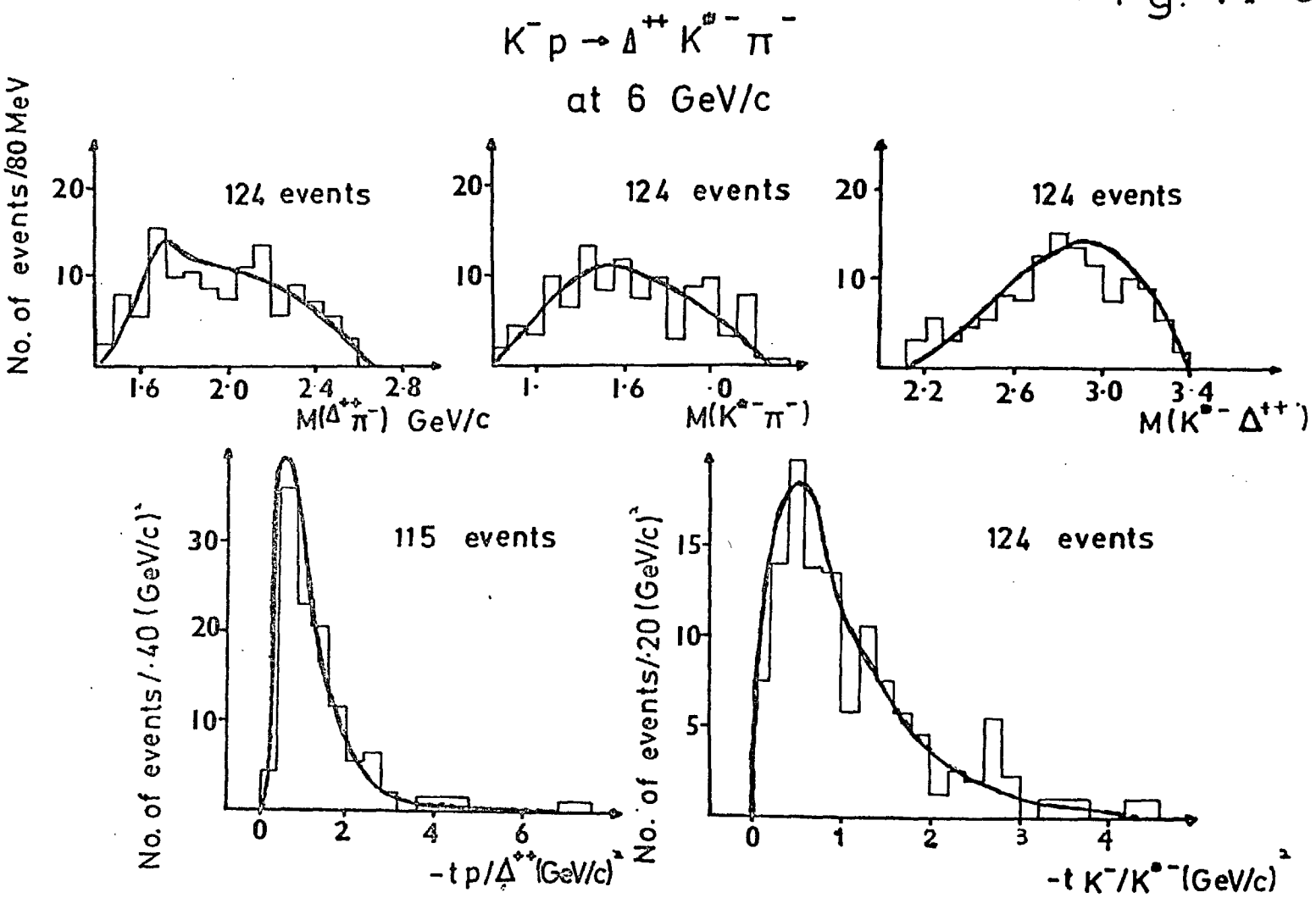

$K^- p \to \Delta^{++} K^{*-} \pi^-$
115 events
$P_L^{\Delta^{++}}$
$P_T^{\Delta^{++}}$
GeV
124 events
K^{*-}
P_L
P_T
No. of events / ·2
No. of events / ·1
π^-

Fig. VI-6


$K^- p \to \Delta^{++} K^{*-} \pi^-$
at 6 GeV/c
No. of events/80 MeV
124 events
$M(\Delta^{++}\pi^-)$ GeV/c
124 events
$M(K^{*-}\pi^-)$
124 events
$M(K^{*-}\Delta^{++})$
No. of events/·40 (GeV/c)²
115 events
$-t\, p/\Delta^{++}$ (GeV/c)²
No. of events/·20 (GeV/c)²
124 events
$-t\, K^-/K^{*-}$ (GeV/c)²

a. 10 GeV/c

Fig. VI-7

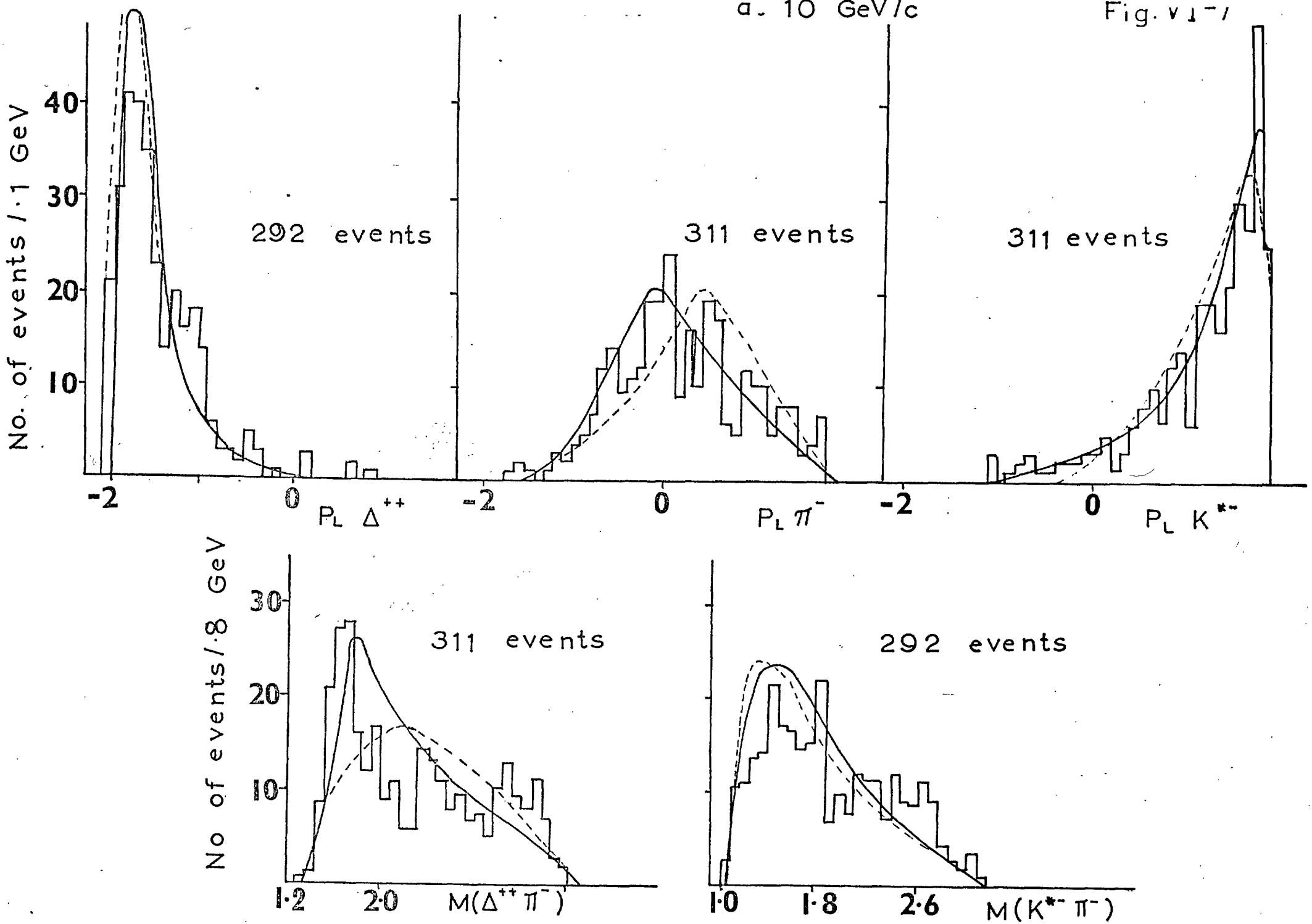


Fig. VI-8

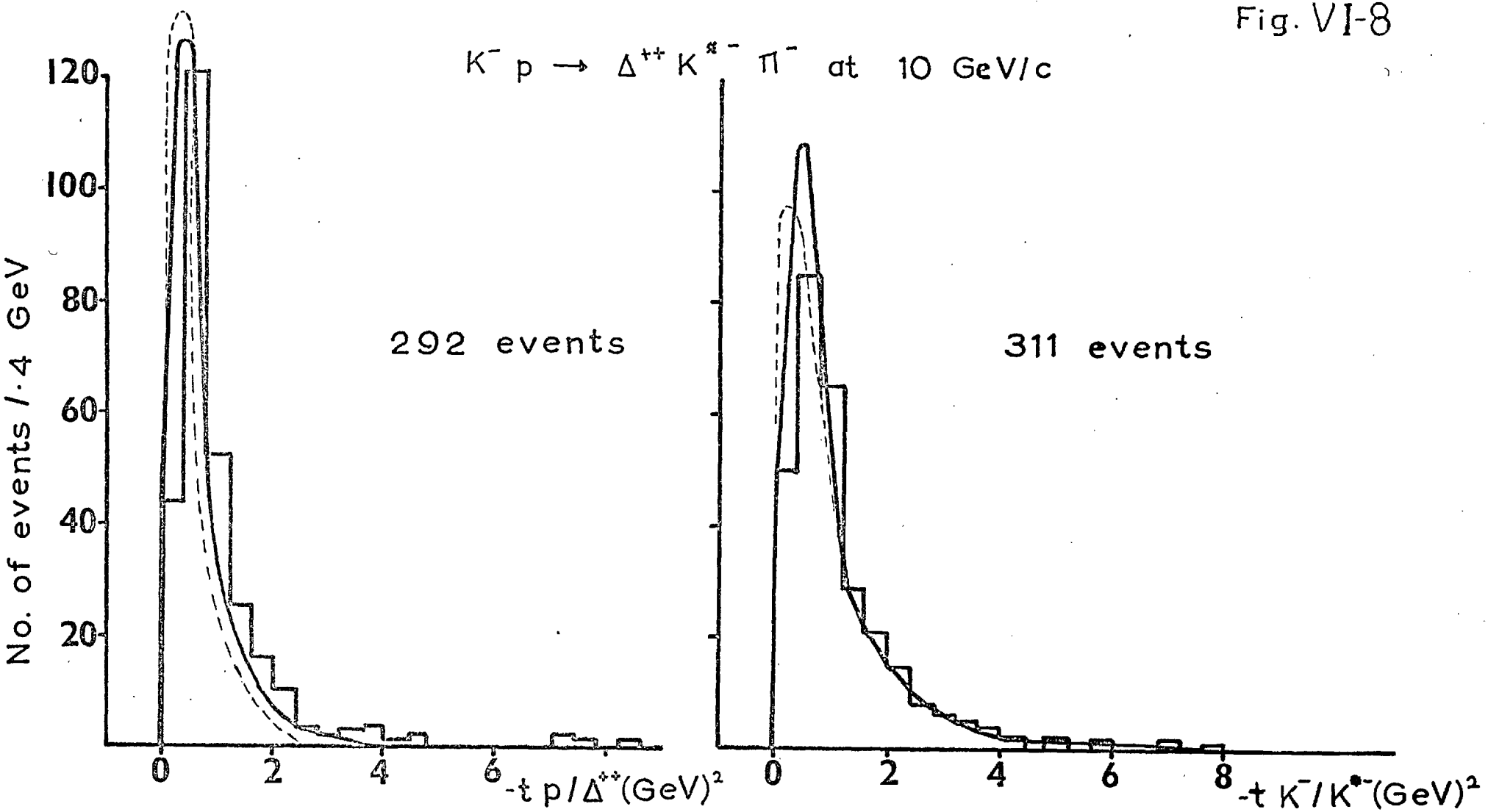

$K^- p \rightarrow \Delta^{++} K^{*-} \pi^-$ at 10 GeV/c
292 events
311 events
No. of events / ·4 GeV
120
100
80
60
40
20
0
2
4
6
8
$-t\ p/\Delta^{++}(GeV)^2$
$-t\ K^-/K^{*-}(GeV)^2$

Fig. VI-9

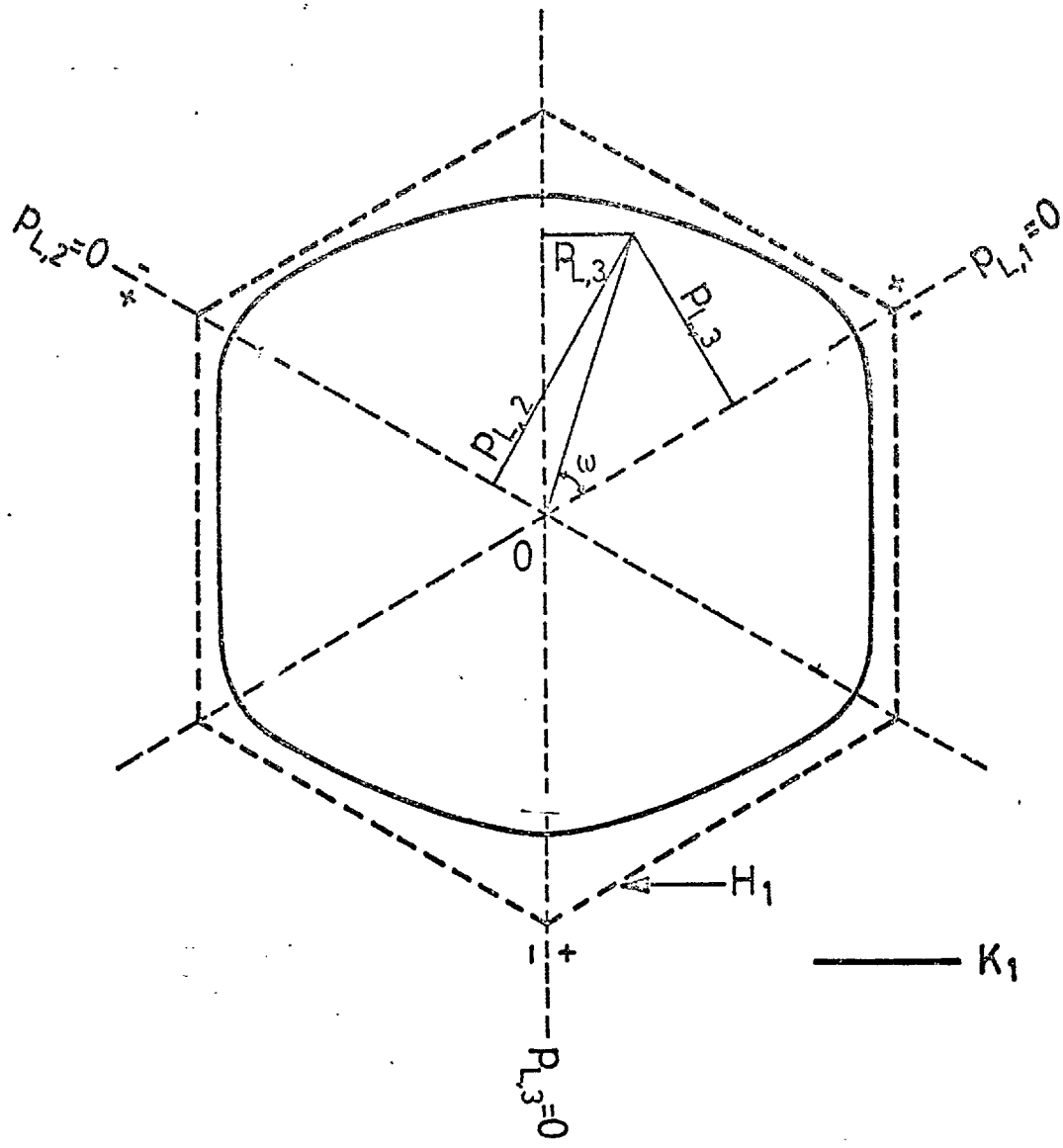
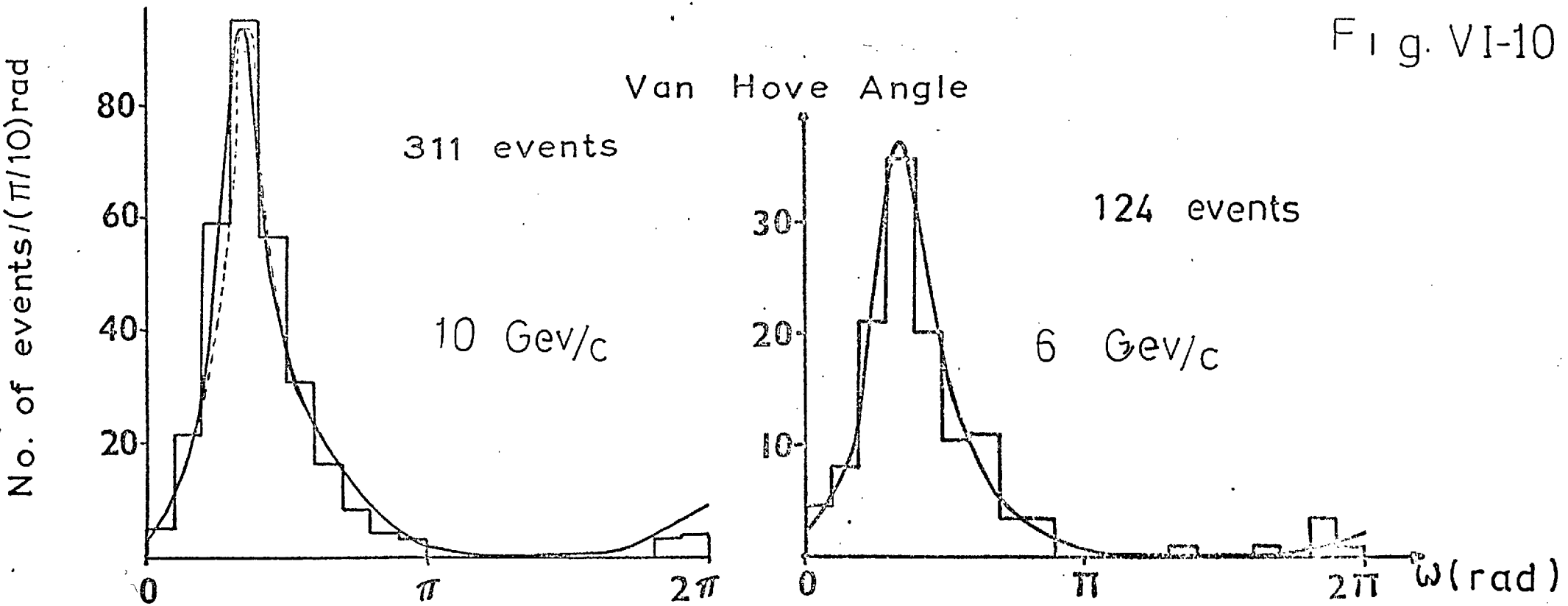


Fig. VI-10


Van Hove Angle
311 events
10 Gev/c
124 events
6 Gev/c
No. of events/(π/10)rad
80
60
40
20
30
20
10
0
π
2π
ω(rad)

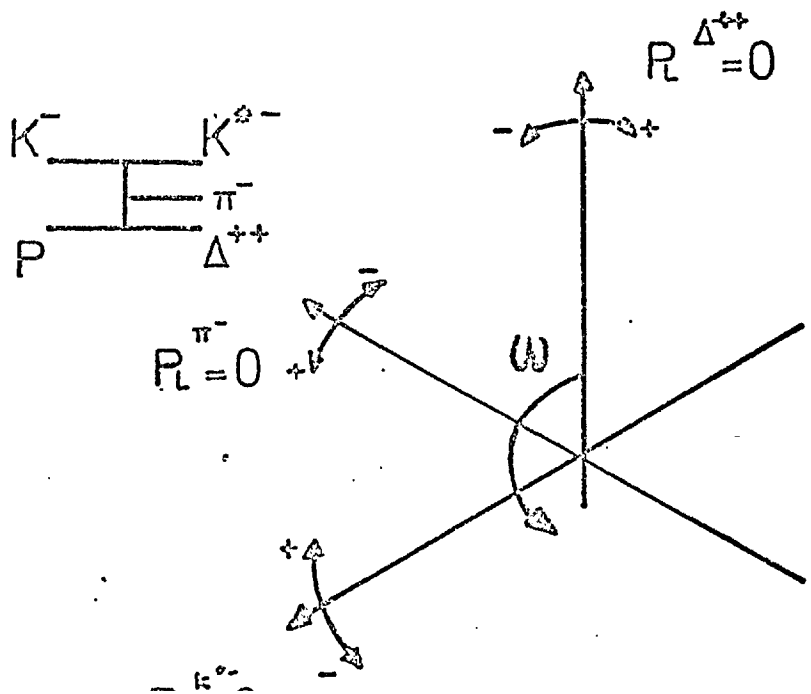

K⁻
K°⁻
π⁻
P
Δ⁺⁺
P_L^Δ⁺⁺=0
P_L^π⁻=0
ω

Fig. VI-11

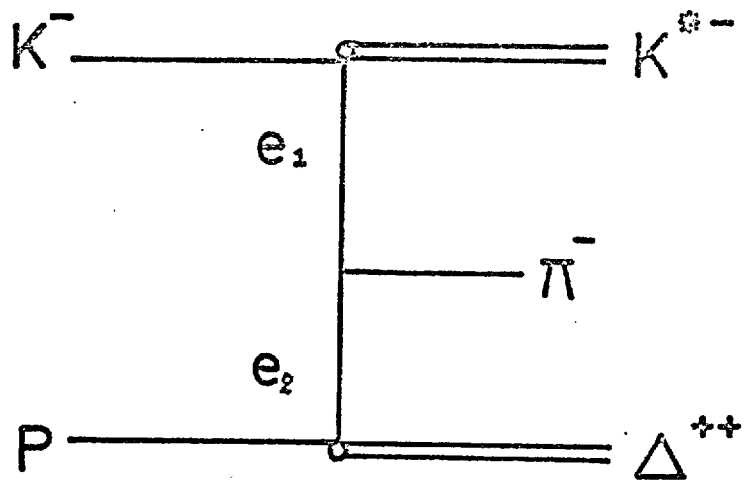
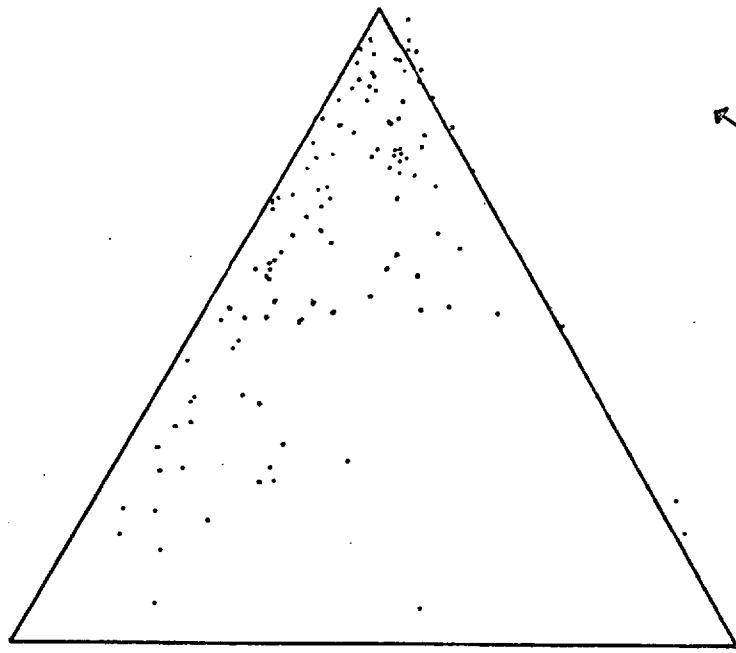
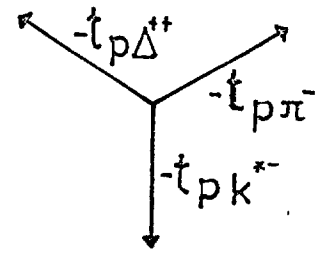


Fig. VI-12

$\bar{K}p \longrightarrow \Delta^{++} K^{*-} \pi^{-}$ at 6 Gev/c





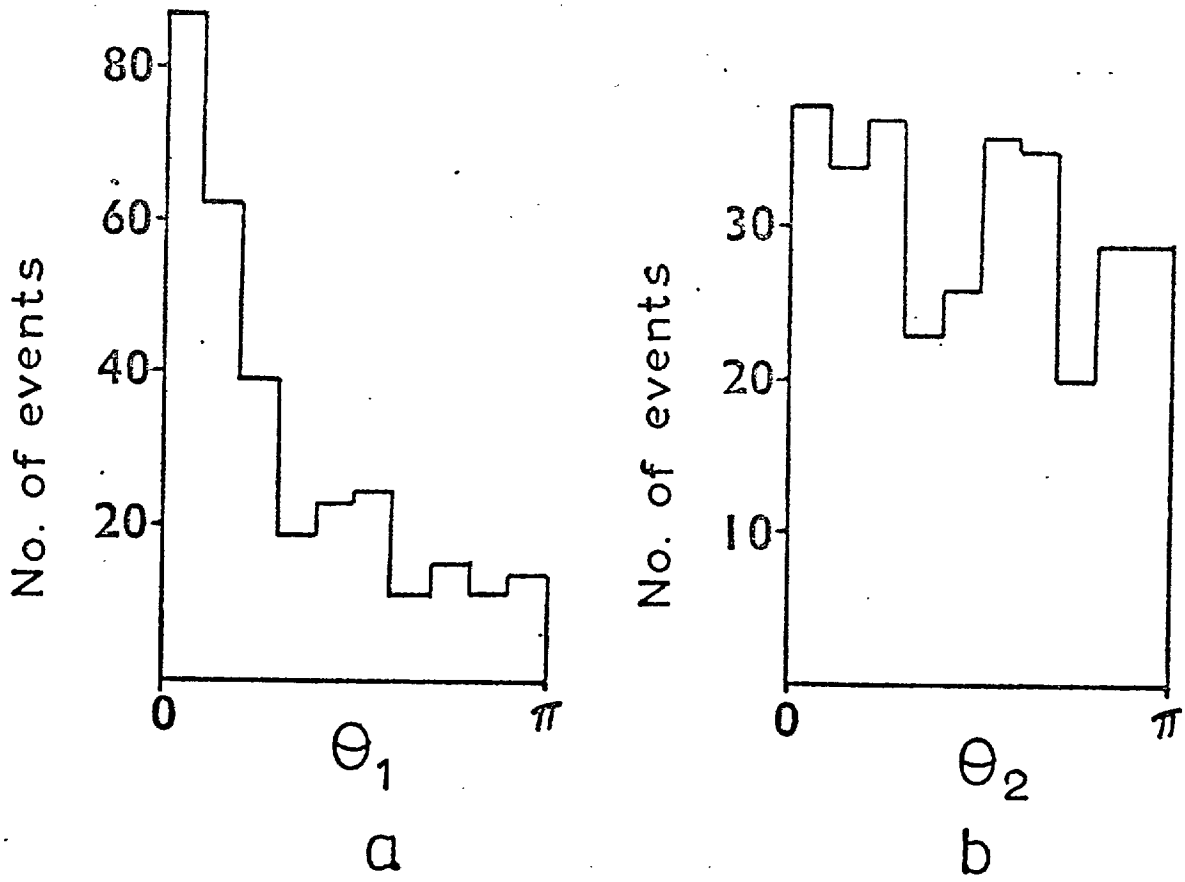
Scale in $(Gev)^2$

0 2 4

Fig. VI-13

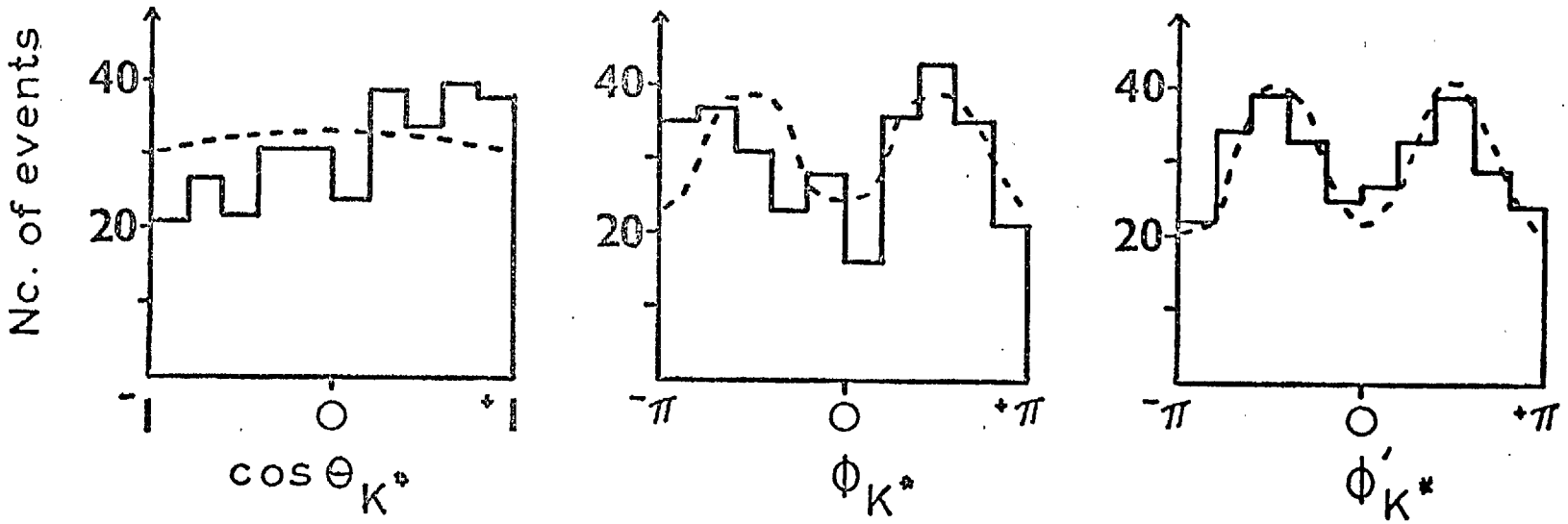
$K^- p \rightarrow \Delta^{++} K^{*-} \pi^-$ at 10 GeV/c

311 events



$K^- p \rightarrow \Delta^{++} K^{*-} \pi^-$ at 10 GeV/c

311 events



292 events

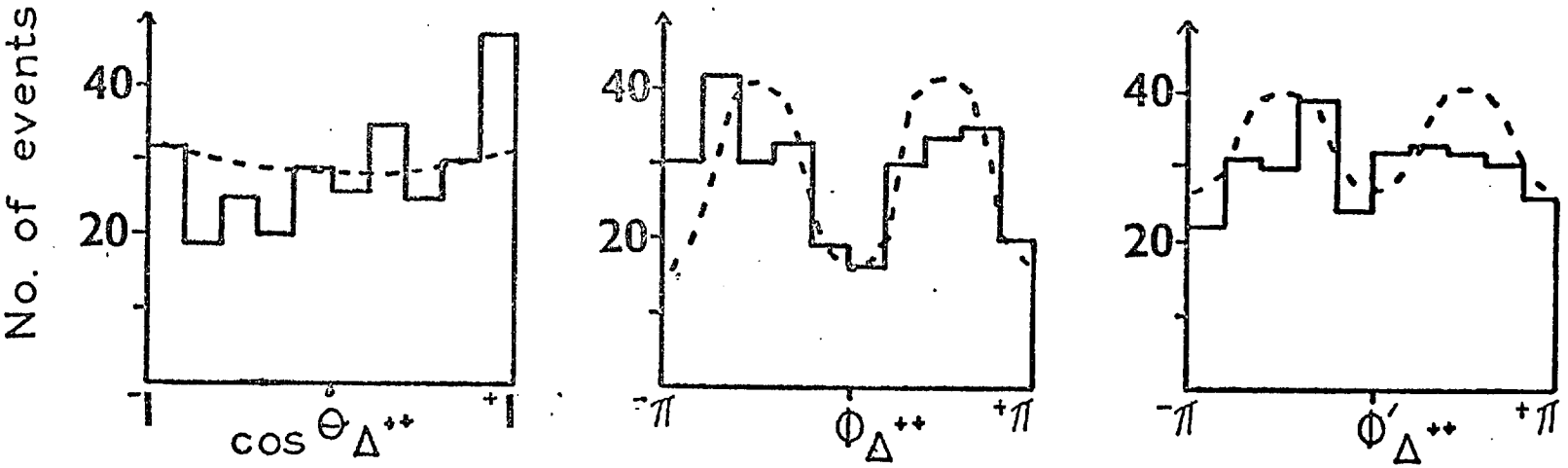


Fig. VI-15

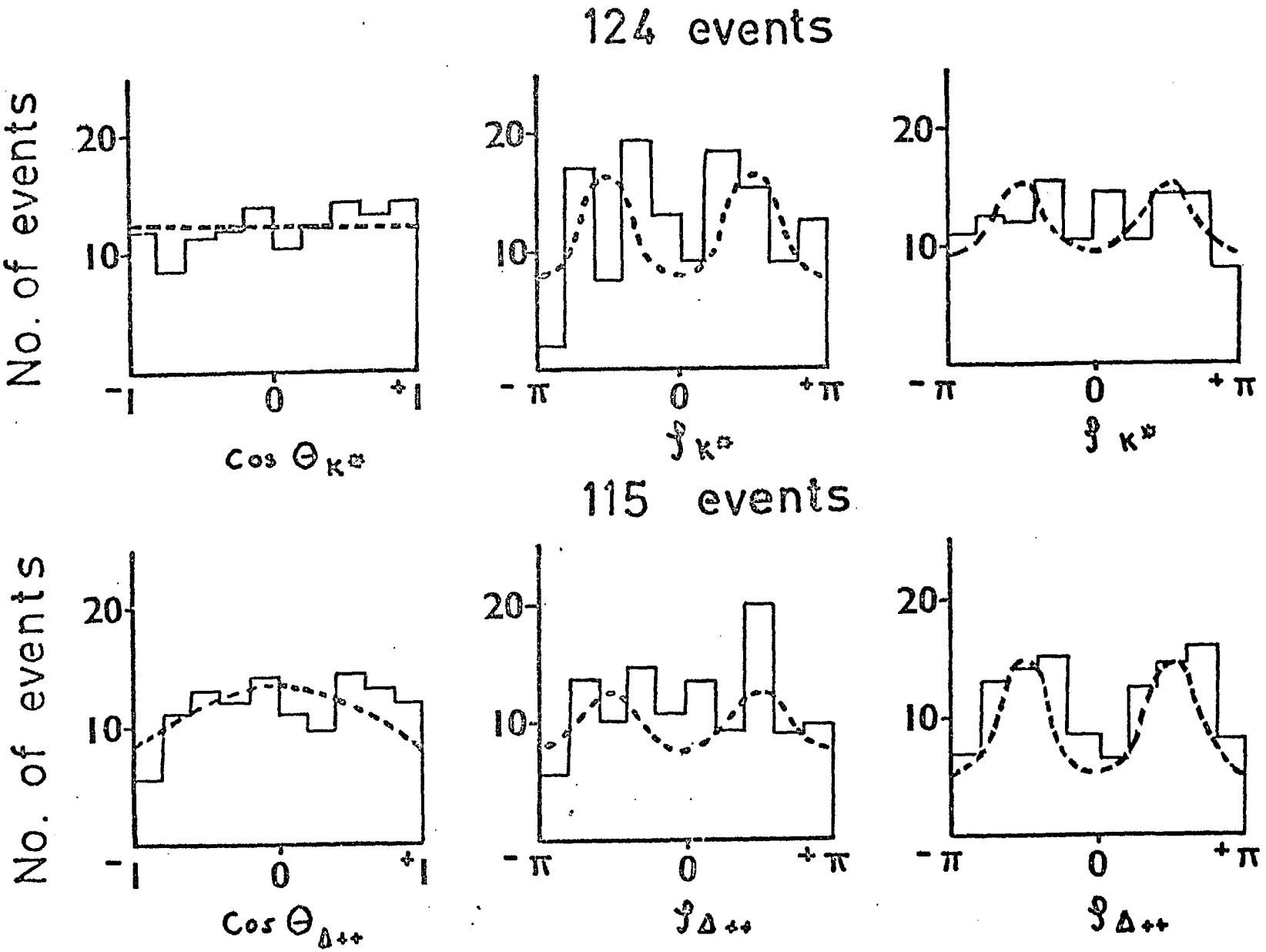
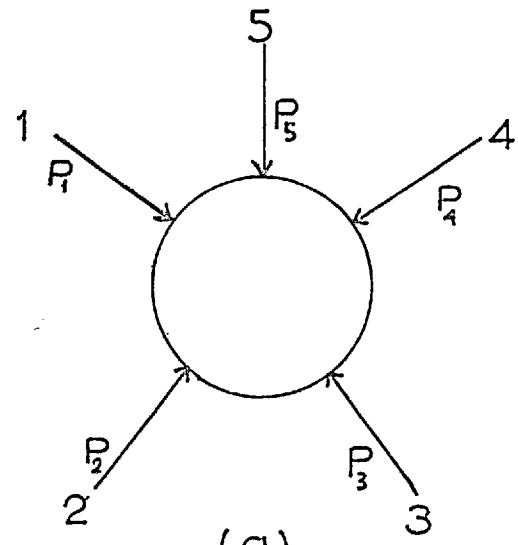
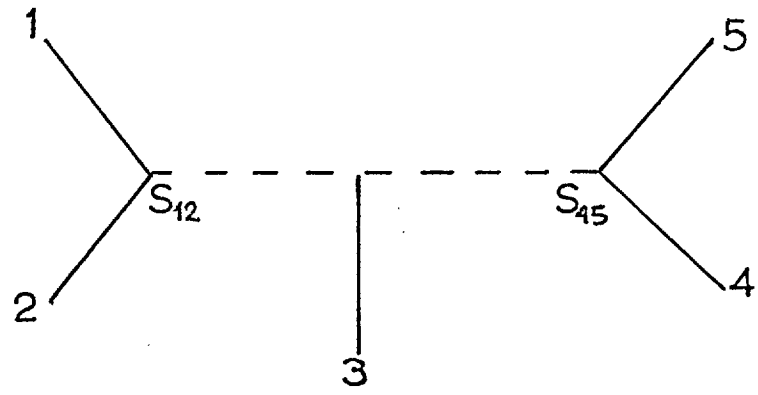

124 events
No. of events
20
10
-1
0
+1
Cos Θ K*
-π
+π
φ K*
115 events
Cos Θ Δ++
φ Δ++

Fig. VI-16

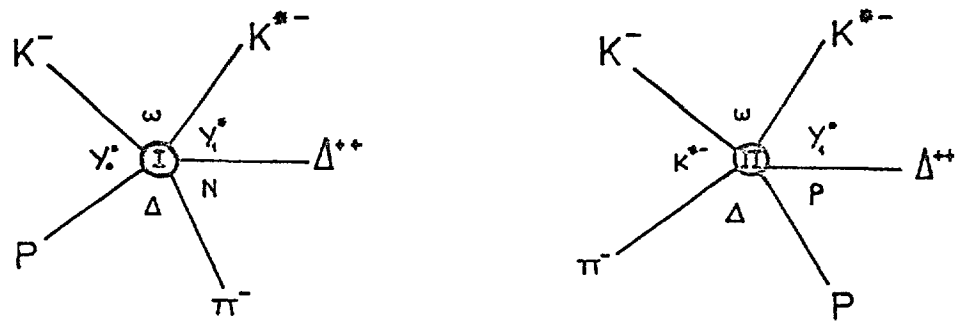


(a)

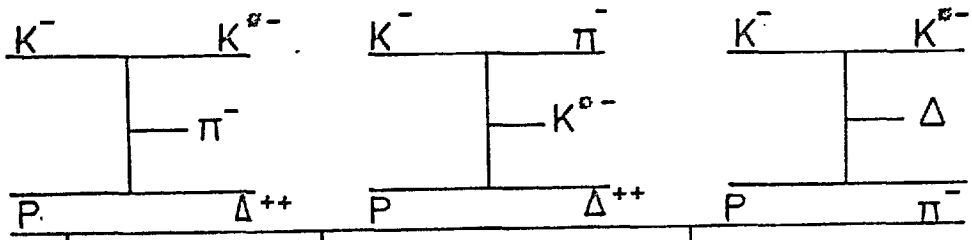


(b)

Fig VI-17

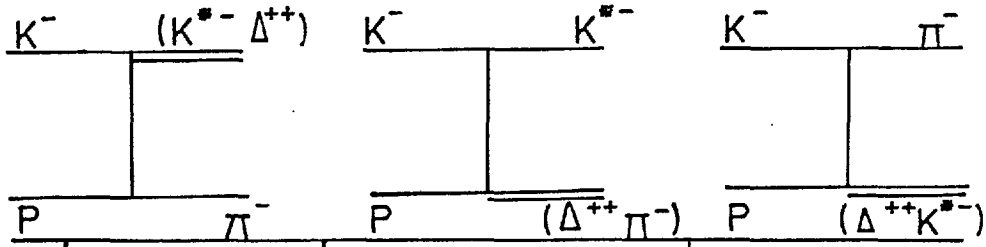


DOUBLE REGGE LIMITS



I	NO	NO	YES
II	YES	YES	YES

SINGLE REGGE LIMITS



I	YES	YES	NO
II	YES	NO	YES

Fig. VI-18

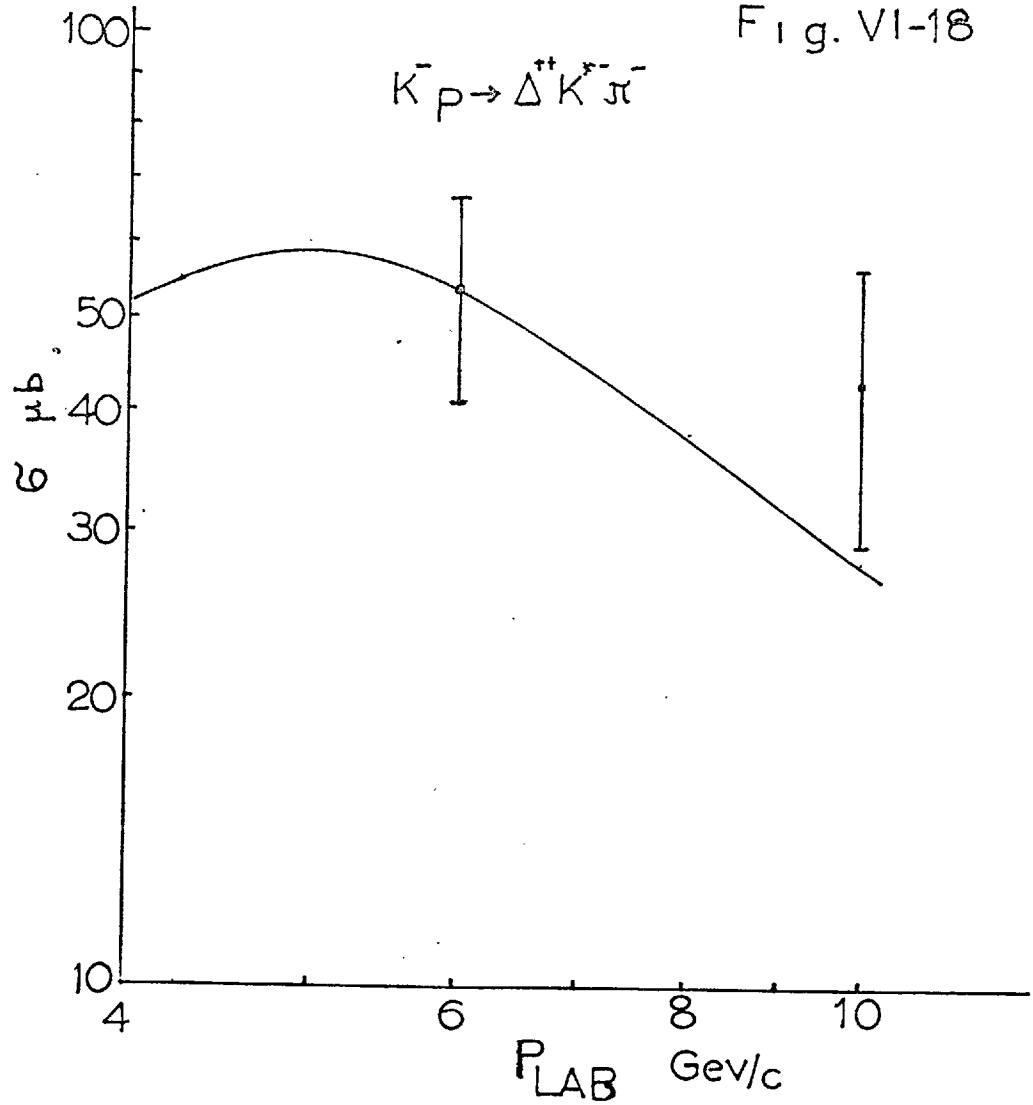
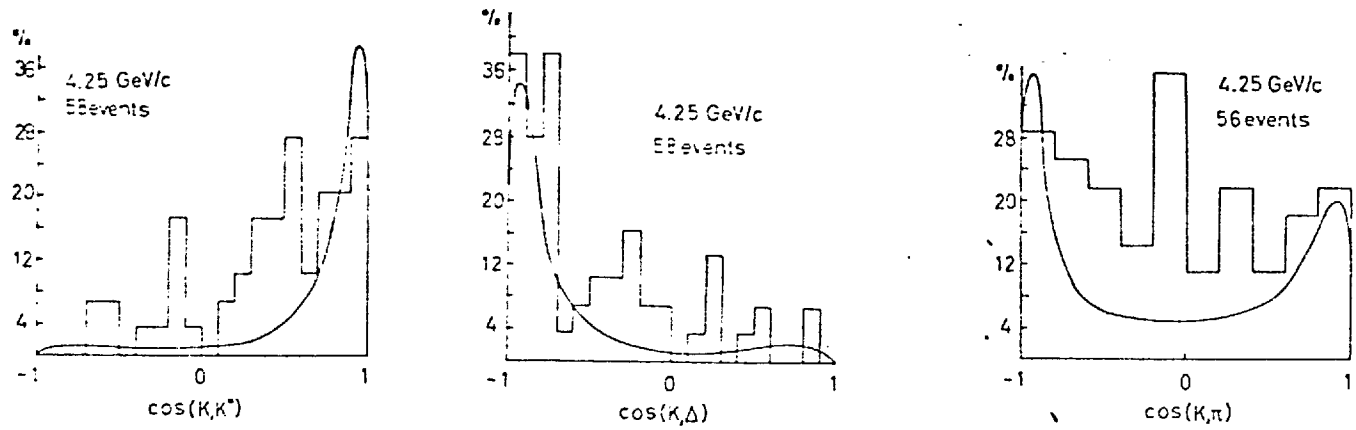
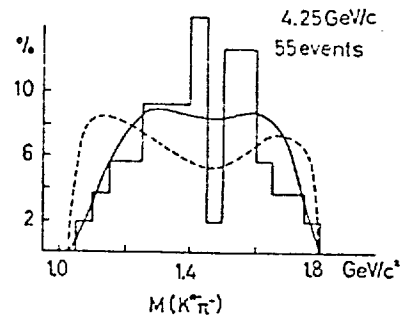


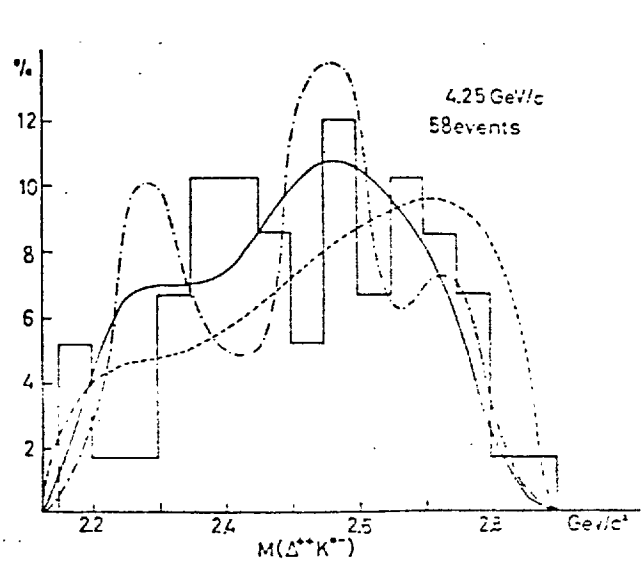
Fig. VI-19



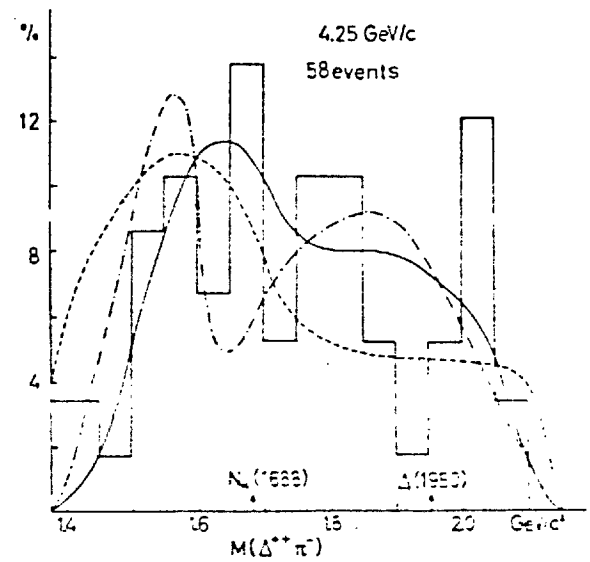
(a)



(b)

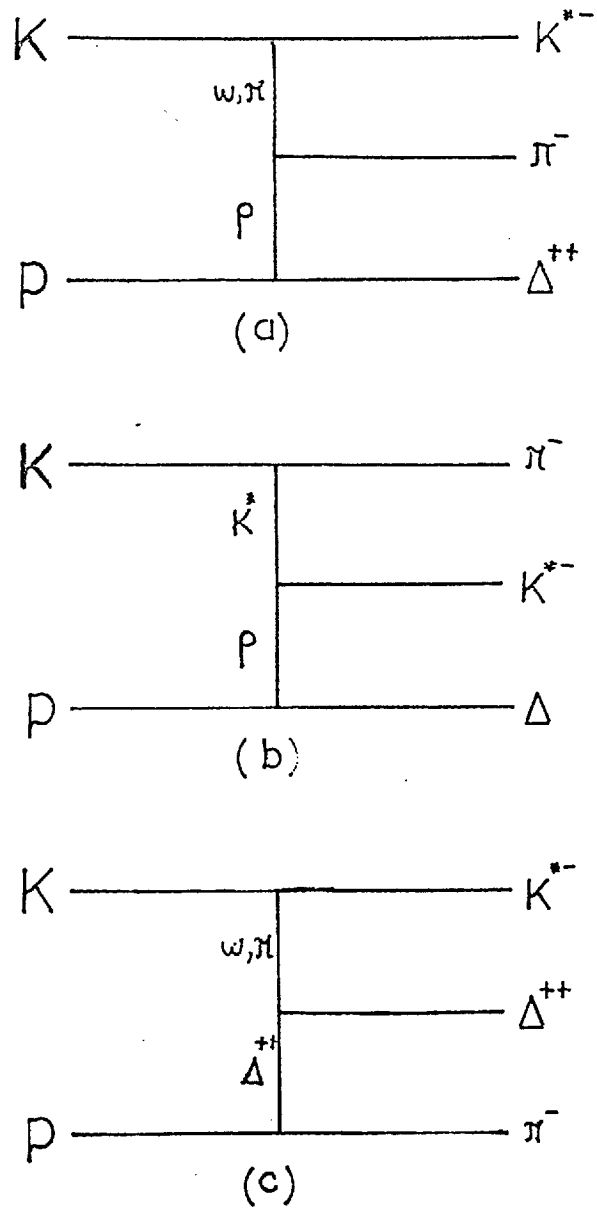


(c)



(d)

Fig VI-20



CHAPTER VII

THE PHYSICS OF 10 GeV/c K^-p EXPERIMENT: A SURVEY

We conclude by presenting a survey of the interesting physics--to which, it is hoped, the present thesis had also something to contribute--so far derived from the 10 GeV/c K^-p experiment. This may in no way be considered as a definite evaluation; because the increased statistics, the appearance of novel ideas and, as data accumulate, the comparison with other experiments allow the efforts to continue towards a better understanding of this particular area of hadron physics.

The survey is divided in four main parts, concerning the two body reactions, the study of resonances, the production of strange particles and the testing of theoretical models. The distinction is rather a matter of convenience than of any physical significance.

1. TOTAL AND DIFFERENTIAL CROSS-SECTIONS IN TWO-BODY REACTIONS

1.1 Total Cross-Sections

Table 1 presents the total cross-sections for the elastic scattering and for the eight most frequent quasi two body reactions at 10 GeV/c K^-p ; the particles that could be exchanged in these reactions are also listed. The elastic cross section amounts to 14.2% of the total K^-p cross section, while that of the inelastic two-body reactions to 4.8% of the total. As an interesting comparison, the fraction of the inelastic two body reactions is about 8% in 8 GeV/c π^+p interactions[1] and about 25% in 5 GeV/c K^+p interactions.[2]

The table gives also the values of the exponent n in the relation

$$\sigma = \text{const.}\ (p_{in})^{-n}$$

where p_{in} is the incident lab momentum

for each of the reactions listed. These values are seen to be consistent with the conclusions of Ref. (3), that is $n \simeq 0.2$ for Pomeron exchange, $n \simeq 1.6$ for non-strange meson exchange and $n \simeq 2$ for strange meson exchange. Furthermore, some of the processes are compared (Fig. 1) with Λ-hyperon producing ones;[4] the cross-section for elastic scattering decreases very slowly with p_{inc} compared with the cross-section for meson exchanges (as in $K^-p \to \Lambda\rho$ and $K^-p \to \Lambda\omega$).

Another interesting result arises from the plot (Fig. 2) of the cross-section variation with energy in the processes

$$K^-p \to Y^{*+}(1385)\pi^- \qquad (1)$$

$$K^-p \to Y^{*-}(1385)\pi^+ \qquad (2)\ .$$

The cross section for the production of the negative hyperon (reaction (2)) is seen to fall off more rapidly than that of the positive hyperon (reaction (1)). This may be due to the positive Y^* states being mainly produced by strange-meson exchange, while baryon exchange must contribute to the production of the negative Y^* states. In support of this explanation it is observed (see Section 3.1) that the positive hyperons are produced mainly backwards in the c.m system, while the negative hyperons are produced preferentially forwards.

1.2 Elastic Differential Cross Section

The K^-p elastic differential cross section has previously been measured in various bubble chamber[5] and electronic[6] experiments. None, however, of the higher-energy electronic experiments have measured the differential cross section for small values of the momentum transfer ($|t| < 0.2$ GeV^2) and there are no published bubble chamber results of K^-p elastic scattering at momenta above 5.5 GeV/c

The experimental $d\sigma/dt$ distribution is shown in Fig. 3 for small values of $|t|$, and in Fig. 4 for the whole $|t|$ range where events have been found; in Fig. 4 the results of electronic experiments at nearby beam momenta, as well as four curve showing the trends at lower energies[7] are also plotted.

The function

$$d\sigma/dt = A\, e^{Bt + Ct^2}$$

fitted over a small $|t|$ range (0.06 - 0.2 GeV^2) was chosen to extrapolate to the forward direction ($t = 0$). The optical theorem point (O.T.P)--also indicated in Fig. 3--is 25.8 ± 0.5 mb GeV^{-2} and the extrapolation gives 25.8 ± 1.0 mb GeV^{-2}. This is consistent with

no real part in the scattering amplitude and leads to an upper limit of 0.28 for the ration $|\alpha|$ of the real to imaginary parts of the forward scattering amplitude. A value of $\alpha = + 0.25$ at 10 GeV/c has been obtained[8] using a Pomeranchuk-theorem violating model fitted to the Serpukhov K^-p total cross-section data.

In the $d\sigma/dt$ distributions at larger $|t|$ there is evidence for a "dip plus secondary peak" structure.

It is interesting to note that, results on polarization in 10 GeV/c K^-p elastic scattering--added to Fig. 4 for comparison--show a change in the sign of the polarization at $t = - 1.1$ GeV^2. It is probable that the change in slope in the differential cross section and the change of sign in the polarization are related phenomena.

No events corresponding to backward elastic scattering were observed. This is of interest, as such a reaction would require either an exotic Z^* exchange or two particle exchanges.

1.3 Inelastic Differential Cross-Section

The differential cross-section distributions $d\sigma/dt'$ for the reactions listed on Table 1 (the elastic included for comparison) are shown in Fig. 5; $t' = |t - t_{min}|$, where t_{min} is the t-value in the forward direction, is used to correct for threshold effects, though these corrections are practically negligible at this energy. In accordance with other experiments, it was found that an exponential distribution of the form

$$d\sigma/dt' = \text{const} \quad \exp(-At')$$

gives a satisfactory fit to the data for small t' values. The coefficient A is an important physical parameter; in the optical

model, for instance, it is directly related to the radius of the interaction region. In general, similar values of A are obtained for a resonance region and for its neighbouring mass bands. If the effective mass M of one of the "bodies" in the final state varies, the angular distribution becomes broader, namely $A \propto M^{-\alpha}$ with $0 < \alpha < 2$; a similar result has also been obtained in the photoproduction reaction $\gamma p \rightarrow p\pi^+\pi^-$.[9]

A general feature of the quasi two body reactions studied is that they have a forward diffraction peak with a slope of the same order as that for elastic scattering. The absence of a backward peak is significant since backward production would require, except in reaction (1), the exchange of a hyperon of positive strangeness.

In Fig. 6, the differential cross sections in a small t' range are presented. The question, as to whether there are dips in the forward direction is often an important one as it can give information on the reaction mechanism. No dips towards $t' = 0$ are observed in the $K^*(1320)$ or $L(1790)$ production; this is consistent with the mechanism of their production being mainly diffractive, in similarity to elastic scattering. In 12.7 GeV/c K^+p interactions a dip, however, has been observed near $t = 0$ in the reaction $K^+p \rightarrow pK^{*+}(1320)$.[10]

A dip near $t' = 0$ is also observed in the $pK^{*-}(890)$ channel (Fig. 6), which is absent in the $nK^{*o}(890)$ channel. This difference in behaviour will be discussed in detail later (Section 2.2).

The solid lines on some of the plots of Fig. 5 are the results of an absorption model calculation. The model reproduces the shape, but not the absolute value of the cross sections for pseudoscalar exchange, and fails completely in describing the reactions dominated by vector exchange.

2. THE STUDY OF RESONANCES

2.1 The Q and L Mesons

(a) The Q and L peaks

For the first time in this experiment, and thereafter observed in many other experiments,[11] an enhancement has been seen in the $(K\pi\pi)^-$ effective mass distribution at around ~1800 MeV; the name L meson was proposed for it. Its production is shown in Fig. 7ab, which presents the $K\pi\pi$ mass system for the reactions

$$K^- p \to pK^-\pi^+\pi^- \qquad (3)$$

$$K^- p \to p\bar{K}^0\pi^-\pi^0 \qquad (4) \ .$$

The well known Q peak is also present in these plots as a broad enhancement between 1100 and 1500 MeV.

By fitting the combined mass distribution of Fig. 7c with a smooth hand drawn background and two Breit-Wigner curves the following mass and width values are obtained for the two peaks

L meson : $M = 1785 \pm 12$ MeV $\quad \Gamma = 127 \pm 43$ MeV

Q peak : $M = 1325 \pm 6$ MeV $\quad \Gamma = 186 \pm 15$ MeV .

It is interesting to note in this point that strong controversy has arisen as to the interpretation of the Q and L enhancements. In the place of the broad 1200 - 1350 MeV enhancement, other experiments see one, two or three real resonances; a Deck mechanism of kinematic origin[12] has also been proposed as a possible explanation, but failed to reproduce the whole peak (Fig. 8). As far as the

L-meson is concerned, while earlier papers reported a variety of decay modes, a high statistics K^+p experiment at 12 GeV/c [13] suggested that the observed peak need not be a meson, as it can be explained as a threshold enhancement in the $K^*(1420)\pi$ system. The data, however, from the present experiment do not agree with this as being a sufficient interpretation: In Fig. 9 the $(K^-\pi^+\pi^-)$ effective mass distribution from the reaction $K^-p \to pK^-\pi^+\pi^-$ is plotted, for all events except those having a $(K^-\pi^+)$ mass combination in the $K^*(1420)$ mass region; there still remains a peak at the L-meson mass, an indication that the $K^*(1420)\pi$ is not the only decay mode. The same conclusion is reached by similar results at 4.6 GeV/c K^-p .[14]

(b) Decay ratios, I-spin, spin and parity

A detailed analysis of the decay ratios is still in progress, although a preliminary examination has been made. No evidence is seen for a Q or L decay into a $(K\pi)$ mode, while the $K\pi^+\pi^-\pi^o$ mass distribution with events having a $\pi^+\pi^-\pi^o$ in the ω region (Fig. 10) indicates the possibility of a $(K\omega)$ decay mode for both resonances. The relative importance of the $K\pi\pi$, $K^*(890)\pi$, $K\rho$ and $K^*(1420)\pi$ contributions on the $(K\pi\pi)^-$ spectrum has been estimated by a maximum likelihood fit, and the results are shown in Figs. 11 and 12.

Since both the $K^*(1320)$ and the L meson are produced via quasi two-body reactions

$$K^-p \to K^*_A \text{ Nucleon}$$
$$\hookrightarrow (K\pi\pi)$$

their I-spin values are restricted to 1/2 or 3/2. The existence of a $(K\omega)$ decay mode already requires some $I = 1/2$. But the strongest

argument against $I = 3/2$ lies in the fact that I-spin conservation would then imply the same cross-section for $K^-p \to pK_A^{*-}$ and $K^-p \to nK_A^{*o}$, and also for $K^-p \to p(K^-\pi^+\pi^-)$ and $K^-p \to n(\bar{K}^o\pi^+\pi^-)$; this prediction strongly disagrees with the experimental results.

By a maximum likelihood analysis of the resonance and background regions, the $K^*(1320)$ is shown to have a spin-parity assignment of 1^+, with 2^- much less probable, while the L-meson has possibly spin-parity assignments of 1^+, 2^- or 3^+.

(c) Production mechanism

It has been suggested[15] that the $K^*(1320)$ and the L-meson are produced by Pomeron exchange. This is supported by our data, as neither of them is observed in reactions in which Pomeron exchange cannot occur since charge is exchanged (the $K^-p \to n\bar{K}^o\pi^+\pi^-$ for instance, see Fig. 13). With the assumption, that the production of the $(K\pi\pi)$ system is a "diffractive" process (as illustrated in Fig. 14) a model for the description of the Q and L-mesons has been formulated,[16] which brings together the resonance and Deck-type interpretations in a convincing way. In short, the amplitude for the reaction is factorized in this model as

$$A = F(p,p')\ S(p', K, \pi, \pi)\ V(K, \mathbb{P}, K, \pi, \pi)$$

where the variables in brackets indicate the momenta on which the three functions can depend. The factor V is a dual five-point Veneziano amplitude which describes the diffractive upper vertex. The factor F is of the form

$$F = \exp (1/2\ bt_{pp'})$$

and describes the lower vertex. The factor S is related to the exchange of the pomeron, and ensures the correct Regge behaviour of the amplitude.

The agreement of the model predictions with the data is quite satisfactory; as an example, the description of the Q and L meson decays in terms of the distributions on the Dalitz plot is presented in Figs. 15 - 16 .

A sensitive method of investigating the properties of diffractive processes has been developed recently, and concerns the axis along which the helicity of the incoming particle is conserved. Results, obtained for the photoproduction reaction $\gamma p \rightarrow p\rho^o$,[17] and also for the πN elastic scattering,[18] established that helicity is conserved in the s-channel; it was suggested that this may be a general property of all pomeron-exchange (or diffractive) processes, such as the $KN \rightarrow QN$.

To investigate the matter, the reaction

$$K^- p \rightarrow pQ \rightarrow p(K^-\pi^+\pi^-)$$

$$\rightarrow p(\overline{K}^o\pi^-\pi^o)$$

was considered in this experiment, and the spin density matrix elements for the Q were calculated as function of the four momentum transfer from proton to proton. Two frames were used, both defined in the rest frame of Q : The helicity frame (H), with quantization axis along

$-\vec{p}_{out}$, and the Gottfried-Jackson (G.J) frame, with quantization axis along $\bar{K}_{in}$; the two frames differ only by a rotation through an angle β about the Y-axis (Fig. 17).

The t-dependence of the element ρ_{00} is plotted in Fig. 18a for both frames. Should s-channel helicity be conserved, the element ρ_{00} is expected to be unity (and the other ρ_{mn} to be zero) at all t-values in the H-system; in the G.J. system ρ_{00} is expected to be unity at $t \simeq 0$ -- where the two systems coincide-- and to decrease as $|t|$ increases (while the other ρ_{mn} elements should be different from zero). The results show that this is not the case; it can be seen, in fact, that in the G.J. system $\rho_{00} \simeq 1$ (all other $\rho_{mn} \simeq 0$) at all t-values. These results indicate that in Q-meson production, it is t-channel, and not s-channel, helicity which is conserved.

In another approach the position of the z-axis of the Donohue-Høgaassen (D.H.) frame[19] is determined from the data; this is by definition the preferential frame of maximum symmetry for the resonance decay. If the D.H. system coincides with the H-system (as, for instance, in the rho photoproduction[20]), an s-channel helicity conservation is indicated.

In applying this method to the Q-mass band we call χ the crossing angle, i.e., the angle between the z-axis of the G.J. and H-frames, and ψ the rotation angle, i.e., the angle between the z-axis of the G.J. and D.H. frames. Figure 18b shows the values of ψ as functions of t ; the curves drawn represent the t-dependence of the crossing angle χ . It can be seen that, at all t-values, the rotation angle ψ is comparable with zero, i.e., the D.H. frame in this case either coincides or lies very close ($\psi < 10^{o}$) to the G.J. frame-- not to the H-frame.

Similar results were obtained for the A_1 production in $\pi^{\pm}p$ reactions. It may thus be concluded that in the production of A_1 and Q mesons in inelastic diffractive reactions it is t-channel helicity that is conserved, at variance with s-channel conservation in hadron-hadron elastic scattering and rho-photoproduction. To interpret these results it is suggested that there is a change in spin in the former reactions but not in the latter, or, alternatively, that different reaction mechanisms operate in the two cases.

2.2 The $K^*(890)$ Resonance

(a) Experimental characteristics

In the interaction of kaons with protons, K^* resonances at 890 MeV and at around 1420 MeV are frequently observed. The production properties of these resonances can be best studied in the three particle final state $NK\pi$--on the basis of cross sections, production and decay angular distributions.

Figure 19 shows the $(K\pi)$ effective mass distribution from these final states at 10 GeV/c; the production of both $K^*(890)$ and $K^*(1420)$ is evident. By superimposing (Fig. 20) two Breit-Wigners and a hand drawn background to the combined (b) and (d) distributions-- where the K and π tracks are directly measured--one gets for the masses and widths

$$K^*(890) : \quad M = 893 \pm 4 \text{ MeV} \qquad \Gamma = 58 \pm 7 \text{ MeV}$$

$$K^*(1420) : \quad M = 1423 \pm 21 \text{ MeV} \qquad \Gamma = 175 \pm 57 \text{ MeV} .$$

The production cross-sections for the reactions

$$K^-p \rightarrow nK^{*o}(890) \qquad (5)$$

and

$$K^-p \rightarrow pK^{*-}(890) \qquad (6)$$

have also been calculated. With data at lower energies they fit well (Fig. 21) a dependence of the cross-section 6 on the lab momentum p_{in} of the form[21]

$$6 = \text{const.}\ p_{in}^{-n}$$

where n is a constant.

Figure 22 shows the differential cross section, $d6/dt$, for reactions (5) and (6) at 10 GeV/c. A "bending over" towards $|t| = 0$ is noticed in the case of pK^{*-}. A similar behaviour has been reported[22] at 4.1 and 5.5 GeV/c, while at lower energies, and in particular at 2.64 GeV/c,[23] the differential cross section is strongly peaked forwards. For the nK^{*o}, the forward peaking observed here is common to all K^- momenta investigated.

(b) Analysis of the $K^*(890)$ production mechanism with the absorption model

The nK^{*o} system

It is assumed that the pseudoscalar (pion) exchange is the dominant process in the production of the $K^{*o}(890)$ resonance; this is consistent with the shape of the decay angular distributions and the forward peaked production angular distribution. The assumption has proved satisfactory in all experiments at lower energies.

The pion exchange model with absorption[24] is then used to calculate total and differential cross-sections, as well as the ρ_{mn} matrix elements and their $|t|$ dependence. The predictions of the model (dashed lines) are compared with the experimental results in Figs. 22 - 23. The overall agreement is reasonable; however, the absolute value of the cross-section is too large by a factor of about four (in the figure the curve is normalized to the data).

The pK^{*-} system

The behaviour of the d6/dt distribution in this case (as discussed earlier) is qualitatively consistent with the interpretation that with increasing energy π exchange and its interference with the ω amplitude become less important and limited to smaller $|t|$ values, while the ω contribution becomes increasingly dominant over the whole $|t|$ range. The assumption of a mixture of π and ω exchange in the production of K^{*-} had produced satisfactory agreement between absorption model calculations and experimental data for all energies up to 5.5 GeV/c; this assumption is further supported by the fact that the value of ρ_{00} steadily decreases with the incoming kaon momentum (ρ_{00} would be zero for pure ω exchange).

In the application of the model at 10 GeV/c the (unknown) coupling constants for ω are left as free parameters to be determined by maximum likelihood fits to one, or more, experimental distributions; relatively better results are achieved by determining these constants from the ρ_{mn} and d6/dt distributions simultaneously. The values obtained radically differ from those at around 3 GeV/c, an indication that the model cannot safely be extended over a large energy range.

The model predictions agree reasonably well with the ρ_{00} and Re ρ_{10} elements and poorly with the $\rho_{1,-1}$ (Fig. 23, dotted lines), while they give a completely wrong shape for the d6/dt distribution (Fig. 22). No other choice of coupling constants or of absorption parameters can bring the model in a better agreement with the data. The inadequacy of the model in describing processes requiring vector meson exchange at high energy was also concluded in a study of several two-body reactions induced by 8 GeV/c collisions of positive pions with protons.[25]

(c) A Regge-pole calculation

To complete the picture, we refer here to an attempt[26] to interpret the experimental data for the $K^*(890)$ production on the basis of a Regge-pole calculation. For reaction $K^-p \to nK^{*o}$ the π, ρ and A_2 trajectories have been considered, and for the $K^-p \to pK^{*-}$ the P, P', π, ρ, ω, ϕ and A_2 trajectories. It is found that the π trajectory gives the dominant contribution in the first reaction, overriding the higher lying trajectories; for the K^{*-} production, on the other hand, the trajectory that includes ω and ϕ is found to be dominant except in the very forward direction ($|t| < 0.02$ GeV^2) where the π trajectory may be more important. The reasons for the different behaviour in the two reactions remain to be explained.

With the exception of the $\mathrm{Re}\rho_{10}$ element in the K^{*-} production, the predictions of the model (solid lines in Figs. 22 - 23) are in reasonable agreement with the data.

2.3 Baryon Resonant States With Strangeness S = -2

Many baryon states of strangeness S = 0 and S = -1 are known to exist, and they are expected to have S = -2 partners. The 10 GeV/c K^-p experiment confirmed one of them--the $\Xi(2030)$ state--first reported elsewhere,[27] and presented evidence for a new Ξ state at around 2500 MeV.

To this, the effective mass distributions of the $\Lambda\bar{K}\pi$, $\Sigma^-\bar{K}\pi$, $\Sigma^+\bar{K}\pi$ and $\Xi^-\pi\pi$ systems from the reactions

$$K^-p \to Y\bar{K}K + \text{pions} \qquad (Y \text{ denotes the hyperon } \Lambda, \bar{\Sigma}^{\pm} \text{ or } \bar{\Sigma})$$

$$\to \Xi^-\bar{K} + \text{pions}$$

are considered in Fig. 24. At around 2050 MeV, a distinct peak is observed in the $\Lambda\bar{K}\pi$ systems, and a weaker signal in the $\Sigma\bar{K}\pi$ systems. The simplest interpretation of this $Y\bar{K}\pi$ enhancement is that it corresponds to a new decay mode of the $\Xi(2030)$ resonance, already seen with a $Y\bar{K}$ decay mode at 3.5 - 5 GeV/c energies and; with smaller statistical significance, in this experiment.

In the "combined" $Y\bar{K}\pi$ and $\Xi^-\pi\pi$ mass distributions of Fig. 24a, another significant peak shows up at around 2500 MeV. It is considered as an evidence for a new Ξ state decaying into $\Lambda\bar{K}\pi$, $\Sigma\bar{K}\pi$ and $\Xi\pi\pi$, with a weak indication (not presented here) of an additional $Y\bar{K}$ decay mode. The new state is also observed at lower energies.[28]

A broad enhancement at around 2240 MeV is in addition noticed in the combined distributions of Fig. 24a; in the individual mass plots the peak occurs at somewhat different central mass values. Although the existence of several Ξ states is predicted by SU3 symmetry to complete the multiplets containing the known $S = 0$ and $S = -1$ baryons,[29] more data are obviously needed to clarify the situation.

A fit to the combined $(Y\bar{K}\pi)$ and $(\Xi\pi\pi)$ mass distribution with three Breit-Wigner curves and a hand-drawn background gives the following values for the mass and width of the three peaks

$$M = (2058 \pm 17)\ \text{MeV} \qquad \Gamma = 57 \pm 30\ \text{MeV}$$

$$M = (2244 \pm 52)\ \text{MeV} \qquad \Gamma = 130 \pm 80\ \text{MeV}$$

$$M = (2500 \pm 10)\ \text{MeV} \qquad \Gamma = 59 \pm 27\ \text{MeV}\ .$$

3. SOME ASPECTS OF STRANGE PARTICLES PRODUCTION

3.1 Λ-Production

An interesting feature of Λ production in reactions of the type

$$K^- p \rightarrow \Lambda + 2 \text{ or more pions}$$

can be observed in the scatter plots of Fig. 25. While the transverse momentum of the Λ's is generally small for all multiplicities, there is a change in the distribution of p_L^* values as the multiplicity changes: At low multiplicities, the Λ's are strongly grouped backwards, while as the multiplicity increases the distribution spreads out and becomes less peripheral; at the highest multiplicity the average value of p_L^* is near zero. Similar data obtained for 6 GeV/c $K^- p$ interactions,[30] have been interpreted as supporting evidence for the multiperipheral model with Regge pole exchange.[31]

In Figs. 26 - 27, a comparison is made of the $(\Lambda\pi^+)$ and $(\Lambda\pi^-)$ effective mass distributions in several many body reactions. As the multiplicity of pions in the final state increases, these distributions become more and more similar. The formation of $Y^{*+}(1385)$ is visible at all multiplicities. While no sign of $Y^{*-}(1385)$ production is detectable in reaction $K^- p \rightarrow \Lambda\pi^+\pi^-$, its presence in the higher multiplicity channels cannot be ruled out .

3.2 Ξ^- Production

The cross-sections for the reaction

$$K^- p \rightarrow \Xi^- K + \text{pion(s)}$$

as a function of particle multiplicity in the final state are presented in Fig. 28. For multiplicity up to four, the cross-sections are seen to be very small; the average number of particles in the final state is about six.

Figure 29 shows scatter plots of transverse versus longitudinal momentum for Ξ^-, kaons and pions for Ξ^- events of all multiplicities. There is a definite tendency of Ξ^- to be produced forwards, which seems to be balanced by a rather backward emission of kaons. This is consistent with the interpretation that at 10 GeV/c production processes requiring baryon exchange play a considerable role, even in events of a rather high multiplicity.

3.3 Ω^- Production

At the stage when about 270000 pictures had been analyzed in the 10 GeV/c K^-p experiment, seven events of Ω^- production were unambiguously identified. In six of them the Ω^- hyperon decays into ΛK^- and in one into $\Xi^0\pi^-$. A mean lifetime of $1.3 \pm \begin{smallmatrix}0.8\\0.4\end{smallmatrix}$ 10^{-10} sec and a mass value of 1671.9 ± 1.2 MeV were obtained for the Ω^- by using the ΛK^- decay events; these values compare well with those given by the Particle Data Group.

The cross-section for the Ω^- production seems to increase with energy in the range from 5 to 10 GeV/c, although the cross section values obtained are not directly comparable because the branching ratios of the Ω^- decay are poorly known . So values of 0.9 ± 0.5 μb and 1.3 ± 0.7 μb have been reported at 5.5 GeV/c[32] and 6 GeV/c[33] respectively, while at 10 GeV/c the cross section was estimated at about 2.5 ± 1.0 μb.

Figure 30 shows that, as for the Ξ^-, there is a tendency for the Ω^-'s to be produced more forward.

3.4 A Comparative Study

A comparative picture of particles emission in the reactions

$$K^- p \rightarrow \Lambda K \bar{K} + \text{pions}$$
$$\rightarrow \Sigma^+ K \bar{K} + \text{pions}$$
$$\rightarrow \Sigma^- K \bar{K} + \text{pions}$$

is presented in Fig. 31. For each reaction the average values of the c.m longitudinal and transverse momenta are calculated for the hyperon, antikaons and kaons, and the average momentum vectors thus obtained are plotted.

A striking difference is observed between the three-body final states $\Sigma^+ K^- K^o$ and $\Sigma^- K^+ \bar{K}^o$; the Σ^+ is produced strongly backwards in the c.m. system, i.e. in the direction of the target proton, and the momentum balance is given by a forwardly emitted K^- ; the Σ^- , instead, is generally produced forwards together with the $\bar{K}^o$, while the K^+ goes backwards. The Λ channels present characteristics similar to those of the Σ^+ channels of the same multiplicity.

In both Σ^+ and Λ channels, with increasing multiplicity, the general features of particle emission remain the same as those observed in the three-body reactions. In the Σ^- channels, instead, they depend strongly on multiplicity: as the multiplicity increases, the average momentum vector of the Σ^- moves to the backward direction and in the six-body channels becomes similar to the momentum vector of the Σ^+ or Λ . In all reactions the pions (not plotted) are emitted with average c.m. longitudinal momentum close to zero.

In the hope of better understanding the production mechanism, these experimental results are compared with the predictions of the CLA model.[31] From the point of view of this model, the $\Sigma^+ K^- K^o$ and

$\Sigma^- K^+ \bar{K}^0$ final states are the simplest ones to study, as in both cases only two graphs (shown in Fig. 32, together with the $p_L^* - p_T$ scatter plots) can contribute. According to these graphs, the Σ^+ can be produced at the proton vertex, but not at the meson vertex, and therefore goes backwards; the opposite is true for the Σ^-, which then is produced forwards.

In Fig. 33, the predictions of the model are compared with the experimental p_L^* distributions for hyperons, antikaons, kaons and pions in the five-body final states $\Lambda K\bar{K}\pi\pi$, $\Sigma^+ K\bar{K}\pi\pi$, $\Sigma^- K\bar{K}\pi\pi$ and $\Xi^- K\pi\pi\pi$. The model reproduces the gross behaviour of each of the hyperons, the difference between the emission of kaons with positive and negative strangeness, and the grouping of pions around the value $p_L^* \simeq 0$.

It is already noted that in all multiplicity channels there is little difference between the emission of the Λ and Σ^+ : both these hyperons have a definite tendency to be produced in the backward direction. On the other hand, a large fraction of the Σ^- and Ξ^- are produced forwards in the c.m. system. These facts are related to the changes in the quantum numbers of the target baryon. In the first group the baryon changes its strangeness by one unit and its charge by not more than one unit, whereas in the second group the charge of the baryon (and also its strangeness in the case of the Ξ^- hyperon) is changed by two units. Since there is no known meson with a charge of two, the production of Σ^- or Ξ^- requires baryon exchange, while Λ and Σ^+ can be produced without baryon exchange. The resulting difference between the two groups of hyperons becomes less evident with increasing multiplicity, because the number of possible graphs rapidly increases and the effect of phase space limitations becomes more important.

4. THE INVESTIGATION OF THEORETICAL MODELS

4.1 A Veneziano Model Study of the Reaction $K^- p \to p\bar{K}^0\pi^-$

The amplitude for the above reaction has in the Veneziano model, the form

$$A = K\{B5(a) + \beta\, B5(b) + \gamma\, B5(c) + \delta B5(d)\}$$

where K is the kinematic factor and B5 (n), n = a, b, c, d are the five point functions corresponding to the four allowed graphs of Fig. 34. The β, γ, δ are real parameters giving the relative strengths of the four five-point functions; they are determined by fitting the experimental data. Graph (b), is interesting to note, violates the rules given by Harari, and hence $\beta = 0$. The duality diagrams[34] for the other three graphs are shown on the right hand side of Fig. 34.

The exchange trajectories considered are also presented in the same figure. While for the three pairs of particles between which meson exchange occurs, arguments can be found to choose a particular trajectory K^*, ω and ρ,[35] for the two pairs of particles between which a baryon is exchanged a unique choice is not obvious i.e. Y_0^* or Y_1^* are possible to be exchanged between (K^-_{in}, p_{in}) and Δ or N between (π^-, p_{out}).

A posteriori, the combination Y_0^* N was found to be the most satisfactory, and with this choice the predictions of the model (solid lines) are compared with the exp. results in Figs. 35 - 36. To a first approximation, the agreement is reasonably good, unquestionably better than that obtained using the absorption model or the CLA version of the multiperipheral model. The difficulties encountered in describing some

of the mass spectra and the $d6/dt$ distributions perhaps derive from the fact that the model does not consider the possibility that more than one trajectory is exchanged between a pair of particles.

Since the production of $\Delta(1236)$ is definitely observed in the reaction studied, it is of interest to present also the calculations with the choice $Y_1^* \Delta$ (dashed lines on the same figures). The description of the data obtained is not worse. It has however to be pointed out that the set of assumptions used in this case cannot describe the experimental situation in the crossed channels, and hence is less desirable.

It is interesting to note that the data were described by using only the allowed duality graphs; when the parameter determining the weight of the forbidden graph (b) was left free and determined by fitting the data, a value consistent with zero was obtained. The situation is different from that encountered for the $\Lambda\pi\pi$ channel,[36] where the forbidden graphs alone produced a satisfactory description of the experimental distributions.

It was also found that the results of the model are sensitive to the choices made and, in particular, to the parametrization of the trajectories; this means, in practice, that though the relative weights of the various graphs are the only free parameters of the model, the many assumptions introduced in the expression of the amplitudes are also parameters one can play with rather freely. Chan, et. al.,[37] for instance, have succeeded in producing a reasonably general description of the same reaction using rather different assumptions and parameters.

4.2 The Veneziano Model with Pion and Pomeron Exchange: reaction $K^- p \to n K^- \pi^+$

This reaction requires facing two of the major difficulties of the model, namely:

(i) pomeron exchange

(ii) dominant contribution of pion exchange, with the possibility of some vector-meson contribution.

As a first step, the assumption of pure π-exchange is made, and two independent diagrams are then considered (called A and B, Fig. 37). The pion trajectory is introduced between the nucleous of diagram A. In choosing the other trajectories, when more than one possibility exists, use of the crossing symmetry property of the model is made: Since strong Y_0^* production is observed in the corresponding crossed channel,[38] the Y_0^* trajectory between the incoming particles is chosen. Similarly, the Δ trajectory is taken between p and π^+ of diagram B, and also for $n\pi^+$, although the evidence for Δ^+ production in the corresponding crossed channels is weak.

The amplitude to describe the reaction is then expressed in the usual way as

$$A = C\,(K_1\ B5(A) + \beta K_2\ B5(B))\ .$$

The kinematic factor of diagram A is chosen to have the form

$$|K_1|^2 = t_{pn}\,(1 - \alpha_\rho - \alpha_{K^*})$$

after some considerations concerning the coupling of nucleons to mesons by a pion, and the need to achieve the correct Regge behaviour.

In diagram B, the trajectory of every channel starts with a P-wave resonance, and the same expression for K_2 as in Refs. (36 - 37) may be used.

When compared with the experimental results the predictions (not shown here) of the amplitude written above may be considered as satisfactory. A large cut in the data is however necessary in order to exclude pomeron exchange.

To improve the situation, pomeron exchange is therefore introduced into the model, following the approach suggested by Pokorski and Satz.[16] The amplitude is assumed to contain two parts, namely:

(i) A $\bar{K}_{in}$ $\bar{K}_{out}$ $\mathbb{P}$ vertex function

(ii) A dual amplitude to describe the idealized reaction

$$p + \mathbb{P} \to n + \pi^+$$

at the bottom vertex of diagram D (which is the pomeron exchange diagram describing the reaction).

The matrix element of diagram D is then given by

$$|M|^2 \simeq e^{\frac{1}{2}\alpha t_{KK}} \; S^2_{c.m.s} \; t_{pn} |V|^2$$

where α is a diffraction parameter, t_{KK} and t_{pn} are the square of the momentum transfers, S_{cms} is the square of the total c.m. energy and V is the dual amplitude for the reaction, as in Ref. (16).

The total amplitude describing the reaction is now

$$A = C\{K_1 B5(A) + \delta K_2 B5(B) + i\,\delta M(D)\}$$

with the parameters β and δ being determined by a maximum likelihood fit.

The predictions of the model (solid lines) are compared with some experimental results in Figs. 38 -42. The general experimental behaviour is seen to be correctly described; a poorer, somehow, agreement is observed with the differential cross-sections and the longitudinal momentum distributions.

This indicates that some vector meson contribution (graph C) needs perhaps to be taken into account, and a term γK_2 B5(C) is for that purpose included in the amplitude. Both the longitudinal momenta and the differential cross sections are then satisfactorily described while the other distributions do not drastically change (dashed lines in Figs. 38 - 42). It is found that about 25% of pomeron exchange and 15% vector meson exchange are added to the dominant pion exchange contribution.

With or without vector meson exchange the model fails, however, to predict correctly the variation of the total cross section with incident momentum (Fig. 43). This is particularly noticeable in the reaction $K^- p \to n K^- \pi^+$ as compared with the $K^- p \to n K^*(890)$, so the difficulty encountered may perhaps be caused by an underestimate of the amount of pomeron exchange.

4.3 Testing the CLA Model on the Reaction $K^- p \to \Delta^{++} K^- \pi^-$

In the context of the CLA model, the reaction

$$K^- p \to \Delta^{++}(1236)\, K^- \pi^-$$

is of interest, because it contains a baryon resonance in the final state, and it cannot proceed by proton or neutron exchange. In the

original formulation of the model[31] Δ-exchange was not included, as in the reactions considered there p- or n-exchange was possible.

For the quantitative comparison of the model predictions with the data, the distribution $dN/d\theta$ of the Van Hove angle[39] has been plotted for the reaction (Fig. 44a). Its dominant feature is a pronounced enhancement near $\theta = 110^{\circ}$. The CLA predictions are calculated with and without Δ exchange, using for the Δ-trajectory the intercept $\alpha(0) = .15$ and for the coupling constant the value $g_{\Delta}/g_{M} = 0.1$. The dot-dashed line in Fig. 44a is without Δ-exchange and is bad fit, principally because it fails to fit the peak at $\theta = 110^{\circ}$. A contribution from the $P\Delta$ exchange graph, as seen in Fig. 44b is obviously needed and when such a graph is included the fit is better (solid lines in Fig. 44a).

To investigate the dependence of the average transverse momentum $\langle p_T \rangle$ of the particles on their longitudinal momentum configuration, the $\langle p_T \rangle$ versus the angle θ is plotted in Fig. 45. The solid lines on the same figure are then the CLA predictions obtained by summing the contributions of all possible exchange graphs. These curves have the correct order of magnitude and describe some of the general structure, but fail to describe it in detail. Various attempts have been made to fit the $dN/d\theta$ and $\langle p_T \rangle$ distributions simultaneously, but in none of these cases was the fit to the distribution better than with the original assumptions.

The work on the $K^- p \to \Delta^{++} K^- \pi^-$ reaction--as summarized here--constituted in fact part of an extensive investigation of the CLA model, where several reactions of 8 GeV/c $\pi^+ p$, 10 GeV/c $K^- p$ and 16 GeV/c $\pi^- p$ have been used. It was concluded that while the gross features of the data were satisfactorily reproduced at all energies, the detailed description met with difficulties especially concerning pomeron-baryon exchange.

APPENDIX

List of 10 GeV/c K^-p Publications This Survey Was Based On

1. Observation of a ($K\pi\pi$) resonance near 1800 MeV
   J. Bartsch, et. al., P.L. 22 (1966) 357.

2. K^-p elastic scattering at 10 GeV/c
   M. Aderholz, et. al., P.L. 24B (1967) 434.

3. Ξ, Ω^- and antibaryon production in 10 GeV/c K^-p interactions
   J. Bartsch, et. al., N. P. B4 (1968) 326.

4. Lambda production in 10 GeV/c K^-p interactions
   M. Aderholz, et. al., N. P. B5 (1968) 606.

5. $K^*(890)$ production in 10 GeV/c K^-p interactions and comparison with Absorption and Regge pole models
   M. Aderholz, et. al., N.P. B5 (1968) 567.

6. Mass dependence of the small angle differential cross-section for high energy interactions
   J. Bartsch, et. al., P.L. 27B (1968) 336.

7. Total and differential cross-sections in 10 GeV/c K^-p interactions
   M. Aderholz, et. al., N.P. B7 (1968) 111.

8. Analysis of the $K^*(1320)$ and L-meson produced in 10 GeV/c K^-p interactions
   J. Bartsch, et. al., N.P. B8 (1968) 9.

9. Evidence for a new Ξ resonance at 2500 MeV in 10 GeV/c K^-p interactions
   J. Bartsch, et. al., P.L. 28B (1969) 439.

10. Ω^- production in 10 GeV/c K^-p interactions
    R. Speth, et. al., P.L. 29B (1969) 252.

11. Production of strange particles in 10 GeV/c K^-p interactions and comparison with the predictions of the multiperipheral model
    J. Bartsch, et. al., N.P. B11 (1969) 373.

12. Production of proton-antiproton and kaon-antikaon pairs in four-body reactions of 8 GeV/c π^+ and 10 GeV/C K^- on protons
    M. Aderholz, et. al., N. P. B14 (1969) 255.

13. A study of the reaction $K^- p \rightarrow p\bar{K}^0\pi^-$ with the Veneziano model

J. Bartsch, et. al., N.P. B20 (1970) 63.

14. Comparison of $\pi^{\pm} p$ and $K^- p$ reactions with a multiperipheral model using the Van Hove Hexagon and Cuboctahedron plots

J. Bartsch, et. al., N. P. B19 (1970) 381.

15. Application of the Veneziano model with pion and pomeron exchange to the reaction $K^- p \rightarrow nK^-\pi^+$ at 10 GeV/c

J. Bartsch, et. al., N. P. B23 (1970) 1.

16. Evidence that the L-meson has decay modes other than $K^*(1420)\ \pi$

J. Bartsch, et. al., P.L. 33B (1970) 186.

17. A dual diffractive model for the Q- and L-mesons

J. Bartsch, et. al., N.P. B24 (1970) 221.

18. Observation of t-channel helicity conservation in diffractive reactions producing A_1 and Q-mesons

J. V. Beaupre, et. al., P.L. 34B (1971) 160.

19. $K^- p$ elastic elastic scattering at 10 GeV/c

J. Bartsch, et. al., N.P. B29 (1971) 399.

TABLE VII - 1

CROSS SECTIONS, ALLOWED PARTICLE EXCHANGES AND VALUES OF THE EXPONENT n FOR TWO-BODY REACTIONS IN 10 GeV/c K^-p INTERACTIONS.

Reaction	Allowed Exchanges	Cross section (μb)	Exponent * n
(a) $K^-p \to pK^-$	$PP'\pi\rho\omega\ A_2$	3200 ± 140	0.36 ± 0.01
(b) $\to pK^{*-}(1320)$	$PP'\rho\omega\ A_2$	575 ± 72	0
(c) $\to pL^-(1790)$	$PP'\rho\omega\ A_2$	171 ± 39	not known
(d) $\to pK^{*-}(890)$	$\pi\rho\omega\ A_2$	92 ± 9	2.01 ± 0.14
(e) $\to pK^{*-}(1420)$	$\pi\rho\omega\ A_2$	54 ± 13	2.3 ± 0.4
(f) $\to nK^{*o}(890)$	$\beta\rho\ A_2$	58 ± 10	1.98 ± 0.37
(g) $\to nK^{*o}(1420)$	$\pi\rho\ A_2$	78 ± 14	2.4 ± 0.3
(h) $\to N^{*+}(1236)K^-$	$\rho\ A_2$	35 ± 4	1.6 ± 0.4
(i) $\to Y^{*+}(1385)\pi^-$	$K^*(890)$	12 ± 4	2.7 ± 0.2

*The horizontal lines in the last column separate reactions that can proceed by P-exchange from those which require non-strange meson exchange or strange meson exchange.

REFERENCES AND FOOTNOTES

1. Aachen-Berlin -CERN Collaboration, P.L. 19 (1965) 608.

2. Brussels -CERN Collaboration, N.C. 46 (1966) 539.

3. D. R. O. Morrison, Proc. Stony Brook Conf. on High Energy Two Body Reactions (1966).

4. Data taken from Ross, et. al., Dubna Conf. (1964) p. 642
   Hague, et. al., Dubna Conf. (1964) p. 654.

5. J. R. Ficenic and W. P. Trower, P.L. 25B (1967) 369
   M. N. Focacci, et. al., P.L. 19 (1965) 441
   J. Gordon, P.L. 21 (1966) 117
   J. Mott, et. al., P.L. 23 (1966) 171.

6. C. Daum, et. al., N.P. B6 (1965) 273
   J. Orear, et. al., P.R.L. 21 (1968) 387
   K. J. Foley, et. al., P.R.L. 11 (1963) 503.

7. Taken from D.R.O. Morrison, Strong Interactions of Kaons, Proc. of the Lund Int. Conf. on Elementary Particles (1969).

8. D. Horn and A. Yeovil, California Institute of Technology preprint CALT-68-238.

9. Aachen-Berlin-Bonn-Hamburg-Heidelberg-Munchen Collaboration, DESY 68/8 (1969).

10. J. C. Berlighieri, et. al., CERN Report 68-7, Vol. 2 (1968) p. 172.

11. For a review of the situation see the article by Chien in the Proceedings of Meson Spectroscopy Conference (Philadelphia, 1970).

12. R. T. Deck, P.R.L. 13 (1964) 169.

13. A. Barbaro-Galtieri, et. al., P.R.L. 22 (1969) 1207.

14. M. Aguilar-Benitez, et. al., P.R.L. 25 (1970) 54.

15. D.R.O. Morrison, P.R. 165 (1968) 1699.

16. Similar in essence to that used to describe diffractive dissociation of the nucleon in the reaction $pp \to pn\pi^+$
   See S. Pokorski and M. Satz, N.P. B19 (1970) 113.

17. Aachen-Berlin-Bonn-Hamburg-Heidelberg-Munchen Collaboration, P.R. 175 (1968) 1669.
   J. Ballam, et. al., P.R.L. 24 (1970) 960.

18. F. J. Gilman, et. al., P.L. 31B (1970) 387.

19. J. T. Donohue and H. Høgaassen, P.L. 25B (1967) 554.

20. Aachen-Berlin-CERN Collaboration, to be published in Nuclear Physics.

21. D.R.O. Morrison, P.L. 22 (1966) 528.

22. F. Schweingruber, et. al., P.R. 166 (1968) 1317.

23. J. H. Friedman and R. R. Ross, P.R.L. 16 (1966) 485.

24. J. D. Jackson, et. al., P.R. 139 (1965) B428.

25. Aachen-Berlin-CERN Collaboration, P.L. 22 (1966) 533.

26. M. MarKytan CERN/Ph.D. II/ Physics 67-33 (1967).

27. J. Alitti, et. al., paper submitted to the XIVth Int. Conf. on High Energy Physics, Vienna (1968).

28. J. Alitti, et. al., P.R.L. 22 (1969) 79.

29. H. Harari, Rapporteur's talk at XIVth Int. Conf. on High Energy Physics, Vienna (1968).

30. L. K. Sisterson, et. al., N.P. B6 (1968) 205.

31. Chan Hong-Mo, J. Loskiewicz and W.W.M. Allison, N.C. 57A (1968) 93.

32. R. F. Schultz, et. al., P.R. 168 (1968) 1509.

33. D. Scotter, et. al., P. L. 26B (1968) 474.

34. H. Harari, P.R.L. 22 (1969) 562.
J. L. Rosner, P.R.L. 22 (1969) 689.

35. Between $(\pi^-, \overline{K}^o)$ there can be only K^* exchange. Between (p_{in}, p_{out}) many exchanges are a priori possible, but since it has been found experimentally that for the reaction $K^- p \to pK^*(890)$, ω-exchange is dominant, specially at high energies, it is reasonable to take only ω-exchange here. Finally, ρ-exchange is considered between $(K^-_{in}, \overline{K}^o)$, in that it is required by the double Regge limit of the five-point Veneziano function.

36. B. Peterson and N. A. Tornquist, N.P. B13 (1969) 629.

37. Chan Hong-Mo, et. al., N.P. B19 (1970) 173.

38. J. C. Schener, et. al., N.P. B8 (1968) 503.
K. F. Galloway, et. al., N.P. B8 (1968) 545.
A. Barbaro-Galtieri, et. al., P.L. 6 (1963) 269.

39. L. Van Hove, P.L. 28B (1969) 429 ; N.P. B9 (1969) 331.
A. Bialas, et. al., N.P. B11 (1969) 479.

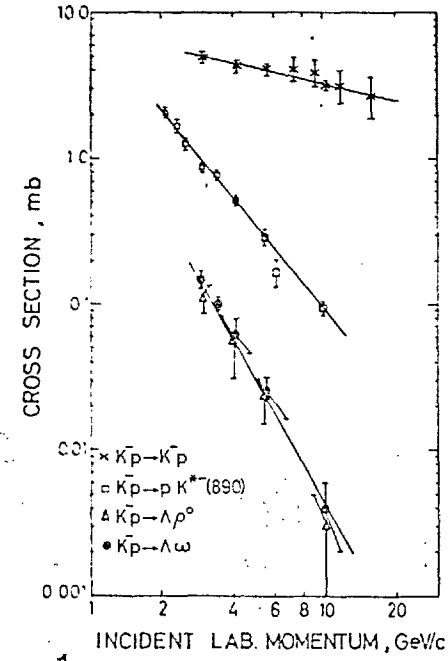


Fig.1 Cross sections as a function of the incident K^- lab momentum for the reactions:

$$K^-p \to K^-p,$$
$$K^-p \to pK^{*-}(890),$$
$$K^-p \to \Lambda\rho^0,$$
$$K^-p \to \Lambda\omega.$$

The straight lines have been obtained from fits to the experimental data using the empirical relation, $\sigma = K(p_{in}/p_0)^{-n}$.

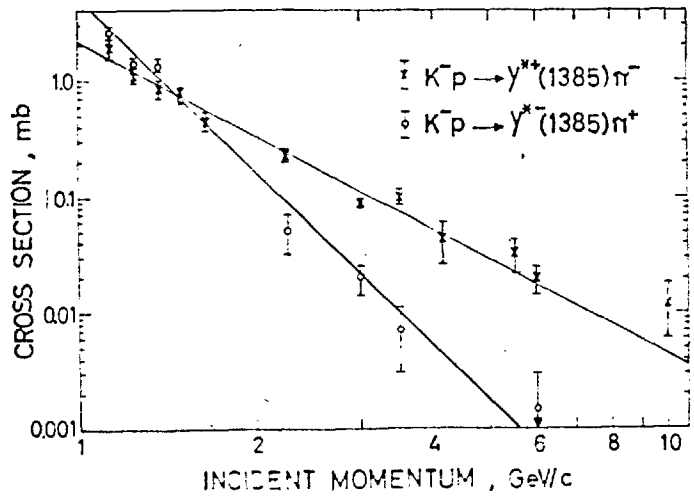


Fig.2 Cross sections as a function of the incident K^- lab momentum for the reactions:

$$K^-p \to Y^{*+}(1385)\pi^-,$$
$$K^-p \to Y^{*-}(1385)\pi^+.$$

The two straight lines have been obtained from fits to the experimental data using the empirical relation $\sigma = K(p_{in}/p_0)^{-n}$.

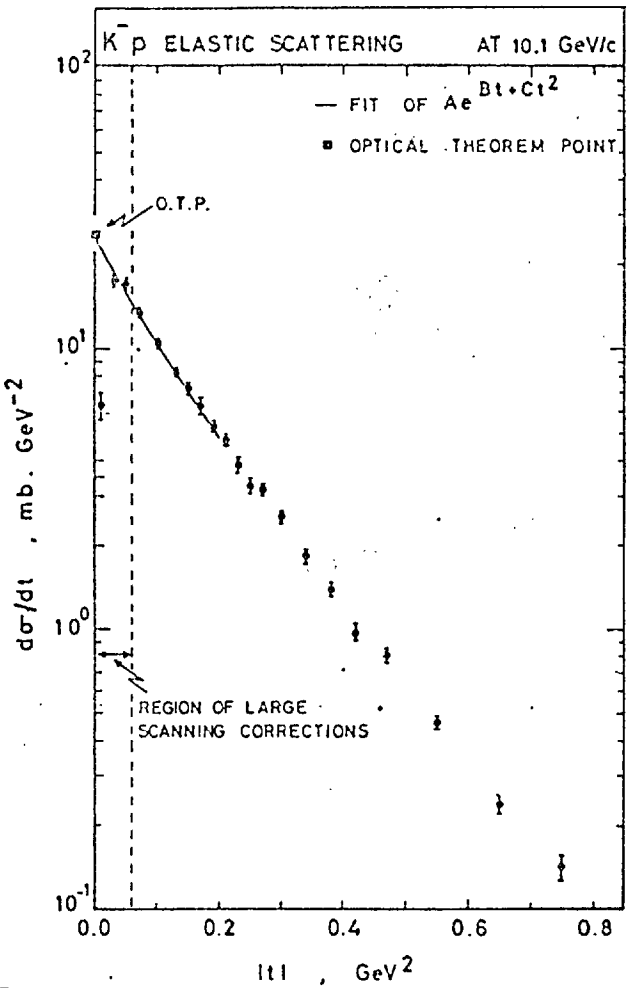


Fig. 3 K^-p elastic differential cross section $d\sigma/dt$ at 10.1 GeV/c for $0 < |t| \leq 0.8$ GeV^2 showing the extrapolation to the optical theorem point (OTP).

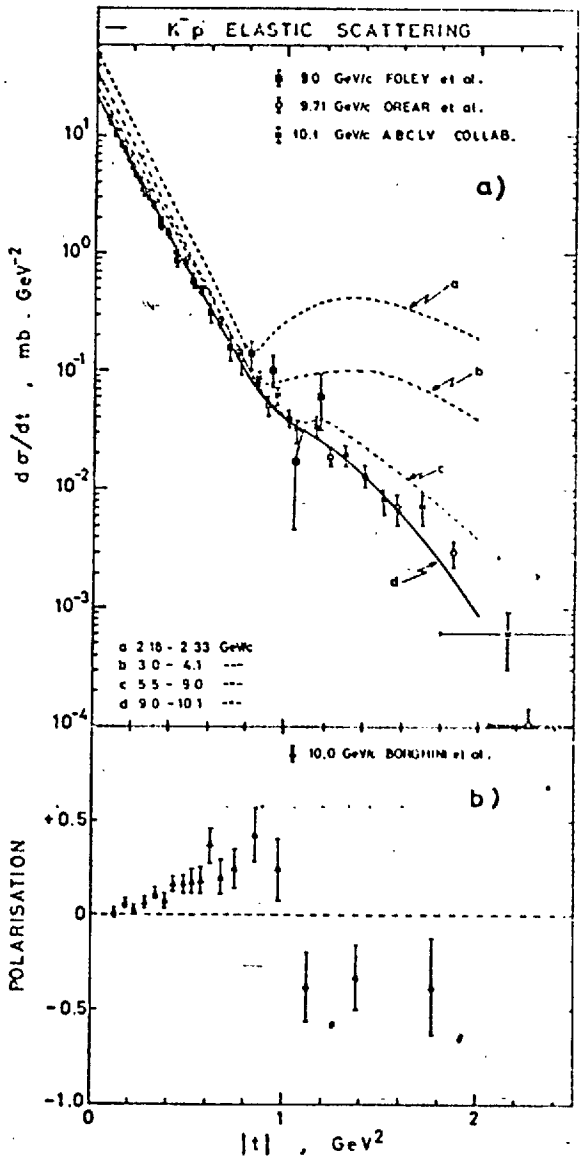


Fig. 4 (a) Compilation of data on the elastic differential cross sections in the $|t|$-range of 0-2.5 GeV^2 for beam momenta near 10.1 GeV/c. (b) Proton polarisation measurements of Borghini et al. at 10.0 GeV/c.

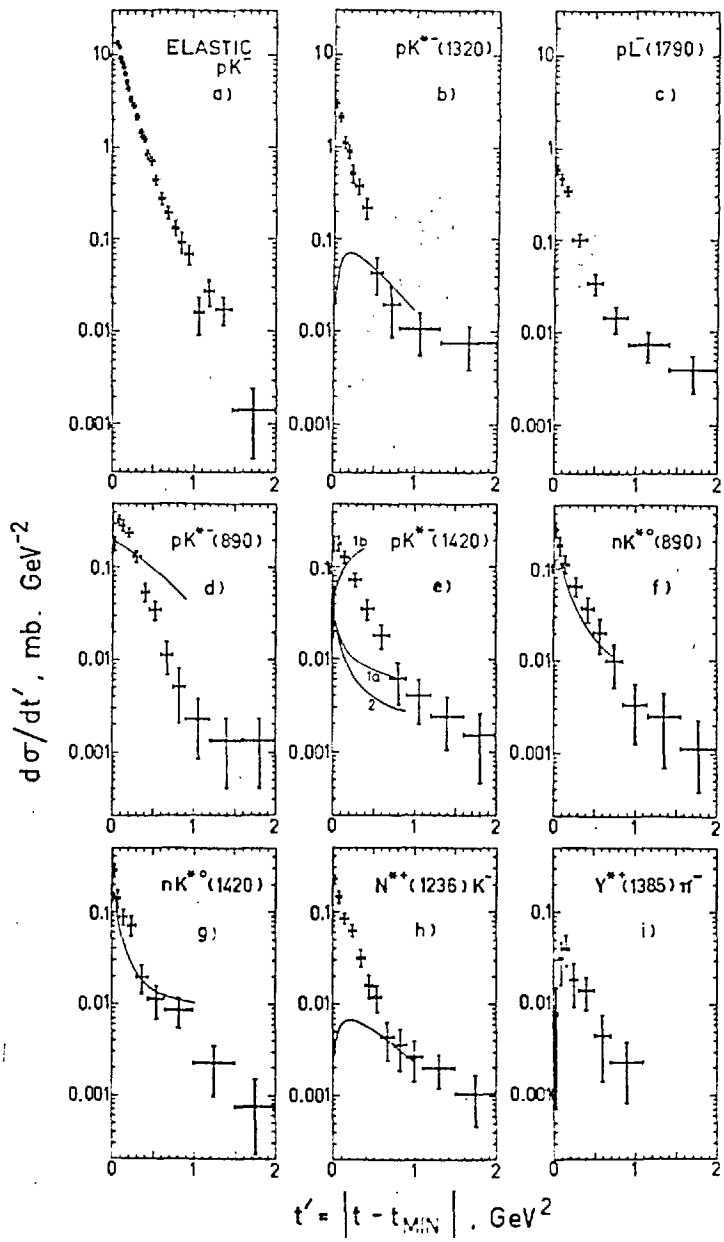


Fig.5 Differential cross section, $d\sigma/dt'$, versus t' for the reactions (a) to (i) in the t' range from 0 to 2.0 GeV^2. The solid lines are the results of absorption model

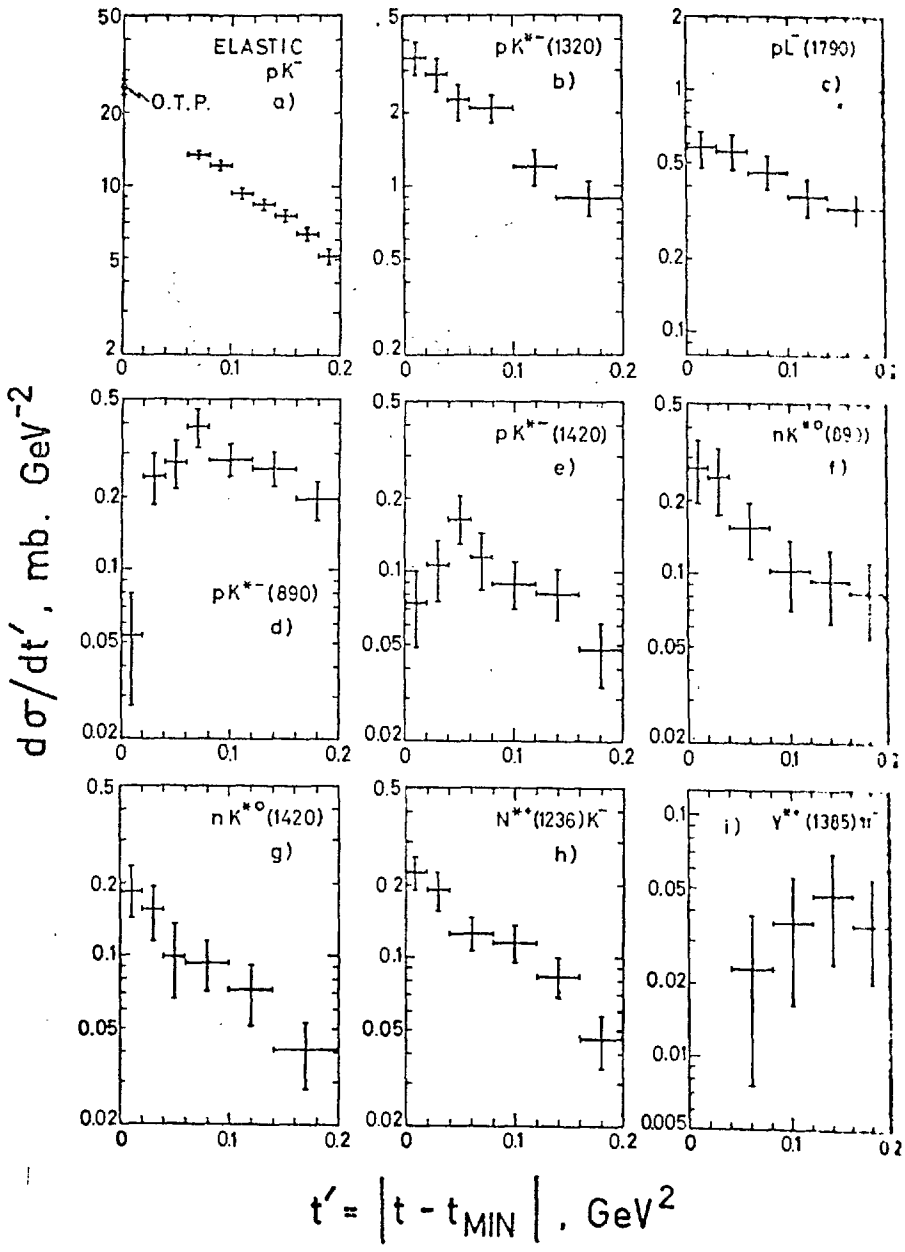


Fig 6 Differential cross sections for reactions (a) to (i) in the small t-region, $0 < t' < 0.2$ GeV^2. For elastic scattering, the value of $d\sigma/dt$ at $t=0$ is calculated from the total cross section using the optical theorem and is indicated as O.T.P.

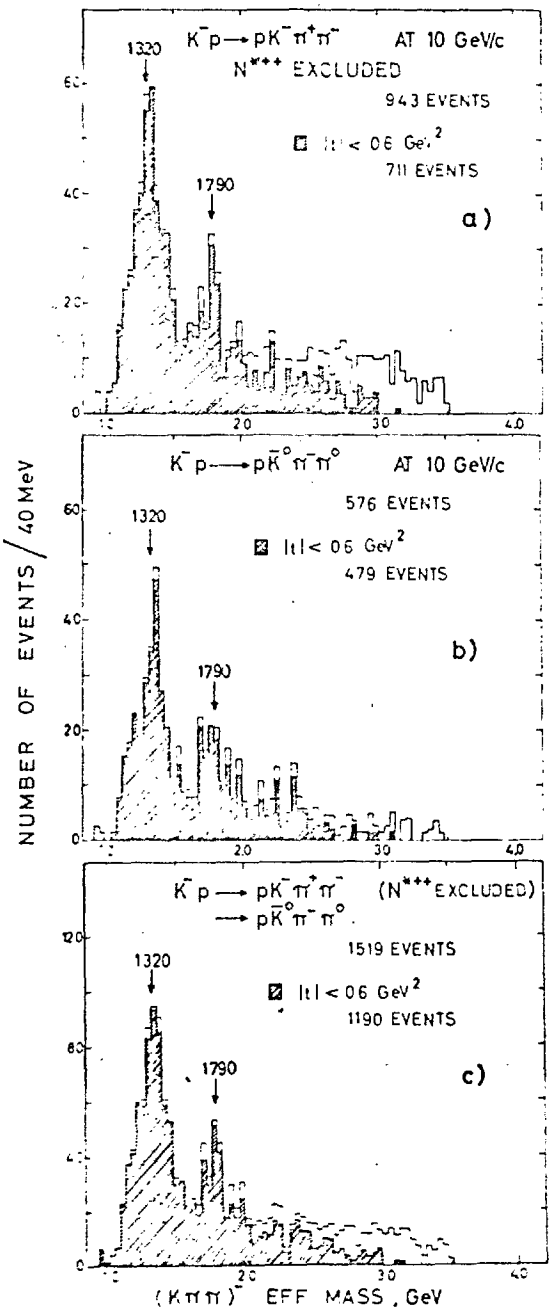


Fig. 7 a) Effective mass distribution of the $(K^-\pi^-\pi^-)$ system for events of reaction (3) (N^{***} excluded). The shaded area corresponds to the events with $|t| < 0.6$ GeV^2. b) Effective mass distribution of the $(\bar{K}^0\pi^-\pi^0)$ system for events of reaction (4). The shaded area corresponds to the events with $|t| < 0.6$ GeV^2. c) Sum of the distributions in a) and b).

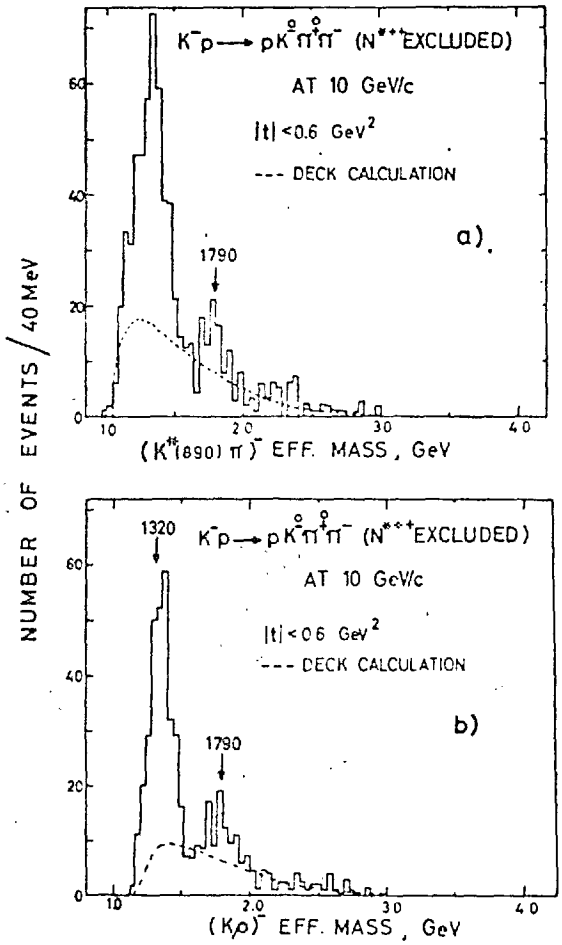


Fig. 8 a) Effective mass distribution of the $(K\pi\pi)^-$ system for events of reactions (3) (N^{*++} excluded) and (4), both with the restriction $|t| < 0.6$ GeV^2, and with the condition that the $(\bar{K}^0\pi^-)$ or $(\bar{K}^0\pi^0)$ or $(K^-\pi^-)$ mass lies in the mass region of the $K^*(890)$ resonance. The Deck curve is drawn as a dotted line. b) Effective mass distribution of the $(K\pi\pi)^-$ system for events of reactions (3) (N^{*++} excluded) and (4), both with the restriction $|t| < 0.6$ GeV^2 and with the condition that the $(\pi^-\pi^0)$ or $(\pi^+\pi^-)$ mass lies in the mass region of the ρ meson. The Deck curve is drawn.

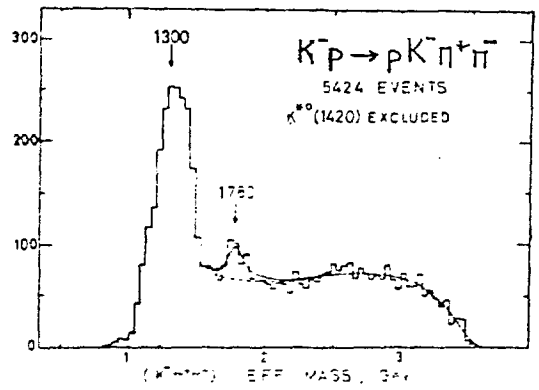


Fig. 9

$(K^-\pi^-\pi^-)$ effective mass distribution for all events except those having $(K^-\pi^-)$ mass in the region 1320–1520 MeV.

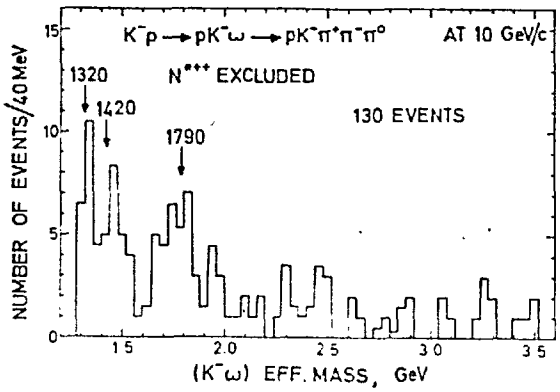


Fig.10 The mass distribution of $(K^-\pi^+\pi^-\pi^0)$ with the restriction that the $(\pi^+\pi^-\pi^0)$ system is in the mass region of the ω meson (Reaction $K^-p \to pK^-\pi^+\pi^-\pi^0$)

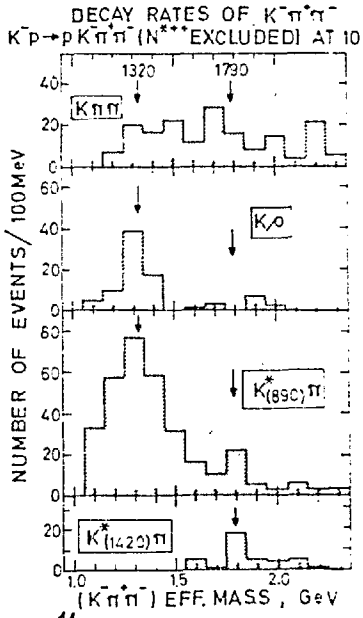


Fig.11 Results of a maximum likelihood fit. The numbers of events of the system $(K^-\pi^+\pi^-)$ from reaction (3) (N^{*++} excluded) decaying into the channels $K^-\pi^+\pi^-$, $K^*(890)^0\pi^-$, $K^-\rho^0$, and $K^*(1420)^0\pi^-$ are given in 100 MeV intervals.

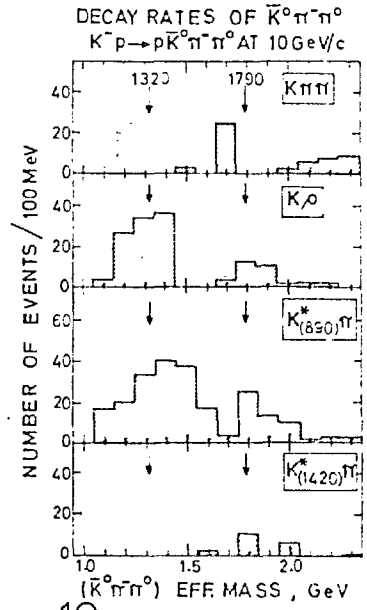


Fig.12 Results of a maximum likelihood fit. The numbers of events of the system $\bar{K}^0\pi^-\pi^0$) from reaction (4) decaying into the channels $\bar{K}^0\pi^-\pi^0$, $K^*(890)^-\pi^0$ or $K^*(890)^0\pi^-$, $\bar{K}^0\rho^-$ and $K^*(1420)^-\pi^0$ or $K^*(1420)^0\pi^-$ are given in 100 MeV intervals.

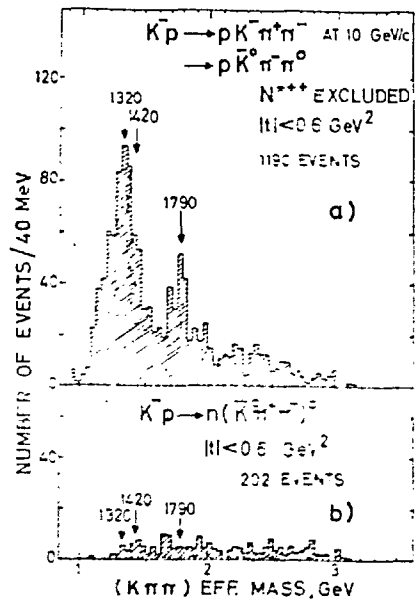


Fig 13 a) $(K\pi\pi)^-$ effective mass distribution for reactions (3) (with N^{*++} excluded) and (4), with $|t| < 0.6$ GeV^2. b) $(K\pi\pi)^0$ effective mass distribution for reaction $K^-p \to n\bar{K}^0\pi^+\pi^-$

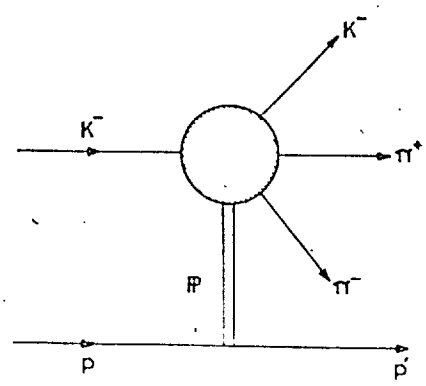


Fig.14 Schematic graph for the diffractive contribution to the process $K^- p \to pK^-\pi^+\pi^-$. The symbol P is used to represent the pomeron.

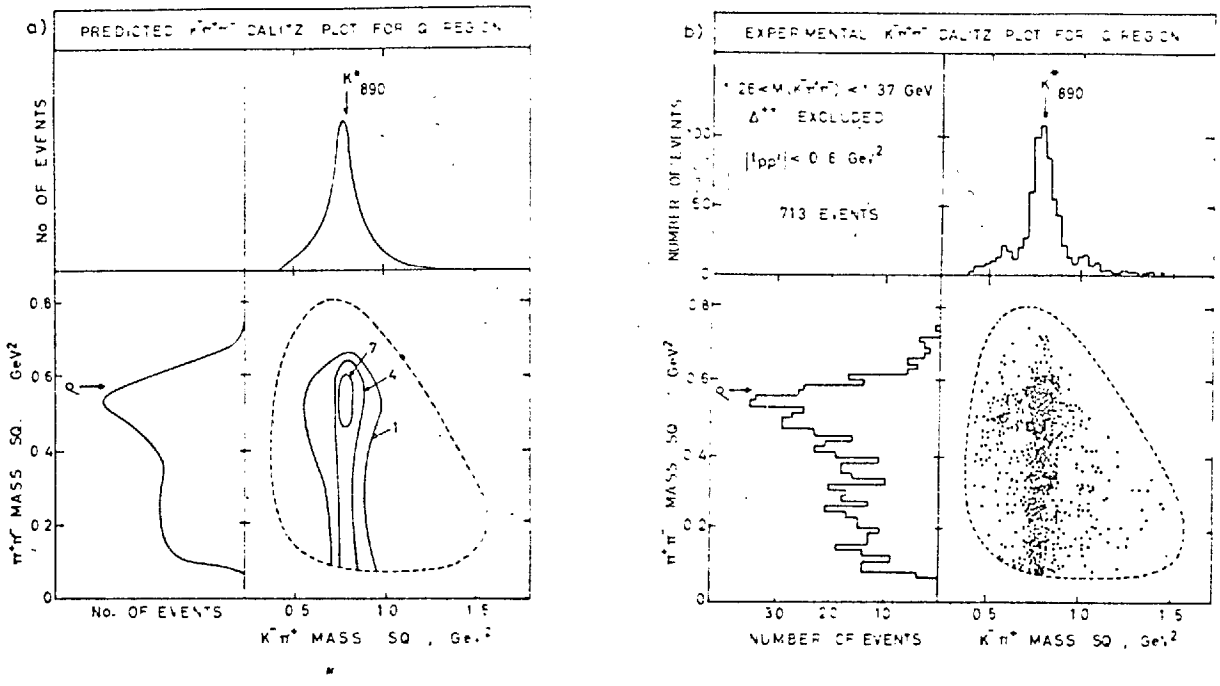


Fig.15 (a) Predicted $K\pi\pi$ Dalitz plot for the Q-region. The contours correspond to densities in the ratio 7 : 4 : 1.
(b) Experimental $K\pi\pi$ Dalitz plot for the Q-region.

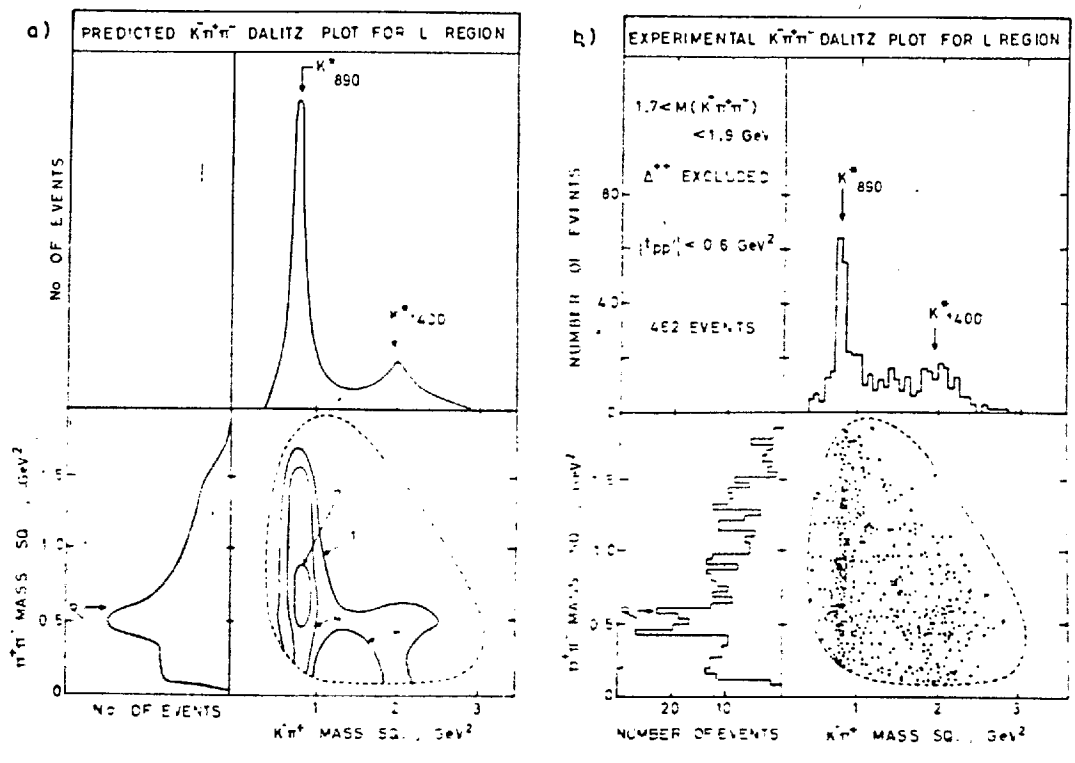


Fig.16 (a) Predicted $K\pi\pi$ Dalitz plot for the L-region. The contours correspond to densities in the ratio 7 : 4 : 1.
(b) Experimental $K\pi\pi$ Dalitz plot for the L-region.

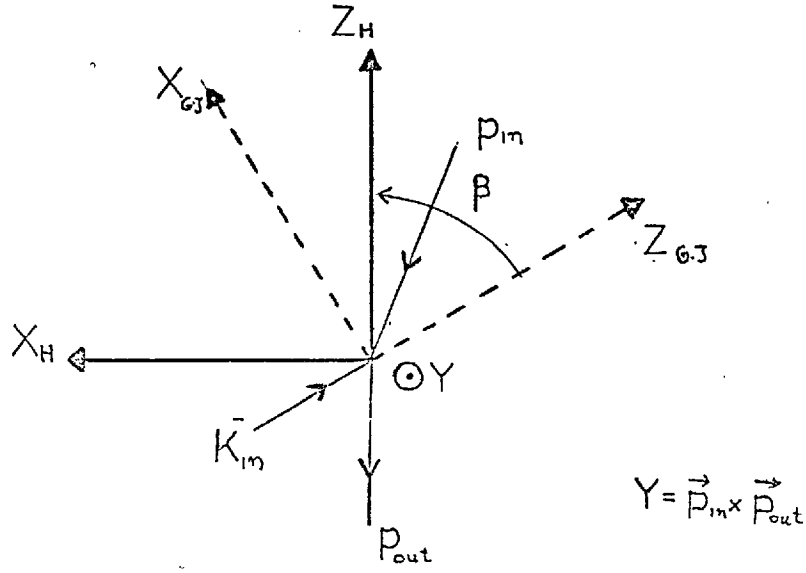


Fig.17

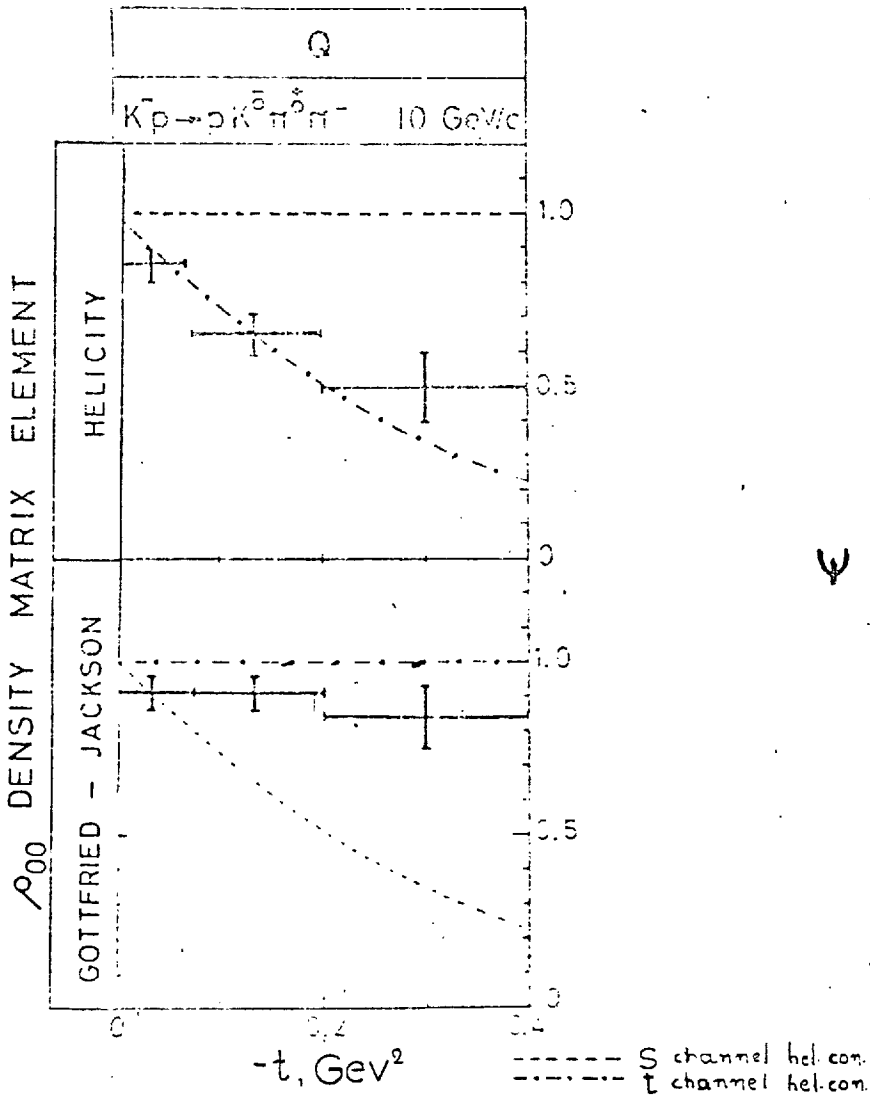


Fig.18a

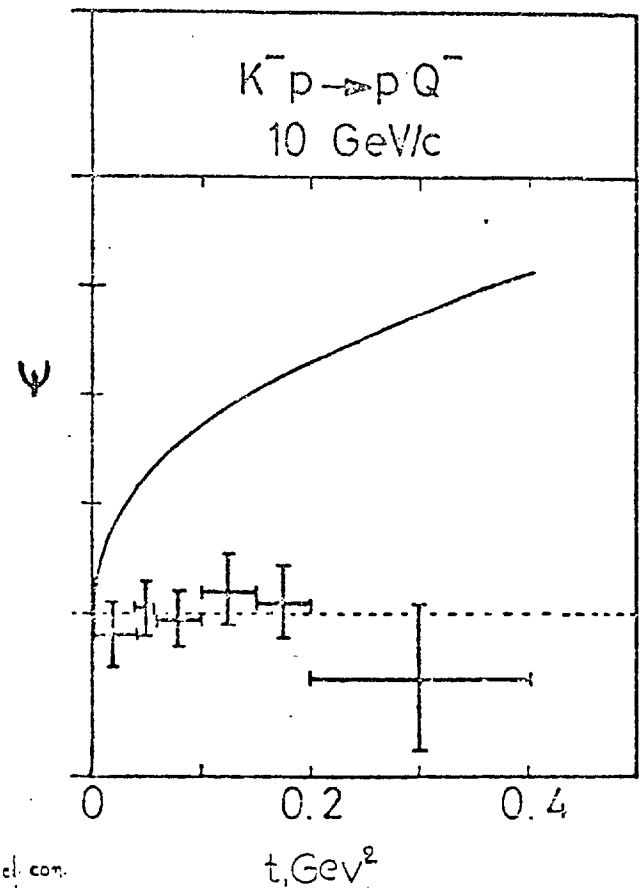


Fig.18b

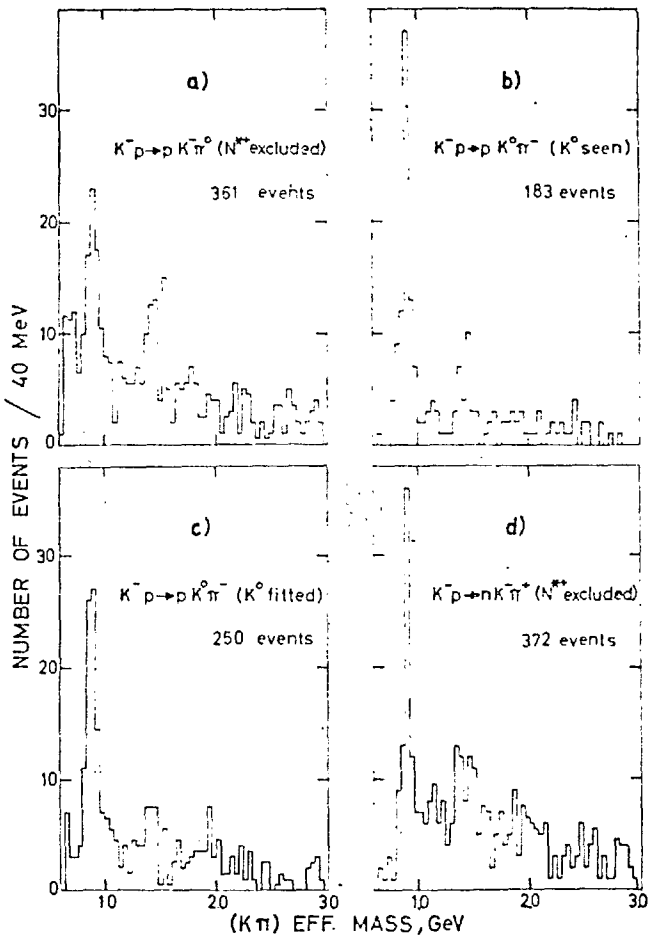


Fig.19 Effective mass distribution of the $(K\pi)$ systems in the reactions $K^-p \to pK^-\pi^0$ (a), $K^-p \to pK^0\pi^-$ (b) and (c), and $K^-p \to nK^-\pi^+$ (d) at 10.1 GeV/c. For reactions (a) and (d) the events for which the $(p\pi^0)$ and $(n\pi^+)$ systems, respectively, are in the mass region of the N^{*++} isobar (1.12–1.34 GeV) have been excluded.

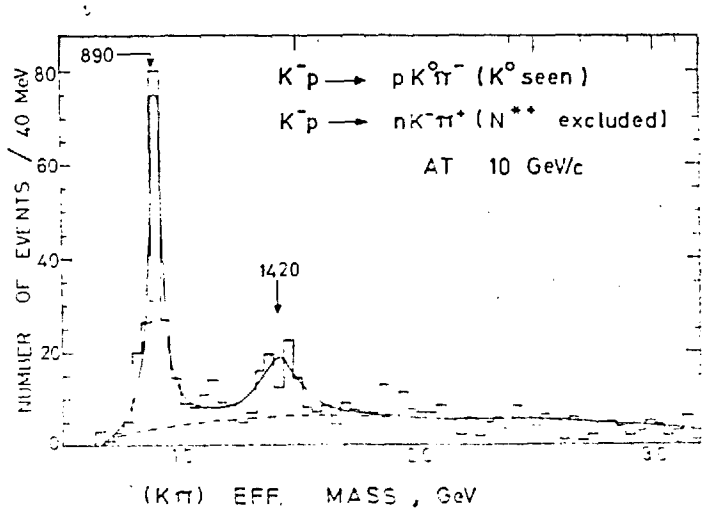


Fig.20 Effective mass distribution of the $(K\pi)$ systems in reactions (b) and (d) fitted with two Breit-Wigner curves and the hand-drawn background shown.

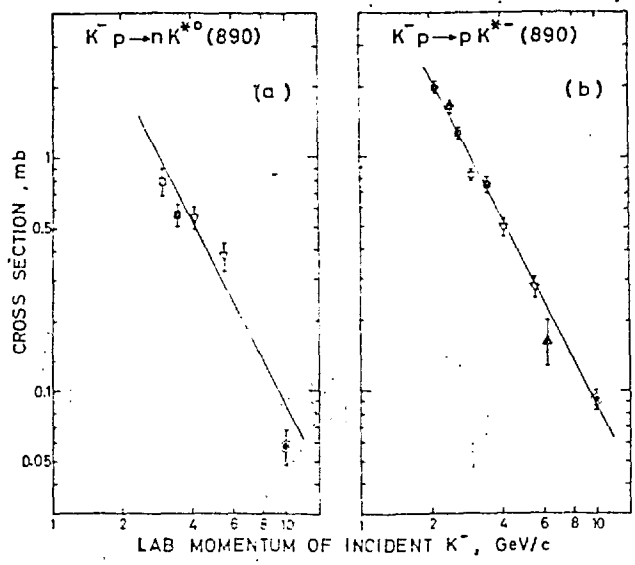


Fig 21 Total cross section for $K^-p \to nK^{*0}(890)$ and $K^-p \to pK^{*-}(890)$ versus the laboratory momentum of the incoming kaon.

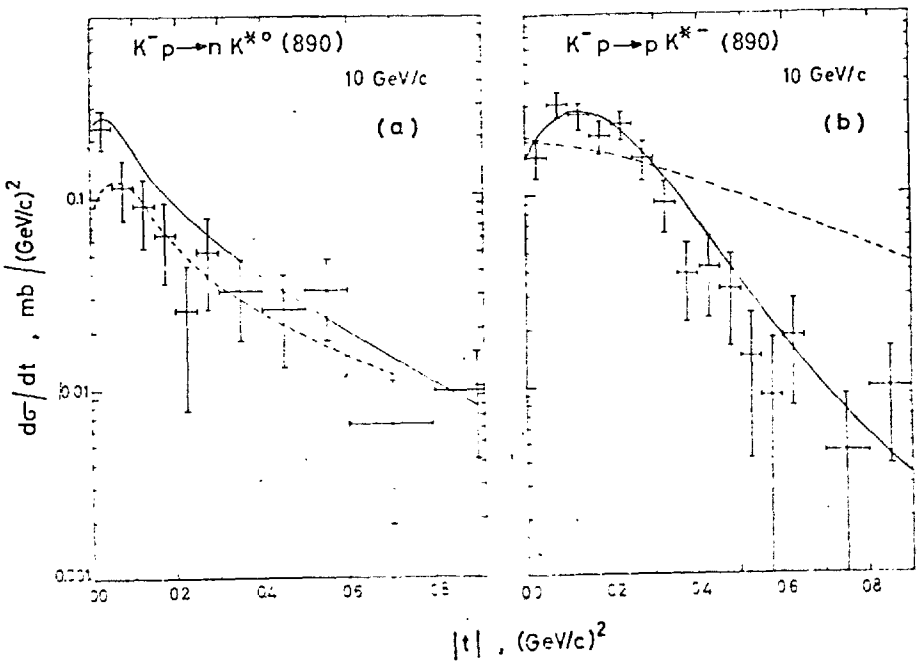


Fig 22 Differential cross section for $K^-p \to nK^{*0}(890)$ (fig. a) and $K^-p \to pK^{*-}(890)$ (fig. b) at 10 GeV/c. The dotted lines are predictions of the absorption model, the solid lines predictions of a Regge pole model with the assumptions explained in the text.

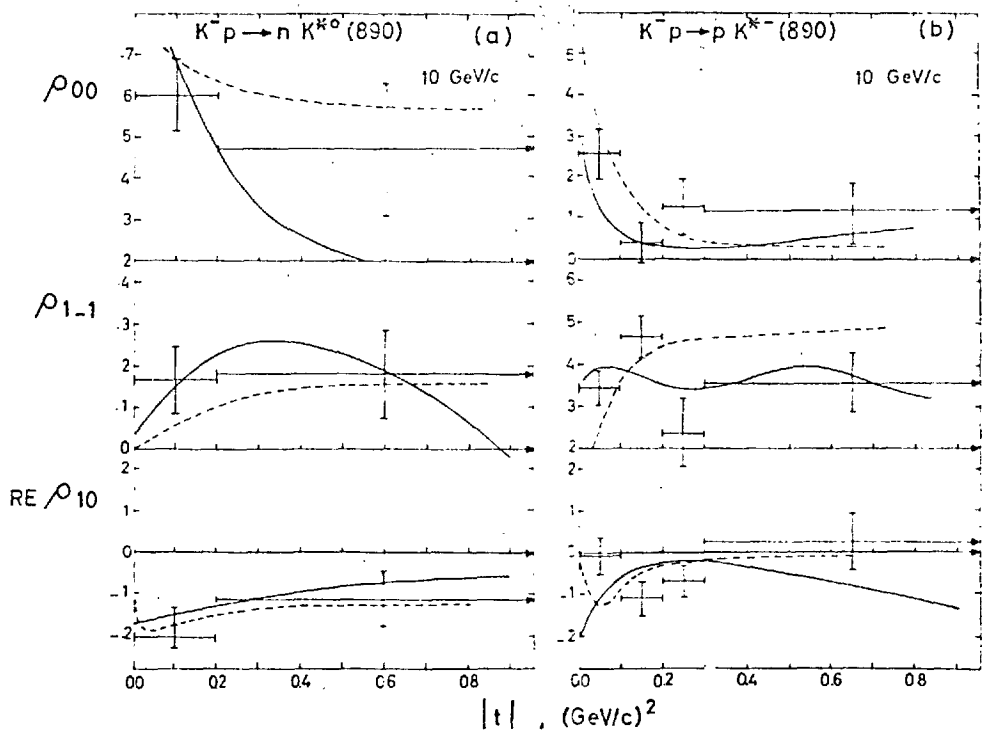


Fig23 Dependence of the ρ_{mn} density matrix elements on the squared four-momentum transfer t . The dotted lines are predictions of the absorption model, the solid lines are predictions of a Regge pole model with the assumptions explained in the text.

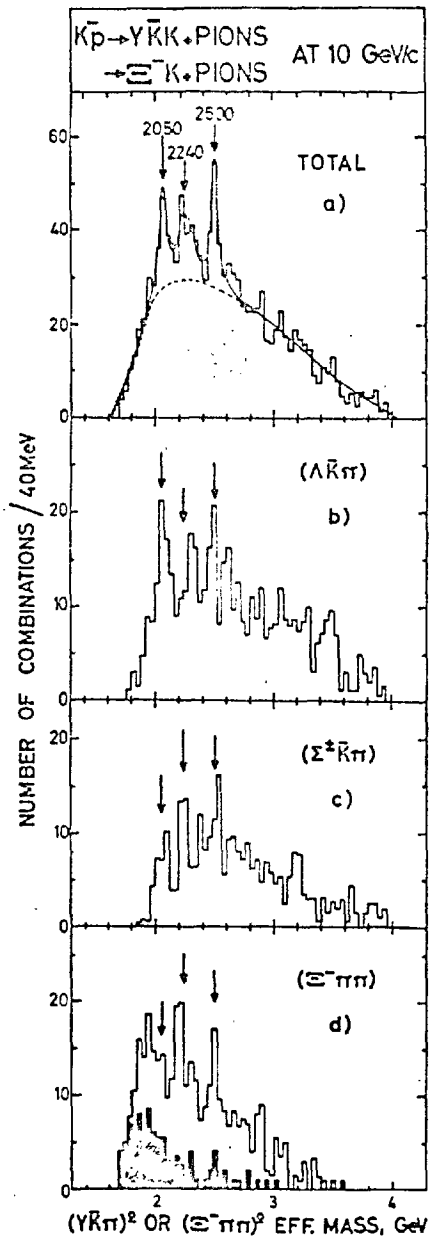


Fig 24 Effective mass distributions of the $(Y\bar{K}\pi)$ and $(\Xi^-\pi\pi)$ systems of charge 0 and −1.
a) $(\Lambda\bar{K}\pi)$, $(\Sigma^-\bar{K}\pi)$, $(\Sigma^+\bar{K}\pi)$ and $(\Xi^-\pi\pi)$ systems.
b) $(\Lambda\bar{K}\pi)$ systems.
c) $(\Lambda^-\bar{K}\pi)$ and $(\Sigma^+\bar{K}\pi)$ systems.
d) $(\Xi^-\pi\pi)$ systems. The shaded area represents the $\Xi(1530)\pi$ combinations.

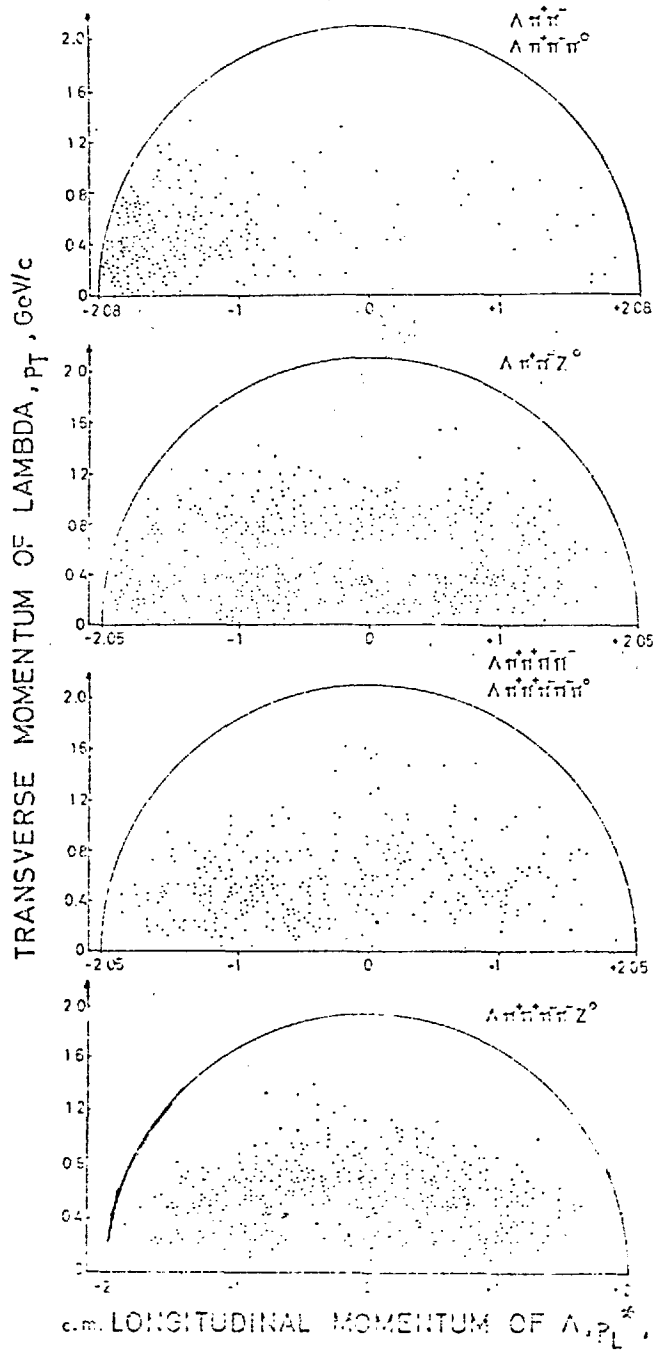


Fig. 25 The plot of transverse momentum, p_T, versus centre-of-mass longitudinal momentum, p_L^*, for the lambdas for reactions $K^-p \rightarrow \Lambda$ + pions

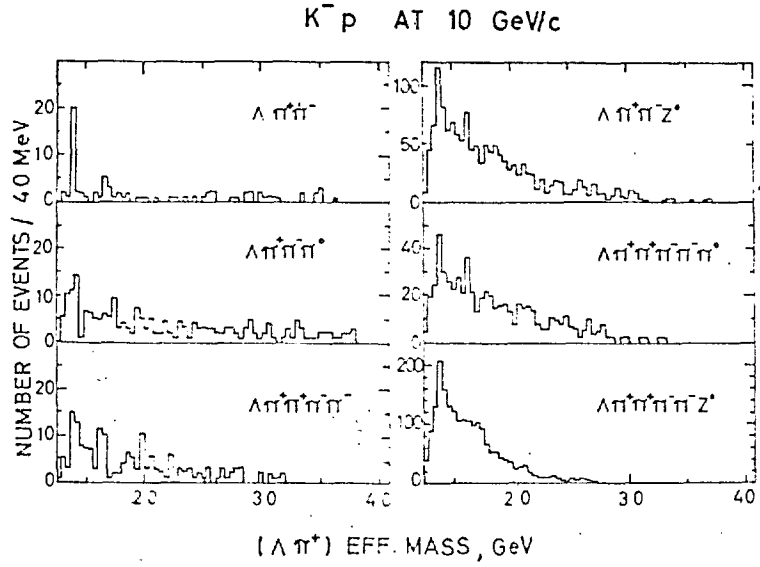


Fig 26 The $\Lambda\pi^-$ effective mass distributions for reactions $K^-p \rightarrow \Lambda$ + pions

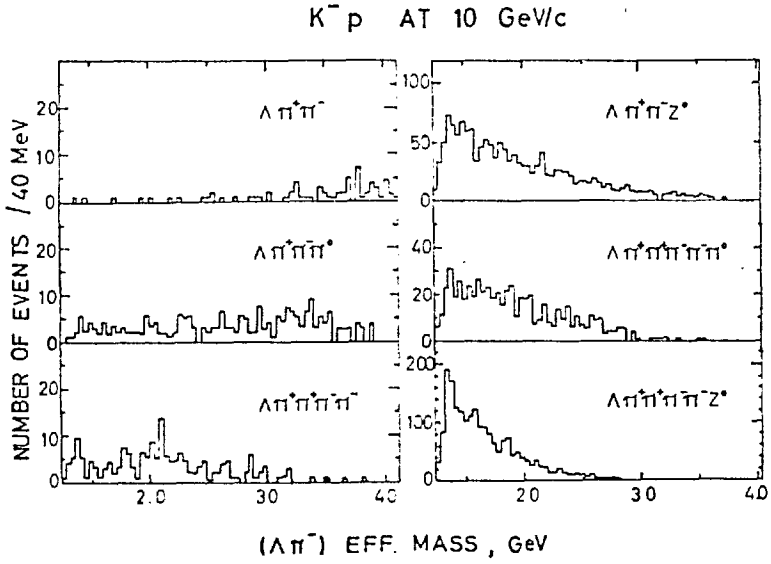


Fig 27 The $\Lambda\pi^-$ effective mass distributions for reactions $K^-p \rightarrow \Lambda$ + pions

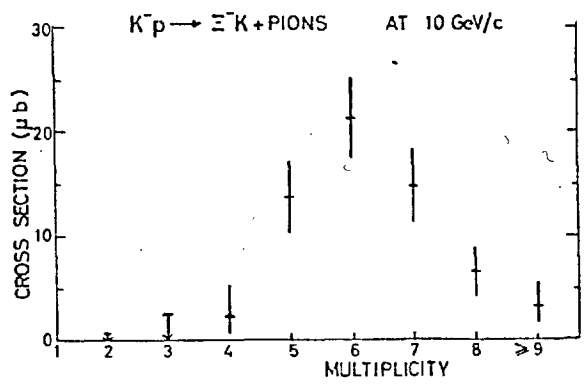


Fig 28 Cross sections for reaction $K^-p \rightarrow \Xi^-K$ + pion(s), at 10 GeV/c as a function of multiplicity of particles in the final state.

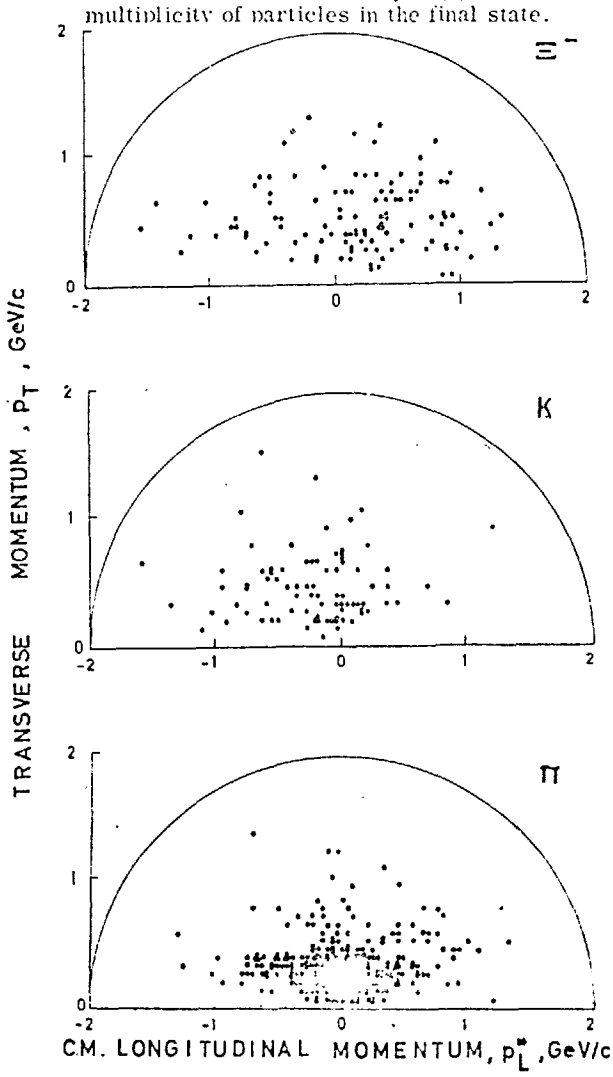


Fig 29 Transverse momentum versus c.m. longitudinal momentum for Ξ^- events of all multiplicities.

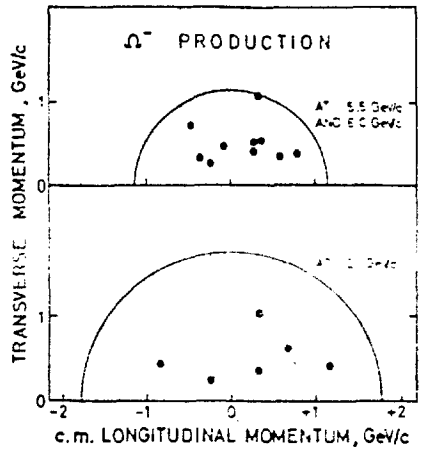


Fig 30 Distribution of Ω^- hyperons in the plane of transverse momentum versus c.m. longitudinal momentum, at 5.5 and 6.0 GeV/c (top graph) and at 10 GeV/c (bottom graph). The contours correspond to maximum c.m. momentum allowed in 3-body reaction at 6 and 10 GeV/c, respectively.

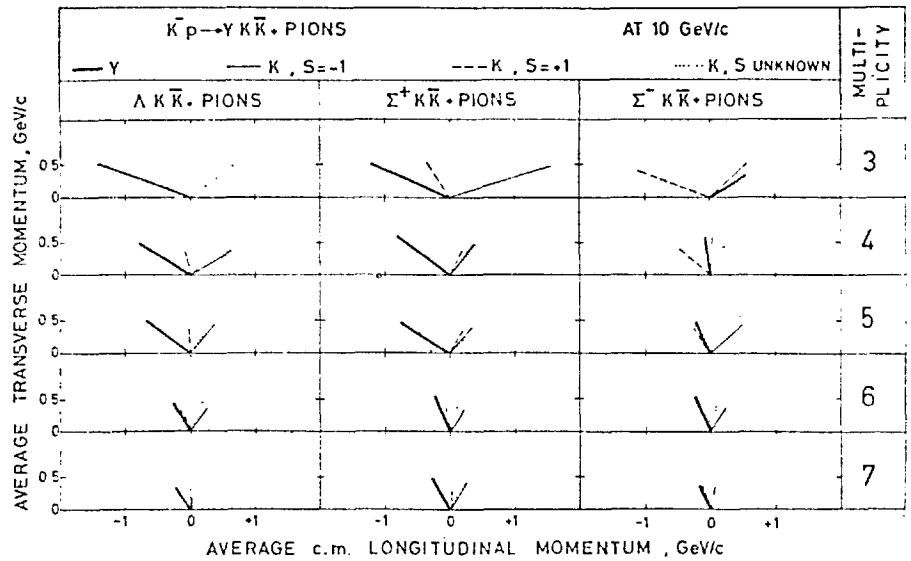


Fig. 31 c.m. momentum vectors, composed of the average c.m. longitudinal momentum and average transverse momentum, for hyperons (thick line), antikaons (thin line), kaons (dashed line) and kaons with unknown strangeness (dotted line) from the Λ, Σ^- and Σ^+ fitted channels of multiplicity 3, 4, 5, 6 and 7.

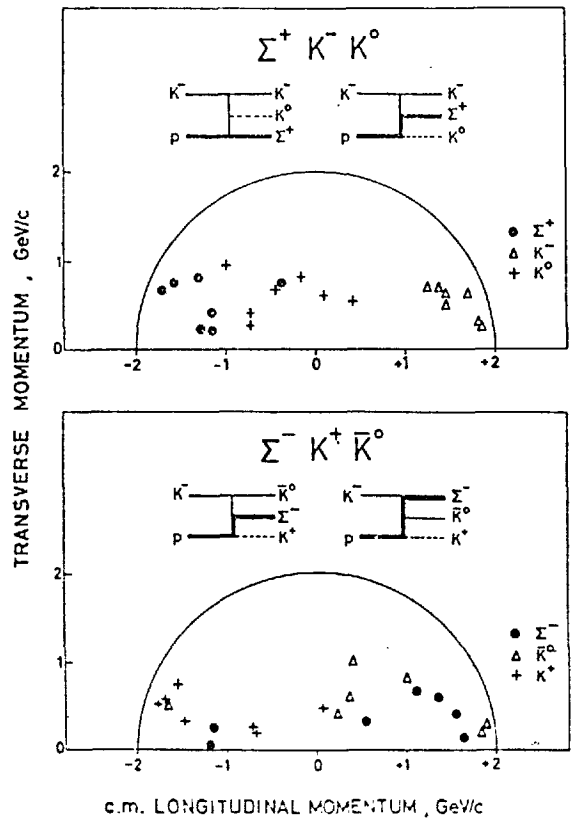


Fig. 32 Transverse momentum plotted against the c.m. longitudinal momentum for the particles produced in the channels $\Sigma^+K^-K^0$ and $\Sigma^-K^+\bar{K}^0$. The multiperipheral graphs contributing are shown.

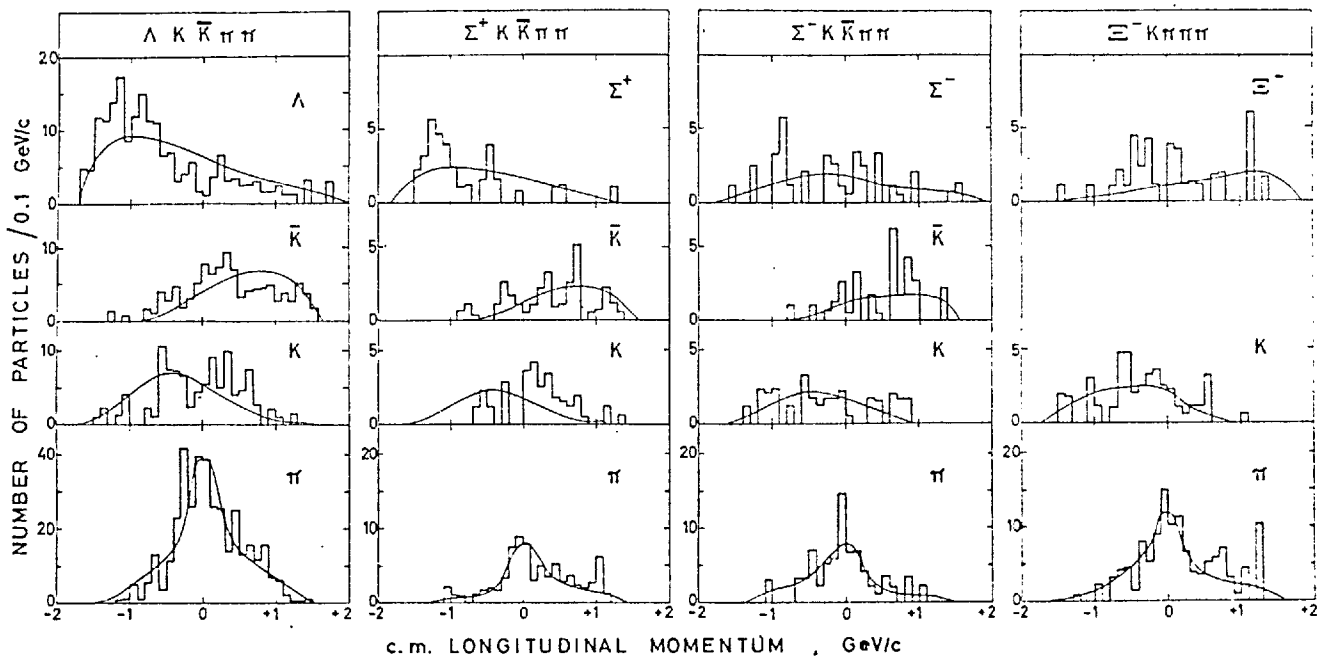


Fig 33 Distributions of the c.m. longitudinal momentum for hyperons, antikaons, kaons and pions produced in five-body final states, compared with the predictions of the multiperipheral model (see text).

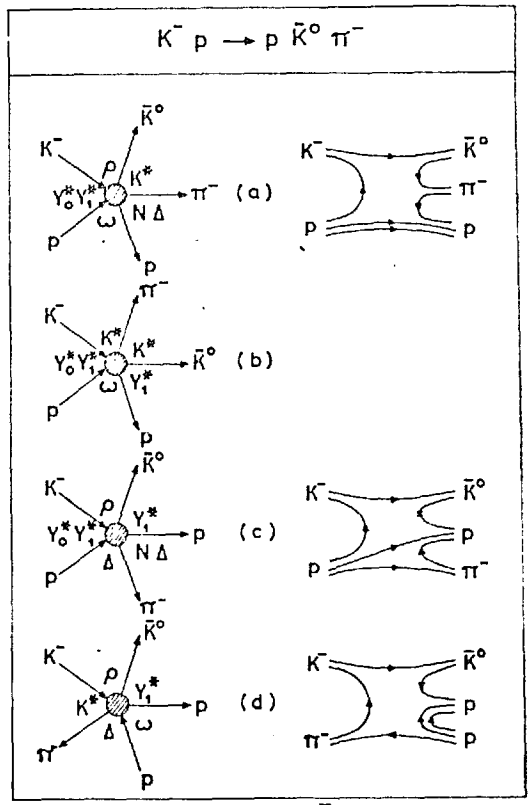


Fig. 34 The four graphs describing $K^- p \to p \bar{K}^0 \pi^-$ in the Veneziano model and the Harari-Rosner diagrams corresponding to the three allowed graphs.

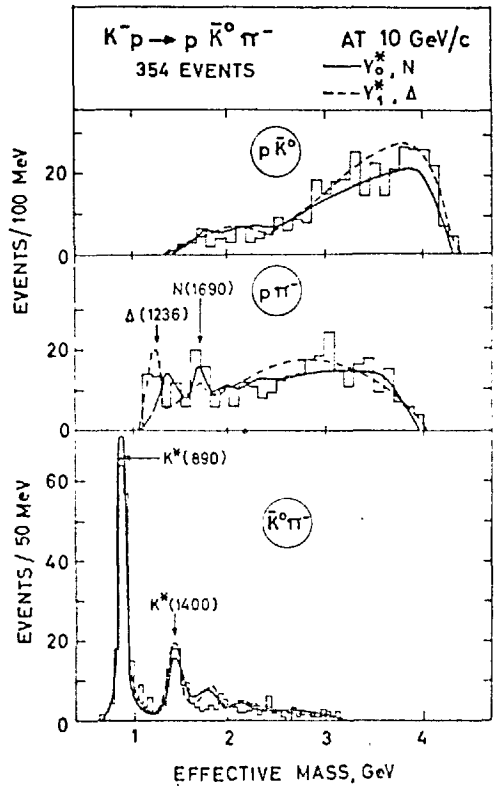


Fig. 35 Experimental distributions of the $(p\bar{K}^0)$, $(p\pi^-)$ and $(\bar{K}^0\pi^-)$ effective mass at 10 GeV/c. The curves are the Veneziano model predictions with the sets of assumptions and parameters described in subsect. 4.1

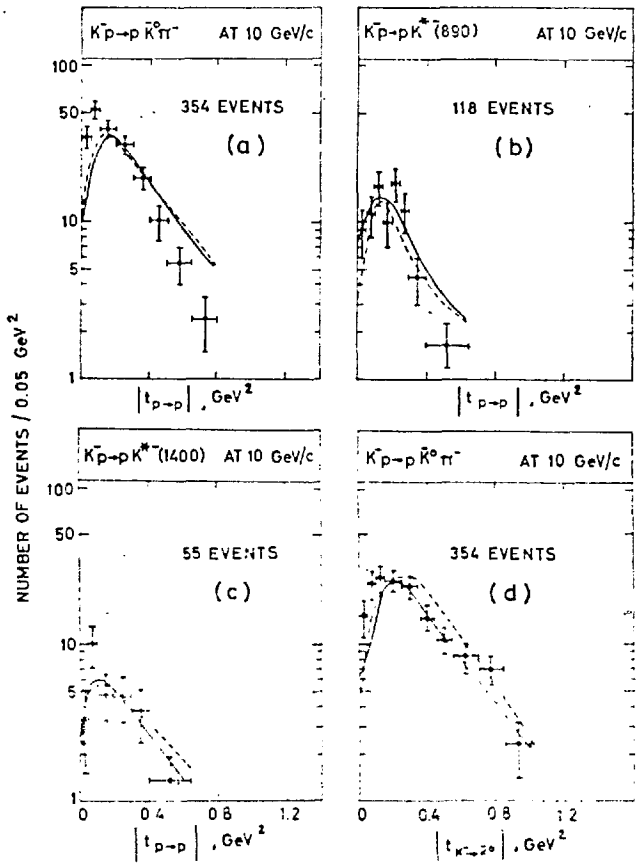


Fig. 36 Experimental results for the indicated differential cross sections at 10 GeV/c. The curves are the Veneziano model predictions with the sets of assumptions and parameters described in subsect. 4.1

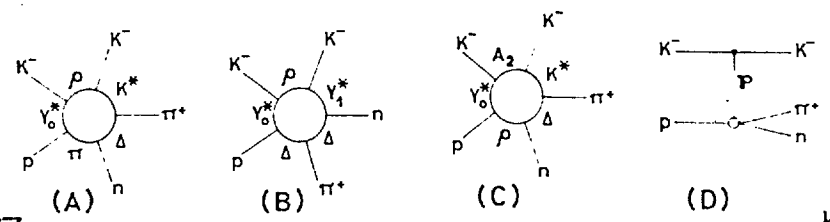


Fig. 37 Dual diagrams and the pomeron exchange diagram describing reaction $K^-p \to nK^-\pi^+$. The dominant trajectories in each channel are also indicated.

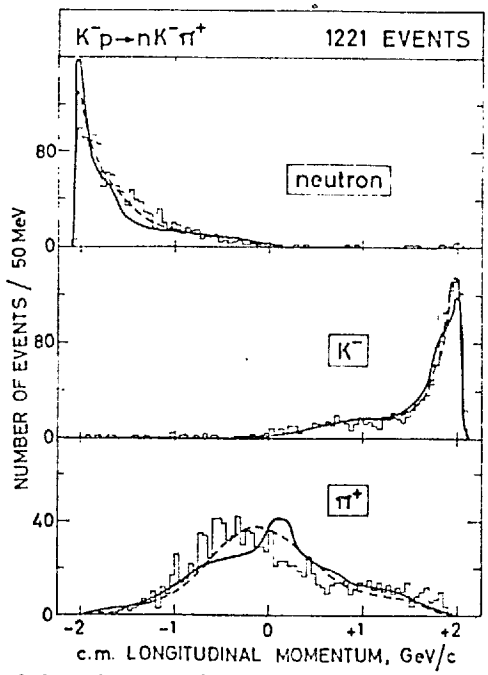


Fig. 38 Experimental distributions of the c.m. longitudinal momentum of the particles produced in $K^-p \to nK^-\pi^+$ at 10 GeV/c. The curves are the Veneziano model predictions described in subsect. 4.2.

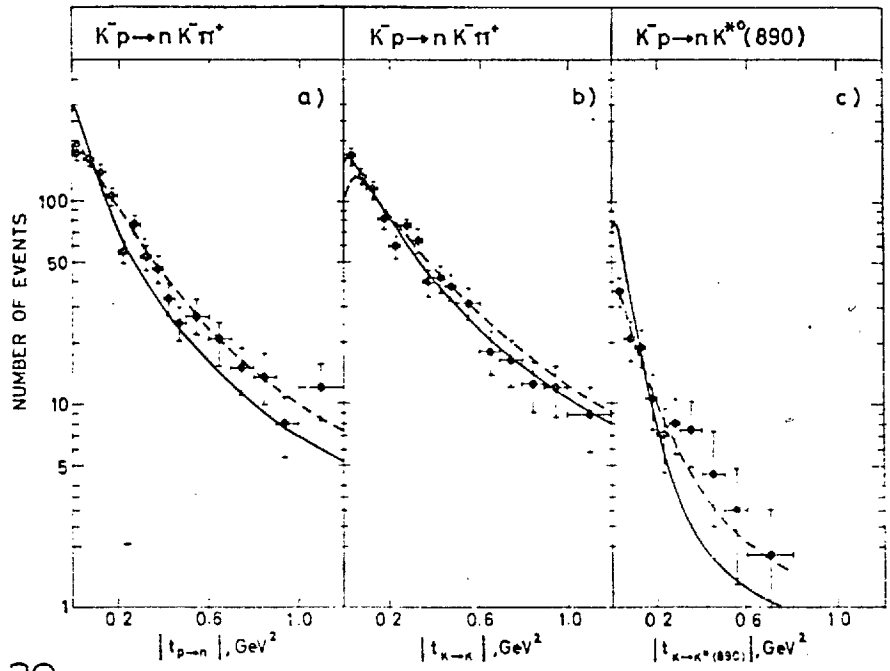


Fig. 39 Experimental results for the indicated differential cross sections at 10 GeV/c. The curves are the Veneziano model predictions described in subsect. 4.2.

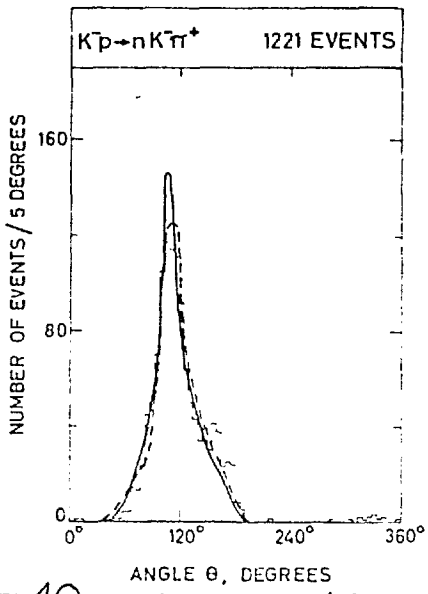


Fig. 40 Polar distribution $dN/d\theta$ of the events from $K^-p \to nK^-\pi^+$ at 10 GeV/c. The curves are the Veneziano model predictions described in subsect. 4.2

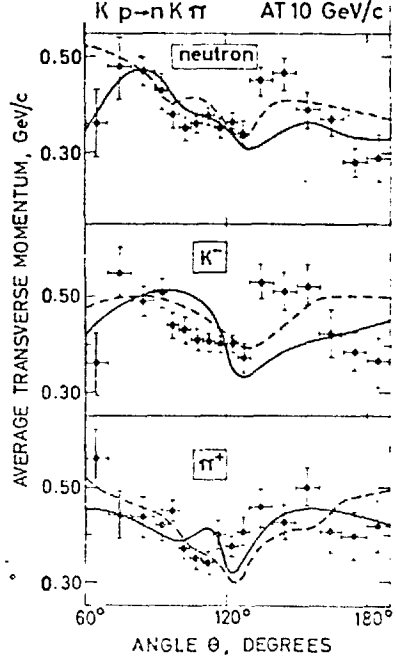


Fig. 41 Polar distribution of the average transverse momentum of the secondaries from $K^-p \to nK^-\pi^+$. The curves are the Veneziano model predictions described in subsect. 4.2

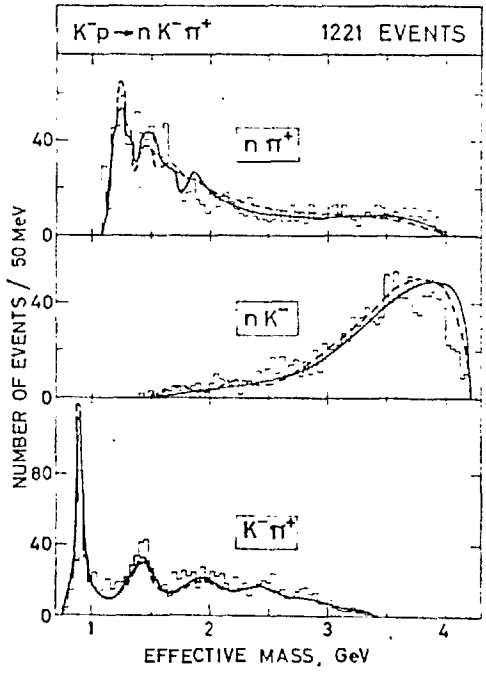


Fig. 42 Experimental distributions of the $(n\pi^+)$, (nK^-) and $(K^-\pi^+)$ effective mass. The curves are the Veneziano model predictions described in subsect. 4.2

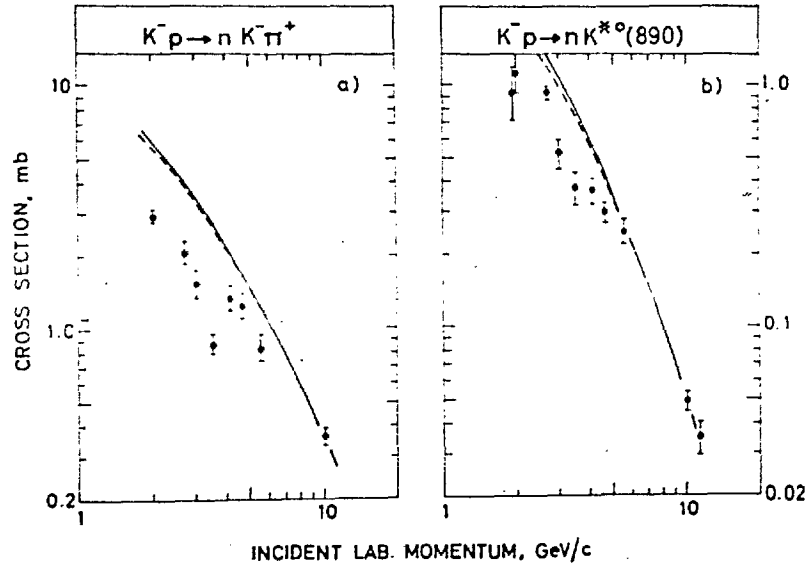


Fig. 43 Variation of the total cross sections for reactions shown with the momentum of the incident kaon, in the lab system. The curves are the Veneziano model predictions described in subsect. 4.2

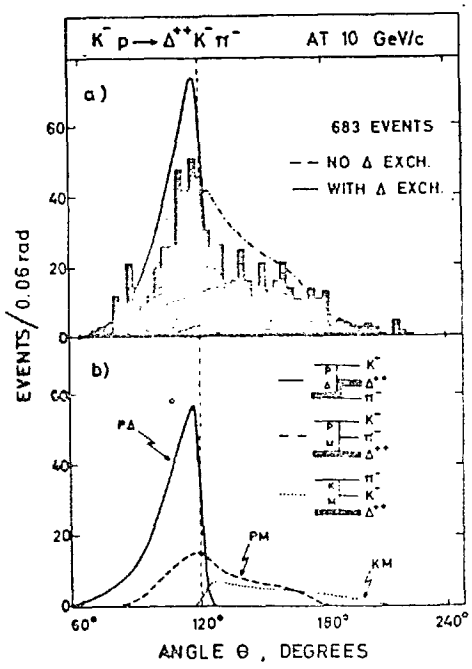


Fig.44 Polar distribution $dN\,d\theta$ of the events from reaction $K^-p \to \Delta^{--}K^-\pi^+$ at 10 GeV/c (fig.44a), where θ is the Van Hoye angle. The dot-dashed lines give the CLA predictions without Δ-exchange and the full lines give the prediction including Δ-exchange. All curves are normalized to the total number of events. The individual CLA exchange graphs considered for the reaction and their contributions to the polar distribution $dN/d\theta$ are in fig.44b. The Δ^{--} mass band is defined as 1.12 - 1.34 GeV.

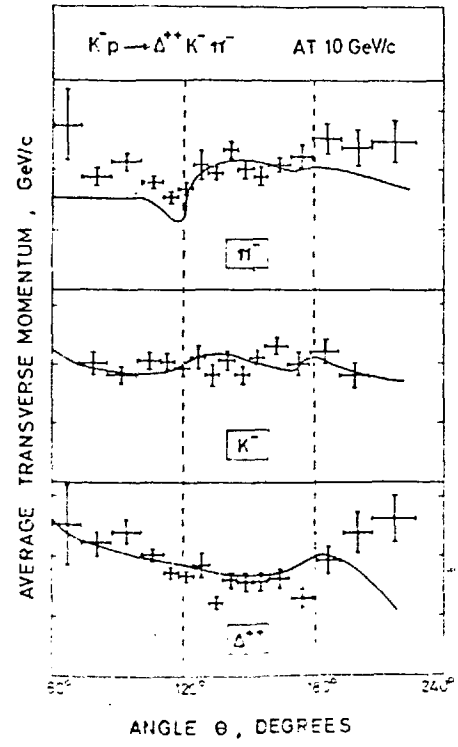


Fig.45

AS AN EPILOGUE

Some Hesitant Thoughts on the Future

The reactions, whose study has formed the main part of the work in this thesis, are typical examples of high multiplicity final states in hadronic collisions. The phenomena of multiparticle production play a role of great importance in the energy reached by the present generation of accelerators, and they have received the due attention in recent years. The new generation of accelerators, shifting the center of research from the energy domain of a few GeV to that of several hundred GeV, will make available high quality data on these processes and will establish a link with the energy region of cosmic rays.

At first, a better understanding of the dynamics governing the production of many particles is essential. The difficulty here rises mainly from the large number of independent variables one has to deal with and the related problem of organizing the existing data. The lack of a true theory makes unclear the direction towards which one should move, but experience with the longitudinal phase space technique suggests that the problem can be mastered to multiplicity four; higher multiplicities would perhaps be qualitatively no more difficult.

From the theoretical point of view, the use of dual amplitudes of the multi-Veneziano type emerges as a significant advance. But the unitarity question still remains open, and the treatment of fermions will become more important as the analyses become more detailed. Also, it is to be emphasized that the complexity of the expressions and the consequent amount of technical effort increases with the particle multipicity. An important task will perhaps be to simplify the Veneziano form for large number of particles without losing its attractive features. Crude though they are, the models which are already calculable

for these processes (the CLA multiperipheral model for instance) do provide us with the indication that our picture is basically correct. It seems, however, that this picture will only be valuable for intermediate energies, say up to 20 GeV or so; above that, the reactions will be dominated by vacuum exchanges, and even at the phenomenological level the emphasis will be posed at other features and regularities.

* * *

Needless to say, the progress that high energy physics has made in the last 20 years is impressive. A great number of particles have been discovered and succesfully assigned to supermultiplets. But we still don't understand the law of force that makes hypothetical quarks combine to form particles, or particles combine to form other particles. If quarks do indeed "exist", they could perhaps be created and detected by a giant accelerator, such as the one now contemplated for construction in Europe. The ageold search for ultimate design in matter would then have reached a deeper layer of the physical reality. And yet, another major question awaits some anser: Are the four basic forces of nature really independent? Some physicists believe that they are not, and the hope remains for a unified theory interelating them. Though (even in science) the historical comparisons are risky, today's situation bears a similarity with that of the early twenties, when the periodic table of the elements was known, but the great theoretical breakthrough of quantum mechanics was needed to establish a true understanding of nature at the atomic level.

In fact, as in all science, progress is made constantly in physics; the ideas though to revolutionize our thinking usually come from rather unexpected directions. The reversal of parity conservation in weak processes, discovered in the past decade, has led the physicists to a whole new way of approach; yet before Lee and Yang made their famous suggestion, the preserving of mirror symmetry by nature was a self evident truth. This is a revealing experience one perhaps ought to have in mind when trying to anticipate the future.

ACKNOWLEDGEMENTS

> ...If the ordinary man sees a bird for some years, which is not normally seen, he immediately gives it a name, and a characteristic name. But take ten learned men and how incapable they are of finding a name. Usually they can think of nothing better than calling the animal or the plant after their own names.
>
> KIERKEGAARD

Professor C.C. Butler presented me with the opportunity to work with the High Energy Group of Imperial College. The advice offered by Dr. S.J. Goldsack in the subsequent years assisted in the orientation of my research and valuably influenced its progress. Mr. N.C. Barford supervised my studies and made many useful suggestions in reading the manuscript of this document. To them I am indebted.

Of much benefit to me was the visit to our group of Dr. G. Otter from Vienna. His guidance and criticism has proved to be of exceptional value for this work, and are recalled with gratitude.

To the cooperative effort required by the experiment, all my colleagues contributed accordingly. Particular thanks are due to Dr. M. Mermikides, a colleague and a friend; he showed a constant interest in my work and was always willing to discuss its specific problems.

The success of an experiment in high energy physics depends in fact on the cooperation, mostly in anonymity, of numerous scientific and technical staff. It is to all these people--from the accelerator crews to the measurers in each of the laboratories--I wish also to express my thanks. Special mention deserve Miss U. Urqhart and

Mrs. J. Davies, efficient and charming technical assistants, and A. Jamdagni, who promptly provided his programming experience.

Lastly, I am grateful to the Greek "Committee of Technical Assistance", which awarded me a grant for postgraduate studies, and to the College, for a subsequent post as Research Assistant.